Theoretical Investigations of Solid interfaces:

1. The Position of The Fermi Level at

a Metal-Semiconductor Interface

2. Geometric Lattice Match and Its Application to Heteroepitaxy

3. Ab-initio Calculation of the Elastic Properties of Silicon,

Using Small Clusters

Thesis by

Amikam Zur

In Partial Fulfillment of the Requirements

for the Degree of

Doctor of Philosophy

California Institute of Technology

Pasadena, California

Submitted: December 20, 1983

To my parents

ACKNOWLEDGEMENTS

I would like to thank Dr. T. C. McGill for his support and guidance throughout my work; his insights provided the direction for my research, and helped me avoid many pitfalls along the way. Dr. McGill also furnished me with excellent computing facilities and created a very stimulating research group to which I was proud to belong.

During the course of this work I benefited substantially from many discussions, including fruitful conversations with Dr. D. L. Smith, R. T. Collins, and A. Nedoluha regarding chapter 1 of my thesis; Dr. M. A. Nicolet and Dr. J. McCaldin regarding Chapter 2; and Dr. W. A. Goddard III, Dr. A. Redondo, Dr. C. A. Swarts, J. J. Low, and R. J. Hauenstein regarding Chapter 3.

I am deeply grateful to Vere Snell for her superb secretarial work; to T. E. Schlesinger, A. Prabhakar, and R. T. Collins who read parts of this manuscript and made many useful suggestions; to C. Mailhiot who kept the computer in good shape; and to S. R. Hetzler who helped with the word processing.

The financial support of the California Institute of Technology and the Office of Naval Research is greatfully acknowledged.

Finally, I wish to thank my family in Israel and in the United States for their encouragement, and I am especially grateful to Herta and Paul Amir, who made my stay here so much more pleasant and easy.

ABSTRACT

The work presented in this thesis is concerned with theoretical investigations of the electronic, geometric, and elastic properties of solid interfaces. The interfacial electronic property studied was the effect of doping on the Fermi-level position at a metal-semiconductor interface. Geometric lattice match in heteroepitaxy was studied using a novel method of systematically determining every possible orientation of the two crystals which would result in lattice match at the interface between the two crystals. Finally, the parameters of several elastic models that can be used in calculating the elastic properties of silicon interfaces were computed, using ab-initio quantum-chemistry methods. The predictions of these models to bulk elastic properties were compared to experimental results to test the models.

(1) Chapter 1 presents the effect of semiconductor doping on the Fermi-level position at a metal-semiconductor interface. A model based on the concept of a dipole layer was used. The number of chargeable defects at the interface required to pin the Fermi level was determined in the limits of thin and thick metallic coverages. The calculations included the metal response to large charge transfer at the interface, using a jellium model for the metal.

The major findings of this chapter are:

- It takes about 10^{14}defects $\cdot$ cm^{-2} to pin the Fermi level in a bulk metal-semiconductor interface, but only about 10^{12}defects $\cdot$ cm^{-2} during the initial stages of metallization.
- The Fermi-level position at the metal-semiconductor interface may be very different for n- and p- type semiconductors during the initial steps of metallization. These Fermi-level positions seem to stabilize after the creation of about 10^{12} defects$\cdot$cm^{-2} (which usually corresponds to less than a monolayer

of metallic coverage). However, as the metallization proceeds, the two Fermi-level positions on n- and p-type semiconductors should merge to within 0.05 eV at the interface (for doping not exceeding 10^{17} cm^{-3}).

- During the initial steps of metallization most of the carriers required to charge the defects come from the semiconductor. When the metallic overlayer is fully grown, it is the metal that contributes most of the charge.
- The potential difference between the metal surface and bulk, in the jellium model, changes quadratically with charge removed or added to the surface. For a charge density of 10^{14}electrons/cm^2 removed from the surface, the slope of the potential vs. charge removed is of the order of $1V$ per $10^{14}e \cdot$ cm^{-2} or less.

(2) In Chapter 2 the relevance of lattice mismatch to heteroepitaxial growth was investigated. A novel method to determine all the possible lattice matches between any two given materials, with any given crystal structure, has been developed. This method allows for an arbitrary **periodic** reconstruction of the interface. Such reconstruction results in two-dimensional superlattices on both sides of the interface, that have to be similar to each other. The input parameters to these calculations, besides the crystal structure of both materials, are the upper bound on the superlattice unit cell areas, and the maximum allowed mismatch in unit cell dimensions. This method was applied to study known heteroepitaxial interfaces of CdTe on GaAs, CdTe on sapphire, silicon on sapphire, and transition-metal silicides on silicon, to determine the relevance of lattice match in heteroepitaxy. For the last class of materials, namely, silicides on silicon, we list many possible lattice matches, including many that have not been grown so far.

The principal results described in Chapter 2 are:

- A good lattice match is **not** necessary for epitaxial growth of a single crystal on another.
- In those cases checked in which the epitaxial layer is metallic (silicide on silicon) and a single crystal, there is a good lattice match (bulk mismatch of 2.5% or less).
- Even a polycrystalline epitaxial layer may have some epitaxial relations, that is, some preferred orientations of the crystallites with respect to the substrate. In this case mismatches of up to 15% may be present; this means that the lattice match requirement is probably irrelevant.

(3) In Chapter 3 the elastic properties of silicon are calculated using four models. The parameters of these models were calculated from the elastic constants of a small silicon cluster (Si_5H_{12}) using ab-initio quantum-chemistry methods. The calculated elastic properties were compared to experimental results to assess the quality of the models.

The main findings are:

- All four different models yield a phonon-band structure which is qualitatively correct but not very accurate numerically.
- The deviations of the model predictions from experimental results were attributed to the models and **not** to the quantum-chemistry methods used to obtain their parameters.
- The LA branch of the phonon-band structure agreed very well with experiment in all the different models used.
- The TA branch of the phonon-band structure was in poor agreement with experiment in all the four models; in particular, the slopes of the TA branch near the Γ point (which determine the elastic constants c_{12} and c_{44}) were

inaccurate.

- The accuracy of the calculated optical phonons varied among the four models.
- Elastic properties associated with bond stretching were calculated much more accurately than elastic properties associated with bond bending.

Parts of this thesis have been or will be published under the following titles:

CHAPTER 1

- A. Zur, T. C. McGill, and D. L. Smith, "The Effect of Doping on Fermi-Level Position At a Semiconductor-Metal Interface" (Extended Abstract), *J. Vac. Sci. Technol.* **B1**, 608 (1983).
- A. Zur, T. C. McGill, and D. L. Smith, "Dipoles, Defects and Interfaces," *Surf. Sci.* **132**, 456 (1983).
- A. Zur, T. C. McGill, and D. L. Smith, "The Fermi-Level Position at a Semiconductor-Metal Interface," *Phys. Rev.* **B**, 2060 (1983).

CHAPTER 2:

- A. Zur and T. C. McGill, "Lattice Match: An Application to Heteroepitaxy," to appear in *J. Appl. Phys.*
- A. Zur, T. C. McGill, and M. A. Nicolet, "Lattice Matches in the Silicon-Silicides system," in preparation.

CHAPTER 3:

- A. Zur, T. C. McGill, and W. A. Goddard-III, "Ab-initio Calculations of the Elastic Properties of Silicon, Using Small Clusters," in preparation.

CONTENTS

GENERAL INTRODUCTION

A. Background

In recent years there has been a growing interest in the physics of interfaces which stems from both increasing technological needs and capabilities. The realization of the importance of interface properties to device performance, as well as the desire to introduce novel devices, created a need to understand the details of interfaces. At the same time the ability to grow more uniform and controlled interfaces, due mainly to the introduction of Ultra High Vacuum (UHV) techniques of growth and diagnostics, allowed researchers in this field to better understand the physics of interfaces. This thesis is concerned with a theoretical investigation of electronic, geometric, and elastic aspects of solid interfaces. Following this introduction, each of the three chapters treats one topic that is related to either electronic, geometric, or elastic properties of interfaces. Each chapter is independent of the others.

Chapter 1.

In chapter 1, the metal-semiconductor interface is treated. This interface has a long history which will not be recounted here. Instead, we shall trace briefly only those works which have a direct influence on ours. The metal-semiconductor interface was first discussed in a classical paper by Schottky[1], who proposed that the electronic barrier formed upon contact will be equal to the difference between the work function of the metal and the electron affinity of the semiconductor (in the case of n-type semiconductor). This was later demonstrated not to be the case, and Bardeen[2] improved the model by introducing a finite charge density trapped at the interface. Bardeen's model is still used in current textbooks as a phenomenological model (see, for example, Sze,[3] Chap. 5). However, the nature

of the trapped charge at the interface, as well as its influence on the barrier height, are still under debate. Bardeen[2] originally attributed this charge to intrinsic surface states of the semiconductor. Silicon is known to have intrinsic surface states within the energy gap, and these states could pin the Fermi level at a particular energy. Since the pinning phenomenon (the same barrier height for a number of different metals with different work functions) was observed experimentally, Bardeen's model seemed plausible. During the last fifteen years, however, much evidence has accumulated that has pointed to the fact that intrinsic surface states cannot always account for the pinning, and other mechanisms were suggested. First, it was demonstrated that clean cleaved surfaces of III-V semiconductors do not possess intrinsic surface states in the gap,[4] with the possible exception of GaP. Second, it was shown that surface relaxation and reconstruction may vary the energies of surface states substantially.[5] Since the positions of the atoms near a clean surface are, in general, different from those of atoms near an interface, one can no longer count on the energies of clean-surface states to be equal to those of the interface states. The emphasis, thus, shifted from surface states to interface states. Recent experiments on III-V semiconductors indicate that metallic adatoms interact with the semiconductor substrate, causing structural changes (defects) in the semiconductor.[6] Some of these defects are electrically active, that is, they act as donors or acceptors, and they may pin the Fermi level somewhere in the gap. Since many of these defects are formed at the initial steps of metallization (submonolayer coverages), researchers in this field started to pay close attention to the behavior of the Fermi level at such low coverages. The tendency to look at very low coverages was also facilitated by many UHV experimental techniques,[7] especially ultraviolet photoemission spectroscopy (UPS) and soft X-ray photoemission spectroscopy (SXPS). These techniques allow one to measure the

position of the Fermi level relative to the band edges, but require the photoemitted electron to penetrate the metallic overlayer. Therefore, the metallic overlayer has to be smaller than the electron escape depth, which is of the order of few angstroms.

The connection between thin and thick metallic coverages still remains to be investigated. The experiments for very low coverages of metals on III-V semiconductors, indicate that the Fermi-level position in the gap stabilizes after about a monolayer coverage. This Fermi-level position is almost the same for a number of different metals, but varies by as much as 0.2 eV, depending on whether the substrate is an n- or a p-type semiconductor.[8-11] The defect density required to pin the Fermi level is estimated at about 10^{12} cm^{-2}. It is the object of chapter 1 of this thesis to show that this behavior changes when the metallic coverage becomes thick; we show that there are, in fact, two different pinning mechanisms in the limits of thin and thick metallic coverages. While our model confirms the behavior of the Fermi level at low coverages, it predicts that in the limit of a very thick coverage, the Fermi-level position on n- and p-type semiconductors would merge, to within 0.05 eV. Our model also predicts that the defect density required to pin the Fermi level, in the limit of a thick coverage, is about 10^{14} cm^{-2}. This fact indicates that the defects observed at the initial steps of metallization are not enough to pin the Fermi level in a macroscopic Schottky barrier. To pin the Fermi level, the interface-state density will have to increase by two orders of magnitude. These extra interface states could either be due to additional defects, or to some other factor that is not yet determined.

Chapter 2.

In Chapter 2 we discuss geometric lattice match, and its relevance to heteroepitaxy. The motivation for the investigation of lattice match was the possibility of growing epitaxial single-crystal layers of one material on another. Such structures

may open the door for a whole new class of devices. Currently, there is an interest in developing silicide-silicon devices which might be integrated into the existing silicon based VLSI technology. Since the silicide-silicon interface would then be an active one, that is, with carriers going through it, it is likely to be important to have an almost defect-free interface. A good lattice match seemed to be a necessary condition for such a defect-free interface. With a systematic way of finding all possible lattice matches, one could check this assumption. In addition to the silicide-silicon interface, there has been an interest in heteroepitaxial growth of other pairs of materials. Silicon on sapphire (SOS) devices are being commercially produced, mainly silicon (100) on sapphire ($1\bar{1}02$), but the physics of that interface is still not well understood. We had hoped to have understood more clearly the particular orientation relations in this interface by considering geometric lattice match. CdTe is an important substrate material for infra-red detectors, but has very poor mechanical properties. Attempts to grow it on more mechanically stable substrates, like GaAs and sapphire, have recently proved successful,[12-13] and we investigated these interfaces.

At this point we should clarify the meaning of "lattice match". Lattice match, in the case of, say, $Ga_xAl_{(1-x)}As$ on $GaAs$, is quite clear; the two crystals have the same crystal structure (zincblende) and the epitaxial layer actually continues the structure of the substrate. The only difference is that in the epitaxial layer, some gallium atoms are replaced by aluminum atoms, and the average interatomic distance is slightly changed. We, therefore, measure the lattice mismatch by comparing the lattice constant, a, of the substrate and the film. When the substrate and the film have either a different crystal structure or a different growth orientation, the definition of lattice match is more involved. Instead of looking at the three-dimensional lattices in their entirety, we should confine our attention to the interface

region. The idea is to define two crystals as lattice matched if a slab containing several atomic layers on **both sides of the interface** has a translational symmetry. The exact definition, as well as a novel method to systematically determine all the possible lattice matches between any two crystalline materials, is presented in Chapter 2.

It is not simple to assess the relevance of geometric lattice match to heteroepitaxy. By considering the geometric factors and completely neglecting the local chemistry, we probably miss the most important factor. It is clear, however, that in a solid interface the chemistry has to operate within some geometrical constraints. The first layer of film atoms probably bonds to the substrate at the most favorable positions. Lattice match plays little or no role at this step. As the film grows thicker, it tends to crystallize in its most stable structure for that temperature. Sooner or later the free energy gain due to the crystallization of the film in its most stable form exceeds the elastic strain energy caused by the mismatch, and this crystallization occurs. What happens to the atoms near the interface? If the strain is large, there is a tendency to relieve it by creating defects. These defects may or may not propagate throughout the film. Although this discussion is somewhat qualitative and inaccurate, it seems reasonable that geometric lattice match plays a minor role in determining the actual growth direction of the film. On the other hand, we might expect it to play a more significant role in defects formation at the interface, and in determining whether the film will grow as a single crystal or as polycrystalline material. In chapter 2 we check this assumption by comparing lattice match predictions with experimental results of heteroepitaxial growth.

Chapter 3.

We calculate the elastic properties of bulk silicon in chapter 3. The calculations are performed using four models. These models relate the elastic strain energy

to the atomic positions, and models of this sort are currently used in calculating elastic properties of interfaces and defects.[14-15] Each model has between two and five adjustable parameters, but the parameters are calculated, using ab-initio quantum-chemistry calculations of deformed Si_5H_{12} clusters, rather than fitted to the experimental phonon-band structure.

One might wonder about the need to calculate the phonon-band structure of silicon from first principles, since the phonon-band structure is readily available from neutron scattering experiments.[16] Moreover, one might also wonder why we chose not to use a method that incorporates the translational symmetry of the crystal. The explanation is that we were looking for a reasonable method to calculate the elastic properties of interfaces and defects. Near interfaces and defects, where the translational symmetry of the crystal breaks down, one can observe vibrational states that do not belong to the bulk phonon-band structure. These states decay in amplitude, more or less exponentially, into the bulk. There is no good experimental method to obtain the complete spectrum of these decaying states, and researches often apply theoretical tools to interpret the experimental results. These theoretical tools involve models similar to those used in Chapter 3, whose parameters are either adjusted to fit the experimental results, or fitted to the bulk phonon-band structure. This fitting procedure is at best unsatisfying and at worst leads to the wrong conclusions. In Chapter 3, we used ab-initio cluster calculations to obtain these parameters; this method enabled us to verify the models used.

It now remains to justify the use of ab-initio quantum-chemistry methods. In principle, one could also obtain the parameters of the models from experimental vibrational spectra of small molecules. This was actually done for diamond, using spectroscopic data of saturated hydrocarbons.[17-18] However, silicon hydrides are

harder to synthesize and are unstable. Therefore, less spectroscopic data are available for them. In addition, high-quality quantum-chemistry methods have some attractive features. First, one can calculate the frequency of any mode, not only normal modes. Second, one can "tune" some of the atoms to have some specific properties. In any case, it is important to realize that quantum-chemistry methods are accurate enough for our purpose. The only real limitation imposed by the calculations is the size of the cluster; this, in turn, limits the complexity of the models used.

In Chapter 3, we also compare the discrepancies between the elastic constants of silicon measured experimentally and calculated using quantum chemistry, to the discrepancies between the elastic constants of diamond measured experimentally and calculated from spectroscopic data. The two discrepancies are very similar, leading us to conclude that it is actually the model, rather than the quantum-chemistry calculations, that is at fault.

B. Outline of the thesis

The body of this thesis is organized into three chapters. Each chapter is independent of the others and describes one research topic. Every chapter contains a detailed introduction, several sections of body describing the methods used and the results obtained, a section with a summary and conclusions, and a section with references. Twelve appendices are included at the end of this thesis, four for each chapter. In these appendices one can find material that is relevant to the text of the thesis, but is either too mathematical or too bulky to permit the free flow of ideas in the thesis.

Chapter 1 deals with the metal-semiconductor interface. Following the introduction section 1.2 treats the physics of dipole layers that are the fundamental concept in our model. Section 1.3 treats metal surfaces using the jellium model, and section 1.4 treats semiconductor surfaces containing defects which model a submonolayer metallic coverage. Section 1.5 deals with the metal-semiconductor interface. This section is further divided into subsections: subsection (a) treats the three regions of the model (metal, semiconductor, and interface regions, each modelled differently); subsection (b) describes the method of calculation; subsection (c) contains the results for various possible defects at the interface.

Chapter 2 is dedicated to lattice match and its relevance to heteroepitaxy. Following the introduction to Chapter 2, section 2.2 describes the lattice match search algorithm in a descriptive rather than a rigorous way. To further clarify the method, section 2.3 contains a detailed step by step application of the method to one particular interface, that of CdTe on GaAs. Other interfaces, namely, CdTe and silicon on sapphire, and silicides on silicon are treated in section 2.4. Here the emphasis is not on the method, but rather on comparing experimental results to our lattice match predictions.

Chapter 3 is devoted to the investigation of the elastic properties of silicon clusters and bulk silicon. Section 3.2 describes the quantum chemistry methods used in this research. This section is descriptive, with an emphasis on general ideas, rather than on exact formalism. Section 3.3 contains the results of the cluster calculations and applies them to obtain phonon-band structure and elastic constants; this is done by using four models that progressively become more and more complicated. The calculated band structures are also compared to experimental phonon-band structure in that section.

The appendices of Chapter 1 contain the more highly mathematical parts of that chapter. They have been included to substantiate the material in the body of the chapter, but might disrupt its flow with heavy formalism. The first appendix, A-1.1, contains the statistics of carriers in bulk semiconductors and derives a formula connecting the Fermi-level position at the interface with the total depletion charge in the semiconductor. The second appendix, A-1.2, describes the jellium model and the local density formalism used to treat the jellium model; the third and fourth appendices give some sum rules that were used in the jellium calculations. The Sugiyama sum rule in Appendix A-1.3 relates charge conservation (or lack thereof) to phase shifts in the jellium bulk. The derivation of this sum rule due to Langreth[19] was slightly modified here to account for nonneutral surfaces. The Budd-Vannimenus theorem[20] in Appendix A-1.4 relates the electrostatic potential difference between the jellium surface and bulk to the energy functional in the local density approximation. The derivation of this theorem by Mahan and Schaich[21] was modified in this appendix to nonneutral surfaces.

There are four appendices to Chapter 2: Appendix A-2.1 contains crystallographic material and deals mainly with notations and transformations from one set of notations to another. Appendix A-2.2 is mathematical in nature and repeats

in a rigorous fashion the description of the lattice match determination procedures. Appendix A-2.3 shows the results of the calculations for the silicides on silicon system. Again, the natural place for these results is in the body of the chapter, but this set of tables is too bulky and they were best placed at the end. Appendix A-2.4 lists the crystal structures of all the currently known binary transition-metal silicides, and the data here was used to calculate lattice matches of silicides on silicon.

Chapter 3 also has four appendices. Four models were used in chapter 3 to relate the crystal and cluster strain energy to the atomic positions. Three of these models used only direct bond lengths and angles. These can be called "geometric models". The fourth, first introduced by Vasil'ev *et al*,[22] uses hidden coordinates that must be calculated. Appendix A-3.1 describes the three geometric models and derives the static-elastic properties of bulk silicon for each one of these models. Appendix A-3.2 derives formulae for various points in the phonon-band structure for each one of these three models. Appendix A-3.3 describes Vasil'ev's model and calculates special points in the phonon-band structure as well as the static-elastic constants using this model. Appendix A-3.4 describes how the parameters of Vasil'ev's model were obtained from the cluster calculations.

C. Summary of the major results

In Chapter 1 it was confirmed that the behavior of the Fermi-level position at the first stages of metallization could be explained by the unified defect model of Spicer *et al.*[6] Our calculations, based on the assumption that the metallic adatoms create defects at the surface but do not contribute significant amount of charge, were able to reproduce the qualitative behavior observed experimentally. It was also found that the positions of the Fermi levels for n- and p- type semiconductors, that seemed to stabilize at about a monolayer of adatoms, do not in fact stabilize. If one plots the Fermi-level position as a function of defects created at the surface, then at a defect density of about $10^{12} \cdot \mathrm{cm}^{-2}$, there is a drastic change in slope. After this defect density is achieved, the two curves corresponding to the Fermi-level position at the interface for n- and p- type semiconductors, flatten out and have **almost** a zero slope. They would finally merge, due to compensation, but approximately $10^{14}\mathrm{defects} \cdot \mathrm{cm}^{-2}$ are required for this. At the same time a different mechanism occurs: as the metallic coverage becomes bulk-like, it will become the major contributor of charge to the defects. A change of one volt in the Fermi-level position at the interface can change the charge in the depletion region of the semiconductor by about $10^{12}\mathrm{e/cm}^2$, but will change the metal charge density by almost two orders of magnitude more. This means that the dipole layer formed between the defects and the depletion charge in the semiconductor will become less and less important, while the dipole layer that forms between the defects and the metal would eventually become more important in determining the Fermi-level position. As a result, for a thick metallic coverage, $10^{14}\ \mathrm{cm}^{-2}$ would be needed to pin the Fermi level, and the positions of the Fermi level on n- and p-type semiconductors would be the same, to within 0.05 eV.

In Chapter 2, a method of determining all the possible lattice matches for

any pair of materials was devised. Known cases of heteroepitaxial growth were compared with lattice-match predictions to determine how relevant lattice match is to epitaxial growth of single crystalline films. In the CdTe on GaAs system, The CdTe(111) on GaAs(100) grown by Cheung and Magee[12] using LADA, corresponds to a good lattice match. On the other hand CdTe(111) grown on GaAs(111) by Schmit[23] using MO-CVD, corresponds to a poor lattice match (14%) for a small unit cell. Similarly, the CdTe(111) grown on sapphire by Myers *et al.*[13] using MBE, corresponds to a poor match (4%),[24] and most of the known silicon on sapphire single-crystal growth by various techniques correspond to a poor match, of up to 14%. Both the silicon on sapphire[25] and the CdTe on sapphire[24] interfaces are known to be heavily defective or polycrystalline. Some silicides are known to grow epitaxially on silicon. $NiSi_2$,[26] $CoSi_2$[27] and Pd_2Si[28] grow as a single crystal with an ordered interface, and they all correspond to good lattice matches. PtSi and Pt_2Si[29] grow epitaxially but polycrystalline on silicon, and they correspond to poor matches. It appears that a good lattice match with a large unit cell area cannot compete with a poor lattice match for a smaller unit cell area, and that the growth in this case will be polycrystalline, at least initially. Sometimes, an epitaxial layer that starts out as polycrystalline can later become a single crystal. In other words, a good lattice match is not necessary for single-crystal epitaxial growth. Several counterexamples were found, in all of them the epitaxial layer had an open structure (zincblende). However, in the silicide-silicon cases, in which the epitaxial layer has a rather close-packed structure, wherever an abrupt single-crystalline film was grown, it always corresponded to a good lattice match.

In Chapter 3, we used four models to calculate the elastic properties of bulk silicon. The parameters of the models were calculated from the elastic properties of a Si_5H_{12} cluster. These elastic properties were calculated using ab-initio quantum-

chemistry methods. The resulting phonon-band structures had the right qualitative appearance, but were not very accurate numerically. For all the four models the LA phonon branch agreed well with experiment, but the TA phonon branch was in poor agreement. The optical branches varied in quality among the four models. The bulk modulus and the elastic constant c_{11} were in good agreement with experiment, while c_{12} and c_{44} were in poor agreement in all four models. Similar calculations for carbon[17] using experimental spectroscopic data for molecules rather than ab-initio cluster calculations yielded similar results. We can propose an explanation for this behavior: symmetry consideration strongly affect the general shape of the phonon-band structure. All the models are guaranteed to take this symmetry into account, therefore the general shape of the band structure should be qualitatively right. In addition, the bond stretching force constant is greater than any angle-restoring force constant or any mixed term of bond-bond, bond-angle and angle-angle, by at least an order of magnitude. The bond-stretching force constant is also a good physical quantity, in the sense that it is rather insensitive to changes in the other bonds in the crystal or molecule. This is not the case with bond bending, however. Bond-bending restoring force constants are bad physical quantities, in the sense that they are sensitive to changes in the adjacent bonds. None of the four models considered was consistently better than the others in treating the bond bending.

References

1. W. Schottky, *Z. Phys.* **113**, 367 (1939).
2. J. Bardeen, *Phys. Rev.* **71**, 717 (1947).
3. S. M. Sze, *Physics of Semiconductor Devices*, 2nd ed., Wiley-Interscience, New York (1981).
4. J. van Laar, A. Huijser, and J. L. Van Rooy, *J. Vac. Sci. Technol.* **14**, 894 (1977).
5. J. E. Rowe, S. B. Christman, and G. Margaritondo, *Phys. Rev. Lett.* **35**, 1471 (1975).
6. W. E. Spicer, I. Lindau, P. Skeath, and C. Y. Su, *J. Vac. Sci. Technol.* **17**, 1019 (1980).
7. cf. review article by L. J. Brillson, *J. Phys. Chem. Solids* **44**, 703, (1983).
8. W. E. Spicer, P. W. Chye, P. R. Skeath, C. Y. Su, and I. Lindau, *J. Vac. Sci. Technol.* **16**, 1422 (1979).
9. P. Skeath, I. Lindau, P. W. Chye, C. Y. Su, and W. E. Spicer, *J. Vac. Sci. Technol.* **16**, 1143 (1979).
10. W. E. Spicer, P. Skeath, C. Y. Su, and P. W. Chye, *Phys. Rev. Lett.* **44**, 420 (1980).
11. R. W. Grant, J. R. Waldrop, S. P. Kowalczyk, and E. A. Kraut, *J. Vac. Sci. Technol.* **19**, 477 (1981).
12. J. T. Cheung and T. Magee *J. Vac. Sci Technol.* **A1**, 1604 (1983).
13. T. H. Myers, Y. Cheng, R. N. Bicknell, and J. F. Schetzina, *App. Phys. Lett.* **42**, 247 (1983).
14. A. Grimm, A. A. Maradudin, I. P. Ipatova, and A. V. Subashiev, *J. Phys. Chem. Solids* **33**, 775 (1972).
15. R. J. Hauenstein, T. C. McGill, and R. M. Feenstra, *Phys. Rev.* **B28**, 5793

(1983).

16. G. Dolling, *Inelastic Scattering in Solids and Liquids* **2**, IAEA, Vienna, 37 (1963).
17. M. J. P. Musgrave and J. A. Pople, *Proc. Roy. Soc.* **A268**, 474 (1962).
18. H. L. McMurray, A. W. Solbrig, J. K. Boyter, and C. Noble, *J. Phys. Chem. Solids* **28**, 2359 (1967).
19. D. C. Langreth, *Phys. Rev.* **B5,** 2842 (1972).
20. H. F. Budd and J. Vannimenus, *Phys. Rev. Lett.* **31,** 1218 (1973).
21. G. D. Mahan and W. L. Schaich, *Phys. Rev.* **B10,** 2647 (1974).
22. L. N. Vasil'ev, Yu. A. Logachev, V. Ya. Moizhes, and M. S. Yur'ev, *Soviet Physics – Solid State* **13,** 363 (1971).
23. J. L. Schmit, *private communication.*
24. J. F. Schetzina, *private communication.*
25. J. Blanc and M. S. Abraham, *J. Appl. Phys.* **47**, 5151 (1976).
26. K. N. Tu, J. Mayer, *Thin Films – Interdiffusion and Reactions,* edited by J. M. Poate, K. N. Tu, and J. W. Mayer, (Wiley, New York 1978).
27. R. T. Tung, J. C. Bean, J. M. Gibson, J. M. Poate, and D. C. Jacobson, *Appl. Phys. Lett.* **40,** 684 (1982).
28. W. D. Buckley and S. C. Moss, *Solid State Electronics* **15,** 1331 (1972).
29. H. Ben Ghozlene, P. Beaufrère, and A. Authier, *J. Appl. Phys.* **49,** 3998 (1978).

CHAPTER 1
THE POSITION OF THE FERMI LEVEL AT A METAL-SEMICONDUCTOR INTERFACE

1.1 Introduction.

In this chapter we investigate the position of the Fermi level at a metal-semiconductor interface. We discuss dipole layers, which are responsible for a large class of contact phenomena and, in particular, determine the position of the Fermi level relative to the band gap of the semiconductor. Three classes of interfaces (and dipole layers) are investigated. The first is a free, ideal metallic surface, which will serve as a model for all the other interfaces to be investigated. It will enable us to study some of the energy levels at the interface; to see the problems involved in using some of these energy levels, particularly the work function and the vacuum level, and to estimate the changes that occur in the metal side of a metal-semiconductor interface when a very high charge density is moved across this interface. The second interface is the free semiconductor surface containing defects; this surface serves as a model for the initial steps of metallization, that is, submonolayer coverage. The third case is that of a metal-semiconductor interface in the limit of a very thick metallic coverage.

The motivation for this work originated from what appeared to be a contradiction between a new and an old way of looking at Schottky barriers. Recent experiments involving submonolayer coverage of metal atoms on semiconductor surfaces

suggested that the Fermi-level position at the surface for n- and p- type semiconductors may differ by as much as 0.2 eV.[1-4] In measurements of Schottky barriers consisting of a bulk metal against a bulk semiconductor, however, the Fermi-level position at the metal-semiconductor interface was found to be the same for both n- and p-type semiconductors, that is, to within 0.1 eV.[5] Moreover, from a theoretical point of view, the metal-semiconductor interface is usually treated using a model proposed by Bardeen[6] in which the Fermi-level position at the interface cannot be substantially different in the case of n- and p- type semiconductors. Despite this difference in behavior, there are certain qualitative similarities between thin and thick metallic coverages: the Fermi level pins at approximately the same position for a number of different metals. This being the case, one might ask what the connection should be between the experimental results for submonolayer coverages and those for macroscopic Schottky barriers.

The position of the Fermi level at the interface is governed by two phenomena: the formation of interface states and the bending of bulk levels due to the formation of dipole layers. The nature of the interface states is still not established. Various authors have attributed these states to surface states,[6] Metal-Induced Gap States (MIGS),[7-8] or native defects in the semiconductor.[9] It is also possible that more than one type of interface state plays a role in a given interface, and that different types of interface states exist in different interfaces. In this work, we do not address the question of the exact nature of these interface states, we only assume that these states do exist, that they are localized both in energy and in space, and that their density is high (we estimate their density in this work). It is the second phenomenon, namely, the effect of the various dipole layers at or near the interface, that is the main object of this chapter.

In general, the physics of a dipole layer is very simple. At thermal equilibrium,

the chemical potential of the electronic system has to be constant throughout space. The chemical potential is a sum of two terms: internal and external. The internal part of the chemical potential is local and consists of many-body effects, that is, kinetic, exchange, and correlation energy. The external part of the chemical potential is the electrostatic potential. Far away from the interface, the internal parts of the chemical potentials are fixed for the bulk materials on both sides of the interface. Thus, the external part has to vary to compensate for the difference in the internal parts. This results in the formation of a dipole layer. Some finite density of electrons will "spill over" from one side of the interface to the other, creating a layer of negative charges and leaving behind a layer of positive charges. This general picture holds for any interface, but the details of the charge redistribution may be different for different types of interfaces.

In this chapter we present a detailed study of the variation of the Fermi-level position at a metal semiconductor interface for a macroscopic Schottky barrier, and contrast it with a simple model for submonolayer coverage. Our discussion is based on the recently proposed Unified Defect Model of Spicer *et al.*[9] which assumes pinning of the Fermi level by charged defects at the interface. In the course of this research, it was shown that the density of such defects required to pin the Fermi level is very large, of the order of 10^{14} cm^{-2}, in the case of a thick metallic coverage. Upon charging, these defects alter the electron density on the metal side of the interface. In the classical Bardeen model, the metal is assumed to be insensitive to charge depletion or enhancement. This assumption is no longer valid when the metal-surface charge is altered by as much as 10^{14} $e \cdot cm^{-2}$. In this study we used a jellium model[10] to obtain a more realistic behavior for the metal.

Various models of spatial arrangements of defects are considered. In detail the models may not precisely conform to the experimental situation (that is, in

distribution of defects, etc.), but we can draw a model independent conclusion about the Fermi-level position at the interface. We conclude that for n- and p-type semiconductors, it is difficult to have a substantially different Fermi-level position ($>$ 0.1 eV) for a macroscopic Schottky barrier, while it is possible in submonolayer coverage. Hence, we must conclude that if the experimental results for submonolayer coverage were extended to include thicker overlayers, the Fermi-level position on n- and p- type semiconductors would eventually merge to within 0.1 eV.

Chapter 1 is organized in the following way: in section 1.2 the physics of dipole layers is discussed; section 1.3 is devoted to the jellium model, its justification and its limits, as well as to various methods of solution for that model. The important property of jellium, as applied to the metal-semiconductor interface, is its response to changes in charge density near its surface. This section serves also to define the energy levels near the interface and to point to some problems associated with the traditional use of work-function and the vacuum level. Section 1.4 treats the free surface of a semiconductor containing defects and contrasts it to a fully grown Schottky barrier. This surface is a good model for submonolayer metallic coverage of a semiconductor; indeed, the theoretical plots of the Fermi-level position at the interface as a function of defect density closely resemble experimental plots of the Fermi-level position at the interface as a function of adatom coverage. Section 1.5 treats the metal-semiconductor interface for a thick metallic coverage. This section is the centerpiece of this chapter and is further divided into subsections: the first treats the physics of each region in the interface, the second describes the calculational technique, and the last subsection describes the results for this interface. Section 1.6 summarizes the conclusions based on this study.

The more mathematical parts of this work appear in the appendices at the

end of this thesis. Appendix A-1.1 will summarize the statistics of carriers in a bulk semiconductor and the charge distribution in a semi-infinite semiconductor. Appendix A-1.2 will summarize the more mathematical formulation of the jellium model. Two sum rules concerning the jellium model are reproduced in Appendices A-1.3 and A-1.4.

1.2. The physics of dipole layers.

One of the most useful concepts in understanding what governs the relative positions of electronic levels on either side of an interface is the concept of a dipole layer. A dipole layer is made of two layers of opposite charges in a state of thermal equilibrium: the electrostatic potential acts to merge the two layers, but a difference in chemical potential acts to separate them, and the two exactly balance each other. This phenomenon is very common, and occurs whenever there is a contact between two conducting materials having a different chemical potential.

Electrically, a dipole layer can be viewed as a charged parallel plate capacitor. The properties of the dipole layer are characterized by the charge per unit area on one of the plates σ, the dielectric constant of the medium between the plates ϵ, and the distance between the plates d. The electric field in the region between the two plates is given by

$$E = \frac{\sigma}{\epsilon\epsilon_0}.$$

The electric potential changes by an amount $\Delta\phi$ in going from one plate to the other.

$$\Delta\phi = \frac{\sigma d}{\epsilon\epsilon_0}.$$

In this simple example, we can see that an overall neutral charge distribution can abruptly change the electric potential. In real problems, the dipole layer can be produced by various distributions of charge. For our purposes here, however, the important properties of dipole layers are that they are neutral overall, and that they lead to an abrupt change in the potential.

In examining the properties of interfaces, dipole layers play a very important role since they are responsible for adjusting the chemical potential on one side of the interface with respect to the other. This adjustment is achieved by rearrangement of the charge within the interface region, but without carrying a net charge away

from the interface. In examining the dipole layers that play a role in semiconductor and metal surfaces and interfaces, it is important to determine the origin of the charge that produces the dipole layer.

The mathematical treatment is straightforward. The electronic chemical potential can be written as a sum of an internal and an external part.

$$\mu = \mu^{(\mathrm{int})} + \mu^{(\mathrm{ext})} = \mu^{(\mathrm{int})} + q\phi = \text{const.} \tag{1.2.1}$$

The internal part is a function of the local charge density, and it contains all the local many body effects, namely, the average kinetic, exchange, and correlation energies. The external part is simply the electrostatic potential energy, which obeys Poisson's equation,

$$\frac{\partial^2 \mu^{(\mathrm{ext})}}{\partial x^2} = \frac{q^2 n}{\epsilon \epsilon_0}. \tag{1.2.2}$$

Here q is the electron charge, taken as positive, and n is the number density of positive charges. Eq. (1.2.2) could be solved using (1.2.1) if we knew how to relate the internal chemical potential $\mu^{(\mathrm{int})}$, to the number density n.

1.3 Metal surfaces in the jellium approximation.

Why it is important to treat the metal surface

In this section ideal metal surfaces are considered. The metal-vacuum interface was chosen to be treated first since it can serve as a model for other, more complicated interfaces. We shall examine the charge transfer as well as the various electronic energy levels, and derive the boundary conditions for a general interface. Having the metal-semiconductor interface in mind, we are interested in the metal response to a depletion or an enhancement of a significant charge density near the surface. We are interested in this feature since we estimate in Section 1.5 that a defect density of $\approx 10^{14}$ cm^{-2} is required to pin the Fermi level in a metal-semiconductor interface. Screening of such high charge densities (one electron per several surface atoms) might alter the surface potential significantly. In this section we shall estimate the change in surface potential as a function of electrons removed.

The quantitative treatment of the metal surface is performed using the jellium model. To assess the quality of this model, we compare its predictions for work function with experimental results for real metals. We also compare various methods of solution for this model.

The jellium model

Jellium was first suggested as a model for a metal by Bardeen.[10] This model consists of an electron gas interacting with a uniform positive background of density n^+, extending from $x = -\infty$, and ending abruptly at $x = 0$. The resulting electron-gas density profile is shown schematically in Fig. 1.1. One can see that the electron density extends beyond the positive background. Thus, the outside of the metal surface becomes negatively charged with respect to the inside, producing a dipole layer. The energy levels associated with this interface are also displayed

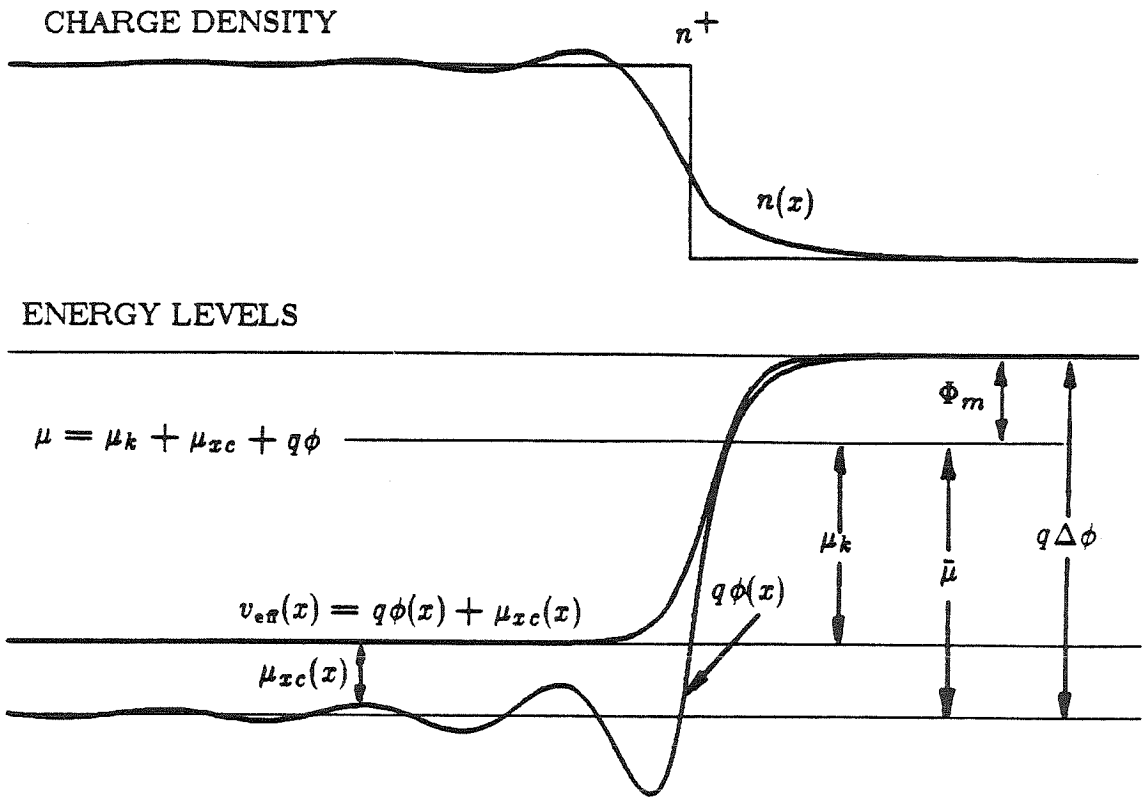

Fig. 1.1. Schematic of the charge density and the energy levels near the jellium surface. The positive background density of n^+ extends from $-\infty$ to $x = 0$. The electronic density $n(x)$ extends beyond $x = 0$. The electronic density $n(x)$ results from summing individual electron densities $|\psi_k(x)|^2$ for k-vectors in the Fermi sphere. Each $\psi_k(x)$ is a solution of Schrödinger's equation with an effective potential $v_{eff}(x)$. This effective potential is the sum of electrostatic potential energy, $q\phi$, and an exchange-correlation term, μ_{xc}. The electrostatic potential can be obtained by integrating Poisson's equation with a total charge density of $q(n^+ - n(x))$. The exchange-correlation term also depends on the local density $n(x)$. In this figure, μ_{xc} is positive, but it may have either sign. The total chemical potential, μ, is the sum of the kinetic term, μ_k, the exchange-correlation term, μ_{xc}, and the electrostatic term, $q\phi$. Its individual components are functions of position but μ itself is constant at thermal equilibrium. The work function, Φ_m, is the work required to remove an electron from the metal. It is equal to the difference between the dipole barrier $q\Delta\phi$ and the bulk chemical potential $\bar{\mu}$.

in Fig. 1.1. Many-body effects are treated in a single-electron approximation using the density-functional formalism[11] of Hohenberg and Kohn,[12] and Kohn and Sham.[13] The density-functional formalism is briefly reviewed in Appendix A-1.2. In this approximation the electrons are subject to an effective potential which is the sum of the exchange-correlation interaction and the electrostatic potential energy.

$$v_{\text{eff}}[n;x] = \mu_{xc}(n(x)) + q\phi(x).$$

Solving Schrödinger's equation with this effective potential results in wave functions $\psi_k(x)$, which oscillate on the metal side of the interface, and decay into the vacuum. Summing $|\psi_k(x)|^2$ over all the wave vectors in the Fermi sphere results in the electronic density $n(x)$, shown in Fig. 1.1. The total charge density is obtained by subtracting the electronic charge density from the positive background charge density. By integrating the total charge density twice, using Poisson's equation, one obtains the electrostatic potential $\phi(x)$. Adding the exchange and correlation interaction μ_{xc}, which depends on the local density, to the electrostatic potential, one obtains the effective potential. This scheme enables one to find the effective potential, electrostatic potential, and charge density, in a self-consistent way. The weakest link in this self-consistent chain is obtaining the exchange and correlation interaction from the local charge density. Theoretical many-body calculations provide reasonable expressions for μ_{xc} as a function of the local density n, provided that this density varies slowly. This is, obviously, not the case near the surface.

The Fermi level μ, shown in Fig. 1.1, is the sum of the effective potential and the local kinetic energy

$$\mu = \frac{\hbar^2 k_f^2}{2m} + \mu_{xc} + q\phi.$$

Every term on the right hand side of this equation is a function of position, but their sum, μ, is constant at thermal equilibrium. Another important quantity in Fig. 1.1

is the "dipole barrier" $\Delta\phi$, which is the electrostatic potential difference across the surface. It is readily calculated from the charge density by integrating Poisson's equation twice. In the case of real metals, this dipole barrier is **not** an intrinsic function of the metal, and may change substantially by surface reconstruction, adsorption of impurities, etc. The most directly measurable quantity in Fig. 1.1, is the work function Φ_m, defined as the work required to remove an electron from the bulk to infinity. In doing that, we have to overcome the dipole barrier energy $q\Delta\phi$, but we gain back the bulk chemical potential, $\bar{\mu}$

$$\Phi_m = \Delta\phi - \bar{\mu}.$$

While $\bar{\mu}$ is a function of the bulk properties alone, $\Delta\phi$ depends heavily on the rearrangement of charge near the surface, and that is the reason why the work function is sensitive to the structure of the surface.

The idea behind the jellium model is that metals can be well approximated by a free electron gas, whose single most important property is the charge density. This model, therefore, classifies all metals according to a single parameter, namely, the charge density, and neglects all the other effects due to nonhomogeneity of the positive charges, ionic and covalent bonding, peculiarities of the band structure, etc. This is a very convenient approximation that enables us to put all the different metals on a single scale. We pay the price for such simplicity by compromising accuracy. On comparing jellium results to experimental values for such properties as work function, cohesive energy, and surface energy, one observes deviations of as much as 1 eV per particle. These large deviations usually occur in the rightmost columns of the transition metals, in which the d-core is very large and there is much s-d mixing in the band structure. For simple metals the accuracy is usually better.

To illustrate this point, consider Fig. 1.2, in which we plot the experimental work-function of most of the elements of the periodic table, up to row 6, versus

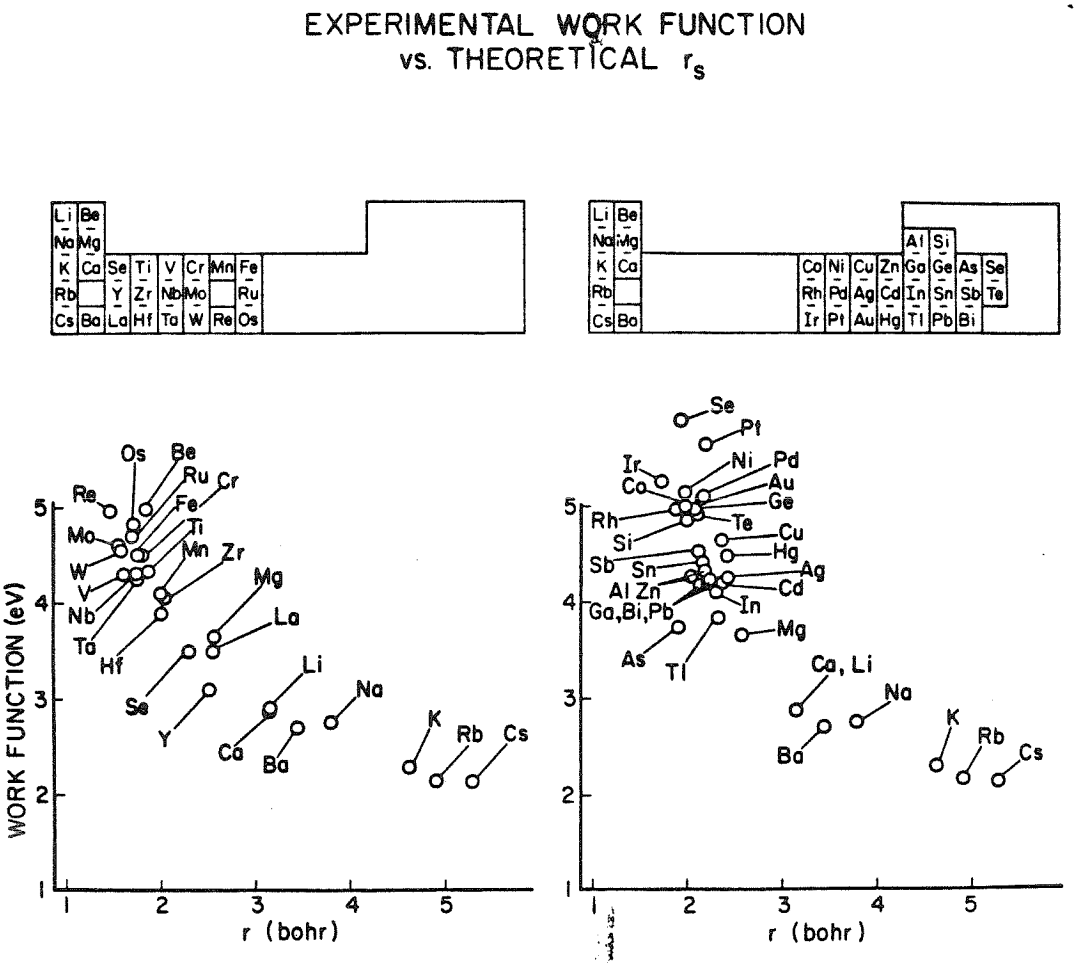

Fig. 1.2. Experimental work functions versus calculated r_s for elements of the periodic table. The work functions were taken from a compilation by Michaelson (Ref. 17) and the r_s's were calculated using data from Animalu and Heine, Animalu, and Kittel (Ref. 14–16). The figure is divided into two halves featuring two parts of the periodic table (the shaded areas).

their calculated r_s. The parameter r_s is the radius, in bohrs, of a sphere whose volume contains a positive-background charge of one electron. This quantity is closely related to the positive-background charge density; it ranges from 2 to 6 bohrs in most metals. The positive-background charge density was calculated here by dividing the number of valence electrons by the volume of the valence electrons. The volume of the valence electrons is the total volume minus the volumes of the cores. The valence, the core volumes, and the atomic volumes were taken from papers by Animalu and Heine,[14] Animalu,[15] and Kittel[16] respectively. The values of the work function are taken from Michaelson.[17] Fig. 1.2 was divided into two parts, one featuring the simple metals as well as the left side of the transition table (Sc–Fe columns), the other featuring the simple metals, the right side of the transition table (Co–Zn columns), and post-transition elements. One can see that there is a clustering of the data points along some curve which gives the work function as a function of the single variable r_s. This functional relationship between the work function and r_s, however, does not coincide for both halves of the periodic table: in the left half the r_s corresponding to the same work- function will be approximately half a bohr less than in the right half. Note also that elemental semiconductors such as silicon, germanium and selenium, continue the trend of the post-transition elements.

Methods of solution for the jellium model

Despite its simplicity, the jellium model is not easly formulated in precise mathematical terms. The main difficulty here is to obtain good expressions for the internal chemical potential, namely, the kinetic, exchange, and correlation energies. Such expressions are well known for the bulk jellium, in which the density is almost constant, and are given in Appendix A-1.2. Near the surface, however, the density changes rapidly over a characteristic distance of $1/k_f$, and

the assumptions leading to the energy expressions obtained for the bulk, are no longer valid. Moreover, attempts to correct the energy expressions for rapid density variations using density gradient terms, do not seem to improve the results.[18] With this difficulty in mind, there are two possible ways to proceed. One way is to solve the density self-consistently, using the best known bulk energy expressions, even near the surface. Such an approach was employed in a series of papers by Lang and Kohn.[19-21] Another approach is to assume a model effective potential with a few (1-3) adjustable parameters, whose values are fitted to obey exact sum rules. Such an approach was employed by Sahni *et al.*,[22-24] in which they used the sum rules of Sugiyama,[25] Budd-Vannimenus,[26] and Mahan-Schaich.[27] These sum rules are discussed in Appendices A-1.3 and A-1.4.

This second approach is intrinsically non-self-consistent; consequently, it is much easier to use. It is quite surprising, however, that its results are not inferior to those predicted by the self-consistent approach. This can be clearly seen in Fig. 1.3, in which we superimpose the predictions of the self-consistent as well as the non-self-consistent calculations on the experimental results seen in the left part of Fig. 1.2. The line denoted by L+K refers to the self-consistent calculations of Lang and Kohn.[20] The three curves denoted by SKG are non-self-consistent calculations. They use a linear model potential of the form,

$$v_{\text{eff}} = \frac{\hbar^2 k_f^3}{2m} \cdot \begin{cases} 0, & x < a \\ \tan\theta \cdot (x - a), & x > a \end{cases} \tag{1.3.1}$$

in which the two adjustable parameters a and θ were fitted to obey the Sugyiama sum rule[25] and the Budd-Vannimenus sum rule.[26] Each one of these three curves uses a different correlation expression. These correlation expressions were derived by Wigner (W),[28] Pines and Nozières (PN),[29] and Vashista and Singwi (VS),[30] and are given in (A-1.2-3), (A-1.2-4), and (A-1.2-5) of Appendix A-1.2. The three

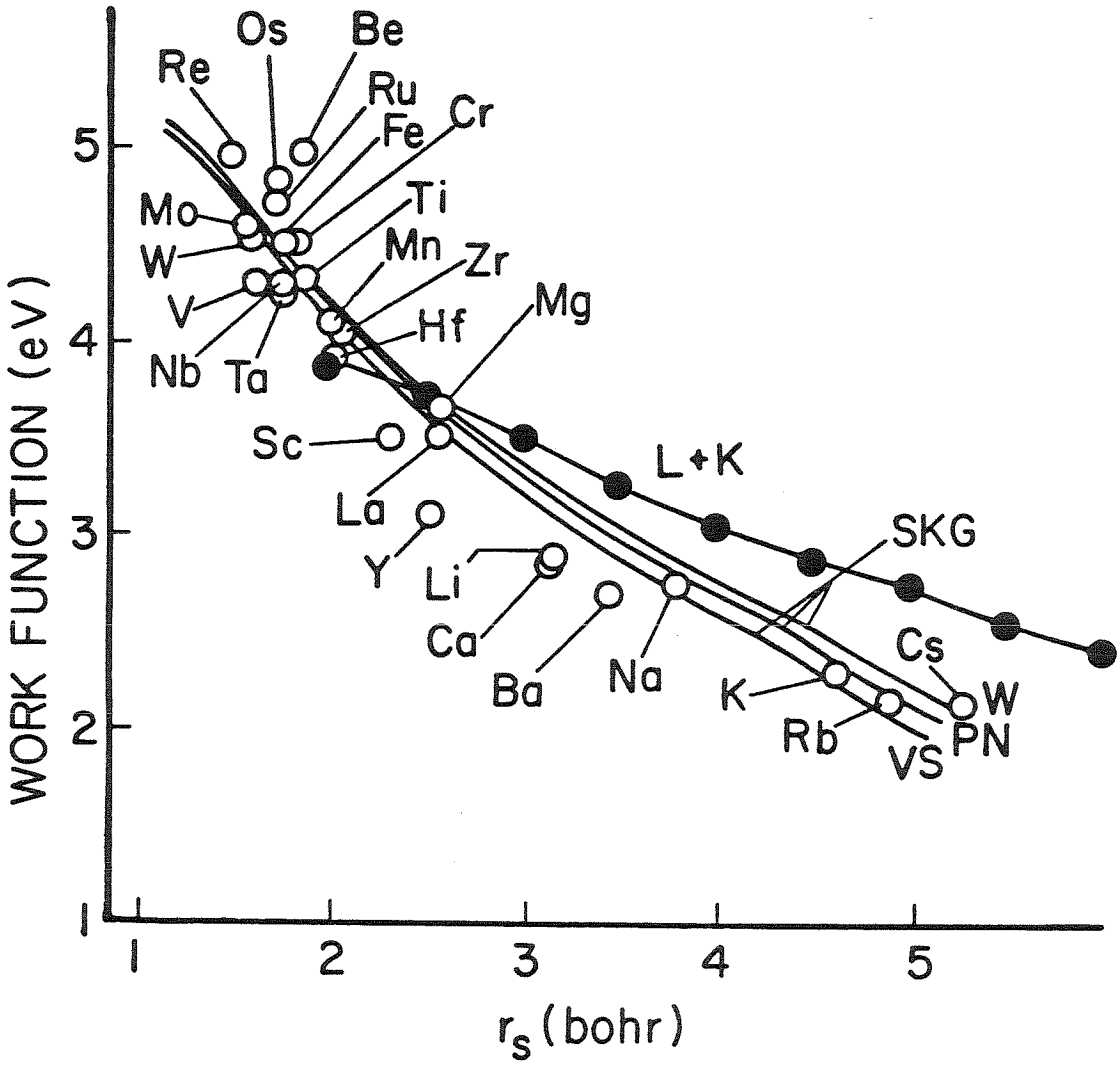

Fig. 1.3. Theoretical calculations of work function versus r_s in the jellium approximation. The line denoted L+K is from Lang and Kohn (Ref. 19) using a self consistent calculation assumming the local density approximation. The three lines denoted SKG were calculated by Sahni et al. (Ref. 23) for $r_s < 4.3$, and were continued analitically beyond $r_s = 4.3$ in this work. They represent three **non-self-consistent** calculations, using an effective potential whose parameters were fitted to two exact sum rules. Each one of these three lines uses a different correlation expression. These correlation expressions were given by Wigner (W, Ref. 28), Pines and Nozieres (PN, Ref. 29) and by Vashista and Singwi (VS, Ref. 30). The experimental data points are the same as in Fig. 1.2. This figure shows that non-self-consistent calculations may be superior to self-consistent ones, and that the jellium model is a reasonable model to describe the energy levels of metals.

curves are identical to the results of Sahni *et al.*[23] for $r_s < 4.3$. As r_s increases, so does θ, and that at $r_s = 4.3$, θ becomes a right angle, beyond which there is no physical meaning to the potential (1.3.1). Since the calculations were performed analytically, however, it was easy to continue the expressions for the work-function beyond $r_s = 4.3$. This continuation was not presented in the paper of Sahni *et al.*, and we can only justify this analytic continuation a-posteriory; the agreement to the work function of K, Rb, and Cs seen in Fig. 1.3 is very good.[31] It is also clear that the non-self-consistent calculation is better in this case than the self consistent one. Consequently, we chose to calculate the metal response to surface charge depletion, using a non-self-consistent approach, and an exact sum rule. This sum rule is derived in Appendix A-1.4.

The boundary condition of contact phenomena

We can use the jellium model described above to write the correct boundary conditions for contact phenomena. One of the more prevailing models for contact phenomena uses the so called "vacuum level" (see for example Sze[32] p.246). This level is defined to be the energy of an electron at rest, removed from the metal, with respect to the metal bulk. It takes, therefore, an amount of energy Φ_m to raise an electron from the Fermi level to the vacuum level. Before contact, the vacuum level is assumed flat; therefore, the lower the work function the higher the Fermi level. Upon contact of two conducting materials (metals or semiconductors), electrons will flow from the lower-work-function material to the higher, establishing a dipole barrier, that is, a bending in the vacuum level, which is equivalent to the difference in work functions. The notion of a vacuum level is bothersome, however. The work function is a function of the charge distribution at the metal surface; consequently, in a single crystal it may have different values for different crystal faces. Therefore the vacuum level is not well defined for a single crystal. Moreover,

this model neglects any charge redistribution upon contact. In view of (1.2.1), the true potential difference across a contact should be equal to the difference in bulk-internal chemical potentials:

$$q\Delta\phi = -\Delta\bar{\mu}, \tag{1.3.2}$$

rather than the difference in work functions.

$$q\Delta\phi = \Delta\Phi_m$$

implied by the "vacuum level" idea.

The relationship between the work function Φ_m, and the bulk internal chemical potential $\bar{\mu}$ for the jellium model is shown in Fig. 1.4. The three lines denoted by W, PN and VS are similar calculations performed using the three correlation expressions (A-1.2.3), (A-1.2.4) and (A-1.2.5). The interesting result here is that for jellium, the bulk chemical potential $\bar{\mu}$, increases rather than decreases with the work function Φ_m. That means that on contact, electrons will transfer from the side of the lower internal chemical potential to the higher.

The surface potential response to charge depletion

The goal of the calculations mentioned above, is to gauge the quality of jellium calculations with respect to real metals. Another important aspect is the metal response to the removal of charge from its surface. What we want to obtain is the potential $\phi(0)$ at the metal surface as a function of charge removed from, or added to the metal. It will be shown in Appendix A-1.4 that for jellium

$$\phi(0) = n^+ \frac{dE[n^+]}{dn^+} + \frac{q^2\sigma^2}{2n^+\epsilon_0}. \tag{1.3.3}$$

Here n^+ is the jellium positive background density, and E[n] is the electron energy functional. σ is the excess surface charge near the jellium surface, that is,

$$\sigma = \int_{-\infty}^{\infty} [n^+ - n(x)]\, dx \quad .$$

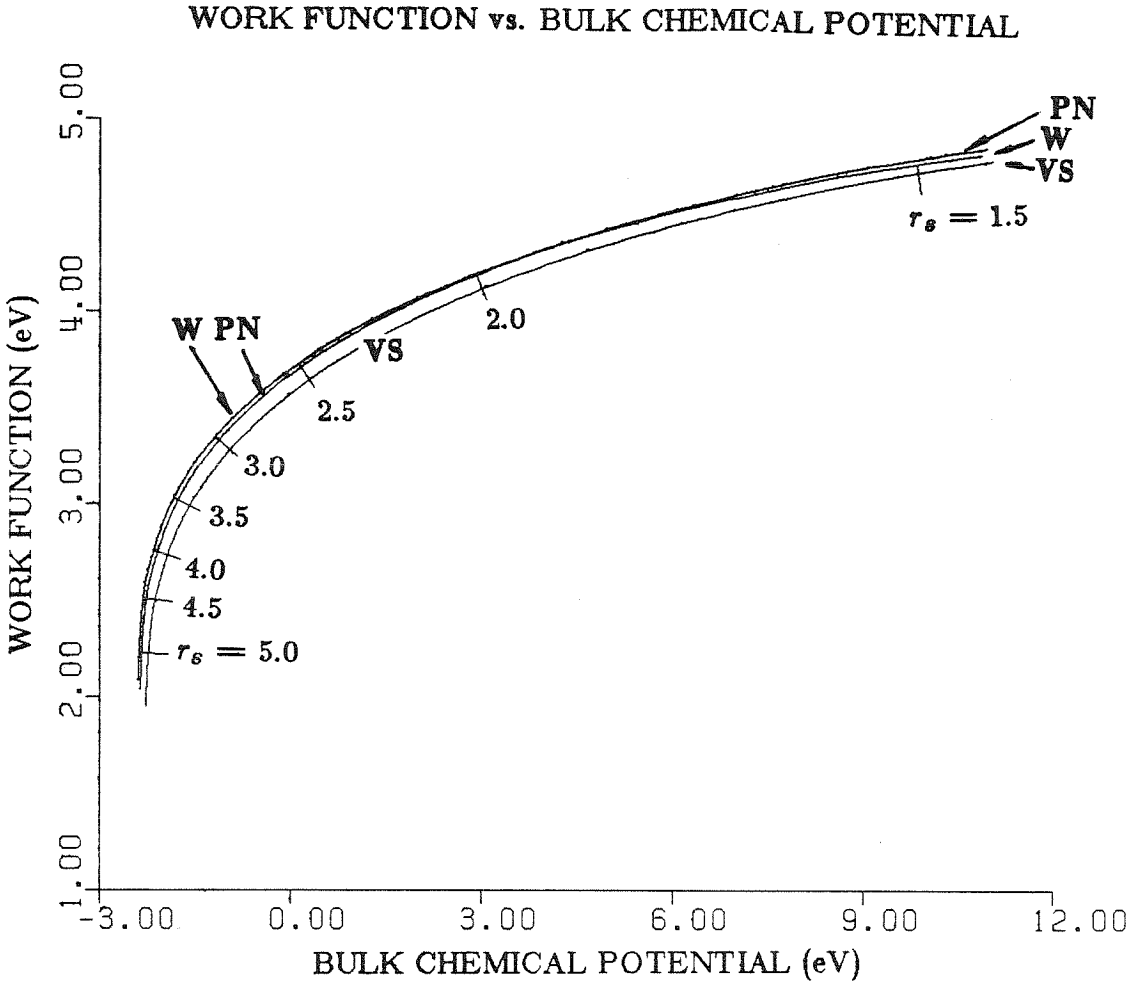

Fig. 1.4. Work function versus internal bulk chemical potential for jellium, using the linear model potential of Sahni et al, (Ref. 23). The three lines denoted by W, PN and VS are calculations performed using three different correlation expressions described in Fig. 1.3. The corresponding Wigner-Seitz radius r_s (in bohrs) is also shown in this figure. One can see that the internal bulk chemical potential changes by several electron volts over the whole metallic range, as does the work function.

Formula (1.3.3) without the extra term containing σ, is exactly the Budd-Vannimenus theorem.[26] The extra term will be of some importance in section 1.5, dealing with the metal-semiconductor interface. For most metals, one can use the jellium model with $r_s < 5$. For $r_s = 5$, and $\sigma = 10^{14}\text{cm}^{-2}$, we have

$$\left(\frac{\partial\phi(0)}{\partial\sigma}\right) = \frac{q^2\sigma}{n^+\epsilon_0} = \frac{1.1\text{V}}{10^{14}\text{cm}^{-2}}.$$

Summary of section 1.3

We have treated the ideal metal surface using the jellium model. This model was demonstrated to give reasonable results for work-function calculations. The energy levels in the one-electron picture were explained, and it was shown that the difference in bulk chemical potential, rather than the difference in work functions is the relevant quantity in calculations of interface dipole barrier. Finally, the metal surface response for charge depletion was estimated. In the jellium model, the surface potential increases quadratically with depleted charge density. For metals with $r_s < 5$ and depleted charge density of less than 10^{14}cm^{-2}, the slope of this curve is of the order of one volt per 10^{14}cm^{-2} or less.

1.4 Semiconductor surfaces with defects.

Why do we want to treat this interface

As was mentioned in the introduction to this chapter, there is a lot of interest in the initial steps of metallization. Since Bardeen[6] proposed that surface or interface states may play a role in pinning the Fermi level at the interface, there has been a persistent effort to study and characterize these interface states. One of the major recent contributions in this direction is the Unified Defect Model[9] of Spicer *et al.* They have noticed that a clean smooth surfaces of GaAs and InP, cleaved under ultra-high vacuum conditions, have virtually no surface states in the band gap; however, minute quantities of adatoms (less than a monolayer) would create many such states and pin the Fermi level at some fixed position in the gap. These experiments showed that the Fermi-level position as a function of coverage became almost flat at less than a monolayer coverage, the Fermi-level position was the same for many different metals, and that the Fermi-level position was different on n- and p-type semiconductors. In this section we shall model this interface by a clean semiconductor surface containing defects. It will be demonstrated that this simple model reproduces very well the experimental results. The success of this model strongly suggests that the metallic adatoms induce the creation of the interface states, but do not contribute significant amount of charge to the system. In the next section, when we treat the limit of a thick metallic overlayer, we shall see that it is the metal which contributes most of the charge. Consequently, there is a major change in behavior between the cases of thin and thick metallic coverage, and we must conclude that the experimental positions of the Fermi level, established for very thin metallic coverages, may change substantially when the metallic overlayer becomes thick.

The physics of the model

According to the Unified Defect Model[9] of Spicer *et al.*, the Fermi-level position at the interface between a metal and a semiconductor is influenced by the presence of chargeable defects near the semiconductor surface. Since the system as a whole is electrically neutral, there must be charges that compensate the defects, somewhere in the system. For free surfaces or a surface with a sub-monolayer coverage of adatoms, these charges must be the shallow impurities in the depletion region of the semiconductor. This case will be treated in this section. When there is a thick metallic coverage on the semiconductor, there could be another major source of charge, namely, the screening charge in the metal. That case will be treated in the next section. In each case, the equal and opposite charges form a dipole layer analogous to a parallel plate capacitor. In both cases, the voltage across this capacitor should be of the order of 1 V. The distance between the plates, however, is very different in the two cases resulting in very different charge densities that are required to pin the Fermi level. For the sub-monolayer case, this distance is typically of the order of a few thousand angstrom. In that case, a potential difference of a volt is achieved with a depletion charge of $10^{11} - 10^{12} \cdot cm^{-2}$. In the thick metallic coverage, the separation of charge is essentially the distance between the defects and the metal. This distance is of the order of few angstroms. Therefore the density of chargeable defects required to pin the Fermi level should be of the order of $10^{14} \cdot cm^{-2}$.

The sign of the charges on the interface defects is also determined by different physical mechanisms in the two cases. In the submonolayer coverage, the depletion region can charge only one way (positive for n- , negative for p- type). Hence, only defect acceptors can charge on n-type, and only defect donors can charge on p-type semiconductors. Therefore, the sign of the charge on the interface defects is

determined by the bulk doping type. The position of the Fermi level is determined by the energy level of that defect that can charge with the right sign, assuming both surface donors and acceptors are present. Thus the Fermi-level position can depend on the doping type for submonolayer coverages. In the thick metallic coverage case, the metal can supply charges of either sign, and the magnitude of the metal screening charge can greatly exceed that of the semiconductor depletion charge. The sign of the charges on the defects will be determined by the metal bulk chemical potential relative to the defect energies prior to any charge transfer. Therefore, the charge on the defects will be determined mainly by the metal chemical potential (work function) with semiconductor doping playing only a minor role, owing to the much larger charging capacity of the metal. The Fermi-level position in the interface is determined by the energy level of the defect that is being charged. This defect level is determined by the metal chemical potential, but not by the semiconductor doping.

The spatial arrangement of the charge for the submonolayer coverage is shown in Fig. 1.5. For this case, we have assumed defects that are very close to the surface. The only sources of charge are these defects and the bulk doping of the semiconductor. We assume here that the adatoms do not contribute any significant amount of charge. We also assume that both defect donors and defect acceptors are present on the surface.

The calculation of the Fermi-level position at the semiconductor surface is very simple, using conservation of charge. For a given Fermi-level position at the surface, the total charge density in the defects is given by

$$\sigma^{+}(\eta) = \frac{\sigma}{g_s \exp(\frac{\mu - E_s}{k_B T}) + 1} = \frac{\sigma}{g_s \exp(\frac{\eta + E_c - E_s}{k_B T}) + 1} \quad , \qquad (1.4.1)$$

where σ is the total density of defects and g_s is the state degeneracy. The parameter $\eta \equiv \mu - E_c$ is the Fermi-level position relative to the conduction band edge.

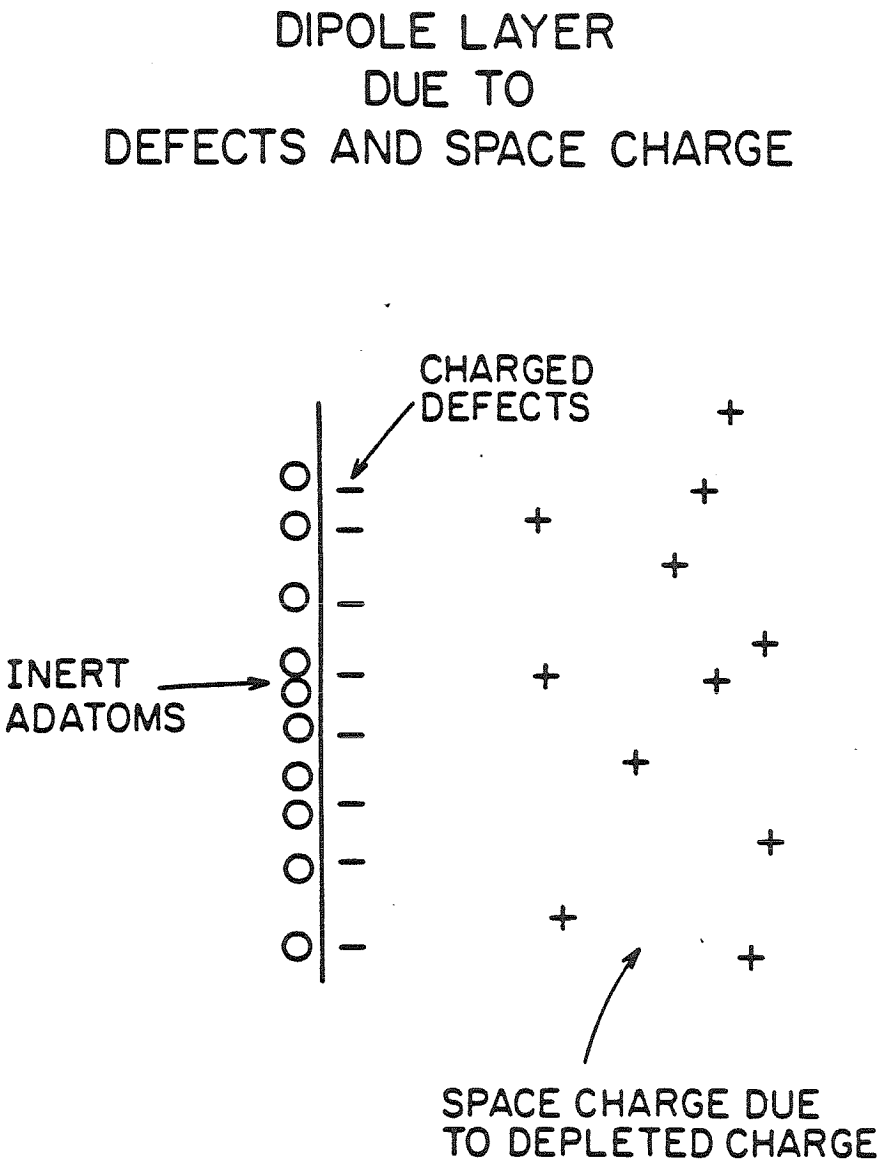

Fig. 1.5. The spatial arrangement of charge for the semiconductor with a submonolayer coverage of adatoms. We assume that the adatoms cannot contribute a significant amount of charge to the dipole layer, and their only role is to create defects near the surface. If both defect donors and acceptors are present, they will charge according to the depletion charge, i.e. defect donors will charge on p-type material, and defect acceptors on n- type material.

Equation (1.4.1) refers to a defect donor, and there is an analogous formula for a defect acceptor. The compensating charge density in the bulk depletion layer is given by

$$\mathcal{Q}_s(\eta) = \pm\sqrt{\frac{2\epsilon\epsilon_0}{q^2}\int_{\eta(\infty)}^{\eta}\left[n(\eta') + \begin{pmatrix} -N_D^+(\eta') \\ +N_A^-(\eta') \end{pmatrix} - p(\eta')\right] d\eta'} \qquad \begin{matrix} \text{n-type} \\ \text{p-type} \end{matrix}$$

where n, p, N_D^+, and N_A^- are the densities of electrons in the conduction band, holes in the valence band, ionized donors (in an n- type semiconductor), and ionized acceptors (in a p- type semiconductor). The formula above is derived in Appendix A-1.1. Since these two sources of charge must balance, a solution is obtained by equating the two charges, thus, obtaining the Fermi level at the surface.

The results of our calculation for submonolayer coverages are presented in Figure 1.6. In this figure we show results for the case of two separate defects, one a donor and the other an acceptor, in equal concentration. The donor level is taken to be 0.5 eV from the valence band edge, and the acceptor level is taken to be 0.75 eV from the valence band edge. These values were picked to be consistent with those obtained by Spicer *et al.*;[9] however, the qualitative behavior of the results does not depend on the specific energy levels as long as the defect acceptor level is higher than the defect donor level. If not, compensation occurs, and the n- and p- type lines would be closer. The behavior of the Fermi level with increasing density of surface defects is qualitatively like that obtained by Spicer *et al.*,[9] and the pinning position, that is, the position of the Fermi level for n- and p-type semiconductors differs by a substantial amount. For the case considered in Fig. 1.6, only the acceptor defects are charged, and the donors are neutral for the n- type semiconductor. For the p- type semiconductor the situation is reversed. Thus, for n- type semiconductors, the Fermi-level position is determined by the defect acceptor level, and for p- type semiconductors, it is determined by the defect

donors.[33] Since these energy levels will, in general, be different, the Fermi level pins at different energies for n- and p- type semiconductors. At defect densities of $\approx 10^{12} \cdot cm^{-2}$, the Fermi-level position is seen to be largely stabilized.[33]

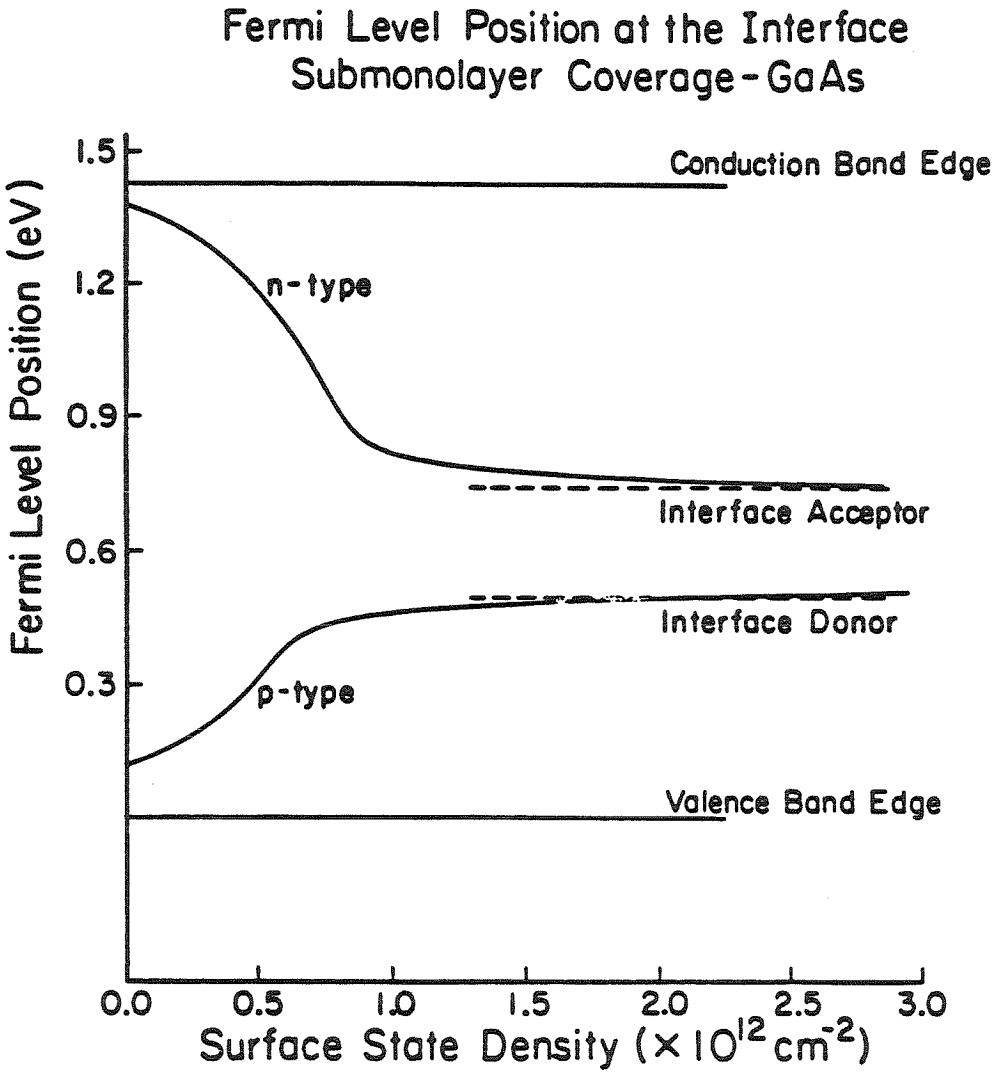

Fig. 1.6. Fermi level position vs defect density for the metal submonolayer coverage model (clean surface with defects). The concentration of surface acceptors and donors was assumed equal, and their ionization energies were picked from the results of Spicer *et al.* (Ref. 9).

1.5. The metal-semiconductor interface.

A. The three regions of the model

The schematic of our metal-semiconductor interface is given in Fig.1.7, and the charge density as well as the electronic energies near the interface are shown in Fig. 1.8. We assume that the metal-semiconductor junction consists of three regions: semi-infinite bulk metal, semi-infinite bulk semiconductor, and an interface region. We now discuss those three regions in more detail.

The interface region in the semiconductor

The interface region in the semiconductor is the narrow region where the charged defects are located. We assume that this region is located between $x = 0$ and $x = d$ in Fig. 1.8. The region is sufficiently narrow that transport of carriers through this region is uninhibited. Hence, the dipole layer that exists between the charged defects and the metal is included in the abrupt barrier that is usually assumed and is not measurable separately.

We will assume that there is no charge inside this layer, and that the defects are all on one side of this layer ($x = d$). Later we will show that our model is insensitive to that assumption, that is, the effect of distributing the defects throughout the interface region is equivalent to putting them all on a single plane at some effective distance from the metal. The electrostatic-potential-energy difference across this layer is given by

$$\Delta V_i = \int_0^d q^2 \mathcal{E}_x \, dx \quad , \tag{1.5.1}$$

where $\mathcal{E}_x$ is the electric field in this interface layer, and q is the electron charge (taken positive). In our calculations we neglect the tailing of the metallic charge

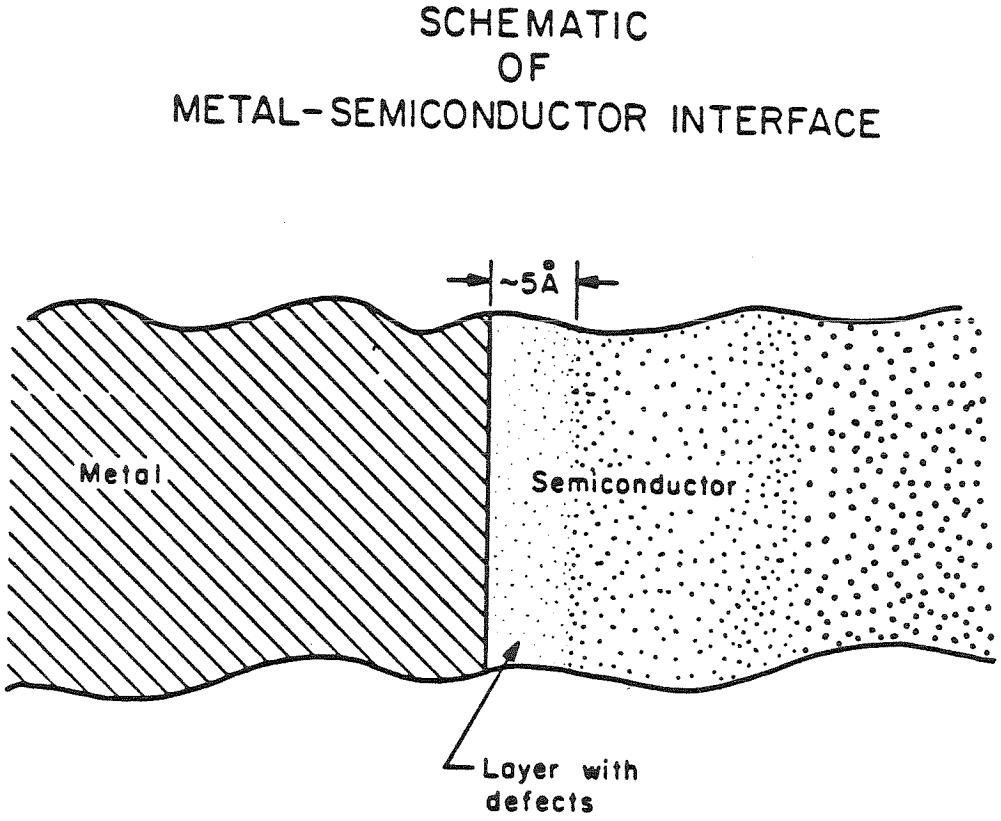

Fig. 1.7 The geometry of our metal – semiconductor model. We assume that the metal terminates sharply at $x = 0$ and that all the interfacial transition occurs at $0 < x < d$, so that the semiconductor from $x = d$ and on has a regular crystalline structure with few imperfections and the bulk band structure is meaningful for $x > d$. All the defects are localized in the intermediate region $0 < x < d$, and we assume that they are all on the plane $x = d$. The plane $x = d$ is also the place where we calculate the Fermi-level position.

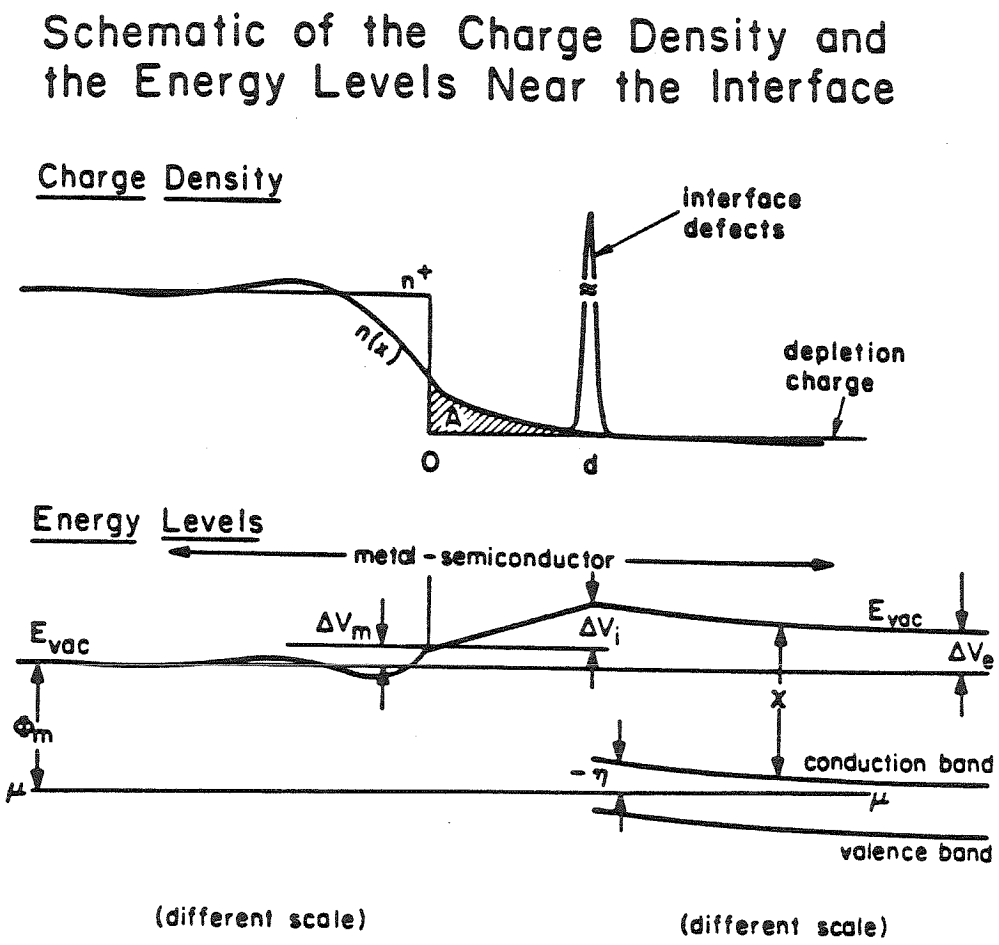

Fig. 1.8. Charge density and energy levels at a metal surface using our model. In the upper part we show the charge density profile. We used the jellium model for the metal side, having a uniform background of n^+ extending up to $x = 0$. The charged defects at $x = d$ are shown here as a very sharp Gaussian. In our calculations we took it to be infinitely sharp. The finite charge distribution outside the metal surface (the hatched region denoted by A) which in a free metal surface would balance the charge inside the metal is neglected in our calculation of the electrostatic potential. In the lower part we show the energy levels as functions of position. μ is the chemical potential which is constant throughout space at equilibrium. Φ_m is the metal work function, ΔV_m is the potential difference between the jellium surface and bulk; ΔV_i is the potential difference across the dipole layer; d is the dipole layer width, assumed here to be 5Å; $\eta(x)$ is the Fermi level position relative to the conduction band edge, and χ is the semiconductor electron affinity. The total potential difference across the interface is ΔV_e. Note the change in scale between the metal and the semiconductor side. We expanded the metal side for clarity.

density (denoted by "A" in Fig. 1.8), and consider it to be all concentrated on the metal surface ($x = 0$). Under this assumption $\mathcal{E}_x$ in (1.5.1) is constant.

The most important parameters of this layer are its effective width (d), its dielectric constant (ϵ), the defect density (σ), and their ionization energies. We will assume that almost all the defects are localized within few Å of the metal surface; in this model we take this width to be 5Å, that is, 2-3 atomic layers. We will also assume that the dielectric constant in this layer equals that of the bulk semiconductor.

The metal

We have used the jellium model, treated in section (1.2), to describe the metal. The electronic energies near the metal surface in this jellium approximation are shown schematically on the left side of Fig. 1.8. In this figure Φ_m is the work function; μ is the chemical potential which is constant throughout space at equilibrium. The electrostatic potential in this figure is the thick line denoted by E_{vac}. This notation goes back to the classical model of Bardeen,[6] according to which, the total potential difference across the interface, ΔV_e, should be equal to the difference between the work-functions of the semiconductor and the metal. This model is not quite right, since the work functions involve charge distributions across the metal-vacuum and semiconductor-vacuum interfaces, which might be quite different than that of the metal-semiconductor interface. Instead, in view of (1.2.1), ΔV_e should be equal to the difference in chemical potentials, rather than the difference in work functions. In spite of that fact, we have chosen to show the Bardeen model Φ_m, χ and E_{vac}, as well as the more reasonable model with $\bar{\mu}_m$ and $\bar{\mu}_s$.

Near the interface, the electrostatic potential varies due to non-cancelling

charge densities. The variation in the potential results in an offset between the electrostatic potential at the interface and far inside the metal. The parameter of interest to us is this difference ΔV_m , which might change somewhat in order to screen charges in the semiconductor. In this section we are interested in variations between metal interfaces to n- and p- type semiconductors, and this ΔV_m will have to screen the difference in depletion charge between the two cases. We do not expect this difference in ΔV_m between n- and p- type semiconductors to be large, but it might play some role, and we want to estimate its magnitude. In general, ΔV_m will be a function of the net excess charge inside the metal $\mathcal{Q}_m$, where

$$\mathcal{Q}_m = \int_{-\infty}^{d} [n^+ - n(x)]\, dx \quad ,$$

and where n^+ and $n(x)$ are the jellium positive background and the electron densities, respectively. In the linear approximation a change in ΔV_m can be related to a change in $\Delta \mathcal{Q}_m$ by

$$\Delta V_m(\Delta \mathcal{Q}_m) \approx \Delta V_m^0 + \left(\frac{\partial \Delta V_m}{\partial \mathcal{Q}_m}\right)_0 \Delta \mathcal{Q}_m \quad , \tag{1.5.2}$$

where the zero point refers to a contact to an intrinsic semiconductor, and $\Delta \mathcal{Q}_m$ is the difference in $\mathcal{Q}_m$ between this case and either n- or p- type semiconductors. The parameter $\left(\frac{\partial \Delta V_m}{\partial \mathcal{Q}_m}\right)_0$ could play some role in our calculation. In order to estimate the size of this parameter, we replace the metal-semiconductor interface, by a jellium-vacuum interface, and use the Mahan-Schaich Theorem.[27] According to this theorem, modified for a non-neutral jellium surface,

$$\Delta V_m(\mathcal{Q}^*) = n^+ \frac{d\epsilon[n^+]}{dn^+} + \frac{q^2 \mathcal{Q}^{*2}}{2n^+ \epsilon_0}. \tag{1.5.3}$$

This formula is derived in (A-1.4.5) of Appendix A-1.4. Here n^+ is the jellium positive background density, and $\epsilon[n]$ is the electron energy functional of Appendix

A-1.2 (not to be confused with the static dielectric constant ϵ_0). $\mathcal{Q}^*$ is the excess surface charge near the jellium surface, that is,

$$\mathcal{Q}^* = \int_{-\infty}^{\infty} [n^+ - n(x)]\, dx \quad ,$$

and it is somewhat different from our $\mathcal{Q}_m$. This difference is due to the tail of the charge distribution in the region $x > d$, which is missing in the definition of $\mathcal{Q}_m$, but for d=5Å, this difference is negligible.

Using (1.5.3), we obtain,

$$\left(\frac{\partial \Delta V_m}{\partial \mathcal{Q}^*}\right) = \frac{e^2}{n^+ \epsilon_0} \mathcal{Q}^* .$$

In our results section, we are going to find that as many as 10^{14} defects per cm^2 are required to pin the Fermi level. Upon charging, these defects may deplete the metal by a similar amount of charge. Therefore we should use $|\mathcal{Q}^*| < 10^{14} cm^{-2}$. For $\mathcal{Q}^* = 10^{14} cm^{-2}$ and for n^+ corresponding to $r_s = 5$, we have $\left(\frac{\partial \Delta V_m}{\partial \mathcal{Q}^*}\right) = 1.1 \times 10^{-14} V \cdot cm^2$. For most metals, $r_s < 5$, and this number will be even smaller. Since jellium is only a rough approximation to real metals, and since $\mathcal{Q}^*$ and $\mathcal{Q}_m$ are not exactly the same, we consider this number to be an order of magnitude estimate; in this section we take ΔV_m^0 and $\left(\frac{\partial \Delta V_m}{\partial \mathcal{Q}_m}\right)_0$ to be parameters of the model, and allow $\left(\frac{\partial \Delta V_m}{\partial \mathcal{Q}_m}\right)_0$ to change between 0.1 and 1.0 $eV/10^{14} e \cdot cm^{-2}$. Our results will show that these two cases are very similar, suggesting that the effect of $\left(\frac{\partial \Delta V_m}{\partial \mathcal{Q}_m}\right)_0$ is not critical.

The Bulk Semiconductor

We want to find the position of the chemical potential with respect to the conduction band edge as a function of position $\eta(x) = \mu - E_c(x)$. We will take the semiconductor to occupy the space along the positive x-axis, with $d < x < \infty$.

We know $\eta(\infty) = (\mu - E_c(\infty))$, the relative position of the Fermi level at $x = \infty$, for a given host semiconductor, doping, and temperature, but $\eta(x) = \mu - E_c(x)$ for $x < \infty$ is yet to be determined. The important property of this semi-infinite semiconductor is that knowing $\eta(x)$ at $x = d$, we can find $\eta(x)$ for any $x > d$, and calculate the total number of charges ($\mathcal{Q}_s$) per unit area of the semiconductor by solving Poisson's equation:

$$\begin{array}{ll} \frac{d\eta}{dx} = \frac{q^2}{\epsilon\epsilon_0}\mathcal{Q}_s(x) & \eta = (\mu - E_c) \\ \frac{d\mathcal{Q}_s}{dx} = n(\eta) + \begin{pmatrix} -N_D^{+}(\eta) \\ +N_A^{-}(\eta) \end{pmatrix} - p(\eta) & \end{array}, \tag{1.5.4}$$

where expressions for $n(\eta)$, $p(\eta)$, $N_D^{+}(\eta)$, and $N_A^{-}(\eta)$ are given in Appendix A-1.1. Here, n, p, N_D^{+}, N_A^{-} are the densities of electrons in the conduction band, holes in the valence band, ionized donors (in n-type semiconductor), and ionized acceptors (in p-type semiconductor). Poisson's equation (1.5.4) can be reduced to an integral

$$\mathcal{Q}_s(\eta(d)) = \sqrt{\frac{2\epsilon\epsilon_0}{q^2}\int_{\eta(\infty)}^{\eta(d)} \left[n(\eta) - N_D^{+}(\eta) - p(\eta)\right]\, d\eta} \tag{1.5.5}$$

for an n-type semiconductor, with a similar formula for a p-type one, in which there is a minus sign in front of the square root, and $+N_A^{-}(\eta)$ replaces $-N_D^{+}(\eta)$.

In this work it was assumed that the semiconductor is not degenerately doped, and that the Fermi level at the interface is inside the gap, at least $2k_BT$ from the gap edges. In this case, we could assume that the carriers in the semiconductor obey Maxwell Boltzmann statistics; the integral in (1.5.5) was then calculated analytically.

B. Calculation of the Fermi-level position.

We may calculate the Fermi-level position using the model described above. The electrostatic-potential-energy variation from deep in the metal to deep in the semiconductor is given by ΔV_e

$$\Delta V_e = \int_{-\infty}^{+\infty} q^2 \mathcal{E}(x)\, dx \quad , \tag{1.5.6}$$

where $\mathcal{E}(x)$ is the electric field at x. By comparison with Fig. 1.8 we see that ΔV_e must be given by

$$\Delta V_e = \bar{\mu}_m - \bar{\mu}_s = \bar{\mu}_m - \bar{\mu}_s^0 - \eta(\infty).$$

where $\bar{\mu}_m$ is the internal chemical potential of the bulk metal, $\bar{\mu}_s$ is the same for bulk semiconductor, and $\bar{\mu}_s^0 = \bar{\mu}_s + E_c - E_f$. ($\Delta V_e = \chi - \eta(\infty) - \Phi_m$ in the Bardeen model). Breaking the integral in Eq.(1.5.6) into three parts, $(-\infty, 0)$, $(0, d)$, and (d, ∞), we have

$$\eta(d) + \bar{\mu}_s^0 + \Delta V_m - \bar{\mu}_m = -\int_0^d q^2 \mathcal{E}(x)\, dx \quad . \tag{1.5.7}$$

We can write the electric field $\mathcal{E}(x)$ in the interface layer as a sum of two contributions, one ($\mathcal{E}_x^s$) due to dipoles formed by charged defects, and the other ($\mathcal{E}_x^b$) due to dipoles formed by space charges in the semi-infinite semiconductor. In general, ($\mathcal{E}_x^s$) is much larger than ($\mathcal{E}_x^b$). ($\mathcal{E}_x^b$), however, is responsible for any difference between n- and p- type semiconductors. We neglect any charge due to doping in the interface layer since their number in such a thin slab of a semiconductor is very small.

If we know the statistics of charged defects in the interface layer as a function of $\eta(d)$, we can find their contribution to the electric field inside that layer. The

bulk contribution is known, and equals

$$\mathcal{E}_x^b = \frac{-q}{\epsilon\epsilon_0}\mathcal{Q}_s(\eta(d)) \quad ,$$

where $\mathcal{Q}_s(\eta(d))$ is given by Eq.(1.5.5), and ϵ is the dielectric constant in this layer, which is assumed to be the same as in the semiconductor bulk. Now, given $\bar{\mu}_m, \Delta V_m^0, \left(\frac{\partial \Delta V_m}{\partial \mathcal{Q}_m}\right)_0$, and $\bar{\mu}_s$, we can solve Eq.(1.5.7) to obtain $\eta(d)$ as a function of $\bar{\mu}_s^0 + \Delta V_m^0 - \bar{\mu}_m$. The plot of $\eta(d)$ vs $\bar{\mu}_s^0 + \Delta V_m^0 - \bar{\mu}_m$ for different cases will give the variation of the Fermi level with metal work function for a fixed semiconductor.

Throughout our calculations, we arbitrarily chose all the semiconductor parameters that enter implicitly into Eq.(1.5.5), (effective masses, dielectric constant, band gap, impurity levels) to be those of GaAs. ($E_{gap} = 1.43$ eV, $m_e^*/m_0 = 0.068$, $m_h^*/m_0 = 0.5$, $\epsilon = 13.1$, and the shallow impurity levels are taken to be 5 meV and 25 meV for donors and acceptors, respectively.) Actually, the only relevant parameters are the dielectric constant and the band gap; consequently, it is very easy to correct the results for any other semiconductor.

C. Results for bulk metal-semiconductor interface.

To indicate the role of different types of defects, we have treated a number of different spatial arrangements and possible charge states for the defects.

Defects with two charge states

The simplest case is an interface state which has only two charge states, neutral or charged. We have examined the role of spatial distribution by considering two cases: one with all the defects located in a single plane at $x = d$, and the other with the defects located on two separate planes. The defect density is varied from 0 to 10^{14}cm^{-2}. In the case where all the defects are located in a single plane at $x = d$, Eq. (1.5.7) becomes

$$\bar{\mu}_s^0 + \Delta V_m - \bar{\mu}_m = -\eta(d) + \frac{q^2 d}{\epsilon\epsilon_0}\left[\sigma^+(\eta(d)) + \mathcal{Q}_s(\eta(d))\right],$$

where q is the electron charge (positive), d is the interface layer width, ϵ is the dielectric constant in this layer, $\mathcal{Q}_s$ is the number of charges per unit area in the semiconductor bulk, and σ^+ is the density of (positively) ionized defects. σ^+ will be positive if the defects are all donors, and negative if these defects are acceptors. In our calculations we assume all the two charge states to be donors. A similar calculation for acceptors is straightforward, and will not be presented here. $\sigma^+(\eta)$ can be calculated if we know the ionization energy of the interface state; this energy is given in (1.4.1) for a donor defect.

Fig. 1.9 shows $\mathcal{E}_x^s$ and $\mathcal{E}_x^b$, the interface and bulk contributions to the field in the interface layer, (or σ^+ and $\mathcal{Q}_s$, the corresponding density of charges) as a function of η, the relative Fermi-level position, for two different values of defect density: $\sigma = 10^{13} cm^{-2}$ and $\sigma = 10^{14} cm^{-2}$. The interface energy level appearing

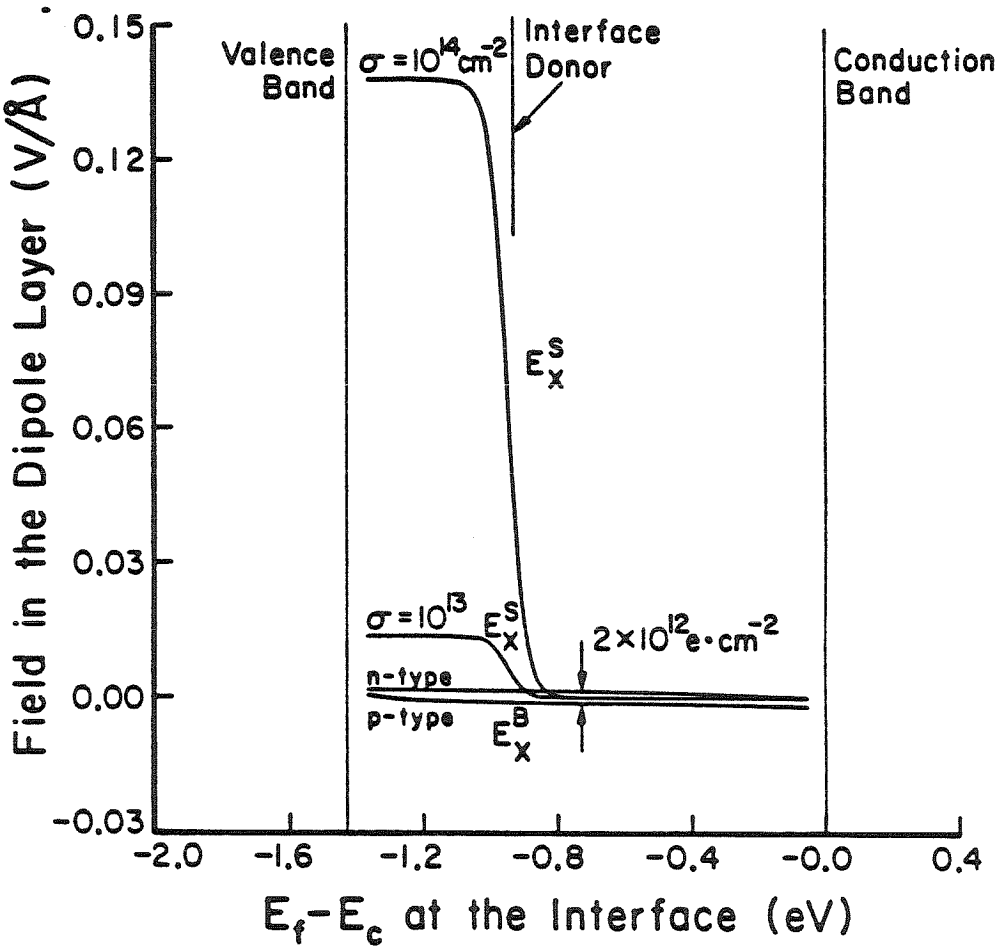

Fig. 1.9. Electric field in the dipole layer vs Fermi level position in the gap at $x = d$, for defect densities of $10^{13} - 10^{14} \cdot cm^{-2}$. The lines 'n-type' and 'p-type' correspond to the bulk contributions of n- or p-type GaAs having impurity concentration of $10^{17} cm^{-3}$. The E_x^s lines correspond to the defects contribution, for two defect densities (σ). The interface defects in this case were chosen to be donors.

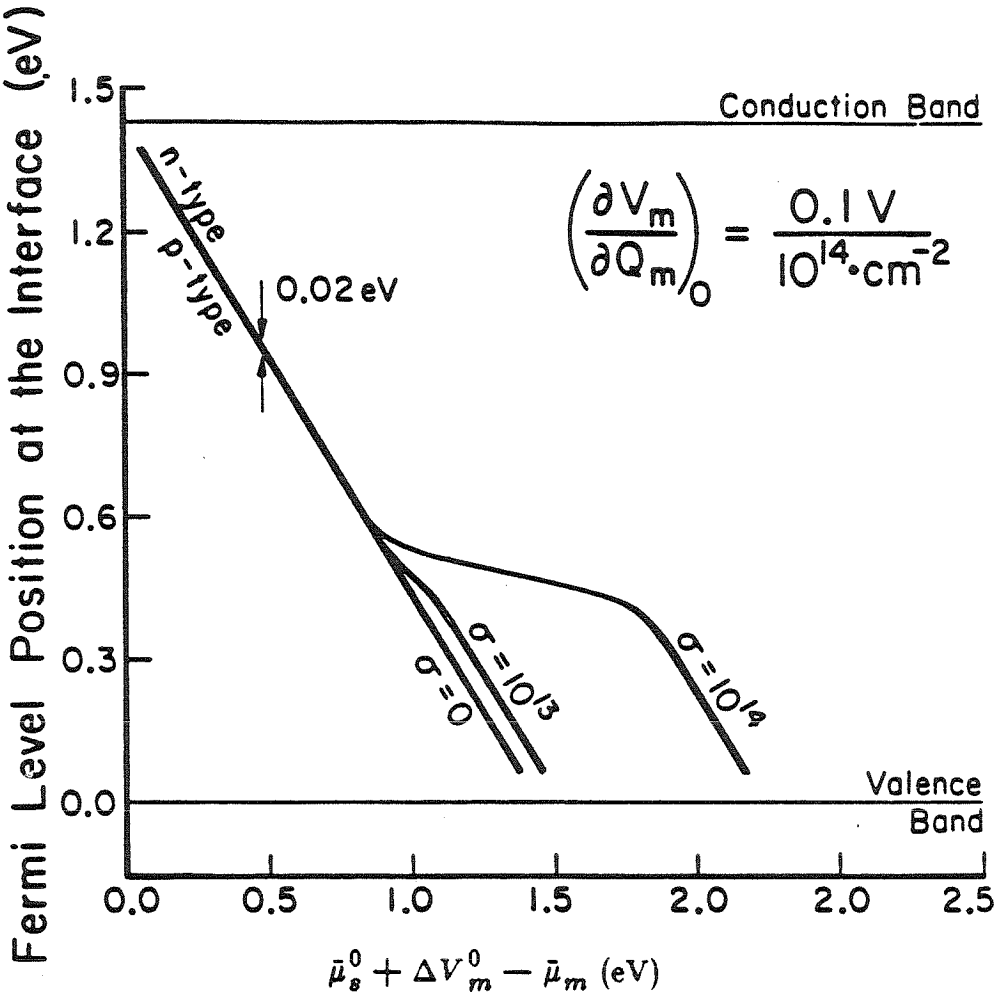

Fig. 1.10. Fermi level position in the gap at $x = d$ vs $\bar{\mu}_s^0 + \Delta V_m^0 - \bar{\mu}_m$, for three values of the defect density (σ, in units of cm^{-2}). The metal response term, $\left(\frac{\partial \Delta V_m}{\partial Q_m}\right)_0$ equals $0.1eV/10^{14}e \cdot cm^{-2}$. Here $\bar{\mu}_s^0 + \Delta V_m^0 - \bar{\mu}_m$ is the difference in bulk internal chemical potential between the semiconductor and the metal (see text), plus a term ΔV_m^0 which is the potential difference between the metal surface and the metal bulk (cf. Fig. 1.8). The expression $\bar{\mu}_s^0 + \Delta V_m^0 - \bar{\mu}_m$ replaces $\Phi_m - \chi$ in the Schottky-Bardeen model. It is a theoretical quantity, to which we cannot, as yet, assign numerical values for any specific metal – semiconductor pair. However, as was shown in Fig. 1.4, we expect this quantity to change by several volts upon changing metals. In this figure we can see that a defect density of the order of $10^{14} \cdot cm^{-2}$ is required to pin the Fermi level, i.e. to have the Fermi level fixed when $\bar{\mu}_s^0 + \Delta V_m^0 - \bar{\mu}_m$ changes by about 1 eV. The difference between the Fermi level positions on n- and p-type semiconductors is estimated here to be 0.02 eV. In this figure, we assumed that only defect donors exist at the interface. This assumption was made to decrease the number of details in this figure, but it should not restrict the conclusions drawn.

in this figure was chosen to agree with Spicer's value for the GaAs defect donor;[9] g_s was arbitrarily chosen to be equal to 2. The two lines denoted by n-type and p-type are the corresponding $\mathcal{E}_x^b$ for n- and p- type semiconductors. The doping concentration in each case is $N_D = N_A = 10^{17} cm^{-3}$. It should be noted in Fig. 1.9 that the electric field in the interface region is very large, on the order of 0.1 V/Å, when $\sigma = 10^{14} \cdot cm^{-2}$. It is clearly seen that at a defect density of $10^{14} \cdot cm^{-2}$, the defect contribution to the field dominates the depletion charge contribution. At a defect density of $10^{13} \cdot cm^{-2}$, the two contributions are comparable.

In Fig. 1.10 we show η vs $\bar{\mu}_s^0 + \Delta V_m^0 - \bar{\mu}_m$ for the same σ's and $\mathcal{Q}_s$'s that we have used in Fig. 1.9. ΔV_m was calculated from (1.5.2) using

$$\left(\frac{\partial \Delta V_m}{\partial \mathcal{Q}_m}\right)_0 = 0.1eV/10^{14} e \cdot cm^{-2} \quad .$$

In all three plots the interface layer was assumed to be 5Å wide. In Fig. 1.10, one can see three pairs of lines. The upper one in each pair corresponds to an n-type, and the lower one to a p-type bulk semiconductor. The defect density σ varies from $\sigma = 0$, through $\sigma = 10^{13} cm^{-2}$, to $\sigma = 10^{14} cm^{-2}$.

For $\sigma = 0$, the two lines are almost exactly straight lines with slope equal to -1 corresponding to the equation

$$\eta(d) = -\bar{\mu}_s^0 - \Delta V_m^0 + \bar{\mu}_m \quad .$$

If $\Delta V_m = 0$, this would be the curve predicted by the classical Schottky model assuming no interface layer between the metal and the semiconductor. The slopes of the two lines in Fig. 1.10 are approximately -1, since the change in ΔV_m is negligible in this case. We can estimate the variation in ΔV_m for each pair of lines using Eq.(1.5.2). $\Delta \mathcal{Q}_m$ is seen in Fig. 1.9 to change by not more than $2 \cdot 10^{12} e \cdot cm^{-2}$; therefore, ΔV_m changes by not more than $2meV$ throughout the

whole range of the $\sigma = 0$ pair. Knowing that the maximal slope of each pair of lines in Fig. 1.10 is -1, we will be able to estimate $\Delta\eta$, the difference in Fermi-level position at the interface, by estimating $\Delta(\bar{\mu}_s^0 + \Delta V_m^0 - \bar{\mu}_m)$. (They will be approximately equal to each other.)

Using the abrupt (full depletion) model, we can estimate this difference to be

$$\Delta\eta \approx \Delta(\bar{\mu}_s^0 + \Delta V_m^0 - \bar{\mu}_m) = \frac{q^2 d\,\Delta\mathcal{Q}_s}{\epsilon\epsilon_0} < 2qd\sqrt{\frac{N_D(Ec - Ev)}{\epsilon\epsilon_0}} \quad (1.5.8) \quad .$$

The reason that $\Delta\eta \neq 0$ even for $\sigma = 0$ is partially an artifact of our model, even though we do not have any dipoles, we nevertheless assume an interface layer with a finite width. $\Delta\eta(0) \approx 0$ but at $x = d$, $\Delta\eta(d) \neq 0$ due to different band bending in this 5Å layer.

The maximum difference in Fermi-level position occurs when there is no pinning, that is, when the slopes of the n- and p-type lines are approximately -1. To see this note that in the $\sigma = 10^{14}$ lines when E_f approaches the defect level, the defects charge rapidly, and both the n- and the p-type lines are shifted in parallel to the right. The low slope of the two lines around E_s reduces $\Delta\eta$ between the n- and p-type cases. Using (1.5.8) we can estimate the maximum difference to be $\approx$3 meV/Å times the effective interface layer width for GaAs, when the doping concentration is $10^{17} cm^{-3}$, and $\left(\frac{\partial \Delta V_m}{\partial \mathcal{Q}_m}\right) = 0$. When $\left(\frac{\partial \Delta V_m}{\partial \mathcal{Q}_m}\right) = 0.1eV/10^{14} e \cdot cm^{-2}$, there will be an extra contribution of $2meV$ for GaAs to this difference. As one can see in this figure, the range of $\bar{\mu}_s^0 + \Delta V_m^0 - \bar{\mu}_m$ in which η is approximately constant is quite small for $\sigma = 10^{13} \cdot cm^{-2}$. In other words, a defect density of $\sigma = 10^{13} \cdot cm^{-2}$ is **not quite enough to pin the Fermi level.** When $\sigma = 10^{14} cm^{-2}$, however, the range of $\bar{\mu}_s^0 + \Delta V_m^0 - \bar{\mu}_m$ in which $\Delta\eta$ is constant is quite large, on the order of $1eV$.

Fig. 1.11 is the same as Fig. 1.10, but with what is likely to be a very large

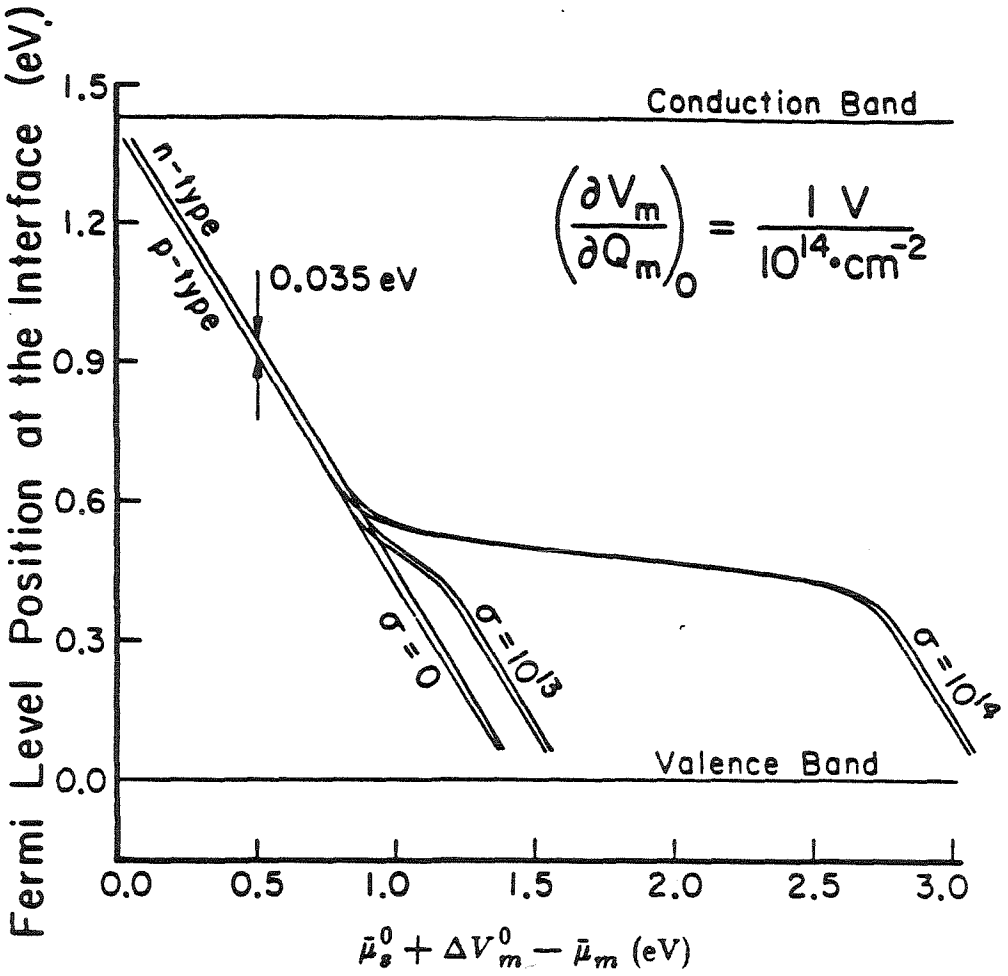

Fig. 1.11. Fermi level position in the gap at $x = d$ vs $\bar{\mu}_s^0 + \Delta V_m^0 - \bar{\mu}_m$ for three values of the defect density. The metal response $\left(\frac{\partial \Delta V_m}{\partial Q_m}\right)_0$ is $1.0eV/10^{14}e \cdot cm^{-2}$. We can see that the pinning of the Fermi level is more pronounced here than in Fig. 1.10, and also that the difference between the Fermi level positions on n- and p-type semiconductors is slightly larger than before, but still very small (0.035 eV). We show in the text that the value of $\left(\frac{\partial \Delta V_m}{\partial Q_m}\right)_0$ is $1.0eV/10^{14}e \cdot cm^{-2}$, is an upper bound for most metals.

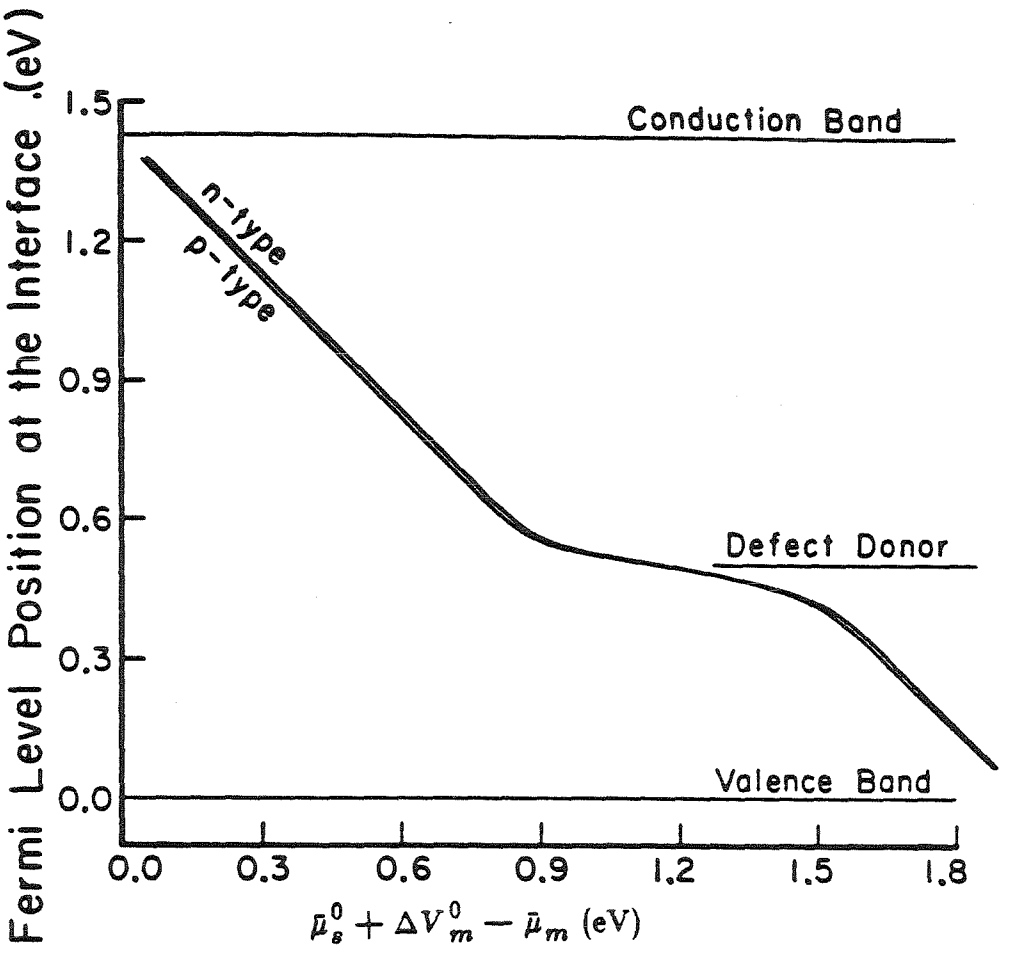

Fig. 1.12 Fermi level position in the gap at $x = d$ vs $\bar{\mu}_s^0 + \Delta V_m^0 - \bar{\mu}_m$ when the 10^{14} defects per cm^2 are divided between two planes: half on $x = d$ and half on $x = d/2$. To show only one effect, $\left(\frac{\partial \Delta V_m}{\partial Q_m}\right)_0$ was set to be zero. By comparing this figure with Fig. 1.10, one can see that the effect of distributing the defects over more than one plane does not change the curve drastically. Therefore, the assumption made in our model, namely, that all the defects are on a single plane, does not restrict the conclusions based on our model.

value:

$$\left(\frac{\partial \Delta V_m}{\partial \mathfrak{Q}_m}\right)_0 = \frac{1.eV}{10^{14} e \cdot cm^{-2}} \quad .$$

Here exactly the same conclusions can be drawn regarding the fact that $10^{13} cm^{-2}$ are not enough defects to pin the Fermi level, while 10^{14} are more than enough. When no pinning occurs, the difference in Fermi-level position between n- and p-type semiconductors $\Delta\eta$, is still small, though it is bigger than before, and is now $\approx 0.035eV$.

It is important to understand what causes the pinning. Depending on the relative Fermi-level position, the defects will charge from 0 to $\pm q\sigma$ (+ for donor type state, — for acceptor) when we change Φ_m. The source of this charge will be mainly the **metal**; since the metal is thick enough, it can supply the necessary charges with relatively small change in the boundary conditions due to loss of charge. The field in the interface layer due to the charged defects will tend to diminish the effect of changes in Φ_m, but effective pinning will happen only when there are enough defects around, that is, when

$$\frac{q^2\sigma}{\epsilon\epsilon_0} d \approx 1 \cdot eV \quad .$$

For $d \approx$few Å and $\epsilon \approx 10$, that implies $\sigma \approx 10^{14} cm^{-2}$.

To explore the role of spatial distribution we have treated the case when the defects lie on two parallel planes. We assume that half the defects are located at a distance d, and the other half at $d/2$ from the metal. d was taken as before to be 5Å. In this case one can integrate (1.5.1) from $d/2$ to d, and find $\eta(d/2)$. Then find out how many charges will be on that plane; substitute back into (1.5.7), and find $\bar{\mu}_s^0 + \Delta V_m^0 - \bar{\mu}_m$. In Fig. 1.12, we display the Fermi-level position at the interface for this case. The doping is $10^{17} cm^{-3}$, and the defect density is $10^{14} cm^{-2}$, half of them on the plane $x = d$, and the other half on the plane $x = d/2$. The defects on

the plane closer to the metal charge more rapidly when we decrease $\eta(d)$; therefore, the width in terms of $\eta(d)$ of the pinning region will not increase. The width in terms of $\bar{\mu}_s^0 + \Delta V_m^0 - \bar{\mu}_m$, however, will decrease since the integration (1.5.7) is performed for the same amount of charged defects as before, only to half the distance, while in the other half, we have contributions to the field from only half the defects. This effect introduces an effective interface layer width, as can be seen in Fig. 1.12 For simplicity, we have only examined the case of $\left(\frac{\partial \Delta V_m}{\partial Q}\right)_0 = 0$. It is apparent that the effect of putting all the defects on a single plane is not a crucial assumption; it was made for convenience only.

Defects with three charge states

Defects that have three charge states (for example, negative, neutral, and positive) were suggested as a possible mechanism for pinning the Fermi level.[34] The statistics of such defects is different from that of two independent defects, one a donor and the other an acceptor, localized on different centers. The difference comes from the fact that the three-charge-state defect has only one neutral state, while the independent donor and acceptor can be neutral in two distinct ways, namely, when both are neutral, or when both are charged. In the case of a single type of defect, with three charge states, we can write down the equilibria equations,

$$S^- \mapsto S^0 + e^-, \qquad \Delta E = \mu - E_s^D,$$

$$S^0 \mapsto S^+ + e^-, \qquad \Delta E = \mu - E_s^A.$$

From these equations we can calculate the ratios of positive and negative to neutral defects.

$$\frac{\sigma^+}{\sigma^0} = \frac{1}{g_s^D} \exp(\frac{E_s^D - \mu}{k_B T})$$

$$\frac{\sigma^-}{\sigma^0} = \frac{1}{g_s^A} \exp(\frac{\mu - E_s^A}{k_B T}).$$

Here $\sigma^+, \sigma^0, \sigma^+$ are the surface densities of positive, neutral, and negative defects. g_s^A and g_s^D are the degeneracy factors, respectively. Since the total defect density σ must satisfy

$$\sigma^- + \sigma^0 + \sigma^+ = \sigma \quad ,$$

we have

$$\sigma^0 = \frac{\sigma}{\frac{1}{g_s^A} \exp(\frac{\mu - E_s^A}{k_B T}) + 1 + \frac{1}{g_s^D} \exp(\frac{E_s^D - \mu}{k_B T})} \tag{1.5.9}$$

with similar expressions for σ^+ and σ^-.

We see that there are two different cases, one when $E_s^D > E_s^A$; the other when $E_s^D < E_s^A$. If $E_S^D < E_S^A$, then for values of μ such that $E_S^D < \mu < E_S^A$, most defects are neutral. (This case would correspond to GaAs according to Spicer *et al.*[9] E_s^A and E_s^D were picked to be their values of 0.75 and 0.5 eV from the valence band edge). This region of μ separates two rapid charging regions around E_S^D and E_S^A as can be seen in Fig. 1.13; the whole system behaves as if there are two types of two-charge states (one neutral or negative, the other neutral or positive) which act independently, rather than a single three-charge state. There will be, therefore, two different pinning positions depending on the metal work function, but independent of the semiconductor type.

If $E_S^A < E_S^D$, the denominator of (1.5.9) will be large for every possible value of η. ($\sigma^0 \ll \sigma$ for every η). S^0 will be unstable,[35] that is, S^+ will capture, and S^- will release electrons in pairs; there will be only one value of $\eta(d)$ around which rapid charging will occur, as can be seen in Fig. 1.14. E_s^A and E_s^D were picked to be 0.9 and 1.2 eV, respectively, from the valence band edge; a band gap of 1.35 eV corresponding to InP was used. Since the defects change their charges in quantities of $2e$ instead e, as well as reversing the sign, it is a very efficient way to pin the Fermi level; if there are enough defects, $\eta(d)$ can be pinned for any possible value of $\bar{\mu}_s^0 + \Delta V_m^0 - \bar{\mu}_m$ at the same place.

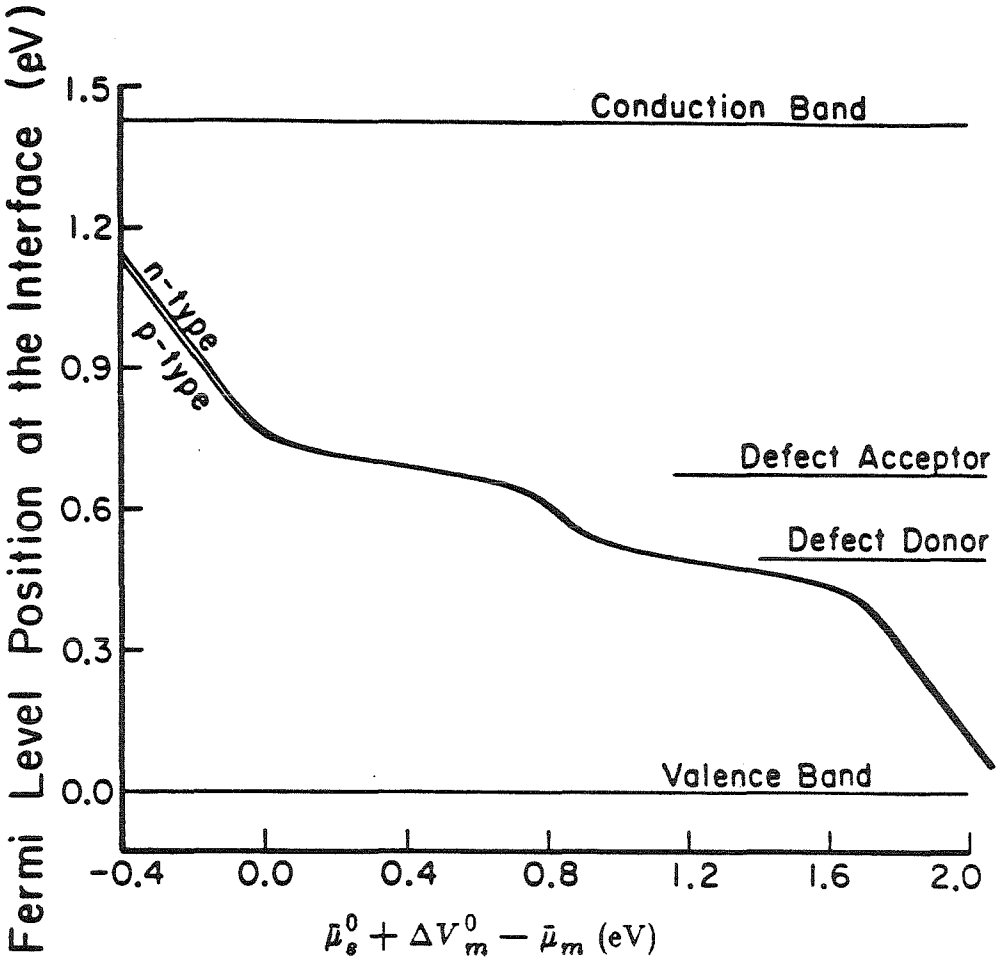

Fig. 1.13 Fermi level position in the gap at $x = d$ vs $\bar{\mu}_s^0 + \Delta V_m^0 - \bar{\mu}_m$ for the case when each defect acts both as a donor and an acceptor, and the donor level is **lower** than the acceptor level. We assume here that the defect density is $\sigma = 10^{14} \cdot \text{cm}^{-2}$. The defect energy levels were taken from Spicer *et al.* (Ref. 9), and correspond to those of GaAs. One can see that when the defect donor is **lower** than the defect acceptor, the two levels are independent of each other. Depending on the work function of the metal, or equivalently, on $\Delta V_m^0 - \bar{\mu}_m$, the Fermi level pins either at the donor level or at the acceptor level, or does not pin at all.

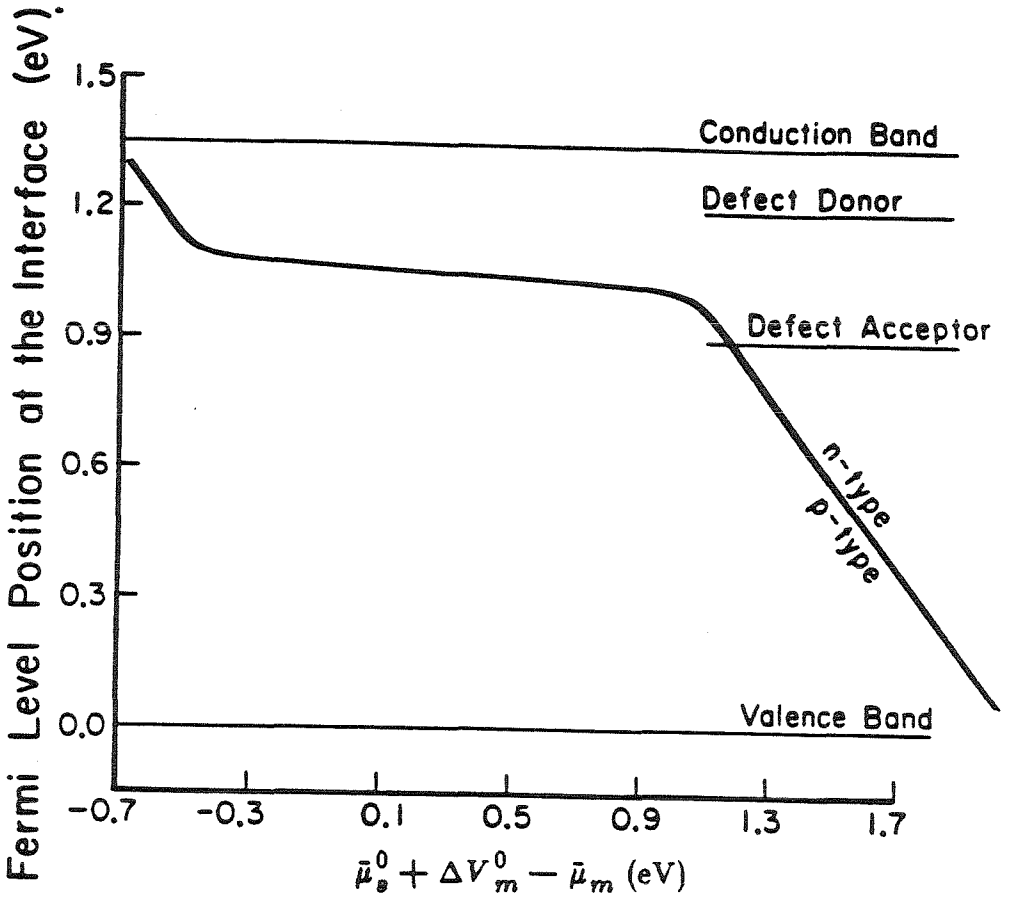

Fig. 1.14 Fermi level position in the gap at $x = d$ vs $\bar{\mu}_s^0 + \Delta V_m^0 - \bar{\mu}_m$ for the case when each defect acts both as a donor and an acceptor and the donor level is **higher** than the acceptor level. We assume here that the defect density is $\sigma = 10^{14} \cdot \text{cm}^{-2}$. The defect energy levels were taken from Spicer *et al.* (Ref. 9), and correspond to those of InP. One can see that when the defect donor is **higher** than the defect acceptor, the defect captures and releases **pairs** of electrons. Instead of two independent pinning positions, there is only one, half-way between the defect donor and the defect acceptor levels.

1.6. Summary and conclusions

We have investigated the phenomenon of Fermi-level pinning at the metal-semiconductor interface by charging defects. We estimated the defect density required to pin the Fermi level to be $\approx 10^{14} cm^{-2}$, assuming that most of these defects are localized not more than a few angstroms from the metal, and that the electrostatic potential at the metal surface responds to excess charges by not more than $1eV/10^{14} e \cdot cm^{-2}$. Under these conditions, we also estimated the difference in Fermi-level position between n-type and p-type semiconductors to be less than $0.05eV$. This difference is the sum of two terms, one due to the difference in metal response, the other due to a different band bending in the interface region. Since the maximal difference in bulk semiconductor charge between n- and p-type GaAs for a given Fermi-level position is about $2 \cdot 10^{12} e \cdot cm^{-2}$ for a doping concentration of $10^{17} cm^{-3}$, we can estimate the metal response term to be at most 0.02 eV, and the "interface dipole layer" term to be not more than 3 meV/Å. This difference was shown to be the maximum possible one, and to occur only when there is no pinning; when there is pinning, this difference is even smaller. For the submonolayer coverage we have found that a defect density of only $10^{12} \cdot cm^{-2}$ will pin the Fermi level, and that the Fermi-level position for n- and p- type semiconductors can differ by a substantial amount.

The difference between the results of submonolayer coverage and thick metallic coverage, as related to both the difference in Fermi-level position and the defect density required to pin the Fermi level, could be attributed to the fact that these are **two different pinning mechanisms**,[36] originating from the main source of charge that balances the charge on the defects. With $10^{11} - 10^{12}$ defects/cm^2 but **without** substantial metal coverage, these charges can come almost entirely from

the semiconductor bulk. The requirement of total charge neutrality will determine the Fermi-level position; the Fermi-level position can differ substantially between n- and p-type semiconductors.

For the case of a bulk metal, the charge in the interface layer is balanced mainly by charge in the metal, setting up a very thin dipole layer. The charge in the metal can easily respond in such a way as to balance the depletion charge; hence, the n- and p- type pinning positions are very similar.

References for Chapter 1.

1. W. E. Spicer, P. W. Chye, P. R. Skeath, C. Y. Su, I. Lindau, *J. Vac. Sci. Technol.* **16**, 1422 (1979).
2. P. Skeath, I. Lindau, P. W. Chye, C. Y. Su, W. E. Spicer, *J. Vac. Sci. Technol.* **16**, 1143 (1979).
3. W. E. Spicer, P. Skeath, C. Y. Su, and P. Chye, *Phys. Rev. Lett.* **44**, 420 (1980).
4. R. W. Grant, J. R. Waldrop, S. P. Kowalczyk, E. A. Kraut, *J. Vac. Sci. Technol.* **19**, 477 (1981).
5. C. A. Mead, *Solid State Electron.* **9**, 1023 (1966)
6. J. Bardeen, *Phys. Rev.* **71**, 717 (1947).
7. S. G. Louie and M. L. Cohen, *Phys. Rev.* **B13**, 2461 (1976).
8. S. G. Louie, J. R. Chelikowsky, and M. L. Cohen, *Phys. Rev.* **B15**, 2154 (1977).
9. W. E. Spicer, I. Lindau, P. Skeath, C. Y. Su, *J. Vac. Sci. Technol.* **17**, 1019 (1980).
10. J. Bardeen, *Phys. Rev.* **49**, 653 (1936)
11. N. D. Lang, *Solid State Physics, Advances in Research and Applications*, edited by H. Ehrenreich, F. Seitz, and D. Turnbull (Academic, New York, 1973) Vol. 28, p. 243
12. P. Hohenberg and W. Kohn, *Phys. Rev.* **136,**, B864 (1964) .
13. W. Kohn and L. J. Sham, *Phys. Rev.* **140,** A1133 (1965) .
14. A. O. E. Animalu and V. Heine, *Philos. Mag.* **12,** 1249 (1965).
15. A. O. E. Animalu, *Phys. Rev.* **B8,** 3542 (1973).
16. C. Kittel, *Int. to Solid state Phys. p129, 4-th ed.*

17. H. B. Michaelson, *J. App. Phys.* **48,** 4729 (1977).

18. J.P Pedrew, D. C. Langreth, and V. Sahni, *Phys. Rev. Lett.* **38,** 1030 (1977).

19. N. D. Lang and W. Kohn, *Phys. Rev.* **B1,** 4555 (1970).

20. N. D. Lang and W. Kohn, *Phys. Rev.* **B3,** 1215 (1971).

21. N. D. Lang and W. Kohn, *Phys. Rev.* **B7,** 3541 (1973).

22. V. Sahni, J. B. Krieger, and J. Gruenebaum, *Phys. Rev.* **B12,** 3503 (1975).

23. V. Sahni, J. B. Krieger, and J. Gruenebaum, *Phys. Rev.* **B15,** 1941 (1977).

24. V. Sahni, J. Gruenebaum, *Phys. Rev.* **B15,** 1929 (1977).

25. A. Sugiyama, *J. Phys. Soc. Japan* **15**, 965 (1960).

26. H. F. Budd and J. Vannimenus, *Phys. Rev. Lett.* **31**, 1218 (1973).

27. G. D. Mahan and W. L. Schaich, *Phys. Rev.* **B10**, 2647 (1974)

28. D. Pines, *Elementary Excitations in Solids,* Chapter 3. Benjamin, New York, (1963).

29. D. Pines and P. Nozières, *The Theory of Quantum Liquids,* (Benjamin, New York, 1966) p.330.

30. P. Vashista and K. S. Singwi, *Phys. Rev.* **B6,** 875 (1972).

31. Another possible way to have $r_s > 4.3$ is to let the positive background relax too. This approach was used by J. W. Allen and S. A. Rice, *J. Chem. Phys.* **67,** 5105 (1977).

32. S. M. Sze, *Physics of Semiconductor Devices* 2nd ed. Wiley- Interscience (1981).

33. One should keep in mind that due to thermal effects, some small fraction of the defect donors are charged even when the Fermi-level position is above the donor level, and some defect acceptors are charged when the Fermi level is below the defect acceptor level. This will result in partial compensation; therefore, when

the defect density increases, eventually the n- and p- type lines will merge. The required defect density for this merger is much higher, and is temperature dependent.

34. G. A. Baraff, E. O. Kane, and M. Schlüter, *Phys. Rev. Lett.* **43**, 956 (1979).
35. M. S. Daw and D. L. Smith, *Phys. Rev.* **B20**, 5150 (1979)
36. M. S. Daw and D. L. Smith, *J. Vac. Sci. Technol.* **17**, 1028 (1980)

Chapter 2:
Geometric Lattice Match and Its Application to Heteroepitaxy

2.1. Introduction

What is lattice match?

In recent years there has been a growing interest in the epitaxial growth of one material on another. In the past, most of the interesting systems were those whose epitaxial layer had the same crystal structure and the same orientation as that of the substrate. There are many important cases, however, where the epitaxial layer has either a different orientation than the substrate (CdTe (111) on GaAs (100)[1]) or a totally different crystal structure (silicon on sapphire,[2] CdTe on sapphire,[3] and others). For such systems the old criterion of lattice match, namely, comparison of the lattice parameters, is no longer applicable; a new criterion should be used. Instead of comparing the bulk lattice parameters, we compare the interface translational symmetry with that of the bulk materials on both sides of the interface. We define two lattices as matching, if the interface translational symmetry can be compatible with the symmetry on both sides of the interface, to within a given precision.

To clarify this point, refer to Fig. 2.1, in which we display the two-dimensional translations parallel to the (100) face of GaAs and to the (111) face of CdTe. Both materials possess the face-centered cubic zincblende structure. The lattice constants of GaAs and CdTe are 5.653 and 6.481 Å respectively.[4] The lattice translations

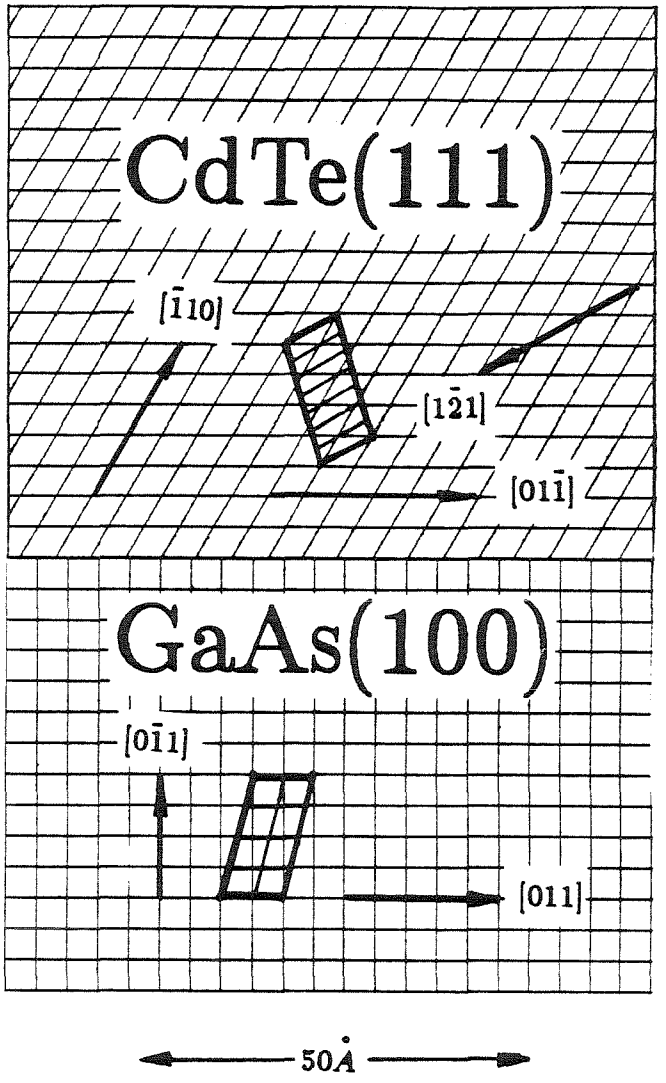

Fig. 2.1. The lattice translations parallel to the GaAs(100) and CdTe(111) faces. A cell made of eight GaAs unit cells has almost exactly the same dimensions as a cell made of seven CdTe unit cells. Several crystal directions on each of the two faces are also shown for clarity. GaAs and CdTe are face-centerd cubic with a=5.352Å and a=6.481, respectively.

parallel to the GaAs (100) face form a two-dimensional lattice, with a square unit cell, $a/\sqrt{2} = 3.997\mathring{A}$ on a side. The lattice translations parallel to the CdTe (111) face form a two-dimensional lattice, having a 120° rhombic unit cells, with edges of $a/\sqrt{2} = 4.583\mathring{A}$. These two-dimensional lattices are diplayed by the fine line grids in Fig. 2.1. One can now form superlattices by taking larger unit cells. If one takes eight GaAs unit cells and seven CdTe unit cells in the manner seen in Fig. 2.1, one obtains cells that are very similar. The GaAs superlattice cell is a parallelogram, 7.995Å by 16.48Å, with an acute angle of 75.96°. The CdTe superlattice cell is also a parallelogram, 7.938 by 16.52Å, with an acute angle of 76.10°. The mismatch is about 0.7% in the short edge, 0.3% in the long edge, and 0.2% in the angle. One can see that the $GaAs[011]$ direction is parallel to one of the three equivalent $CdTe[1\bar{2}1], [11\bar{2}], [\bar{2}11]$ directions. This example serves merely to illustrate that there are some possible orientations of the interface that match to within a high precision. Nevertheless, the reported growth direction of CdTe(111) on GaAs(100) agrees with this example.[1]

What is the importance of lattice match?

Lattice match, as defined above, is a very similar idea to the concept of coincidence-site lattice[5] that appears to play an important role in high-angle grain boundaries.[6] The main difference between the two is that, in grain boundaries, both sides of the interface consist of the same material, while in heteroepitaxy, this is generally not true. When the same material occupies both sides of the interface, the match across the interface can be exact. When the interface is between two different materials, such an exact match cannot be found, and there will always be some finite mismatch. This finite mismatch forces one to abandon the number-theoretical calculations that are popular in coincidence-site lattice theory.[7] Instead, we present a different approach in the next section, based on

a reduction scheme used in Minkowski's geometry of numbers.[8] This approach is similar to the one developed by Santoro and Mighell,[9] but involves several shortcuts that make our method faster and more powerful than theirs.

The role of lattice match in epitaxial growth is still not well understood. In general, the structure of both materials far away from the interface is determined by the bulk properties. At the interface local chemistry considerations might favor different positions for the atoms which might not be compatible with the bulk structure. In case of a conflict between the local chemistry at the interface and the geometric properties of the bulk materials, one of the two usually dominates. We cannot say which effect is more important in the most general case, but we can try to describe what happens in the extreme cases, that is, when either the chemistry or the geometry is much more important than the other. Then we can proceed to compare experimentally known interfaces with the predictions of our model. It is important to emphasize here the disparity between the chemical and the geometrical considerations. The geometrical problem is **completely solvable**, and most of this chapter is devoted to this solution. On the other hand the chemical considerations are much harder to formalize and to solve. Because of this disparity our treatment is skewed toward geometry, and we shall characterize and classify interfaces according to their geometric mismatch. We do not mean to imply, by this treatment, that the chemical properties we completely neglect are unimportant. We shall merely try to compile lists of interfaces for which there is a very small geometric mismatch. The question of whether or not one can actually grow such an interface is beyond the scope of this work. Let us now characterize the two limiting cases, namely, the one in which the chemistry dominates the geometry, and the one in which the reverse is true.

Consider first the case in which the chemistry dominates. This will probably

be true if every adatom has a unique, energetically favorable position in the surface unit cell. It is more likely, therefore, to encounter situations like this when the bonding in the interface region is directional. This will be the case when the bonding is either covalent or ionic. As the film grows it has to transform its structure to that of the bulk. Small mismatches can be accommodated elastically, especially if the structure of the interface is open (for example, tetrahedral covalent bonding). If the mismatches are larger, the strain can be relieved by creating defects.

Next, let us consider the case in which the geometry dominates. This will probably be the case when the adatoms have many adjacent positions which are almost identical energetically. A typical case is a metallic, close-packed interface. Here the atoms may move around to order themselves in the best packing order; if a low mismatch orientation exists, it might be a strong candidate for growth.

The discussion above is clearly quite vague and qualitative in nature. To be more precise and predictive, one has to find the energies associated with bonding at various positions, the creation of defects, etc. This is beyond the scope of this research. Instead, we shall characterize lattice match, develop a scheme to obtain all the possible orientations of a given interface that result in a good lattice match, and compare them with experimental results.

Characterization of lattice match

We have seen that the lattice match is characterized by two parameters: the precision of the match and the minimal unit-cell area. The common unit cell in Fig. 2.1 has a mismatch of at most 0.7% in both the lateral dimensions and the angle between them. The unit-cell area is $128\mathring{A}^2$. This cell is the smallest possible one that will enable a mismatch of less than 1% in the unit-cell sides and angle. One can see that there is a trade-off between the precision of a match and the size of the superlattice cells. If one allows matches with a very large

superlattice cell, there are many such cells to be considered, and one increases the odds of finding a more precise match. On the other hand the larger the size of the interface unit cell, the less likely it is that the chemical forces will reinforce the lattice match condition. So far, we do not have any criteria which indicate when a match is too poor to allow epitaxial growth. The precision of the match gives a lower bound to changes in lateral interatomic distances. Suppose the mismatch in one of the sides of the common unit cell is 1%, For example. This 1% can then be accommodated at best by a lateral movement of $\pm 0.5\%$ of every atom on both sides of the interface. In reality, not all the atoms will move by the same amount, and there will be some lateral interatomic distance that will change by more than 0.5%. Such changes in interatomic distances will introduce strain in the crystal. Thick epitaxial film will tend to relieve this strain energy either elastically, or by creating defects. Qualitatively speaking, the elastic strain energy grows like the square of the mismatch in a given direction, while the energy associated with creating defects scales like the number of defects per unit length, which is roughly proportional to the mismatch. Therefore, we should expect defects to occur if the mismatch is too large. How large is too large is yet to be determined.

The common unit cell is a unit of periodic reconstruction at the interface. Therefore, the common unit-cell area should be limited to a value that is reasonable for interfacial periodic reconstruction. Once again, this value is yet to be determined, but we can roughly estimate its size. We know that some free surfaces reconstruct over relatively large distances. For example, the free (111) face of silicon reconstructs spontaneously to form a (7x7) unit cell with an area of $625\mathring{A}^2$. We believe, therefore, that common unit cells of a few hundred square angstroms are still reasonable. In this chapter the limits of 1% on the match precision and $150\mathring{A}^2$ on the common unit-cell area will be shown to be sufficient to reproduce the

experimental results of CdTe(111)/GaAs(100) of Cheung and Magee.[1] $600\mathring{A}^2$ are required to reproduce the experimental results of CdTe(111)/$Al_2O_3(1\bar{1}02)$, $(11\bar{2}0)$ and (0001) of Myers *et al.*[3] which are examples of covalent epitaxial layer. In this last case, at least for the growth on the (0001) face, the interface is known to be defective, and its orientation does not agree with ours.[10] Mismatch of 2.5% and unit-cell area of $50\mathring{A}^2$ will suffice to reproduce the known experimental results for $CoSi_2$, $NiSi_2$ and Pd_2Si on silicon, which are examples of metallic film.

With the match precision and the common unit-cell area taken as parameters, the problem of lattice match is now well defined. A computer can easily scan many possible pairs of materials in various directions, and find all the possible good lattice matches. In this way, one can generate a list of interfaces that match to within a prescribed precision, and this list can help reduce the number of "interesting" interfaces. This reduction comes in very handy when one considers the number of possible interfaces.

Organization of this chapter

This chapter is organized in the following way. In section 2.2, we discuss the geometrical principles of lattice match, and the systematic way to find matches to within a given precision and size. This will be done in a descriptive rather than a rigorous way; for the rigorous proofs, the reader is referred to Appendix A-2.2 at the end of this thesis. Section 2.3 illustrates the method by applying it to the CdTe/GaAs. In section 2.4 we discuss three other systems, namely, CdTe on sapphire, silicion on sapphire, and silicides on silicon. The emphasis is not so much on the technique, in that section, but rather on comparing the experimental results with the lattice match predictions. These systems were chosen because recent experimental results of actual heteroepitaxial growth are available. We draw some conclusions based on this study in section 2.5.

2.2. The geometrical principles of lattice match

A cut in any crystal direction through a three-dimensional lattice results in a surface which has a two-dimensional translational symmetry. Any additional reconstruction of the atoms near the interface during the interface formation may, in general, reduce the symmetry of the unreconstructed surface. Thus, the symmetry group of the reconstructed surface will be a subgroup of the symmetry group of the unreconstructed surface. One sees, therefore, that the problem of lattice match is reduced to scanning the two-dimensional cuts in a given pair of lattices, and then comparing the two resulting two-dimensional lattices, looking for a common superlattice.

The most fundamental question is how to tell when two 2-dimensional lattices are actually the same (or nearly the same). The difficulty arises from two sources. First, the two similar lattices may be rotated with respect to each other, or one could be a rotation of a mirror image of the other. In this case, one wants to be able to identify the two lattices as being "the same". Second, there is no simple and unique way to describe a lattice. A lattice is uniquely determined once its primitive translations are given. The primitive translations are a set of vectors such that every lattice point can be expressed uniquely as a linear combination of these vectors with integer coefficients. While a set of primitive translations determines the lattice, the converse is not true; there are an infinite number of possible sets of primitive translations generating a given lattice. One wants to be able to identify two such sets as belonging to the same lattice or to the same lattice rotated or reflected. The way to achieve this is by using a reduction scheme.[8] The reduction process selects a particular set of primitive translations from all the possible ones in almost a unique way. In this process, only intrinsic properties of the lattice (that is,

lengths and angles) determine the final choice of primitive translations without any reference to a particular coordinate system. Therefore, any rotation or reflection of the lattice, which amounts to a different coordinate system, will not have any influence on the choice of the primitive translations.

To be more specific, given a two-dimensional lattice, a set of primitive translations $(\vec{a},\vec{b})$ is called reduced if it satisfies the following three conditions:

A. $\vec{a}$ is the shortest possible non-zero vector of the lattice.

B. $\vec{b}$ is the shortest possible lattice vector, linearly independent of $\vec{a}$.

C. The angle between $\vec{a}$ and $\vec{b}$ is non-obtuse.

One needs a constructive procedure to obtain a reduced translations set from a non-reduced one. Such a procedure is given in the flow chart of Fig. 2.2. One can see in that figure that the procedure is very simple, and amounts to successive additions or subtractions of the shorter translation vector from the longer until no further reduction in size of the translation vectors can be achieved. Finally, the sign of one of the vectors is being reversed, if the angle between the two vectors is obtuse. The procedure is guaranteed to end after a finite number of steps, and to result in a reduced set of translations. Another important feature of this procedure is that it conserves the area of the parallelogram $(0,\vec{a},\vec{b},\vec{a}+\vec{b})$ in every step.

In general, a lattice may have more than one reduced set of primitive translations; the lengths of the reduced translation vectors, as well as the angle between them, however, is unique. These three numbers, namely,

$$a = |\vec{a}|, \qquad b = |\vec{b}| \quad \text{and} \quad \cos\alpha = \frac{|\vec{a}\cdot\vec{b}|}{|\vec{a}|\cdot|\vec{b}|},$$

are uniquely determined by the lattice, and also uniquely determine the lattice up to an arbitrary rotation or reflection. Thus, the procedure of determining when two lattices are the same (up to an arbitrary rotation, reflection, and a choice of

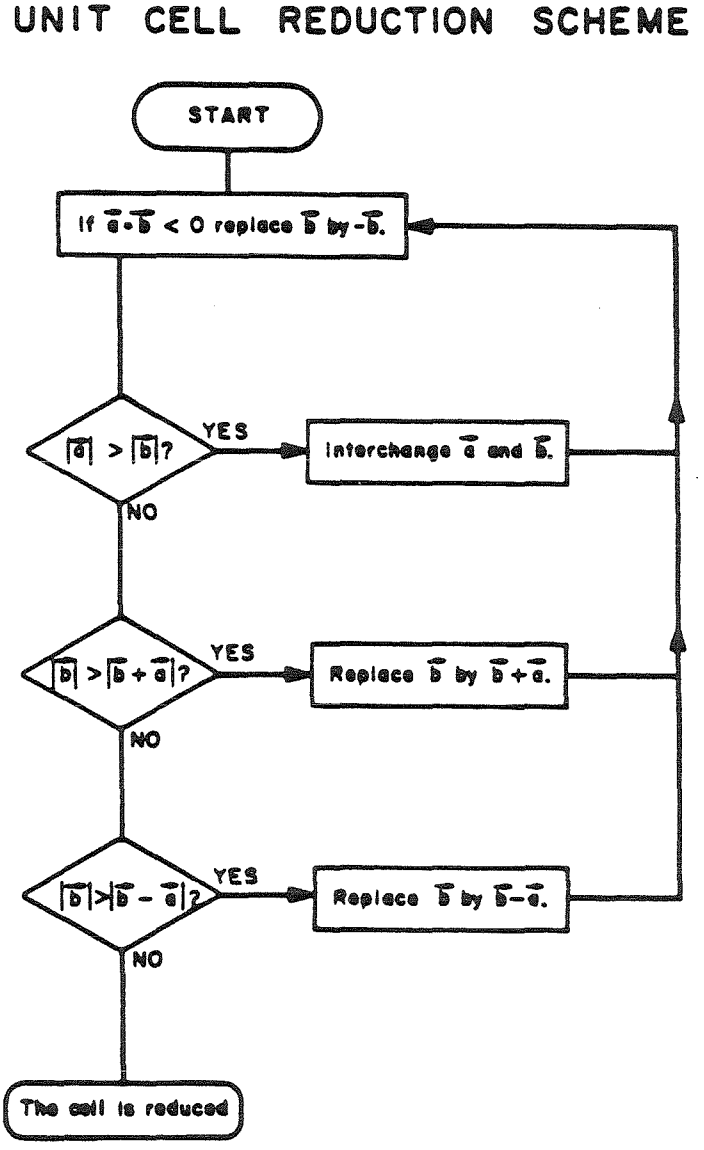

Fig. 2.2. Flow chart of the unit-cell reduction procedure.

primitive translations set) is completely solved. One can also compare the a,b and α mentioned above to determine quantitatively how similar two lattices are.

The next problem is to determine when two 2-dimensional lattices match. One says that two lattices match, if each one of them possesses a superlattice, such that the two superlattices are the same (up to a rotation, reflection, and a choice of primitive translations). The task of scanning and comparing all possible superlattices of the two lattices looks at the outset to be a formidable one. In fact, it is not that bad. Recall the fact that the unit-cell area of a superlattice is an integer times the unit-cell area of the original lattice. If the original lattices had unit-cell areas of A_1 and A_2, then the superlattices have unit-cell areas of $r_1 A_1$ and $r_2 A_2$, respectively, where r_1 and r_2 are integers. Since one wants the superlattices to be the same, they must have the same unit-cell area. Thus $r_1 A_1 = r_2 A_2$, or

$$\frac{r_1}{r_2} = \frac{A_2}{A_1}. \tag{2.2.1}$$

In reality, the two lattices will not match exactly. Therefore, the rational number r_1/r_2 will only approximate A_2/A_1. Prescribing a certain precision to this match, however, will substantially reduce the number of integers, r_1 and r_2, to be considered. An upper limit on the possible values of r_1 and r_2 is introduced by the requirement that the superlattice unit-cell area will not exceed some large prescribed value, say A_{max}. In that case, $r_1 A_1 \approx r_2 A_2 < A_{max}$, or,

$$r_1 < \frac{A_{max}}{A_1}, \qquad r_2 < \frac{A_{max}}{A_2}. \tag{2.2.2}$$

Suppose one has found all those value of r_1 and r_2 that satisfy Eq.(2.2.1) to within a reasonable precision as well as Eq.(2.2.2). One now has to consider all the possible superlattices of the first lattice that have a unit-cell area of $r_1 A_1$, and all the possible superlattices of the second lattice with a unit-cell area of $r_2 A_2$,

and compare them. In general, given a lattice with a unit-cell area A, one wants to characterize all the superlattices with a unit-cell area nA, where n is a given integer. we shall show that there are only a finite number of such superlattices, not more than the sum of the divisors of n. For example, a two-dimensional lattice will have at most 4 distinct superlattices whose unit cells are three times larger than that of the original lattice. In this case 4=1+3 is the sum of the divisors of 3. Similarly, there are at most 12=1+2+3+6 distinct superlattices whose unit cells are six times larger than that of the original lattice.

Suppose one is given a lattice, and a superlattice whose unit cell is n times larger than that of the original lattice; if $(\vec{\mathbf{a}},\vec{\mathbf{b}})$ is a primitive translations set of the original lattice, then one can always find a primitive translations set $(\vec{\mathbf{u}}, \vec{\mathbf{v}})$ of the superlattice, satisfying

$$\begin{pmatrix} \vec{\mathbf{u}} \\ \vec{\mathbf{v}} \end{pmatrix} = \begin{pmatrix} i & j \\ 0 & m \end{pmatrix} \begin{pmatrix} \vec{\mathbf{a}} \\ \vec{\mathbf{b}} \end{pmatrix} \tag{2.2.3}$$

with i,j,m integers, and with

$$i \cdot m = n, \tag{2.2.4}$$

$$i, m > 0, \tag{2.2.5}$$

$$0 \leq j \leq m - 1. \tag{2.2.6}$$

A formal proof of (2.2.3) can be found in Cassels,[8] and will not be reproduced here. The number of superlattices to consider, that is the number of different i,j and m satisfying (2.2.4)-(2.2.6), is reasonably small, and the computer can easily generate all of them, and compare them to the relevant superlattices of the other lattice.

2.3. Application of the method to CdTe on GaAs.

To demonstrate the method and to explore the role of lattice match in heteroepitaxy, we apply our method to a recently reported interface: CdTe on GaAs. CdTe is considered a good candidate for solar applications, as well as a substrate for $Hg_xCd_{1-x}Te$ or CdTe-HgTe superlattices for infra red detectors. Due to its bad mechanical properties, it may have to be grown on another material for support. Recently, successful growth of CdTe films on either GaAs[1] or sapphire[3] has been reported.

Both CdTe and GaAs crystallize in the face-centered cubic, zinc-blende structure. The lattice parameters of these crystals are given by[4]

$$a_{GaAs} = 5.653\mathring{A}, \qquad a_{CdTe} = 6.481\mathring{A}.$$

For both materials, the lattice translations parallel to the (100) face form a grid with square unit cells, $a/\sqrt{2}$ on a side, oriented parallel to the $[01\bar{1}]$ and the $[0\bar{1}1]$ directions. The lattice translations parallel to the (110) face form a grid with rectangular cells, $a/\sqrt{2}$ by a, whose shorter edge is parallel to the $[1\bar{1}0]$ direction, and the longer edge parallel to the [001] direction. The lattice translations parallel to the (111) face form a grid made of 60° rhombes whose sides are $a/\sqrt{2}$ long, and are parallel to the $[1\bar{1}0]$,$[10\bar{1}]$ or $[01\bar{1}]$ directions. In Fig. 2.3, these grids can be seen as the underlying fine lines. Fig. 2.3 is divided into 6 regions, showing CdTe on the left and GaAs on the right; the (111), (110) and (100) faces of each material are displayed from top to bottom. All the grids in Fig. 2.3 are drawn to the same scale; the whole figure being 200 by 150 angstroms.

It is worth mentioning here that the choice of grids with square cells for (100) or rectangular cells for (110), etc. is by no means unique. This choice amounts to a particular choice of a primitive set of translations for each lattice. Had we

picked a different set of primitive translations, the shape of the unit cells would be different, but nevertheless, their areas would be the same. The unit-cell areas of the grids appearing in Fig. 2.3 is summarized in Table 2.1. Next, one forms the ratios A_2/A_1 of (2.2.1). Here A_1 is the unit-cell area of the two-dimensional lattice formed by the translations of the GaAs, parallel to some given face; A_2 is the same for CdTe. The corresponding faces need not be the same for GaAs and CdTe. A partial list of these ratios is given in Table 2.2. we concentrate here only on the three most important faces, namely, the (100), (110) and (111) for each one of the GaAs and the CdTe. This results in nine possible combinations of area ratios, as can be seen in Table 2.2. The unit-cell areas for each row and column were taken from the corresponding entries in Table 2.1. Let us concentrate further only on the main diagonal of Table 2.2. This diagonal corresponds to (100)/(100), (110)/(110), and (111)/(111). The unit-cell areas ratios are all equal to

$$\left(\frac{a_{CdTe}}{a_{GaAs}}\right)^2 = 1.314. \tag{2.3.1}$$

This ratio can be approximated by rational numbers according to (2.2.1). A few of the reasonably accurate rational approximations are given by 4/3, 13/10, 17/13, 21/16 etc. with relative errors of 1.4%, 1.1%, 0.5%, and 0.1%, respectively. It is clear that one may approximate this ratio to arbitrary precision if one allows r_1 and r_2 of (2.2.1) to be arbitrarily large; if one restricts the size of r_1 and r_2, however, then there are only a limited number of such r_1 and r_2 that will approximate the ratio; the relative error, then, might not be small. Restricting the size of r_1 and r_2 is equivalent to restricting the size of the common unit cell area.

Even when one can pick a pair of integers r_1 and r_2 satisfying (2.2.1) to within a good precision, one does not always have a good lattice match. To see this, let me concentrate further on the approximation 4/3 to the ratio (2.3.1). we shall scan

Table 2.1 Two-dimensional unit-cell areas of GaAs and CdTe unreconstructed surfaces in the three major crystal directions. The unit-cell areas are given in units of square angstroms.

	(100)	(110)	(111)
Unit-cell area	$a^2/2$	$a^2/\sqrt{2}$	$a^2\frac{\sqrt{3}}{4}$
CdTe, a=6.481Å	21.00	29.70	18.19
GaAs, a=5.653Å	15.98	22.60	13.84

Table 2.2. Ratios of unit-cell areas of GaAs and CdTe surfaces in the three major crystal directions. The rational approximations to these ratios give us the possible combinations of superlattice-cell sizes.

	Cell area	CdTe(100) $21.00\mathring{A}^2$	CdTe(110) $29.70\mathring{A}^2$	CdTe(111) $18.19\mathring{A}^2$
GaAs(100)	$15.98\mathring{A}^2$	$\frac{21.00}{15.98}=1.314$	$\frac{29.70}{15.98}=1.859$	$\frac{18.19}{15.98}=1.138$
GaAs(110)	$22.60\mathring{A}^2$	$\frac{21.00}{22.60}=.9294$	$\frac{29.70}{22.60}=1.314$	$\frac{18.19}{22.60}=.8049$
GaAs(111)	$13.84\mathring{A}^2$	$\frac{21.00}{13.84}=1.517$	$\frac{29.70}{13.84}=2.146$	$\frac{18.19}{13.84}=1.314$

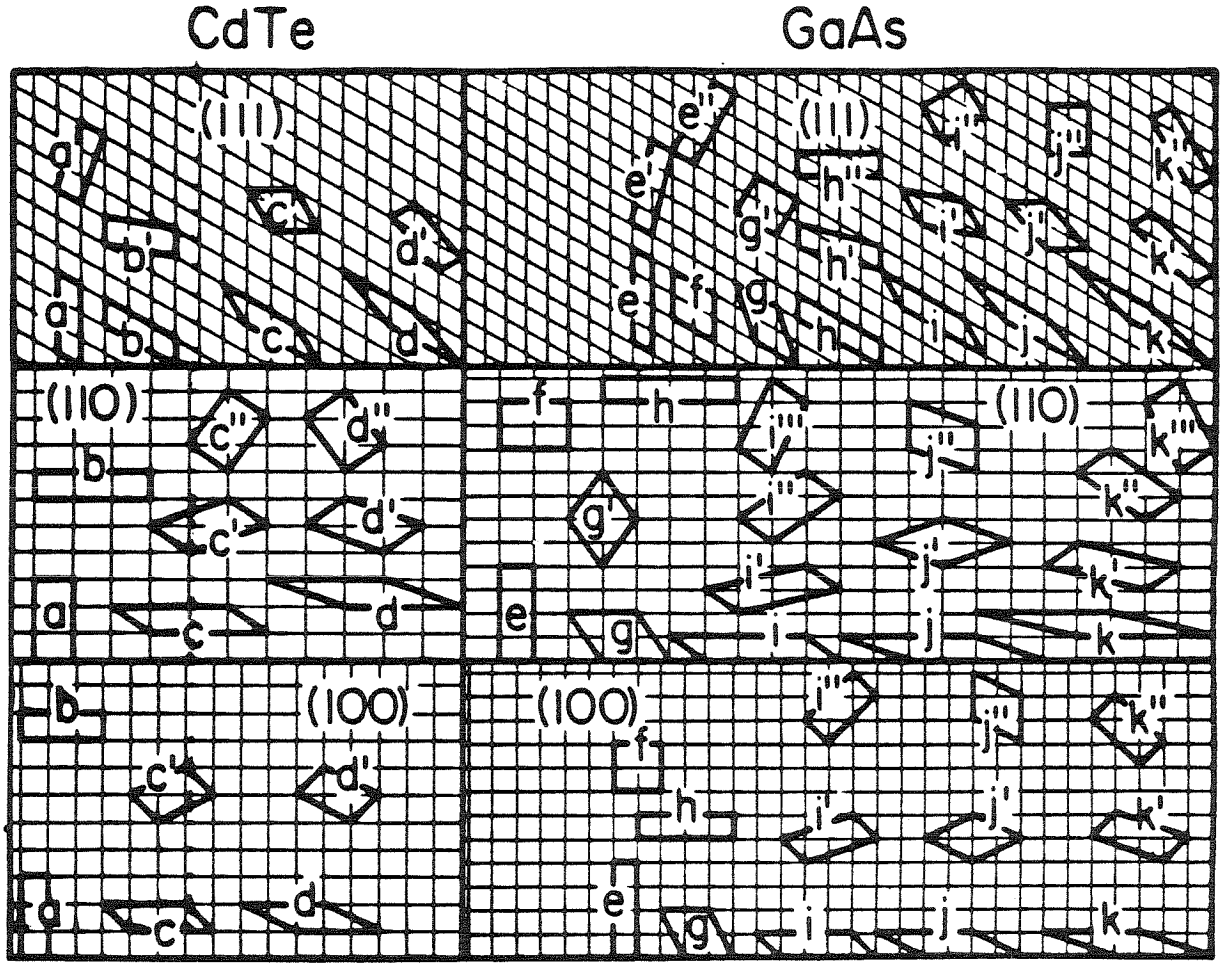

Fig. 2.3. The lattice translations parallel to the (100), (110) and (111) faces of CdTe and GaAs. Non-equivalent unit cells of order 3 for CdTe and 4 for GaAs are shown as parallelograms bounded by thick lines and denoted by unprimed letters. Various stages of the reduction procedure are denoted by primed letters.

all the superlattices of order 3 in the CdTe, and all the superlattices of order 4 in the GaAs, looking for a match. (The order of a superlattice is the area ratio of its unit cell to that of the original lattice. For example, a superlattice of order three has a unit-cell area which is three times that of the original lattice). Such a search for superlattices will be done for each one of the three faces. To find all such superlattices, we apply the transformations (2.2.3) to the primitive translations of the original lattice. The results of these transformations on the unit cells is seen in Fig. 2.3. In general there are 4 such transformation matrices when n=3, namely,

$$(a)=\begin{pmatrix}1 & 0\\ 0 & 3\end{pmatrix},\quad (b)=\begin{pmatrix}3 & 0\\ 0 & 1\end{pmatrix},\quad (c)=\begin{pmatrix}3 & 1\\ 0 & 1\end{pmatrix},\quad (d)=\begin{pmatrix}3 & 2\\ 0 & 1\end{pmatrix}, \tag{2.3.2}$$

and 7 matrices when n=4, namely,

$$(e)=\begin{pmatrix}1 & 0\\ 0 & 4\end{pmatrix},\quad (f)=\begin{pmatrix}2 & 0\\ 0 & 2\end{pmatrix},\quad (g)=\begin{pmatrix}2 & 1\\ 0 & 2\end{pmatrix},\quad (h)=\begin{pmatrix}4 & 0\\ 0 & 1\end{pmatrix},$$

$$(i)=\begin{pmatrix}4 & 1\\ 0 & 1\end{pmatrix},\quad (j)=\begin{pmatrix}4 & 2\\ 0 & 1\end{pmatrix},\quad (k)=\begin{pmatrix}4 & 3\\ 0 & 1\end{pmatrix}. \tag{2.3.3}$$

After one of the transformations (2.2.3), or in this case (2.3.2) or (2.3.3), is applied to the unit cell, a larger cell is obtained. In this case, three times larger for CdTe, and four times larger for GaAs. From these unit cells one can form superlattices by juxtaposing copies of the same cell. Moreover, every superlattice whose unit-cell area is three times larger than that of the original lattice will have a unit cell that is given by one of (a)-(d). Therefore the cells (a)-(d) generate all the possible distinct superlattices of order 3. The same is true for the cells (e)-(k) with regard to superlattices of order 4. The results of the application of each one of the transformations (2.3.2) to the standard unit cells of the CdTe(100), CdTe(110), and the CdTe(111) faces are seen in the left side of Fig. 2.3. These new cells are denoted by the same letter as the corresponding transformation in (2.3.2). Similarly, the

application of the transformations (2.3.3) to the unit cells of the three GaAs faces is seen in the right side of the same figure, and are denoted by (e)-(k).

Each one of the transformations (2.3.2) and (2.3.3), when applied to the original unit cell, results in a particular shape of a superlattice unit cell. These larger unit cells are by no means unique, and the reduction scheme described in the previous section must be applied. The reduction scheme consists of successive vector additions or subtractions of the shorter side of the cell from the longer until no further reduction in length is possible. The reduction steps for each one of the (a)-(k) cells are shown by primed letters in Fig. 2.3. For example, the cell (a) near the upper left corner of Fig. 2.3 corresponds to the matrix (a) of (2.3.2) applied to the unit cell of the CdTe(111) face. If one subtracts the shorter side of this cell (taken as a vector) from the longer side, one obtains the cell (a'). In this figure, we have moved (a') up and away from (a) for clarity, but they should have shared a common side. One can see that the long side of the new cell (a') is shorter than the long side of (a). If one repeats this procedure once again, the longer side of the new cell will not be shorter than the longer side of (a'). One must conclude that the cell (a') is reduced. Similarly, one can apply the reduction scheme to any one of the other cells (b)-(k). For the particular cells appearing in Fig. 2.3, after at most three reduction steps, all the cells are reduced. One should keep in mind that all the different cells generated during the reduction process are unit cells of the same superlattice. For example, suppose one generates two superlattices of the CdTe(111) by juxtaposing an infinite number of copies of either one of (a) or (a'). These two superlattices might appear different only as long as one retains the edges of the cells; if one looks only at the corners of the cells, the two superlattices are identical.

The purpose of the reduction procedure is to select a particular shape of unit

cell among all the possible cells of a given superlattice. After reduction, one can see that, if the original lattice possessed any non-trivial symmetries, some of the larger unit cells are actually equivalent. Thus, in the (100) face of the CdTe, (b) can be obtained from (a) by a 90° rotation, while (c') and (d') are mirror images of each other. The dimensions of the reduced 3-fold enlarged CdTe unit cells, as well as those of the reduced 4-fold enlarged GaAs unit cells of Fig. 2.3, appear in Table 2.3. In that table, each row, denoted by (a)....(k), corresponds to a particular transformation matrix of (2.3.2) and (2.3.3) as well as to the unit cells appearing in Fig. 2.3. The transformation matrices of (2.3.2) and (2.3.3) appear in this table in the second column from the left. The rest of Table 2.3 is divided into three major columns, corresponding to CdTe(100)/GaAs(100), CdTe(110)/GaAs(110), and CdTe(111)/GaAs(111). Each such major column is subdivided into four columns describing the dimensions of the reduced unit cell. In our notation, a, b and α correspond to the shorter side of the cell, the longer side, and the angle between them. Since the structure of both GaAs and CdTe is cubic, these a, b and $\cos(\alpha)$ can be expressed as simple algebraic expressions in the lattice parameter (denoted by italic a). These expressions, together with their numerical values, appear in the body of Table 2.3. We would like to emphasize that the transformation matrices appearing in Table 2.3 are those applied to the unit cells before the reduction, i.e., they are the same as (2.3.2)-(2.3.3), while the unit-cell dimensions appearing in the same table are those of the cells after reduction. By comparing the dimensions of the reduced unit cells in Table 2.3, one can conclude that there is no reasonable 3:4 match of the (100)/(100), but there are 3:4 matches of (110)/(110), namely, (c") or (d") to (f), and there is also a 3:4 match of the (111)/(111), namely, (c') to (f). For the (110)/(110) case, the cells (c") and (d") have their short side oriented along a CdTe[$1\bar{1}1$] direction, and the long side along

Table 2.3. Dimensions of reduced superlattice unit cells for the possible 3:4 lattice match of CdTe(100)/GaAs(100), CdTe(110)/GaAs(110) and CdTe(111)/GaAs(111). All the possible superlattices of order 3 are obtained from the matrices (a) — (d) operating on the CdTe original unit cell. Likewise, all the possible superlattices of order 4 are obtained from the seven matrices (e) — (k) operating on the GaAs unit cell. After an appropriate reduction is applied to the superlattice cells, their dimensions are displayed in this table. a and b are the reduced cell edges in angstroms, and α is the angle between them, in degrees.

cell $\begin{pmatrix} l & j \\ 0 & m \end{pmatrix}$	(100) a	(100) b	(100) cos α	(100) α	(110) a	(110) b	(110) cos α	(110) α	(111) a	(111) b	(111) cos α	(111) α
1. CdTe												
(a) $\begin{pmatrix} 3 & 0 \\ 0 & 1 \end{pmatrix}$	$\frac{a}{\sqrt{2}}=4.58$	$\frac{3a}{\sqrt{2}}=13.75$	0	90.0	a=6.481	$\frac{3a}{\sqrt{2}}=13.75$	0	90.0	$\frac{a}{\sqrt{2}}=4.58$	$\frac{a\sqrt{7}}{\sqrt{2}}=12.12$	$\frac{1}{2\sqrt{7}}$	79.1
(b) $\begin{pmatrix} 1 & 0 \\ 0 & 3 \end{pmatrix}$	$\frac{a}{\sqrt{2}}=4.58$	$\frac{3a}{\sqrt{2}}=13.75$	0	90.0	$\frac{a}{\sqrt{2}}=4.58$	$3a=19.44$	0	90.0	$\frac{a}{\sqrt{2}}=4.58$	$\frac{a\sqrt{7}}{\sqrt{2}}=12.12$	$\frac{1}{2\sqrt{7}}$	79.1
(c) $\begin{pmatrix} 1 & 1 \\ 0 & 3 \end{pmatrix}$	$a=6.48$	$\frac{a\sqrt{5}}{\sqrt{2}}=10.25$	$\frac{1}{\sqrt{10}}$	71.6	$\frac{a\sqrt{3}}{\sqrt{2}}=7.94$	$a\sqrt{3}=11.22$	0	90.0	$\frac{a\sqrt{3}}{\sqrt{2}}=7.94$	$\frac{a\sqrt{3}}{\sqrt{2}}=7.94$	$\frac{\sqrt{3}}{2}$	60.0
(d) $\begin{pmatrix} 1 & 2 \\ 0 & 3 \end{pmatrix}$	$a=6.48$	$\frac{a\sqrt{5}}{\sqrt{2}}=10.25$	$\frac{1}{\sqrt{10}}$	71.6	$\frac{a\sqrt{3}}{\sqrt{2}}=7.94$	$a\sqrt{3}=11.22$	0	90.0	$\frac{a}{\sqrt{2}}=4.58$	$\frac{a\sqrt{7}}{\sqrt{2}}=12.12$	$\frac{1}{2\sqrt{7}}$	79.1
2. GaAs												
(e) $\begin{pmatrix} 4 & 0 \\ 0 & 1 \end{pmatrix}$	$\frac{a}{\sqrt{2}}=4.00$	$\frac{4a}{\sqrt{2}}=15.99$	0	90.0	a=5.65	$\frac{4a}{\sqrt{2}}=15.99$	0	90.0	$\frac{a}{\sqrt{2}}=4.00$	$a\sqrt{6}=13.85$	0	90.0
(f) $\begin{pmatrix} 2 & 0 \\ 0 & 2 \end{pmatrix}$	$\frac{2a}{\sqrt{2}}=7.99$	$\frac{2a}{\sqrt{2}}=7.99$	0	90.0	$\frac{2a}{\sqrt{2}}=7.99$	$2a=11.31$	0	90.0	$\frac{2a}{\sqrt{2}}=7.99$	$\frac{2a}{\sqrt{2}}=7.99$	$\frac{\sqrt{3}}{2}$	60.0
(g) $\begin{pmatrix} 2 & 1 \\ 0 & 2 \end{pmatrix}$	$\frac{2a}{\sqrt{2}}=7.99$	$a\sqrt{\frac{5}{2}}=8.94$	$\frac{1}{\sqrt{5}}$	63.4	$\sqrt{3}a=9.79$	$\sqrt{3}a=9.79$	$\frac{1}{3}$	70.5	$\sqrt{\frac{3}{2}}a=6.92$	$\frac{2a}{\sqrt{2}}=7.99$	0	90.0
(h) $\begin{pmatrix} 1 & 0 \\ 0 & 4 \end{pmatrix}$	$\frac{a}{\sqrt{2}}=4.00$	$\frac{4a}{\sqrt{2}}=15.99$	0	90.0	$\frac{a}{\sqrt{2}}=4.00$	$4a=22.61$	0	90.0	$\frac{a}{\sqrt{2}}=4.00$	$\sqrt{6}a=13.85$	0	90.0
(i) $\begin{pmatrix} 1 & 1 \\ 0 & 4 \end{pmatrix}$	$a=5.65$	$2a=11.30$	0	90.0	$\sqrt{\frac{5}{2}}a=6.92$	$\sqrt{\frac{11}{2}}a=13.26$	$\sqrt{\frac{1}{33}}$	80.0	$\sqrt{\frac{3}{2}}a=6.92$	$\frac{2a}{\sqrt{2}}=7.99$	0	90.0
(j) $\begin{pmatrix} 1 & 2 \\ 0 & 4 \end{pmatrix}$	$\frac{2a}{\sqrt{2}}=7.99$	$\sqrt{\frac{5}{2}}a=8.94$	$\frac{1}{\sqrt{5}}$	63.4	$\frac{2a}{\sqrt{2}}=7.99$	$\frac{3a}{\sqrt{2}}=11.99$	$\frac{1}{3}$	70.5	$\sqrt{\frac{3}{2}}a=6.92$	$\frac{2a}{\sqrt{2}}=7.99$	0	90.0
(k) $\begin{pmatrix} 1 & 3 \\ 0 & 4 \end{pmatrix}$	$a=5.65$	$2a=11.31$	0	90.0	$\sqrt{\frac{3}{2}}a=6.92$	$\sqrt{\frac{11}{2}}a=13.26$	$\sqrt{\frac{1}{33}}$	80.0	$\frac{a}{\sqrt{2}}=4.00$	$\sqrt{6}a=13.85$	0	90.0

a CdTe[$1\bar{1}\bar{2}$] direction (or [$1\bar{1}\bar{1}$] and [$1\bar{1}2$], etc.). The (f) cell has its short side along the GaAs[$1\bar{1}0$] direction, and its long side along the GaAs[001] direction. For the (111)/($\bar{1}\bar{1}\bar{1}$) case, the (c') cell has all its sides oriented along CdTe[$2\bar{1}\bar{1}$] directions, while the (f) cell is oriented along GaAs[$1\bar{1}0$] directions. The mismatch in cell dimensions is 0.7% on a side for both cases. The angles of the cells match exactly.

This lengthy procedure described above corresponds to only one particular rational approximation to (2.2.1) of only three pairs of face orientations. We have applied the same procedure to all the nine combinations of CdTe(100), (110) and (111) faces on each one of the GaAs(100), (110) and (111) faces. We required a mismatch of at most 1% on each one of the sides and the angle of the reduced common unit cell. The common unit-cell area was restricted to less than 400 $\mathring{A}^2$. The results of our calculations are given in Table 2.4. The matching faces are given in the leftmost column. In the second column, we give the epitaxial condition. That is a pair of lattice directions in the interface plane that are parallel to each other. This pair is not unique. We chose to show only one such pair with the smallest possible length. Each vector in this pair corresponds to the short side of the reduced common unit cell, and we give only one typical direction out of a symmetry class. The third column denoted by cell area gives the minimal common unit-cell area in square angstroms, corresponding to that pair of matching faces with that particular epitaxial condition. The reader should bear in mind that this is only the minimal area, and integral multiples of it are also possible, as one can form superlattices of superlattices that also match. In the next six columns to the right, we give the dimensions of the common unit cells. Here a, b and α have the same meaning as in Table 2.3. The last three columns give the relative mismatch of a, b and α between the corresponding cells of the CdTe and the GaAs.

One of the interesting interfaces appearing in Table 2.4 is the CdTe(111)/GaAs(100).

Cheung and Magee[1] had reported an epitaxial growth of CdTe on GaAs in this direction. It is worth noting that one of the [011] directions perpendicular to the (100) GaAs face will align itself with one of the $[11\bar{2}]$ directions perpendicular to the (111) face of the CdTe. The other GaAs [011] direction will align itself with the CdTe $[1\bar{1}0]$, which agrees with Cheung and Magee.[1] Any match of CdTe(111)/GaAs(100) with a different orientation must have a superlattice cell whose area is larger than $400\mathring{A}^2$ as can be seen in Table 2.4.

There are also experimental results concerning growth of CdTe(111)/GaAs(111) and CdTe(100)/GaAs(100) by J. L. Schmit,[11] using MO-CVD in higher temperatures. Though these two interfaces appear in Table 2.4, the experimental epitaxial condition for CdTe(111)/GaAs(111) is $CdTe[1\bar{1}0] \parallel GaAs[1\bar{1}0]$, which does not appear in Table 2.4. No orientation information is available for the (100)/(100). If one would extend Table 2.4 to include larger unit-cell areas, say, up to $900\mathring{A}^2$, one would reproduce the MO-CVD result for (111)/(111) with a good match of 0.3%. It is not at all clear, however, whether lattice match with such a large common unit cell has any meaning at all. In the next section we will treat some other interfaces. The evidence for several interfaces suggest that there is no periodic reconstruction including such large unit cells. Instead, there is a relatively large mismatch between the lattices, resulting in a defected interface.

Table 2.4. Good lattice matches of CdTe on GaAs. The primitive common unit cells in this table do not exceed 400 $\mathring{A}^2$, and the mismatch is less than 1%. Under these conditions, all the possible matches of CdTe (100), (110), and (111) on GaAs (100), (110) and (111) are given in this table. For each possible match, we give here the epitaxial condition, as well as the common unit cell dimensions on each side of the interface. The epitaxial condition is a pair of crystal directions, one on each side of the interface, that will be parallel to each other. Many such pairs are possible, and only one of them is given here. The cells' dimensions in angstroms and degrees are given here for comparison. The mismatch percentage in all the three dimensions of the common unit cell is given in the last three columns.

Matching faces	Epitaxial condition	Cell area	*CdTe*			*GaAs*					
CdTe/GaAs	*CdTe* ‖ *GaAs*	($\mathring{A}^2$)	*a*	*b*	α	*a*	*b*	α	$\%_a$	$\%_b$	$\%_\alpha$
(100)/(100)	[012] ‖ [015]	210	14.49	14.49	90.00	14.41	14.41	90.00	0.5	0.5	0.0
(100)/(100)	[015] ‖ [035]	273	16.52	16.52	90.00	16.48	16.48	90.00	0.3	0.3	0.0
(111)/(100)[a]	$[1\bar{2}1]$ ‖ [011][a]	127	7.938	16.52	76.10	7.995	16.48	75.96	0.7	0.3	0.2
(100)/(110)	[011] ‖ $[1\bar{1}2]$	315	13.75	23.37	78.69	13.85	23.31	78.58	0.7	0.3	0.1
(100)/(110)	[015] ‖ $[3\bar{3}4]$	315	16.52	19.44	78.69	16.48	19.58	78.58	0.3	0.7	0.1
(110)/(110)	$[\bar{1}12]$ ‖ $[1\bar{1}0]$	89	7.938	11.22	90.00	7.995	11.31	90.00	0.7	0.7	0.0
(111)/(111)	$[1\bar{2}1]$ ‖ $[1\bar{1}0]$	55	7.938	7.938	60.00	7.995	7.995	60.00	0.7	0.7	0.0
(111)/(111)	$[1\bar{1}0]$ ‖ $[5\bar{4}\bar{1}]$	291	18.33	18.33	60.00	18.32	18.32	60.00	0.1	0.1	0.0
(111)/(111)	$[23\bar{5}]$ ‖ $[1\bar{1}0]$	346	19.98	19.98	60.00	19.99	19.99	60.00	0.1	0.1	0.0
(111)/(111)	$[1\bar{5}4]$ ‖ $[1\bar{3}2]$	382	21.00	21.00	60.00	21.15	21.15	60.00	0.7	0.7	0.0

[a] Observed experimentally by J. T. Cheung (Ref. 1.)

2.4. Other interfaces.

2.4.1. CdTe on sapphire

We have checked all the possible ways to match one of the (100), (110), (111), (210), (211), or (221) faces of CdTe to one of the (101),(0$\bar{1}$1) and (111) planes of sapphire. The crystal structure of sapphire is rhombohedral with a=5.1286 and $\alpha = 55^{\circ}17.36'$.[4] It is a common practice in the literature to append three rhombohedral unit cells to obtain a hexagonal unit cell with a=4.759 and c=12.991. While this common practice may have some advantages,[12] it is not recommended for lattice match.[13] Therefore, we refer to the rhombohedral notation, and Appendix A-2.1 will clarify the transformation from rhombohedral to hexagonal notation. The sapphire (101),(0$\bar{1}$1) and (111) faces correspond to the (1$\bar{1}$02),(1$\bar{2}$10) and (0001) faces in the hexagonal notation. Out of the 18 possible face combinations, only 10 can match to within 1%, with a superlattice-cell area not exceeding $600\mathring{A}^2$. These matches are shown in Table 2.5, which is structured like Table 2.4. As one can see, the CdTe(111) matches all the three sapphire planes reported by Myers *et al.*;[3] since they do not provide any further information about the orientation of the film with respect to the substrate, further experiments are needed to confirm or reject this theory. At least for the case of CdTe(111) on Al_2O_3(0001), the experimental results do not agree with ours,[10] the orientation of the epitaxial layer is $CdTe[1\bar{1}0] \parallel Al_2O_3[11\bar{2}0]$ (4% mismatch), and the interface is polycrystalline.

Table 2.5. Good lattice matches of CdTe on sapphire. The primitive common unit cells in this table do not exceed 600 $\mathring{A}^2$, and the mismatch is less than 1%. Under these conditions, all the possible matches of CdTe (100), (110), (111), (210), (211) or (221) on Al_2O_3 (101), (0$\bar{1}$1) or (111) are given here. The sapphire faces and directions in this table refer to the rhombohedral notation; transformations from rhombohedral to hexagonal notations are given in Appendix A-2.1. The meaning of the columns in this table are identical to those of Table 2.4.

Matching faces	Epitaxial condition	Cell area	$CdTe$			Al_2O_3					
$CdTe/Al_2O_3$	$CdTe \parallel Al_2O_3$	($\mathring{A}^2$)	a	b	α	a	b	α	$\%_a$	$\%_b$	$\%_\alpha$
(110)/(101)	[1$\bar{1}$1] ‖ [12$\bar{1}$]	505	11.22	45.13	85.24	11.31	45.51	84.87	0.7	0.8	0.4
(110)/(101)	[3$\bar{3}$2] ‖ [31$\bar{3}$]	564	15.20	37.23	85.74	15.17	37.14	85.09	0.2	0.2	0.8
(111)/(101)	[4$\bar{5}$1] ‖ [14$\bar{1}$]	509	21.00	24.25	90.00	21.06	24.34	89.10	0.3	0.4	1.0
(210)/(101)	[1$\bar{2}$5] ‖ [3$\bar{2}\bar{3}$]	564	17.75	31.75	90.00	17.58	31.94	89.10	1.0	0.6	1.0
(211)/(101)	[1$\bar{1}\bar{1}$] ‖ [12$\bar{1}$]	412	11.22	36.66	90.00	11.31	36.70	89.90	0.7	0.1	0.1
(100)/(0$\bar{1}$1)	[013] ‖ [100]	357	10.25	34.90	86.63	10.26	34.84	87.42	0.1	0.2	0.9
(100)/(0$\bar{1}$1)	[011] ‖ [011]	504	9.166	54.99	90.00	9.086	55.00	89.25	0.9	0.0	0.8
(110)/(0$\bar{1}$1)	[001] ‖ [111]	535	12.96	41.24	90.00	12.99	41.22	90.00	0.2	0.1	0.0
(110)/(0$\bar{1}$1)	[1$\bar{1}$0] ‖ [011]	535	9.166	58.51	85.51	9.086	59.07	86.10	0.9	1.0	0.7
(111)/(0$\bar{1}$1)	[01$\bar{1}$] ‖ [011]	327	9.166	35.79	86.33	9.086	35.44	86.10	0.9	1.0	0.3
(221)/(0$\bar{1}$1)	[1$\bar{1}$0] ‖ [011]	504	9.166	54.99	90.00	9.086	55.00	89.25	0.9	0.0	0.8
(100)/(111)	[051] ‖ [2$\bar{1}\bar{1}$]	546	16.52	33.05	90.00	16.49	33.31	90.00	0.2	0.8	0.0
(100)/(111)	[053] ‖ [01$\bar{1}$]	546	18.89	28.98	85.60	19.04	28.95	85.28	0.7	0.1	0.4
(111)/(111)	[31$\bar{4}$] ‖ [1$\bar{2}$1]	236	16.52	16.52	60.00	16.49	16.49	60.00	0.2	0.2	0.0
(111)/(111)	[1$\bar{2}$1] ‖ [1$\bar{1}$0]	491	23.81	23.81	60.00	23.80	23.80	60.00	0.1	0.1	0.0

2.4.2. Silicon on sapphire

The silicon on sapphire system is very interesting from a technological point of view. The physics and chemistry of this interface, however, are very difficult to understand. We are about to see that lattice match conditions play little or no role in the epitaxy of this interface.

The silicon on sapphire system was studied quite extensively, and there are many known cases of epitaxial growth on various sapphire faces. The most popular faces are the $(1\bar{1}02)$ cleavage plane, the $(11\bar{2}0)$ and (0001) which are both slip planes,[14] and the $(11\bar{2}3)$ plane which is the best growth plane. Growth of silicon on other sapphire faces is also reported. The experimental epitaxial relationships of silicon on sapphire[15-19] are summarized in Table 2.6. For the sapphire, we present in this table both the rhombohedral and the hexagonal notations (cf. Appendix A-2.1). This table is sorted according to the parallel lattice directions in the interface plane (the epitaxial condition). One can see that some parallel directions tend to repeat for several growth faces. For example, the epitaxial condition $Si[1\bar{1}0] \parallel Al_2O_2[1\bar{1}00]$ occurs in at least four different interfaces, namely, $Si(111)/Al_2O_3(11\bar{2}4)$, $(111)/(11\bar{2}3)$, $110)/(11\bar{2}0)$, and $(221)/(11\bar{2}2)$. If this tendency is due to lattice match requirement, then the length of the primitive $Si[1\bar{1}0]$ translation should be approximately equal to that of the primitive $Al_2O_3[1\bar{1}00]$ times a rational number with small numerator and denominator.

The lengths of all the parallel directions appearing in Table 2.6 is summarized in Table 2.7, as well as some of the rational approximations to their length ratio. For example, consider the pair $Si[1\bar{1}0] \parallel Al_2O_3[1\bar{1}00]$ mentioned before. $Si[1\bar{1}0]$ is 3.840Å, and the $Al_2O_3[1\bar{1}00]$ is 8.242Å long. The ratio of these two numbers is 0.4659 which cannot be well aproximated by small rational numbers. Either one

Table 2.6. Silicon on sapphire experimental epitaxial relationships. The sapphire faces and directions are presented both in the rhombohedral (three indices) and hexagonal (four indices) notations. Some orientations of the sapphire with respect to the silicon repeat on several faces.

Matching faces	Epitaxial condition	Reference
$(001)/(110), (01\bar{1}2)$	$[100] \parallel [1\bar{1}0], [2\bar{1}\bar{1}0]$	a,b,c
$(001)/(114), (10\bar{1}2)$	$[100] \parallel [1\bar{1}0], [2\bar{1}\bar{1}0]$	d
$(111)/(741), (11\bar{2}4)$	$[1\bar{1}0] \parallel [1\bar{2}1], [1\bar{1}00]$	a,b,c
$(111)/(210), (11\bar{2}3)$	$[1\bar{1}0] \parallel [1\bar{2}1], [1\bar{1}00]$	c
$(110)/(10\bar{1}), (11\bar{2}0)$	$[1\bar{1}0] \parallel [1\bar{2}1], [1\bar{1}00]$	a,b
$(221)/(52\bar{1}), (11\bar{2}2)$	$[1\bar{1}0] \parallel [1\bar{2}1], [1\bar{1}00]$	e
$(111)/(10\bar{1}), (11\bar{2}0)$	$[1\bar{1}0] \parallel [1\bar{1}1], [2\bar{2}01]$	a,b,c
$(11\bar{2})/(121), (\bar{1}104)$	$[1\bar{1}0] \parallel [1\bar{1}1], [2\bar{2}01]$	d
$(111)/(211), (10\bar{1}4)$	$[1\bar{1}0] \parallel [0\bar{1}1], [1\bar{2}10]$	d
$(111)/(211), (10\bar{1}4)$	$[11\bar{2}] \parallel [100], [10\bar{1}1]$	d
$(310)/(100), (10\bar{1}1)$	$[1\bar{3}2] \parallel [0\bar{1}1], [1\bar{2}10]$	d
$(310)/(100), (10\bar{1}1)$	$[\bar{1}35] \parallel [011], [\bar{1}012]$	d
$(111)/(111), (0001)$	$[11\bar{2}] \parallel [1\bar{2}1], [\bar{1}100]$	a,b,c

(a) Ref. 15; (b) Ref. 16; (c) Ref. 17; (d) Ref. 18; (e) Ref. 19.

Table 2.7. Length ratio of parallel directions for silicon on sapphire. These pairs are all found experimentally (cf. Table 2.6) for actual epitaxial layers. The length ratio of the primitive vectors in these directions is given in the second column. This ratio is approximated by rational numbers in the third column, with the relative mismatch indicated in parentheses. The large mismatch for small rational numbers might indicate that lattice match is irrelevant for this interface.

PARALLEL PAIR	LENGTH RATIO	RATIONAL APPROXIMATIONS
$Si[100] \parallel Al_2O_3[2\bar{1}\bar{1}0]$	5.431/4.759=1.141	1/1(14%), 7/6(2.2%), 8/7(0.1%)
$Si[1\bar{1}0] \parallel Al_2O_3[1\bar{1}00]$	3.840/8.242=0.4659	1/2(6.8%), 6/13(0.9%)
$Si[1\bar{1}0] \parallel Al_2O_3[2\bar{2}01]$	3.840/6.996=0.5489	1/2(9.7%), 5/9(1.1%),
$Si[1\bar{1}0] \parallel Al_2O_3[1\bar{2}10]$	3.840/4.759=0.8069	1/1(20%), 4/5(0.8%)
$Si[10\bar{2}] \parallel Al_2O_3[10\bar{1}1]$	6.651/5.128=1.297	4/3(2.7%), 9/7(0.9%), 13/10(0.2%)
$Si[1\bar{3}2] \parallel Al_2O_3[1\bar{2}10]$	10.160/4.759=2.135	2/1(6.7%), 13/6(1.5%), 15/7(0.3%)
$Si[\bar{1}35] \parallel Al_2O_3[\bar{1}012]$	32.130/9.085=3.537	7/2(1.0%), 39/11(0.2%)
$Si[11\bar{2}] \parallel Al_2O_3[\bar{1}100]$	6.651/8.242=0.8070	1/1(20%), 4/5(0.9%)

matches twice the $Si[1\bar{1}0]$ to an $Al_2O_3[1\bar{1}00]$ with a poor match (approximately 6.8%), or one has to commensurate 13-28 $Si[1\bar{1}0]$ translations to 6-13 sapphire translations in order to achieve a good match. It is quite unreasonable to expect a periodic reconstruction over 13 unit cells in one direction.

Two comments about Table 2.7 should be kept in mind. Regarding the rational approximations appearing in this table, they are obviously not the only possible ones. The rational approximations appearing in table 2.7 are only the "best" in the sense that there is no rational approximation that approximates better and has a smaller denominator. Thus, for example, in approximating 0.4659 which is the ratio of $Si[1\bar{1}0]$ to $Al_2O_3[1\bar{1}00]$ (the second row in this table), there is not any rational approximation better than 0.3%with a denominator smaller than 28. Similarly, there is no rational approximation better than 0.9%with a denominator smaller than 13. Another remark concerning Table 2.7. is that the numbers were calculated for silicon and sapphire at room temperature. The growth temperature of silicon on sapphire is high, typically around 800-1000°C. depending on growth technique.[2] The crystal parameters of both silicon and sapphire as functions of temperature are given in Yim and Paff:[20] the cubic lattice parameter of silicon varies from 5.4309 at 25°C to 5.4461 at 813°C; the sapphire hexagonal parameters vary from a=4.7576 and c=12.9834 at 25°C to a=4.7848 and c=13.0675 at 803°C. These variations may change slightly the accuracy of the better rational approximations, but will not change the rational approximations themselves.

In summary, lattice match considerations seem to be irrelevant to the silicon on sapphire system. For a possible explanation for this phenomenon, one might recall the early growth of silicon (100) on sapphire $(1\bar{1}02)$ sapphire, as described by Blanc and Abraham.[21] According to their description, the growth starts with island formation, mostly in the (100) direction, and growing fast; some in the (110)

direction, and growing slow. Eventually, the (100) islands cover the (110) islands resulting in stacking faults at the juncture of the islands. As the growth proceeds, however, the density of faults decreases. In other words, the lattice mismatch results in defects, as predicted by this theory, but for some reason the defects tend to stay near the interface, and do not propagate through the film.

2.4.3. Silicides on silicon.

Recently, there has been a lot of interest in growing transition metal silicides epitaxially on silicon. There are silicides with a much higher melting temerature than aluminium, and at the same time having a reasonably high mobility, that can serve as contacts in VLSI. Silicides are also known to form very good Schottky barriers. For these two classes of applications, polycrystalline silicides will do. However, the possibility of growing a single crystal silicide on a silicon substrate, or even a multi-layer structure, opens the door for a whole new class of novel devices.

There are about 150 known binary transition-metal silicides (cf. Appendix A-2.4). Out of them, only three are experimentally known to grow epitaxially on silicon,[22] and to form single crystals with well defined directions with respect to the substrate. These three are $CoSi_2$,[23-24] $NiSi_2$,[25] and Pd_2Si.[26-27] Other important silicides, $PtSi$ and Pt_2Si, are known to grow polycrystalline on silicon, but with definite orientations with respect to the substrate.[28-30] A list of these known cases is given in Table 2.8. In the first column of Table 2.8, we list the silicide and its crystal structure. The second column gives the orientation of the interface plane for both the substrate and the film. The third column defines the orientation

Table 2.8. Experimental epitaxial silicides on silicon. $CoSi_2$, $NiSi_2$ and Pd_2Si grow single crystals epitaxially on the silicon faces indicated. Pt_2Si and $PtSi$ grow polycrystalline, but nevertheless with several distinct orientations of the crystallites with respect to the silicon. The first column lists the silicide, its Bravais system, and its crystal structure. The second column gives the matching faces, the third column gives the orientation of the film with respect to the substrate, and the last column gives the reference, and sometime the relevant growth condition.

Silicide	Matching faces	Epitaxial condition	Reference
$CoSi_2$, fcc (CaF_2)	$CoSi_2(111)/Si(111)$	$[1\bar{1}0] \parallel [1\bar{1}0]$	(a); less than 1500Å
a=5.367		$[1\bar{1}0] \parallel [\bar{1}10]$	(b)
$NiSi_2$, fcc (CaF_2)	$NiSi_2(111)/Si(111)$	$[1\bar{1}0] \parallel [1\bar{1}0]$	(c)
a=5.407		$[\bar{1}10] \parallel [1\bar{1}0]$	(c)
Pd_2Si, Hex.(Fe_2P)	$Pd_2Si(0001)/Si(111)$	$[2\bar{1}\bar{1}0] \parallel [11\bar{2}]$	(d-e)
Pt_2Si, Tetrag.	$Pt_2Si(001)/Si(001)$	$[1\bar{1}0] \parallel [100]$	(f)
$PtSi$, Orthor.(MnP)	$PtSi(020)/Si(111)$		(g); below 900C; 900Å
a=5.595, b=3.603,	$PtSi(111)/Si(111)$		(g); above 900C; 900Å
c=5.932	$PtSi(100)/Si(111)$	$[010] \parallel [\bar{1}01]$	(g); 200Å
	$PtSi(1\bar{1}0)/Si(001)$	$[001] \parallel [110]$	(h)
	$PtSi(133)/Si(011)$	$[30\bar{1}] \parallel [0\bar{2}2]$	(h)
	$PtSi(120)/Si(011)$	$[00\bar{2}] \parallel [0\bar{2}2]$	(h)
	$PtSi(011)/Si(011)$	$[\bar{1}1\bar{1}] \parallel [400]$	(h)
	$PtSi(\bar{2}11)/Si(001)$	$[0\bar{1}1] \parallel [110]$	(f)
		$[111] \parallel [3\bar{1}0]$	(f)

(a) Ref. 23; (b) Ref. 24; (c) Ref. 25; (d) Ref. 26;
(e) Ref. 27; (f) Ref. 28; (g) Ref. 29; (h) Ref. 30.

of the film with respect to the substrate by giving a pair of parallel directions in the substrate and the film. Some changes were made from the original references to preserve the uniformity of the notation. The last column gives a reference to the original work, and remarks.

From a lattice match point of view, the first two cases in Table 2.8 are straightforward. Both $CoSi_2$ and $NiSi_2$ have the CaF_2 structure which is face-centered cubic, just like silicon. The bulk lattice parameters are 5.367 and 5.407 respectively, compared to 5.431 of silicon (all lattice parameters are given at room temperature); the lattice mismatches, therefore, are 1.2% and 0.5% respectively. Therefore one might expect similar orientations of the film and the substrate, which is indeed the case.

The next entry in Table 2.8 is Pd_2Si. Buckley and Moss[26] were the first to investigate the epitaxial relationship of this interface. They found that Pd_2Si forms spontaneously at the palladium-Si(111) interface even at room temperature, and that no other silicide is formed upon annealing up to 500°C. The orientation of the Pd_2Si was reported to be $Pd_2Si\langle 10.0\rangle \parallel Si\langle 110\rangle$. In this epitaxy, the translations of both the silicon and the silicide form a triangular grid, with three silicon cells fitting into one silicide cell. The lattice mismatch depends on the silicon content of the silicide. Aronsson and Nylund[31] investigated the lattice parameters of Pd_2Si as a function of stochiometry for bulk samples. They found that silicon-poor Pd_2Si has a=6.497 and c=3.432 while silicon-rich Pd_2Si has a=6.528 and c=3.437. This will change the mismatch from 2.3%(silicon poor) to 1.8%(silicon rich), but it is also possible that the lattice parameters of a thin film may be slightly different than those of the bulk. In any case one might expect the silicide near the interface to be silicon rich, which was verified by Ho *et al.*[32]

The epitaxial relationships of Pt_2Si on Si(100) was studied by Ben Ghozlene

et al.[28] They observed this silicide as an intermediate phase before the formation of the more stable $PtSi$. The Pt_2Si, which is tetragonal with a=3.933 and c=5.910, grows with its c-axis perpendicular to the interface. The epitaxial relationship is $Pt_2Si\langle 110\rangle \parallel Si\langle 100\rangle$. The translations in the interface plane form a square grid with a mismatch of 2.4%, if the bulk values of the crystal parameters are taken. It is not clear whether the polycrystalline nature of the Pt_2Si is due to the lattice mismatch or to the formation of $PtSi$.

$PtSi$ was listed in Table 2.8 despite the fact that it grows polycrystalline, because of the definite directions in which it grows on the substrate. These reported directions are listed in Table 2.8, but the tabulated directions have a spread of about half a degree.[33] Among these various directions, one finds larger mismatches, up to 10%, with respect to the substrate. The list of parallel pairs of directions as well as their mismatches is given in Table 2.9, which is structured similar to Table 2.7. One can see in Table 2.9 that the known epitaxial layers that are single crystals, correspond to small unit cells and to a good lattice match. The borderline between a single crystal and polycrystalline film seems to be between 2% and 3% mismatch. The $PtSi$ epitaxy suggests that mismatches of up to 10% may still force certain directions of growth, but they are two big for a single crystal to form. One cannot find in Table 2.9 a case corresponding to a very good match (say 1% or less) with a large unit cell (3/3 or more) similar to the CdTe/GaAs mentioned before. This might be due to the fact that only a limited number of interfaces were tried, or it might suggest a trend for metallic films.

To look for good candidates for silicide on silicon epitaxy, we have compiled a set of tables with all the binary transition metals that match silicon substrates well. The conditions imposed on the search were mismatch of 1% or less on unit-cell dimensions, and common unit-cell area of $200\mathring{A}^2$. To limit the possible faces,

Table 2.9. Length ratio of parallel directions for experimental epitaxial silicides on silicon. This table is structured like Table 2.7. This table indicates that a good lattice match may be necessary for epitaxial growth of a single crystal, when the film is metallic.

PARALLEL PAIR	LENGTH RATIO	RATIONAL APPROXIMATIONS
$CoSi_2[1\bar{1}0] \parallel Si[1\bar{1}0]$	3.795/3.840=0.9883	1/1(1.2%)
$CoSi_2\langle 100\rangle \parallel Si\langle 100\rangle$	5.367/5.431=0.9883	1/1(1.2%)
$CoSi_2\langle 111\rangle \parallel Si\langle 111\rangle$	9.296/9.407=0.9883	1/1(1.2%)
$NiSi_2\langle 100\rangle \parallel Si\langle 100\rangle$	5.406/5.431=0.9954	1/1(0.5%)
$NiSi_2\langle 111\rangle \parallel Si\langle 111\rangle$	9.363/9.407=0.9954	1/1(0.5%)
$Pd_2Si\langle 1\bar{2}10\rangle \parallel Si\langle 1\bar{2}1\rangle$	6.528/6.651=0.9815	1/1(1.8%) (Si rich)
	6.497/6.651=0.9768	1/1(2.3%) (Si poor)
$Pt_2Si[100] \parallel Si[1\bar{1}0]$	3.933/3.840=1.0242	1/1(2.4%)
$PtSi[001] \parallel Si[110]$	5.932/3.840=1.5448	3/2(3.0%)
$PtSi[0\bar{1}1] \parallel Si[110]$	6.940/3.840=1.8073	2/1(9.6%), 7/4(3.2%)
$PtSi[111] \parallel Si[130]$	8.915/8.587=1.0382	1/1(3.8%)
$PtSi[30\bar{1}] \parallel Si[0\bar{2}2]$	17.802/3.840=4.636	9/2(3%)
$PtSi[00\bar{2}] \parallel Si[0\bar{2}2]$	5.932/3.840=1.5448	3/2(3.0%)
$PtSi[\bar{1}1\bar{1}] \parallel Si[400]$	8.915/5.431=1.6415	3/2(9.4%), 5/3(1.5%)
$PtSi\langle 010\rangle \parallel Si\langle 224\rangle$	3.603/6.651=0.5417	1/2(8.3%)
$PtSi[010] \parallel Si[1\bar{1}0]$	3.603/3.840=0.9383	1/1(6.1%)

additional restrictions on the primitive unit-cell sizes were imposed. The prinitive unit cell for the silicon was restricted to $21\mathring{A}^2$, to include only the (111), (100) and (110) faces. The silicide primitive unit cell was restricted to $50\mathring{A}^2$; silicides with larger unit cells will, therefore, have fewer faces compared to the silicon. The faces of each silicide used in the match are written above each table. Since there are so many silicides, the resulting set of tables appears in a special appendix at the end of this chapter, (Appendix A-2.3), together with references to the crystal structures of the binary transition metal silicides (Appendix A-2.4).

Among the interesting matches appearing in this set of tables, we would like to mention especially the $V_3Si(111)/Si(111)$, $CrSi_2(0001)/Si(111)$, $FeSi_2(001)/Si(100)$, $FeSi_2(111)/Si(110)$, $Y_3Si_5(0001)/Si(111)$, $RuSi(111)/Si(111)$, $RhSi(111)/Si(111)$, and $OsSi(111)/Si(111)$ as candidates for epitaxial growth with a good match and a small common unit-cell area. Some of these silicides possess properties that make them particularly interesting. V_3Si is superconducting with a critical temperature of 17°K;[34] $CrSi_2$ and $FeSi_2$ are semiconductors.[35]

2.5. Summary and discussion

The theory of geometrical lattice match was formalized in this chapter. This theory is applicable to any pair of crystal structures, oriented in any direction. We defined two lattices as matching if the two 2-dimensional lattices, formed by the crystal translations parallel to the interface, have a common superlattice. In general, one cannot hope to achieve a perfect match, and instead of a common superlattice, one has a pair of superlattices, one for each side of the interface, that are almost identical. There are two parameters that characterize the match: the mismatch between the two superlattices and the unit-cell area of these superlattices. We have shown how to obtain a standard unit cell for a given lattice. This unit cell is a parallelogram with sides a and b, and an acute angle α. By comparing a, b and α for both superlattices, one obtains the mismatch between them. The unit-cell area can be taken from either one of the two superlattices, since they are almost equal. We have developed a constructive way to find all the possible lattice matches with a given mismatch and a common unit-cell area which is smaller than a prescribed value.

The role of geometrical match in epitaxy is still not clear, since local interface chemistry will always play a major role. Therefore, if two lattices match, it does not mean that they will grow epitaxially on each other. We do hope, however, to establish that a thick, defect free, single crystal epitaxial growth is possible only when there is a good match. We have shown that this is indeed the case for the reported case of epitaxial growth of CdTe(111) on GaAs(100);[1] the common unit-cell in that case is $128\mathring{A}^2$ and the mismatch was less than 1%. The few silicides that grow epitaxially on silicon also indicate the importance of lattice match for a single crystal growth, but they overcome mismatches of up to 2%, with smaller common unit cells. Finally, the silicon on sapphire interface demonstrates a case

in which a single crystal grows epitaxially despite a rather large mismatch. Both the silicon on sapphire and the silicides on silicon indicate that a mismatch of up to 10% may still orient the film with respect to the substrate, however, large density of defects occurs in the interface.

Further theoretical and experimental investigation is required in order to establish general criteria for allowable unit-cell areas and mismatch.

References for Chapter 2

1. J.T.Cheung and T. Magee, *J. Vac. Sci. Technol.* **A1**, 1604 (1983).
2. *Heteroepitaxial Semiconductors for Electronic Devices* edited by G. W. Cullen and C. C. Wang (Springer, New York, 1978), p.50.
3. T. H. Myers, Y. Cheng, R. N. Bicknell, and J. F. Schetzina, *Appl. Phys. Lett.* **42**, 247 (1983).
4. J. D. H. Donnay and H. M. Ondik, *Crystal Data, Determinative Tables,* **V-2** (U. S. Department of Commerce, National Bureau of Standards and Joint Commission on Powder Diffraction Standards, Washington, 1973).
5. G. Friedel, *Leçons de Cristallographie*, (Berger-Levrault, Paris, 1926).
6. P. H. Pumphrey, in *Grain Boundary Structure and Properties*, edited by G. A. Chadwick and D. A. Smith, (Academic, London, 1976) p.139.
7. S. Ranganathan, Acta Cryst. **21**, 197 (1966).
8. J. W. S. Cassels, *An Introduction to the Geometry of Numbers*, (Springer, Berlin 1959).
9. A. Santoro, A. D. Mighell, *Acta Cryst.* **A 29**, 171 (1973).
10. J. F. Schetzina, private communication.
11. J. L. Schmit, private communication.
12. M. Buerger, *Elementary Crystallography*, (MIT, Cambridge, 1978), p.106.
13. The main disadvantages are that using hexagonal instead of rombohedral notation arbitrarily increases every unit cell by a factor of one to three. It also creates ambiguity in the notation. For example, the hexagonal $(1\bar{1}02)$ and $(\bar{1}102)$ faces are not equivalent. One corresponds to the rhombohedral (101), and the other to (141), but there is no way to tell which one is which without knowing whether the hexagonal $(\vec{a}_1, \vec{a}_2, \vec{c})$ axes form a right- or a left-handed system.

14. R. Scheuplein and P. Gibbs, *J. Amer. Ceram. Soc.* **43,** 458 (1960).

15. H. M. Manasevit, A. Miller, F. L. Morritz, and R. L. Nolder, *Trans. TMS-AIME* **233**, 540 (1965).

16. R. L. Nolder and I. Cadoff, *Trans. TMS-AIME* **233**, 549 (1965).

17. C. C. Chang, *J. Vac. Sci. Technol.* **8**, 500 (1971).

18. H. M. Manasevit, R. L. Nolder and L. A. Moudy, *Trans. TMS-AIME* **242,** 465 (1968).

19. A. J. Hughes, *J. Appl. Phys.* **46**, 2849 (1975).

20. W. M. Yim and R. J. Paff, *J. Appl. Phys,* **45,** 1456 (1974).

21. J. Blanc and M. S. Abraham, *J. Appl. Phys.* **47,** 5151 (1976).

22. M. A. Nicolet and S. S. Lau, *Formation and Characterization of Transition Metal Silicides*, in *ELECTRONICS: MICROSTRUCTURE SCIENCE*, N. Einspruch, Series Editor, *SUPPLEMENT A - MATERIALS AND PROCESS CHARACTERIZATION*, G. Larrabee, Guest Editor, (Academic Press, New York, 1983).

23. R. T. Tung, J. C. Bean, J. M. Gibson, J. M. Poate and D. C. Jacobson, *Appl. Phys. Lett.* **40**, 684 (1982).

24. J. M. Gibson, J. C. Bean, J. M. Poate and R. T. Tung, *Surf. Sci.* **93**, 99 (1982).

25. K. N. Tu, J. Mayer, in *Thin Films – Interdiffusion and Reactions,* edited by J. M. Poate, K. N. Tu, and J. W. Mayer (Wiley, New York, 1978).

26. W. D. Buckley and S. C. Moss, *Solid State Electronics* **15**, 1331 (1972).

27. W. Krakow, *Surf. Sci.* **93**, 109 (1982).

28. H. Ben-Ghozlene ,P. Beaufrère and A. Authier, *J. Appl. Phys.* **49**, 3998 (1978).

29. A. K. Sinha, R. B. Marcus, T. T. Sheng and S. E. Haszko, *J. Appl. Phys.* **43,**

3637 (1972).

30. R. M. Anderson and T. M. Reith, *J. Electrochem. Soc.* **122**, 1337 (1975).

31. B. Aronsson and A. Nylund, *Acta Chem. Scand.* **14,** 1011 (1960).

32. P. S. Ho, P. E. Schmid and H. Föll, *Phys. Rev. Lett.*, **46,** 782 (1981).

33. H. Ishiwara, K. Hikosaka, S. Furukawa, *J. Appl. Phys.*, **50,** 5302 (1979).

34. B. W. Roberts, *Nat. Bur. Stan. Techn. Note 724*, N.Y. (1972).

35. V. S. Neshpor and V. L. Yupko, *Zh. Prikl. Khim.* **36**, 1139 (1963).

Chapter 3

AB-INITIO CALCULATIONS OF ELASTIC PROPERTIES OF BULK SILICON USING SMALL CLUSTERS.

3.1 Introduction.

In this chapter we present ab-initio calculations of the elastic properties Si_5H_{12} silicon clusters. The elastic properties of bulk silicon were calculated from the elastic spring constants of the clusters using four different models. This method is particularly suited to treat any system lacking translational symmetry, for example, interfaces and defects. By comparing our calculated results to experimental phonon band structure, we are able to check the validity of the models used.

Why there is a need to calculate elastic properties

One can classify the elastic vibrations of silicon, or any other crystalline material, into two categories: propagating and evanescent. Inside a pure, ideal sample, far from the surface, one can observe only propagating vibrations (phonons). In the vicinity of surfaces, interfaces, and defects, however, one can also observe other types of vibrations that decay exponentially into the bulk (evanescent vibrations).

The spectrum of the propagating vibrations (phonons) can be obtained directly

using thermal-neutron scattering experiments.[1,2] In addition, the slopes of the phonon band structure, in the limit of very long wavelength, can be obtained from the static elastic properties of the crystal. These, in turn, can be obtained very accurately from velocity-of-sound measurements.[3] Simply stated, experimental methods exist to determine the phonon spectrum. On the other hand, the spectrum of evanescent vibrations is very difficult to obtain directly from experiments, since these vibrations always couple to some other elastic excitation. This excitation may involve either a reconstructed structure near a surface or a defect, or a different type of a chemical bond, as is the case near interfaces or impurity atoms. The source of the difficulty lies, therefore, in decoupling the two; this is done by theoretical calculations.

How the elastic properties are calculated

The lack of direct experimental measurement of the spectrum of evanescent vibrations calls for a theoretical investigation. The theoretical approach to this problem involves, typically, some type of elastic model, that relates the elastic strain energy to the positions of the atoms. Such a model usually has a general form and uses several adjustable parameters. There are two problems associated with this approach: finding a good model and obtaining its parameters. Historically, the same problems were encountered by investigators trying to fit the bulk phonon band structure. Some of the many models that were developed are described here. The parameters of these models were obtained, in the past, by fitting the predictions of the model to experimental results, usually to the bulk phonon-band structure. In this work we chose a different approach: we obtained these parameters from the elastic spring constants of small clusters. The main advantage of this approach is that it enables one to estimate the quality of the model used, by comparing the calculated bulk phonon band structure to the experimental one. Such a comparison

gauges the performance of the same model for two radically different systems, namely, small clusters and bulk. It is, therefore, reasonable to assume that a model which performs well both for small clusters and for bulk, with the same set of parameters, will be accurate enough for calculating evanescent vibrations; alternatively, for those models currently used to calculate evanescent vibrations, one can estimate the quality of these calculations based on this research.

The elastic properties of small clusters can be obtained either experimentally, using infra-red vibrational spectroscopy, or theoretically, using ab-initio quantum-mechanical calculations; in general, for small clusters, the agreement between theory and experiment is quite good. In this work we chose to obtain the parameters of the models from theoretical, ab-initio calculations rather than from experimental data. Using ab-initio calculations has some advantages over using spectroscopic data, the most important one being the ability to look at energy levels of molecules that are difficult to synthesize or are unstable. One can even go further and create some pseudo-atoms that do not exist in nature, in order to continuously vary some specific property of the atom. In the calculations presented in this chapter, for example, the hydrogen atoms used to terminate silicon dangling bonds are artificially expanded to match the electronegativity of silicon atoms. In any case we will show that most of the inaccuracy is due to the models used rather than to the method of obtaining their parameters. The use of ab-initio theoretical methods, then, does not limit the accuracy of the results in those four models. The use of ab-initio methods does limit the size of the clusters, however, and consequently it limits the complexity of the models. It should be noted, nevertheless, that the alternative method, namely, obtaining the parameters from spectroscopic data, does not exist. We do not have spectroscopic data for large silicon-hydrogen molecules.

Models used in this work

In the next few paragraphs various elastic models used in this work are presented. All these models were used in the past for fitting the bulk band structure of silicon with various degrees of success. In this chapter, we shall obtain the parameters of these models from ab-initio cluster calculations, and then compare our set of parameters with the one found by fitting the band structure directly.

The first model involves two spring constants, one for bond bending (changing the angle between two adjacent bonds) and one for bond stretching (changing the distance between two adjacent atoms). This model is the simplest one possible (any model involving only one of the two spring constants would predict that either the bulk modulus or the shear modulus should vanish). Due to its simplicity this model is very useful, but one does not expect it to be very accurate. The two parameters can be fitted to any two points on the phonon dispersion curve or to the static elastic properties of bulk silicon. In this work these parameters were fitted to the spring constant of Si_5H_{12} clusters which were calculated from first principles. As we demonstrate in this work, no single pair of parameters can fit all the data points, and a least-squares scheme was applied to find the best fit. The phonon band structure obtained from these two parameters has the right general appearance, but is not very accurate numerically.

An obvious extension of the simple bond-bending-and-stretching model is the addition of a third parameter that gives the mixed term of bond bending and bond stretching. This model was first used with moderate success by Singh and Dayal[4] to fit the phonon band structure of silicon. We have calculated its parameters from the spring constants of the Si_5H_{12} mentioned above. With this set of parameters, the Singh-Dayal model produces a band structure which is as accurate as the one used with parameters fitted directly to the band structure. We, therefore, expect

calculations of evanescent vibrations based on this model to be of equal quality to the phonon-band-structure calculations.

The model employed by Musgrave and Pople[5] is the next step in complexity. Their valence-force-field model assumes that one can write the total ground-state energy of the system as a sum of atomic terms, each depending only on the relative positions of the atom's four nearest neighbors. This model employs not only bond-bending and bond-stretching force constants, but also three mixed terms (stretching-stretching, stretching-bending and bending-bending). All told, this model employs five elastic constants, and it extends the three-parameter model of Singh and Dayal. Ab-initio calculation of the parameters of this model result in a set of parameters almost identical to those of Singh and Dayal, that is, the two extra parameters are very small, and the three that are common to the Singh-Dayal model do not change significantly. This is not to say that these two models are equivalent. If the five parameters of the valence-force-field model were fitted directly to the band structure, this new set of parameters would be different from the ab-initio set, and the fitted phonon band structure would be better than the one calculated from first principles and the Singh-Dayal model. The physical significance of this new set of parameters, however, is questionable since they would not fit the cluster calculations very well. In other words, we expect the calculations of evanescent vibrations based on this model to be inferior to the calculations of phonon-band structure. The question of which set of parameters is to be used for the calculation of evanescent vibrations is left open: we can either take the set of parameters used to fit the small cluster or the set used to fit the band structure. Probably neither one will be consistently better than the other.

The three models described above have a common feature. They all express the elastic energy of the crystal in terms of explicit geometrical elements like

interatomic distances and angles. It is quite clear that one can further improve these models by simply adding more parameters. The valence-force-field model of Musgrave and Pople was extended by McMurry *et al.*[6] They introduced another parameter, namely, angle-angle interaction between two bond pairs with a common bond. Here, a much better fit was achieved for the elastic properties of diamond using experimental spectroscopic data for hydrocarbons as well as some adjustment of the six parameters. This model was used to **fit** the silicon phonon band structure by Singh and Dayal,[4] and Solbrig,[7] but the agreement to experimental band structure was not as good as that of diamond. Solbrig concluded that for silicon the third and fourth nearest neighbor interaction is very important; by extending the model even further to include nine adjustable parameters, he was able to fit the phonon band structure quite well. In order to calculate these parameters from first principles, we would need at least a cluster of Si_8H_{18}; such calculations were beyond the scope of this work.

Vasil'ev *et al.*[8] applied a different method. They took the sp^3 hybridization of the bonds to have constant tetrahedral angles, but allowed each bond to break in the middle. They used two parameters to describe the restoring force acting on the broken bond, as well as two central-force parameters acting on nearest and second nearest neighbors. Using this four parameter model, Vasil'ev *et al.* were able to fit the phonon band structure of diamond, silicon, and germanium very well.[9] One should notice that this model puts an internal orientation on each atom that, in turn, depends on the internal orientation of its neighbors. This introduces a long-range force field, which makes this model very powerful. The success of Vasil'ev's model in describing the phonon band structure using very few adjustable parameters convinced some authors that this model describes very well the electron response in the lattice vibration of a covalent solid.[10] It is important to realize

that the assumption made by Vasil'ev *et al.* about the nature of the bonds, namely, that the angles between the bonds are rigid, and that the bonds are broken in the middle, is actually not necessary. All one has to assume is some orientation for each atom, and some mechanism through which a change in this orientation exerts forces and moments on the neighboring atoms.

We have considered this last model as well. Since the internal coordinate systems of this model have to be calculated, it is much more difficult to translate the cluster results into a set of parameters for this model, and an extensive formalism was developed for that purpose. The phonon band structure calculated by us, using this model and a set of parameters obtained ab-initio, was generally better than any of the three previous band structures. However, the static elastic constants calculated using Vasil'ev's model were not superior to those obtained by the previous three.

Organization of Chapter 3.

In section 3.2 we discuss the quantum-chemistry calculations used to calculate the cluster ground-state energy. The treatment here is qualitative and descriptive; for exact formulations the reader is referred to the extensive literature on the subject. In section 3.3 the results of the cluster calculations are presented, the parameters of the various models are obtained from these calculations, and the elastic properties of bulk silicon predicted by the various models are compared to experimental results. In section 3.4 the conclusions based on this study are drawn.

3.2. Quantum-chemistry methods used in this chapter

We describe the quantum-chemistry methods used to calculate the ground-state energy of the small clusters in this section. Only ab-initio methods were employed. These are the Hartree-Fock (HF), the Generalized-Valence-Bond (GVB), the Restricted Configuration Interaction (R-CI), and the Generalized-Valence-Bond Configuration Interaction (GVB-CI), in increasing order of accuracy and complexity. They will be described qualitatively in the following paragraphs, as will the concepts of effective potential and basis functions used in these calculations.

All of these ab-initio methods make use of the variational principle. This principle states that if $\mathcal{H}$ is the Hamiltonian of the system, Ψ is the ground state, and ψ is any other possible state for the system, then

$$\frac{\langle \psi \mid \mathcal{H} \mid \psi \rangle}{\langle \psi \mid \psi \rangle} \geq \frac{\langle \Psi \mid \mathcal{H} \mid \Psi \rangle}{\langle \Psi \mid \Psi \rangle}, \tag{3.2.1}$$

with strict inequality unless ψ is proportional to Ψ. Therefore, if one tries various trial wave functions ψ in (3.2.1), the one that minimizes the left-hand side is the best approximation to the real ground state, Ψ, and the resulting value of the left-hand side best approximates the real value for the ground-state energy which is the right-hand side of (3.2.1). Thus, all that one has to do is to be able to evaluate the left-hand side of (3.2.1) for an arbitrary trial wave function, and then look for one that minimizes it. In this way, at least in principle, one can come arbitrarily close to the ground-state energy and the ground-state wave function. All the different methods to be described here are merely translations of this principle into practice. One can use arbitrarily large classes of trial wave functions, depending on the desired accuracy, and the amount of work that one is willing to do. The larger the class, the better the answer, but the more difficult the work.

Every trial wave function for a multi-electron system has to obey the Pauli exclusion principle: the wave function has to change sign upon interchanging a pair of electrons, i.e., it has to be antisymmetric. One of the simplest (yet powerful) forms for a many-electron function is a product of single-electron functions:

$$\psi(1,2,\ldots,N) = \psi_1(1)\cdot\psi_2(2)\cdot\ldots\cdot\psi_N(N). \tag{3.2.2}$$

The indices $1,2,\ldots,N$ represent the coordinates (both spatial and spin) of each one of the N electrons. The function (3.2.2) is, of course, not antisymmetric with respect to electron interchange, but can be antisymmetrized. This operation can be described as follows: if from (3.2.2) one subtracts a duplicate but with electrons 1 and 2 interchanged, the resulting function is antisymmetric with respect to the interchange of electrons 1 and 2. One can repeat this process for all the other pairs of electrons, and the resulting wave function is known as a Slater determinant.

$$\psi(1,2,\ldots,N) = \begin{vmatrix} \psi_1(1) & \psi_1(2) & \ldots & \psi_1(N) \\ \psi_2(1) & \psi_2(2) & \ldots & \psi_2(N) \\ \vdots & \vdots & & \vdots \\ \psi_N(1) & \psi_N(2) & \ldots & \psi_N(N) \end{vmatrix}. \tag{3.2.3}$$

Despite their simplicity, Slater determinants are very powerful for describing antisymmetric wave functions, and, in fact, smooth antisymmetric wave functions can be approximated by linear combinations of such determinants to arbitrary precision.

A single Slater determinant may still have too complicated a form, since each of the individual one-electron functions is a function of both spatial and spin coordinates. The Hartree-Fock (HF) trial wave function is such that the electrons pair up. Each pair shares the same spatial part (orbital), with one electron having spin up, the other having spin down. This HF formalism is very convenient, since it replaces the equations for wave functions by equations for

orbitals. Because the Hamiltonian is assumed to be spin independent, the spin enters the formalism only via the Pauli exclusion principle, which is automatically satisfied by the determinant form of the wave function. Schrödinger's equation for the wave function translates into a similar equation for the orbitals, with a slightly different form for the Hamiltonian. The electrostatic interaction between two orbitals splits into two terms, the coulombic (J), and the exchange (K). Expressions for the Hartree-Fock Hamiltonian can be found in many references (see, for example, Goddard and McGill,[11] and references therein) and will not be given here. The HF formalism now requires finding the best shape for the individual orbitals to minimize the energy functional, which is the left-hand side of (3.2.1).

The HF is probably the most widely used ab-initio technique today. It is quite accurate for structure calculations, with errors of about 0.01-0.02Å for bond lengthes, and 1°-3° for bond angles.[11] Its main disadvantage is a poor description of the dissociation of chemical bonds. For example, in the ground state of H_2, both electrons share the same orbital. This means that the probability that both electrons are in the vicinity of the same atom is the same as the probability that each electron is in the vicinity of a different atom. In an H_2 molecule the nuclei are very close to each other; therefore, the vicinity of one is almost the same as the vicinity of the other, and this picture is quite accurate. However, when this molecule dissociates and the nuclei are far apart, it is much more energetically favorable to form two neutral H atoms than one H^+ and one H^- atom. The Hartree-Fock formalism predicts equal probabilities for the two, regardless of interatomic separation. The dissociation energies predicted by the HF method, therefore, are much higher than the experimental values. One should expect a similar trend (though weaker) for elastic constants: the spring constants associated with bond stretching, calculated using the HF method, should be higher than those measured experimentally.

Another important disadvantage of the Hartree-Fock method is heuristic in nature. The molecular orbitals are difficult to interpret physically. Our intuitive picture of bonding relates to pairs of atoms, while each molecular orbital extends throughout the entire molecule.

The General Valence Bond method[12] (GVB) overcomes the main disadvantages of the HF method. Every pair of electrons corresponding to a bond is allowed to relax further, such that each electron in the pair has its own orbital, but the two are finally singlet paired. Put more quantitatively, if, in the HF formalism, both electrons had the same orbital ϕ_1, now we allow one of them to be in $\chi_1 = \phi_1 - \phi_2$, and the other one to be in $\chi_2 = \phi_1 + \phi_2$. The final singlet pairing of the two electrons refers to the combination $\chi_1(1)\chi_2(2)+\chi_2(1)\chi_1(2)$. The GVB method now tries to optimize the shape of $\phi_1, \phi_2, \ldots, \phi_N$, so as to minimize the energy functional (3.2.1). Since the trial functions are taken from a larger set than in the HF case, the GVB method is guaranteed to have lower ground-state energies, which means more accurate solutions. Moreover, the solutions of the GVB formalism describe localized bonds rather than diffuse molecular orbitals.

Further improvements upon the results of the GVB method can be obtained by using Configuration Interaction (CI). This technique involves picking trial functions made of several determinants of the form (3.2.3) rather than one. Various levels of improvement are possible. In the present calculations for Si_5H_{12}, two levels of CIs are used. One, called restricted-CI (R-CI), allows each of the electron pairs in the Si-Si bonds to be triplet-paired as well. A higher level of approximation, called GVB-CI, allows the eight electrons in the four Si-Si bonds to have any possible spin configuration, up to $S = 4$.

All the methods described above assume a certain form for the trial wave functions as a function of spatial orbitals, and then try to find the best shape for

the orbitals. The quality of the shape is measured by the left-hand side of (3.2.1). In practice, one does not optimize the shape of the orbitals among all the possibilities. Instead one choses the best orbital expressible as a linear combination of a given set of **basis functions**:

$$\phi_i = \sum_{j=1}^{m} c_{ij}\chi_j \qquad i = 1, \ldots, n.$$

The functions $\chi_1, \ldots, \chi_m$ are called a **basis set.** Such a simple form has the advantage that the optimization procedure becomes a linear eigenvalue problem for the coefficients c_{ij}. Obviously, with enough basis functions, the shape of the orbitals $\phi_1, \ldots, \phi_n$ can be made arbitrarily close to what they should be. One pays a heavy price, however, for using too many basis functions: the time of the calculation, as well as the storage requirements, increase as the fourth power of the number of basis functions used; therefore, one has to choose the right basis set that includes not too many basis functions. Over the years, theoretical chemists have developed some very economical basis sets. The one used in this work to describe the silicon atoms, was the so called "double-ς".[13] It is made of atomic-like orbitals having s- and p- type angular dependence. Each such orbital is expressed as a sum of several gaussians. This representation in terms of gaussians is done in order to simplify the calculation, and has no physical significance beyond that.

The clusters used in the present calculations consist of silicon and hydrogen atoms. The only role that these hydrogen atoms play is to bond the extra electrons on a silicon atom which is not bonded to other silicon atoms. Therefore we may change the shape of the hydrogen atomic orbitals, in order to satisfy some extra requirements. As it turns out, if one inflates the hydrogenic s-function by a factor of 3.397 (if one takes $\psi(0.2944r)$ instead of $\psi(r)$) then the resulting inflated hydrogen has the same electronegativity as a silicon atom. Thus, the central atom in a Si_5H_{12}

is electrically neutral. Such inflated hydrogens (called "siligens") were introduced by Redondo *et al.*[14]

Another important detail of the calculation is the concept of effective potential. If one takes into account all the electrons of the atoms, the total energy may be in the thousands, or even tens of thousands eV/atom. On the other hand, chemical bond energies are never more than a few eV/bond. Therefore, if one takes into account all the electrons, one has to calculate many electrons that do not participate in bonding, and extract chemical energies (of the order of 1 eV/atom) by subtracting two numbers that may be three or four orders of magnitude higher. On the other hand, chemists have realized, for a long time, that the core electrons are not important for chemical bonding. The way to incorporate this fact into the calculations is by using "pseudo-atoms" that obey Schrödinger's equation with a "pseudo-potential." These pseudo-atoms differ from real atoms in that they only have valence electrons with wave functions that, outside the core region, behave like those of the valence electrons of the real atoms. This pseudo-potential is, in general, not a function of position alone, and involves some angular-momentum projection operators. The pseudo-potential used for the silicons in our calculations was introduced by Redondo *et al.*[13]

Finally, in calculating vibration frequencies in the clusters and solids, the Born-Oppenheimer approximation was assumed. According to this approximation, the nuclei are infinitely heavier then the electrons, and hence the response of the electronic system to motion of the nuclei is instantaneous. Therefore, one can calculate vibrations in the molecules by freezing the position of the nuclei at some various geometries, letting the electrons find their best orbitals, and looking at the total ground-state energy as a function of geometry. The elastic properties of the cluster are then obtained from the curvatures of the ground-state energy at the

equilibrium point.

3.3. Results.

The results of the calculations are presented here. These results can be classified into two categories: the ab-initio quantum-mechanical calculations of silicon clusters and the interpretations of these calculations in terms of bulk silicon using various models. The results of the ab-initio calculations are independent of the models that were later used to interpret them. However, since some cluster calculations are more relevant than others to some models, we chose to present only a few cluster calculations, and then treat those models to which these clusters are relevant, and so on. We start by describing the first fifteen modes and the spring constants associated with them, we then derive the parameters for the first three models, namely, the simple bond-bending-and-stretching model, the Singh-Dayal model and the valence-force-field model, described in the introduction. We then proceed to calculate eight additional modes, and finally we derive the parameters of Vasil'ev's model.

The first fifteen modes of Si_5H_{12}

The first three models to be treated involve only bond lengths and angles between bonds. In order to calculate their parameters from first principles, fifteen deformation modes of Si_5H_{12} (actually $Si(SiH_3)_4$) were calculated. This cluster is seen in Fig. 3.1. The twelve hydrogen atoms in the periphery of this cluster serve merely to saturate the dangling silicon bonds. In this work the emphasis is on $Si - Si$ rather than $Si - H$ bonds, and, consequently, the hydrogen basis functions were inflated in the manner described in the previous section – to match the electronegativity of silicon. In this way, the central atom is electrically neutral,

and the $Si - Si$ bonds are believed to be more bulk-like. Various deformations of the original Si_5H_{12} cluster were considered. These deformations were organized in "modes," each being a continuous, single-parameter deformation. In the first fifteen modes to be described next, every SiH_3 group was moved as a rigid group so that only bond lengths and angles around the central silicon atom were changed.

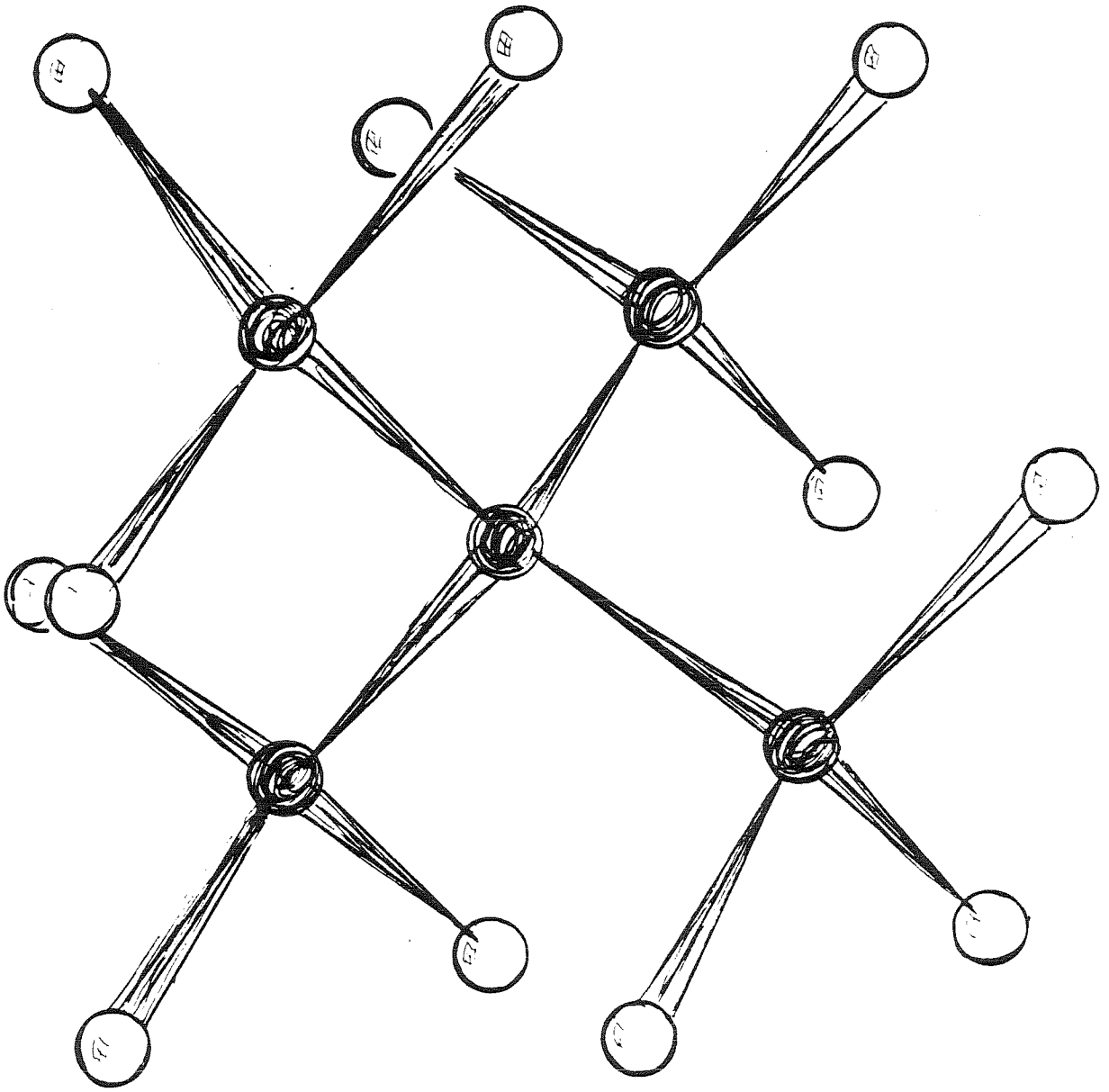

Fig. 3.1. The Si_5H_{12} cluster used in this chapter. All the modes described in this chapter are various deformations of this cluster. The dark spheres represent silicon atoms; the white spheres represent hydrogen atoms, whose basis functions were inflated by a factor of 3.397.

Each mode is a deformation of the original cluster, where the coordinates of each atom are functions of a single variable, t. In the first fifteen modes, the hydrogen atoms were moved in unison with their silicon atoms. Therefore, to describe the mode, it suffices to list the changes in bond lengths and angles, as functions of t, around the central silicon atom only. This is done in Table 3.1. It should be noted that one cannot change the six angles around the central silicon atom at will, since there is one constraint connecting them. This constraint can be written as

$$F(\theta_{12}, \theta_{13}, \theta_{14}, \theta_{23}, \theta_{24}, \theta_{34}) = 0,$$

where $F(\theta_{12}, \theta_{13}, \theta_{14}, \theta_{23}, \theta_{24}, \theta_{34})$ is a rather complicated function. If the strain is very small (which is usually assumed in the harmonic approximation) then all the angles are almost tetrahedral, that is, $\theta_{ij} = \theta_0 + \Delta\theta_{ij}$, where θ_0 is the tetrahedral angle (109.47°), and $\Delta\theta_{ij}$ is very small. In that case the relation between the six angles can be approximated by

$$\Delta\theta_{12} + \Delta\theta_{13} + \Delta\theta_{14} + \Delta\theta_{23} + \Delta\theta_{24} + \Delta\theta_{34} = 0 + O(\Delta\theta_{ij}^2).$$

In Table 3.1, some of the angles $\Delta\theta_{ij}(t)$ are given exactly, and for others only the linear term in t is given. In the harmonic approximation the higher order term can be neglected.

The first three modes involve changes in bond lengths only. The first mode is the symmetric breathing mode, in which all four $Si-Si$ bonds change their length by the same amount, and the angles between them remain tetrahedral. Mode 2 is an asymmetric breathing mode, similar to the first mode, but only two bonds change, and the other two remain at 2.3517Å, which is the experimental equilibrium bond length. Mode 3 is an antisymmetric breathing mode, in which two bonds increase and two bond decrease their length by the same amount. The next four modes

involve changes in angles only. The bond lengths remain 2.3517Å. Mode 4 is a twist mode, in which bonds 1 and 2 rotate clockwise, and bonds 3 and 4 counterclockwise, around the axis bisecting the angles between them. Mode 5 is a symmetric scission mode, in which bonds 1 and 2 open or close the angle between them, and bonds 3 and 4 do likewise by the same amount. Mode 6 is an asymmetric scission mode, in which bonds 1 and 2 change the angle between them, but bonds 3 and 4 do not. Mode 7 is an antisymmetric scission mode. Bonds 1 and 2 open, and bonds 3 and 4 close the angle between them by the same amount. The next eight modes are mixed modes in which both the bond lengths and the angles change. Modes 8 and 9 are both combinations of modes 3 and 7, that is, antisymmetric breathing and scission. In mode 8, the length of one pair of bonds increase simultaneously with the angle between them, and in mode 9 the bond length decrease with increasing angle. Modes 10 and 11 are similar to modes 8 and 9, but with a different bond bending to bond stretching ratio. This ratio for modes 10 and 11 corresponds to that of the optical phonon mode at the Γ point. Modes 12 and 13 are symmetric breathing plus or minus symmetric scission. The ratio of bond-bending to bond-stretching for these two modes corresponds to that of the longitudinal phonon mode at the X point. Modes 14 and 15 are antisymmetric breathing plus or minus antisymmetric scission modes, like modes 8 and 9, and modes 10 and 11. The ratio of bond stretching to bond bending corresponds to that of the TO phonon at the X point.

The total energy as a function of the deformation parameter t was calculated for nine geometries in each mode. These geometries coresponded to different values of t: -0.2, -0.1, -0.05, -0.02, 0.0, 0.02, 0.05, 0.1 and 0.2. For each such geometry, the total energy was calculated using four different methods of calculation: HF, GVB, R-CI and GVB-CI. These methods were explained in the previous section. After the calculation, a polynomial of degree six was fitted to the energies to obtain

the minimum and the curvature at the minimum. This curvature gives the spring constant k_i for the i-th mode. The values of these spring constants are given in Table 3.2 for each of the fifteen modes and each of the four methods of calculation.

TABLE 3.1. The geometries of the fifteen Si_5H_{12} modes. Each mode is a function of a single parameter t. The deviation from equilibrium length (in angstroms) and angles (in radians) are given in this table. The parameter t is assumed to be small, and angles that appear with a $\approx$ sign are actually more complicated, with the entry listed in this table being only the linear term. r_0 appearing in this table is the equilibrium Si-Si distance, 2.3517Å.

Mode	Δr_1	Δr_2	Δr_3	Δr_4	$\Delta\theta_{12}$	$\Delta\theta_{13}$	$\Delta\theta_{14}$	$\Delta\theta_{23}$	$\Delta\theta_{24}$	$\Delta\theta_{34}$
1	t	t	t	t	0	0	0	0	0	0
2	t	t	0	0	0	0	0	0	0	0
3	t	t	$-t$	$-t$	0	0	0	0	0	0
4	0	0	0	0	0	$\approx \frac{t}{\sqrt{2}}$	$\approx \frac{-t}{\sqrt{2}}$	$\approx \frac{-t}{\sqrt{2}}$	$\approx \frac{t}{\sqrt{2}}$	0
5	0	0	0	0	$2t$	$\approx -t$	$\approx -t$	$\approx -t$	$\approx -t$	$2t$
6	0	0	0	0	$2t$	$\approx \frac{-t}{2}$	$\approx \frac{-t}{2}$	$\approx \frac{-t}{2}$	$\approx \frac{-t}{2}$	0
7	0	0	0	0	$2t$	≈ 0	≈ 0	≈ 0	≈ 0	$-2t$
8	t	$-t$	$-t$	t	≈ 0	≈ 0	$2t$	$-2t$	≈ 0	≈ 0
9	t	$-t$	$-t$	t	≈ 0	≈ 0	$-2t$	$2t$	≈ 0	≈ 0
10	t	$-t$	$-t$	t	≈ 0	≈ 0	$\frac{t\sqrt{8}}{r_0}$	$\frac{-t\sqrt{8}}{r_0}$	≈ 0	≈ 0
11	t	$-t$	$-t$	t	≈ 0	≈ 0	$\frac{-t\sqrt{8}}{r_0}$	$\frac{t\sqrt{8}}{r_0}$	≈ 0	≈ 0
12	t	t	t	t	$\frac{-t\sqrt{2}}{r_0}$	$\frac{-t\sqrt{2}}{r_0}$	$\frac{t\sqrt{8}}{r_0}$	$\frac{t\sqrt{8}}{r_0}$	$\frac{-t\sqrt{2}}{r_0}$	$\frac{-t\sqrt{2}}{r_0}$
13	t	t	t	t	$\frac{t\sqrt{2}}{r_0}$	$\frac{t\sqrt{2}}{r_0}$	$\frac{-t\sqrt{8}}{r_0}$	$\frac{-t\sqrt{8}}{r_0}$	$\frac{t\sqrt{2}}{r_0}$	$\frac{t\sqrt{2}}{r_0}$
14	t	$-t$	$-t$	t	≈ 0	≈ 0	$\frac{t\sqrt{2}}{2r_0}$	$\frac{-t\sqrt{2}}{2r_0}$	≈ 0	≈ 0
15	t	$-t$	$-t$	t	≈ 0	≈ 0	$\frac{-t\sqrt{2}}{2r_0}$	$\frac{t\sqrt{2}}{2r_0}$	≈ 0	≈ 0

TABLE 3.2. Calculated spring constants (k in the formula $\Delta E_{\text{elastic}} = \frac{1}{2}k \cdot t^2$) in units of eV per square t. Here t is the parameter describing each mode in Table 3.1. The spring constants are calculated using four methods of calculation: HF, GVB, R-CI and GVB-CI, that were described in section 3.2.

Mode	HF	GVB	R-CI	GVB-CI
1	48.33	44.06	43.97	42.69
2	23.18	20.98	21.06	20.74
3	42.34	41.39	42.04	42.45
4	2.69	2.50	2.45	2.31
5	16.11	15.10	14.78	13.93
6	7.37	6.97	6.69	6.45
7	13.31	12.90	12.22	11.84
8	69.36	67.70	66.80	66.48
9	46.64	45.69	45.93	46.37
10	56.55	55.27	55.65	55.67
11	42.15	41.25	41.88	42.37
12	57.80	51.32	50.83	48.41
13	56.11	51.40	51.08	49.17
14	46.61	45.69	46.37	46.72
15	43.97	43.13	43.86	44.38

In Table 3.2, one can see a tendency toward spring constant softening with improvement of the method of calculation. This tendency is reasonable, since a better method involves a larger set of trial functions (cf. previous section). This means more ways for the electrons of the deformed cluster to relax. This tendency seems not to hold for modes involving antisymmetric bond stretching (modes 3, 8, 9, 10, 11, 14 and 15). The reason for that has to do with the zero point of the antisymmetric mode. This point was chosen to be at the experimental equilibrium bond length which equals 2.3517Å. The theoretical values may be predicted by taking the energy minimum of mode 1. The calculated deviations of the bond length as predicted by the HF, GVB, R-CI and GVB-CI are -0.010, +0.010, +0.012 and +0.017Å, respectively, from the experimental value. That means that the center of antisymmetry for modes 3, 8-11, 14 and 15 is in fact not exactly at the calculated minimum energy, with the GVB-CI being the furthest.

One can also observe quantitatively that most of the improvement is achieved between the HF and GVB methods. The GVB and the R-CI are almost the same, and another slight improvement is attained by using GVB-CI. The total improvement is of the order of 15% or less.

The simple bond-bending-and-stretching model

The simple bond-bending-and-stretching model was presented in the introduction. It has two parameters, or spring constants, namely, k_r and k_θ. k_r is the restoring force constant for changes in bond length, while $r_0^2 \cdot k_\theta$ is the restoring force constant for changes in angle between a pair of adjacent bonds. As was mentioned in the introduction, this model is the simplest possible one that can describe the diamond structure with any precision. Now one can use the results of Table 3.2 to calculate the spring constants of the simple bond-bending-and-stretching model. The spring constant of each mode can be expressed in terms of the two parameters of the model, k_r and k_θ. This means that these two parameters have to satisfy fifteen equations. A least-squares method was used to obtain the best possible fit for this overdetermined system. The equations relating the cluster spring constants $k_1, \ldots, k_{15}$ to the model spring constants k_r and k_θ are given in Table 3.3. The best fitted values of k_r and k_θ are also diplayed in this table, together with the deviations of the fitted values from the target values. Consider, for example, the second column from the left (the "HF" column). The best fit for the Hartree-Fock calculations was $k_r = 11.36$ eV/$\mathring{A}^2$ and $k_\theta = 0.302$ eV/$\mathring{A}^2$. Using these values for k_r and k_θ, the model would predict a certain value for the spring constant of each of the fifteen modes. For example, mode no.1 should have, according to this model, a spring constant which is four times k_r, or 45.44 eV/$\mathring{A}^2$. This value predicted by the model is smaller by 2.89 eV/$\mathring{A}^2$ than the target value of 48.33 eV/$\mathring{A}^2$, calculated quantum mechanically using the Hartree-Fock method for this particular mode. This entry is listed, therefore, as 48.33-2.89 in Table 3.3.

Table 3.3 Fitting the two parameters of the bond bending and stretching model to the Si_5H_{12} cluster calculations. The values of k_r and k_θ in the second and third rows are the best least-squares fit to the data points. They are expressed in units of eV per square angstrom. The expressions relating the spring constants of the various modes to k_r and k_θ are given in the first column. The values of these expressions for the fitted values of k_r and k_θ are given in the second to fifth column. They are expressed as the true cluster value plus a deviation.

	HF	GVB	R-CI	GVB-CI
k_r	11.36	10.78	10.88	10.84
k_θ	0.302	0.305	0.296	0.288
$k_1 = 4k_r$	48.33-2.89	44.06-0.94	43.97-0.43	42.69+0.70
$k_2 = 2k_r$	23.18-0.46	20.98+0.58	21.06+0.71	20.74+0.96
$k_3 = 4k_r$	42.34+3.09	41.39+1.73	42.04+1.49	42.45+0.94
$k_4 = 2k_\theta r_0^2$	2.69+0.64	2.50+0.88	2.45+0.82	2.31+0.87
$k_5 = 12k_\theta r_0^2$	16.11+3.90	15.10+5.16	14.78+4.87	13.93+5.16
$k_6 = 5k_\theta r_0^2$	7.37+0.97	6.97+1.47	6.69+1.50	6.45+1.50
$k_7 = 8k_\theta r_0^2$	13.31+0.03	12.90+0.61	12.22+0.88	11.84+0.89
$k_8 = 4k_r + 8k_\theta r_0^2$	69.36-10.58	67.70-11.07	66.80-10.16	66.48-10.35
$k_9 = 4k_r + 8k_\theta r_0^2$	46.64+12.14	45.69+10.93	45.93+10.70	46.37+9.75
$k_{10} = 4k_r + 16k_\theta$	56.55-6.29	55.27-7.27	55.65-7.38	55.67-7.67
$k_{11} = 4k_r + 16k_\theta$	42.15+8.11	41.25+6.75	41.88+6.39	42.37+5.63
$k_{12} = 4k_r + 24k_\theta$	57.80-5.12	51.32-0.88	50.83-0.19	48.41+1.89
$k_{13} = 4k_r + 24k_\theta$	56.11-3.44	51.40-0.96	51.08-0.44	49.17+1.13
$k_{14} = 4k_r + k_\theta$	46.61-0.87	45.69-2.27	46.37-2.54	46.72-3.03
$k_{15} = 4k_r + k_\theta$	43.97+1.77	43.13+0.29	43.86-0.03	44.38-0.70

One can also see graphically the various spring constants and the predictions of this model in Fig. 3.2. The leftmost column in Table 3.3 relates the spring constants of the fifteen modes to the two parameters, k_r and k_θ, of the model. Thus, each entry in this column can be viewed as a linear equation in the two variables, k_r and k_θ. This linear equation can be plotted as a straight line in the $k_r - k_\theta$ plane, as was done in Fig. 3.3. The values of $k_1, \ldots, k_{15}$ were taken from the GVB-CI column in Table 3.2. If this two-parameter model were exact, then all these fifteen lines would intersect in a single point, which would correspond to the exact values of k_r and k_θ. This is clearly not the case, as can be seen in the figure. Instead, one can find the values of k_r and k_θ which best fits these lines. These values are also marked in Fig. 3.3, as well as a rectangle corresponding to a $\pm 30\%$ deviation from these values. One can see that all the fifteen lines corresponding to $k_1, \ldots, k_{15}$ pass through this rectangle.

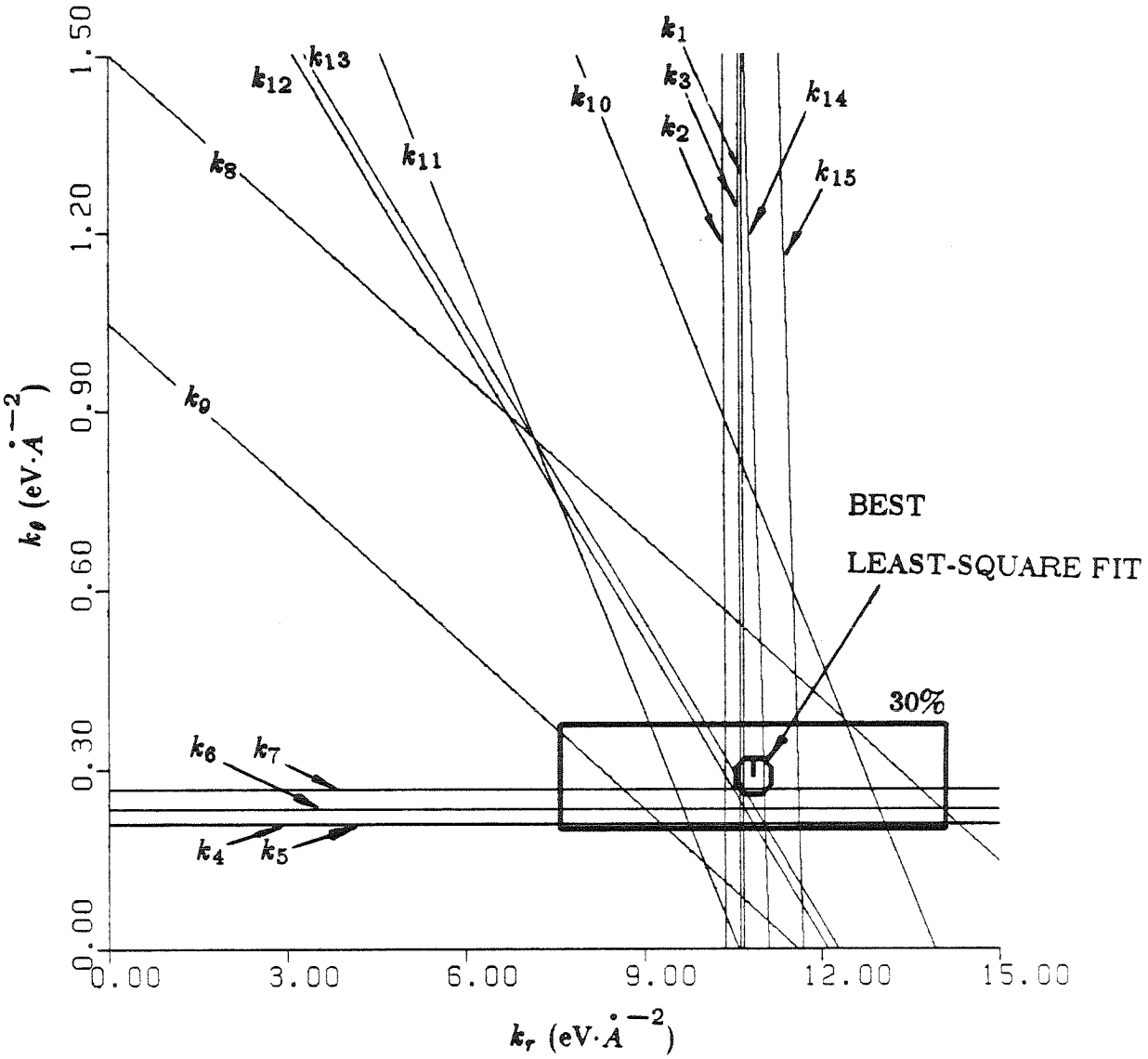

Fig. 3.2. Fitting the parameters of the simple bond-bending-and-stretching model to cluster calculations. Each one of the fifteen lines denoted $k_1, \ldots, k_{15}$ represents one mode. The spring constants of each mode was calculated using the GVB-CI method, and are plotted here as functions of the parameters of the model, k_r and k_θ. The values of these parameters that best fit the fifteen equations are also plotted here, together with a rectangle denoting margins of $\pm 30\%$ of these values.

Comparing the experimental phonon band structure withe the predictions of the simple bond-bending-and-stretching model

We have seen that the simple bond-bending-and-stretching model is useful (as the simplest possible realistic model) but not very accurate. Leeway of $\pm 30\%$ for both parameters of the model was necessary to account for the spring constants of the fifteen modes calculated from first principles. We shall demonstrate now that approximately the same leeway is necessary to account for experimental phonon frequencies, using this model.

Let us now compare the experimental phonon band structure with that predicted by the cluster calculations using this model. Expressions for the dynamical matrices and their eigenvalues, in terms of the parameters of the model, are given in Appendix A-3.2 for the Γ, X, L, $\Delta(q = 1/2)$ and the $\Sigma(q = 1/2)$ points (altogether, eighteen special points on the phonon dispersion curves). Every such eigenvalue is described in this model as a function of k_r and k_θ. Using the experimental frequencies[1,2] one can plot these eigenvalues as curves on the $k_r - k_\theta$ plane, and observe the fit graphically. This was done in Fig. 3.3. There are eighteen curves in this figure, each corresponding to one point on the phonon band structure of silicon. The functional relationship for each point is given in Appendix A-3.2. The solid-line curves represent acoustical phonons, while the dashed curves represent optical phonons. The labeling of each curve in Fig. 3.3 is a standard group-theoretic labeling of phonon modes.[15] Whenever a phonon mode could be labeled as either one of TA, LA, LO, or TO, this notation also appears in parentheses in this figure. For clarity, all the phonon band structure notation used in this figure is also repeated in Fig. 3.4. The curves in Fig. 3.3 denoted by either Σ or Δ represent the special points half way between the Γ and X points. One can see that all these curves pass through the rectangle that

marks $\pm 30\%$ deviation from k_r and k_θ calculated from the clusters. This $\pm 30\%$ leeway was also necessary to accommodate internal inconsistencies in the model when applied to the cluster calculations (refer to Fig. 3.2). Therefore, one must conclude that the phonon band structure predicted by the cluster calculations is as good as any other band structure using the same model. The band structure itself can be seen in Fig. 3.4. The solid lines are the predictions of the model using the parameters obtained from cluster calculations. The triangles with error bars in them are the experimental results of Dolling,[1] and the circles are experimental results of Nilsson and Nelin.[2] The error bars in the work of Nilsson and Nelin are all smaller than the size of the circles. As one can see in Fig. 3.4, this model with its calculated parameters overestimates the frequencies of the optical branch, overestimates the frequencies of the TA branch near the zone edges, and underestimates them near the zone center. The LA branches are predicted accurately, and the slope of the TO branch also agrees quite well with experiment. In other words, the predictions of this model are not very accurate numerically, but the band structure has altogether the right shape. We shall see in our treatment of more complicated models that it is very difficult to improve significantly over this simple model.

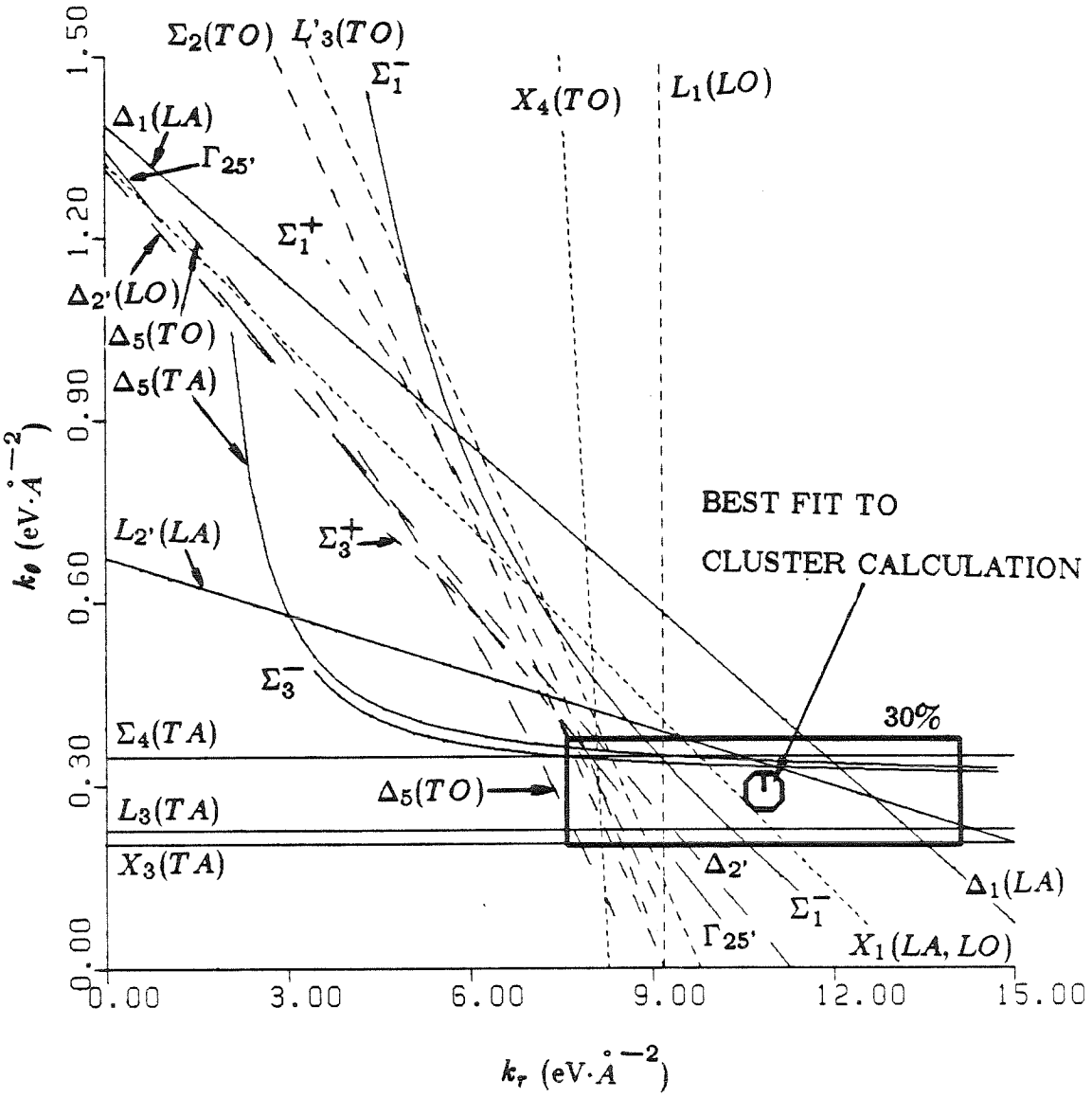

Fig. 3.3. Phonon modes in the simple bond-bending-and-stretching model. Each one of the eighteen curves corresponds to a special point in the phonon band structure and relates the experimental frequency to the two parameters of the model. The value of k_r and k_θ calculated from the clusters using an ab-initio method (GVB-CI) is also displayed here together with $\pm 30\%$ margins around it.

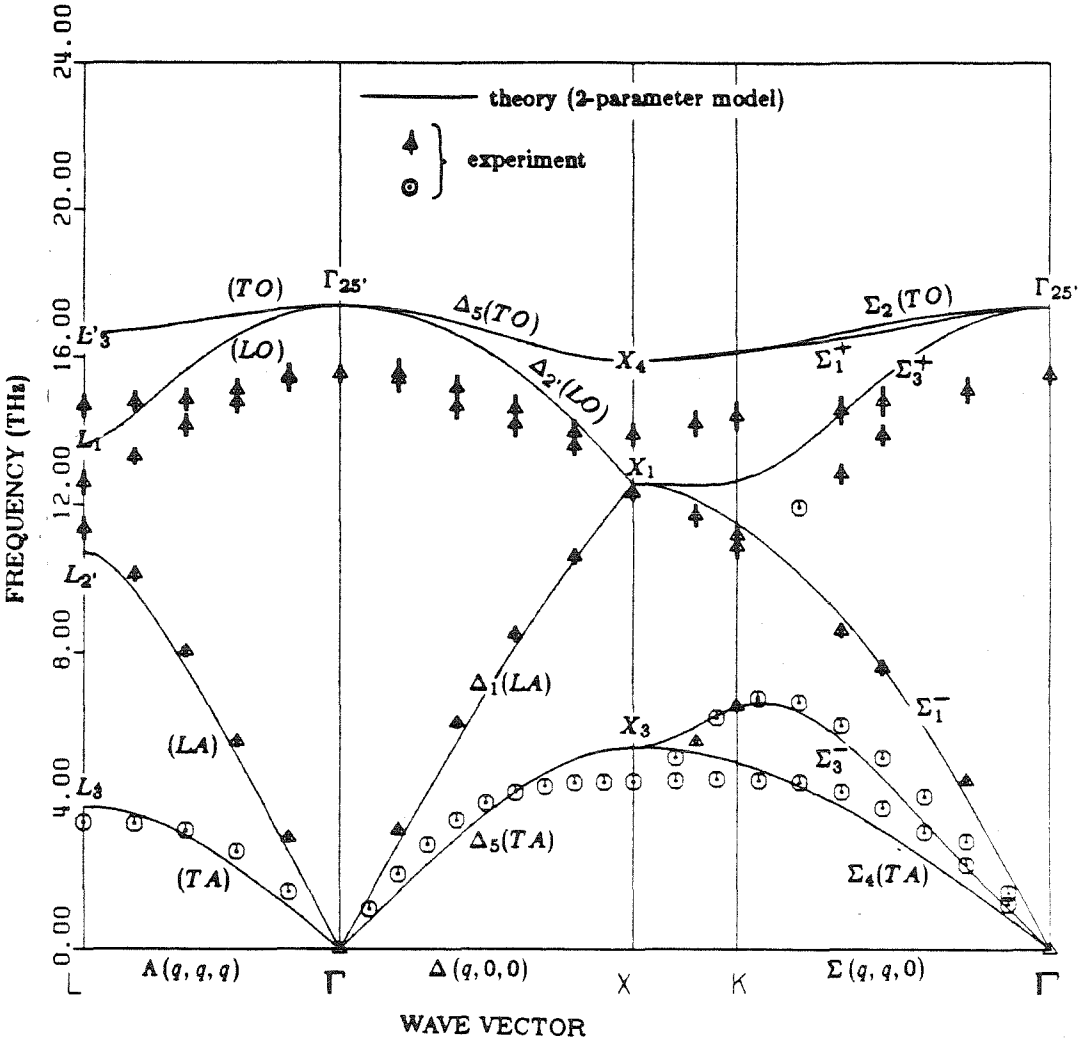

Fig. 3.4. The phonon band structure of silicon. The solid lines are theoretical values, predicted by the simple bond-bending-and-stretching model, whose parameters were calculated from first principles using a small cluster. The triangles and circles are experimental frequencies determined by neutron scattering.

Comparing experimental static-elastic properties with the predictions of the simple bond-bending-and-stretching model

The simple bond-bending-and-stretching model predicts the static elastic properties of bulk silicon even less accurately than it predicts phonon frequencies of special points in the band structure. We shall see in our treatment of more complicated models that it is very hard to improve this accuracy

Some of the experimental static elastic properties are shown as curves on the $k_r - k_\theta$ plane in Fig. 3.5. The quantities plotted are the three stiffness coefficients c_{11}, c_{12} and c_{44}, as well as the bulk modulus B and the Poisson ratio in the (100) direction, ϑ_p. These five quantities are not independent of each other, and in fact one can express any two of c_{11}, c_{12}, B and ϑ_p in terms of the other two (the expressions are given in Appendix A-3.1.). c_{44} on the other hand cannot be expressed in terms of c_{11} and c_{12}. One can see in Fig. 3.5 that the lines labeled c_{11}, c_{12} and c_{44} do not intersect in a point. This is due entirely to internal inconsistency of the model. Moreover, even if we allow some tolerance for the predictions of c_{11}, c_{12} and c_{44}, and obtain the parameters of this model that best fit these three elastic constants, the resulting k_θ will be 3-4 times higher than that predicted from cluster calculations. Since we have seen before that the cluster calculation parameters, plus or minus 30%, can reproduce the frequencies of many special points in the phonon band structure, we must conclude that this model is incapable of treating both static and dynamic elastic properties with the same set of parameters. Furthermore, we can trace most of the error to k_θ, as can be clearly seen in Fig. 3.5. We conclude, therefore, that a restoring force constant for angles is not a good physical quantity, in the sense that it does not stand in its own right even approximately. Depending on the positions of second and higher nearest neighbors, it can change by as much as a factor of two to four.

Further evidence for the peculiarity of bond bending can be found in the work of Musgrave and Pople.[5] They have used a similar model to calculate the static elastic properties of diamond. The parameters of the model were calculated from the natural frequencies of neopentane, obtained by infra-red spectroscopy. They found discrepancies similar to those found by the calculations described above. The bond stretching to bond bending spring constant ratio was found by Musgrave and Pople to be over twice as big in the molecule compared to that of the diamond. The k_r calculated from bulk modulus of diamond was almost exactly the same as the one calculated from the molecule. This supports our theory that k_θ, the restoring force for angle, does not have a well defined physical meaning.

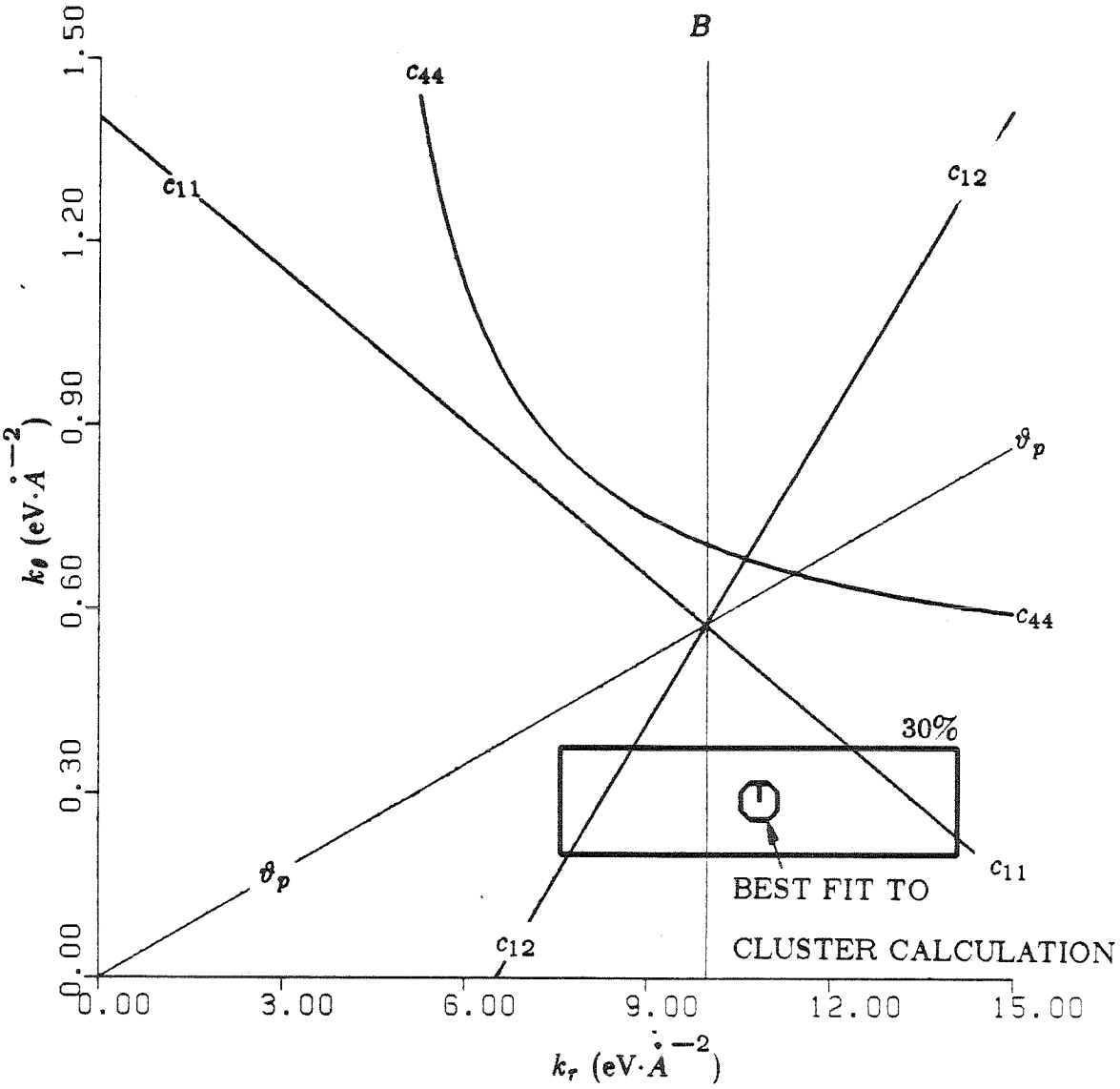

Fig. 3.5. Static elastic properties of silicon in the simple bond-bending-and-stretching model. Each curve relates one static elastic property to the parameters of the model. k_θ corresponding to the static elastic properties is several times higher than that corresponding to the cluster calculations or to the special points in the phonon band structure.

The three parameters model of Singh and Dayal

It was shown in our treatment of the previous model that the internal inconsistency of the simple bond-bending-and-stretching model, as applied to the small clusters, was quite large (on the order of $\pm 30\%$) on both parameters of the model. It was also demonstrated that within this error the model could account for the frequencies of all the eighteen special points of the phonon band structure that were examined. It is quite possible that a more elaborate model with smaller internal inconsistencies will also produce a better phonon band structure. This is, however, not **guaranteed** to be the case, and the answer will determine whether or not the more elaborate model is actually better.

By examining Fig. 3.2, one can see that the largest inconsistencies of that model are attained on two pairs of modes: modes 8 and 9, and modes 10 and 11. For each such pair, the model predicts the same spring constants for both modes, but the calculated spring constants differ by a lot. The difference between the two modes in each pair is that in one of them the angle between bonds increases with increasing bond length, while in the other it decreases. Therefore, most of the internal inconsistency will disappear if we introduce a third spring constant, which is the mixed second derivative of the elastic energy with respect to a bond length and an angle adjacent to this bond.

$$k_{r\theta} = \frac{\sqrt{2}}{r_0}\left(\frac{\partial^2 E}{\partial r_i \partial \theta_{ij}}\right).$$

This model was first used to fit the phonon band structure of silicon by Singh and Dayal.[4] A least-squares fit of the three parameters of this model to the fifteen spring constants of the Si_5H_{12} clusters is presented in Table 3.4.

Table 3.4 Fitting the three parameters of the Singh-Dayal model to the Si_5H_{12} cluster calculations. The values of k_r, $k_{r\theta}$ and k_θ in the second to fourth rows are the best least-squares fit to the data points. They are expressed in units of eV per square angstrom. The expressions relating the spring constants of the various modes to k_r, $k_{r\theta}$ and k_θ are given in the first column. The part of these expressions that depends on k_r and k_θ is identical to the one appearing in Table 3.3, and is denoted here by k_i'. The part that depends on $k_{r\theta}$ is given explicitly. The values of these expressions for the fitted values of k_r and k_θ are given in the second to fifth column. They are expressed as the true cluster value plus a deviation.

	HF	GVB	R-CI	GVB-CI
k_r	11.39	10.72	10.81	10.74
k_θ	0.309	0.303	0.292	0.280
$k_{r\theta}$	0.398	0.386	0.376	0.359
$k_1 = k_1$'	48.33-2.79	44.06-1.16	43.97-0.72	42.69+0.28
$k_2 = k_2$'	23.18-0.41	20.98+0.47	21.06+0.56	20.74+0.74
$k_3 = k_3$'	42.34+3.20	41.39+1.50	42.04+1.20	42.45+0.52
$k_4 = k_4$'	2.69+0.73	2.50+0.85	2.45+0.78	2.31+0.78
$k_5 = k_5$'	16.11+4.39	15.10+5.01	14.78+4.63	13.93+4.62
$k_6 = k_6$'	7.37+1.17	6.97+1.40	6.69+1.39	6.45+1.28
$k_7 = k_7$'	13.31+0.35	12.90+0.50	12.22+0.72	11.84+0.53
$k_8 = k_8$' $+ 8\sqrt{2}r_0k_{r\theta}$	69.36+0.43	67.70-1.12	66.80-0.60	66.48-1.58
$k_9 = k_9$' $- 8\sqrt{2}r_0k_{r\theta}$	46.64+1.97	45.69+0.33	45.93+0.25	46.37-0.58
$k_{10} = k_{10}$' $+ 16k_{r\theta}$	56.55+0.30	55.27-1.34	55.65-1.70	55.67-2.48
$k_{11} = k_{11}$' $- 16k_{r\theta}$	42.15+1.96	41.25+0.31	41.88+0.03	42.37-0.67
$k_{12} = k_{12}$'	57.80-4.85	51.32-1.15	50.83-0.56	48.41+1.26
$k_{13} = k_{13}$'	56.11-3.16	51.40-1.23	51.08-0.81	49.17+0.51
$k_{14} = k_{14}$' $+ 4k_{r\theta}$	46.61+0.83	45.69-0.95	46.37-1.32	46.72-2.03
$k_{15} = k_{15}$' $- 4k_{r\theta}$	43.97+0.29	43.13-1.48	43.86-1.82	44.38-2.56

The quality of the fit can be seen graphically in Fig. 3.6, which is similar to Fig. 3.2. Since there are three parameters to fit, each one of the expressions for $k_1, \ldots, k_{15}$ should be represented by a plane in the $k_r - k_\theta - k_{r\theta}$ space. Fig. 3.2 is a cut of this space at $k_{r\theta} = 0$, while Fig. 3.6 is a similar cut at $k_{r\theta} = 0.0132$, which is the best fit, as can be seen in Table 3.4. The target values of $k_1, \ldots, k_{15}$ are those obtained from GVB-CI calculations (the last column in Table 3.4). Using these values of k_r, k_θ and $k_{r\theta}$, the phonon band structure was calculated and is displayed in Fig. 3.7. This band structure is almost identical to the one obtained by Singh and Dayal[4] using the same model; however, while their parameters were fitted directly to the phonon band structure, ours were obtained from ab-initio calculations. In other words, the parameters obtained by ab-initio calculations are as good as one can have for that particular model.

It is interesting to compare the band structure obtained from the the three parameter model (Fig. 3.7) to the one obtained from the two parameter model (Fig. 3.4). Since the values of k_r and k_θ are almost identical in both cases, the only difference between the two band structures originates from the additional interaction introduced by $k_{r\theta}$. The major difference is seen in the optical branch. In the two-parameter model, the theoretical TO phonon branch is more or less parallel to the experimental data points, but it is higher by about 2 THz. In the three-parameter model the TO branch is almost flat, has the right value at the Γ point, but overshoots the experimental value at the X point by about 1.5 THz. All in all the three-parameter model obtains better values for the frequencies, but worse values for $\frac{\partial \omega}{\partial k}$ for the TO branch. The LA branch of the three-parameter model is slightly worse than that of the two-parameter model, and it bends too sharply near the zone edges. Near the zone center, the LA branches predicted by the two models are almost identical. The TA branch is practically identical for

both models. That also implies that the static elastic properties predicted by both models will be very similar

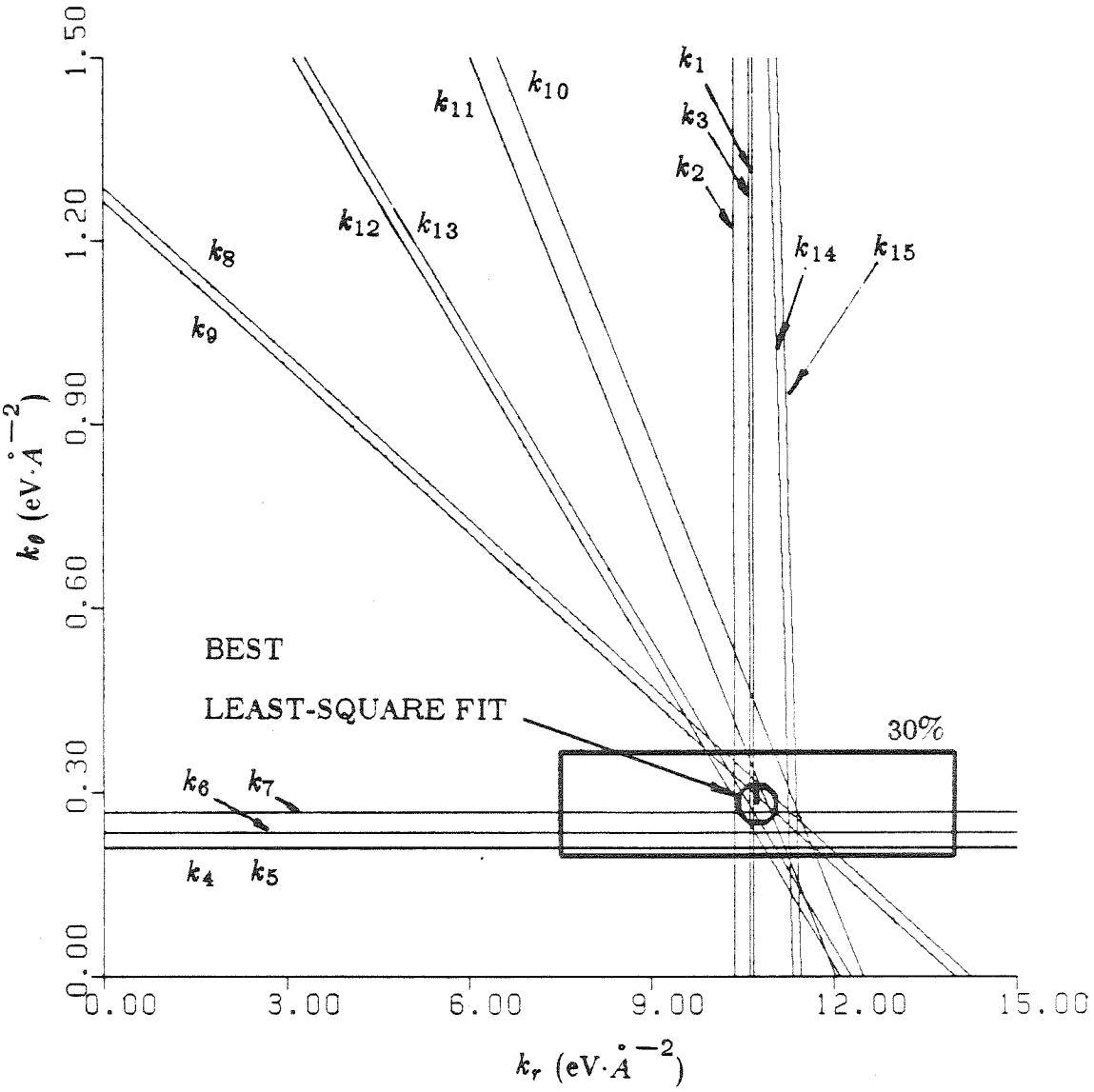

Fig. 3.6. Fitting the parameters of the Singh-Dayal model to the cluster calculations. By introducing a third parameter, $k_{r\theta}$, which equals 0.359 eV/Å^2 in this figure, a much better fit to the cluster calculations was obtained.

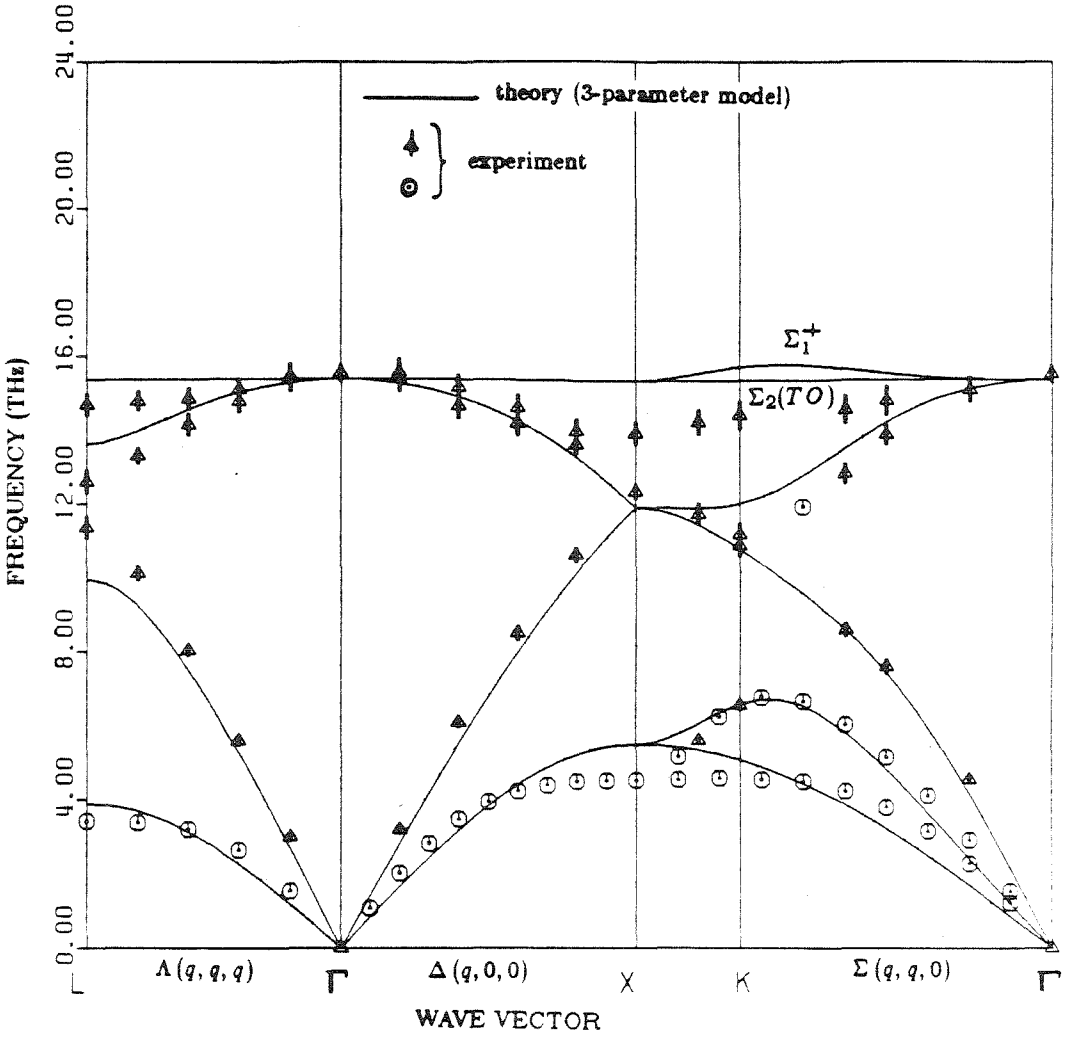

Fig. 3.7. Phonon band structure of silicon. The solid lines are theoretical predictions of the three parameter model of Singh and Dayal, with parameters calculated from cluster calculations. The triangles and circles are experimental frequencies.

The valence force field model.

The remaining inconsistencies of the Singh-Dayal model can be eliminated by further improving the model. The most general model taking into account only first nearest neighbors was formulated by Musgrave and Pople[5] and is described in detail in the Appendix A-3.1. This model has five adjustable parameters, which can be fitted to the fifteen spring constants $k_1, \ldots, k_{15}$ of the cluster. The results of this fitting are given in Table 3.5, and the expressions relating $k_1, \ldots, k_{15}$ to $k_r, \ldots, k_{\theta''}$ are given in Table 3.6. It is interesting to observe that the correction to the bond stretching due to adjacent bonds term (k_{rr}) and the correction to bond bending due to opposite angles (k_{θ}'') are both very small. That means that by adding these two parameters to the Singh-Dayal model, one does not obtain any significant improvement. It is also quite clear that this model, though much more complicated than the simple bond-bending-and-stretching model, still cannot account for the static elastic constants in any reasonable accuracy.

For the Valence Force Field model, it is no longer true that the parameters calculated from the cluster produce the best possible band structure. The addition of two extra parameters to the Singh - Dayal model increase significantly the ability to interpolate the band structure. The fit of the parameters to special points of the band structure, rather than to ab-initio cluster calculation, is presented in Table 3.7, and the resulting band structure is shown in Fig. 3.8. In view of the discussion above, we cannot assign any useful physical meaning to the parameters in Table 3.7, and they can be viewed only as adjustable parameters of some interpolation scheme. In other words, for any use other than phonon band structure, there is no reason to prefer them to the parameters of Table 3.5, obtained from ab-initio cluster calculations.

Table 3.5 Fitting the five parameters of the Valence Force Field model to the Si_5H_{12} cluster calculations. The values of k_r, k_{rr}, $k_{r\theta}$, k_θ and k_θ'' in the second to sixth rows are the best least-squares fit to the data points. They are expressed in units of eV per square angstrom. The expressions relating the spring constants of the various modes to k_r, k_{rr}, $k_{r\theta}$, k_θ and k_θ'' are given in Table 3.6. The values of these expressions for the fitted values of k_r and k_θ are given in the second to fifth column. They are expressed as the true cluster value plus a deviation.

	HF	GVB	R-CI	GVB-CI
k_r	11.27	10.68	10.79	10.77
k_{rr}	0.312	-0.002	-0.060	-0.181
$k_{r\theta}$	0.397	0.385	0.376	0.359
k_θ	0.308	0.306	0.295	0.283
k_θ''	-0.031	-0.031	-0.026	-0.031
k_1	48.33+0.48	44.06-1.37	43.97-1.52	42.69-1.77
k_2	23.18-0.02	20.98+0.37	21.06+0.40	20.74+0.44
k_3	42.34+1.47	41.39+1.34	42.04+1.37	42.45+1.37
k_4	2.69+0.37	2.50+0.54	2.45+0.53	2.31+0.47
k_5	16.11+2.28	15.10+3.15	14.78+3.09	13.93+2.76
k_6	7.37+0.99	6.97+1.32	6.69+1.32	6.45+1.19
k_7	13.31+1.73	12.90+2.01	12.22+1.97	11.84+2.04
k_8	69.36+0.05	67.70+0.20	66.80+0.80	66.48+0.76
k_9	46.64+1.64	45.69+1.69	45.93+1.67	46.37+1.79
k_{10}	56.55-0.94	55.27-0.97	55.65-1.09	55.67-1.09
k_{11}	42.15+0.75	41.25+0.70	41.88+0.64	42.37+0.73
k_{12}	57.80-2.33	51.32-2.03	50.83-1.92	48.41-1.45
k_{13}	56.11-0.65	51.40-2.11	51.08-2.17	49.17-2.21
k_{14}	46.61-0.87	45.69-1.08	46.37-1.14	46.72-1.15
k_{15}	43.97-1.40	43.13-1.60	43.86-1.63	44.38-1.68

Table 3.6 The spring constants of the fifteen modes expressed in terms of the five parameters of the Valence Force Field model of Musgrave and Pople.

k_1	$= 4k_r$	$+12k_{rr}$			
k_2	$= 2k_r$	$+2k_{rr}$			
k_3	$= 4k_r$	$-4k_{rr}$			
k_4	$=$			$2r_0^2k_\theta$	$+2r_0^2k_\theta''$
k_5	$=$			$12r_0^2k_\theta$	$+12r_0^2k_\theta''$
k_6	$=$			$5r_0^2k_\theta$	$+r_0^2k_\theta''$
k_7	$=$			$8r_0^2k_\theta$	$-8r_0^2k_\theta''$
k_8	$= 4k_r$	$-4k_{rr}$	$+8\sqrt{2}r_0k_{r\theta}$	$+8r_0^2k_\theta$	$-8r_0^2k_\theta''$
k_9	$= 4k_r$	$-4k_{rr}$	$-8\sqrt{2}r_0k_{r\theta}$	$+8r_0^2k_\theta$	$-8r_0^2k_\theta''$
k_{10}	$= 4k_r$	$-4k_{rr}$	$+16k_{r\theta}$	$+16k_\theta$	$-16k_\theta''$
k_{11}	$= 4k_r$	$-4k_{rr}$	$-16k_{r\theta}$	$+16k_\theta$	$-16k_\theta''$
k_{12}	$= 4k_r$	$+12k_{rr}$		$+24k_\theta$	$+24k_\theta''$
k_{13}	$= 4k_r$	$+12k_{rr}$		$+24k_\theta$	$+24k_\theta''$
k_{14}	$= 4k_r$	$-4k_{rr}$	$+4k_{r\theta}$	$+k_\theta$	$-k_\theta''$
k_{15}	$= 4k_r$	$-4k_{rr}$	$-4k_{r\theta}$	$+k_\theta$	$-k_\theta''$

Table 3.7 Fitting the valence force field model to the phonon band structure at the Γ, X, L and $\Sigma_{1/2}$ points. The values of k_r, k_{rr}, $k_{r\theta}$, k_θ and $k_\theta//$ in the second row are the best fits to the experimental data points. They are expressed in units of eV per square angstrom. The expressions relating the spring constants of the various modes to $k_r, \ldots, k_\theta//$ are linear combinations, whose coefficients are given in the second to sixth column. The values of these expressions for the fitted values of $k_r, \ldots, k_\theta$ are given in the seventh and eighth column. They are expressed as the target experimental phonon value in column seven, plus a deviation in column eight. The experimental phonon spring constants were calculated from the corresponding frequencies using $k = M\omega^2$ and M=28.09m_p.

	k_r	k_{rr}	$k_{r\theta}$	k_θ	$k_\theta//$	exp.	misfit
fitted value	9.19	0.52	-0.12	0.28	0.02		
$TO, LO(\Gamma)$	8/3	-16/3	-64/3	64/3	-64/3	27.92	-0.35
$TO(X)$	8/3	-16/3	-16/3	4/3	-4/3	22.4	-0.2
$LO, LA(X)$	4/3	8/3	-16/3	40/3	8/3	17.6	-0.1
$TA(X)$				12	-12	2.34	+0.81
$TO(L)$	8/3	-16/3	-40/3	34/3	-16/3	25.0	+0.0
$LO(L)$	2					18.4	+0.0
$LA(L)$	2/3	8/3	-16/3	64/3	-64/3	14.9	-1.7
$TA(L)$				6		1.36	+0.3
$TA(\Sigma_{1/2})$				6		2.07	-0.38
$TO(\Sigma_{1/2})$	8/3	-16/3	-40/3	34/3	-16/3	24.0	+1.0

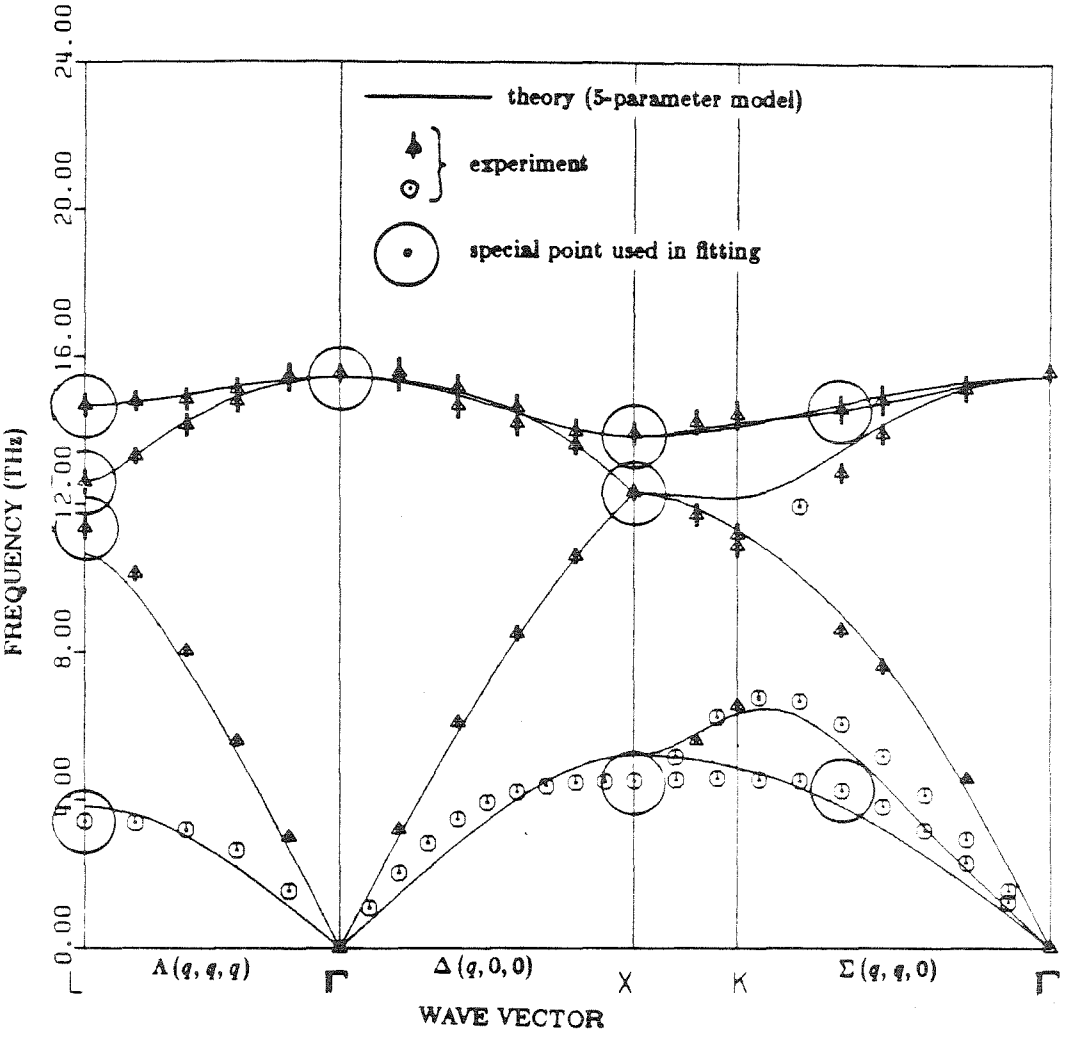

Fig. 3.8. Phonon band structure of silicon. The solid lines are theoretical predictions of the valence force field model of Musgrave and Pople. The parameters of the model in this case were chosen to fit ten experimental special points in the phonon band structure, and were **not** calculated ab-initio.

Modes used in calculating Vasil'ev's model.

The fifteen modes used before are not enough to fit the parameters of Vasil'ev's model, and eight other modes were calculated. In these eight modes, the inflated hydrogen atoms no longer moved together with their corresponding silicon atoms. In modes 16 and 18 the silicon atoms remained in their equilibrium position, while each hydrogen atom rotated in the plane defined by itself, its nearest silicon atom, and the central silicon atom. The angle of rotation was equal to t/r_0. Mode 16 was symmetric, that is, each hydrogen atom moved in the same direction toward or away from the central silicon atom. Mode 18 was antisymmetric, that is, the hydrogen atoms adjacent to two silicon atoms moved toward, while the others moved away from, the central silicon atom. In modes 17 and 19, each SiH_3 group moved together along the z-axis by an amount equal to t. Mode 17 was symmetric, i.e., the two groups whose silicon atoms lie above the xy plane moved up, while the other two groups moved down. Mode 19 was antisymmetric, i.e., all four groups moved in the same direction, a motion which is equivalent to all atoms in rest except the central silicon atom which moves up and down. Mode 20 consisted of a symmetric scission mode, similar to that of mode 5, but the angle of rotation was t/r_0 rather than t, and the hydrogen atoms performed a similar scission motion. This mode can be thought of as the motion of atoms in the diamond structure, with a rigid bond length, under a uniaxial (100) stress. Mode 21 was the antisymmetric form of mode 20, i.e., two groups performed the motion of mode 20 with the angle t/r_0, the other two groups with $-t/r_0$. Modes 22 and 23 were similar to modes 21 and 22, but with an additional symmetric or antisymmetric stretching of the $Si-Si$ bonds. The spring constants of each one of these modes is given in Table 3.8. Table A-3.4.1 in Appendix A-3.4 contains a quantitative description of each one of these modes.

TABLE 3.8. Calculated spring constants in units of eV per square t for the last eight modes. Here t is the parameter describing each mode in Table 3.1. The spring constants are calculated using four methods of calculation: HF, GVB, R-CI and GVB-CI.

Mode	HF	GVB	R-CI	GVB-CI
16	8.03	7.95	8.08	8.05
17	6.83	6.31	6.42	6.64
18	4.54	4.54	4.68	4.68
19	4.57	4.93	4.44	4.46
20	15.35	14.99	14.91	14.61
21	14.23	14.15	14.01	13.93
22	66.61	62.21	61.99	60.16
23	65.20	61.66	61.53	59.97

Vasil'ev's model

The 23 modes calculated so far were used to fit the parameters of Vasil'ev's model. This four-parameter model was described qualitatively in the introduction, and Appendix A-3.3 describes how to obtain the phonon band structure using this model. Unlike the previous models, for which it was straightforward to obtain the parameters from the cluster calculations, this model requires a long and tedious procedure to obtain the parameters. This procedure is described in Appendix A-3.4. As it turns out, we do not obtain all the four parameters of the model, α_1, α_2, β and A, but only the first two, and the combination

$$\beta\Big(1-\frac{1}{12A}\Big).$$

These values are given in Table 3.9, which is an extraction of Table A-3.4.5 of Appendix A-3.4.

TABLE 3.9. Calculated parameters of Vasil'ev's model, in units of eV per square angstrom. α_1 is the central-nearest-neighbor-force constant, α_2 is the second-nearest-neighbor-force constant, β is the non-central-nearest-neighbor force constant, and A is the torque parameter (cf. Appendix A-3.3).

	HF	GVB	R-CI	GVB-CI
α_1	8.65	8.63	8.57	8.76
α_2	0.593	0.449	0.533	0.430
$\beta\big(1-\frac{1}{12A}\big)$	0.430	0.503	0.365	0.411

The parameter A has to obey the stability condition

$$\frac{1}{4} < A < \frac{1}{2}$$

which defines a limited possible range for β. The phonon band structure obtained using these parameters is given in Fig. 3.9. The adjustable value of A was arbitrarily chosen to be $A = 0.26$, which is in the lower part of the possible range. By changing A throughout the entire range, the phonon band structure did not change by a lot, and the major changes were a slight increase in the TA branch for increasing A, and the formation of a cusp in the TO branch at the Γ point for $A \rightarrow 0.25$.

One can see that the four-parameter Vasil'ev's model is slightly better than all the models described before. The TA branch is better than in the previous models, but its slopes near the Γ point (which determine the static elastic properties) are still not accurate enough. In addition, this model gives a slightly better TO branch near the X point, but still, the obtained frequency is too high by almost 1THz.

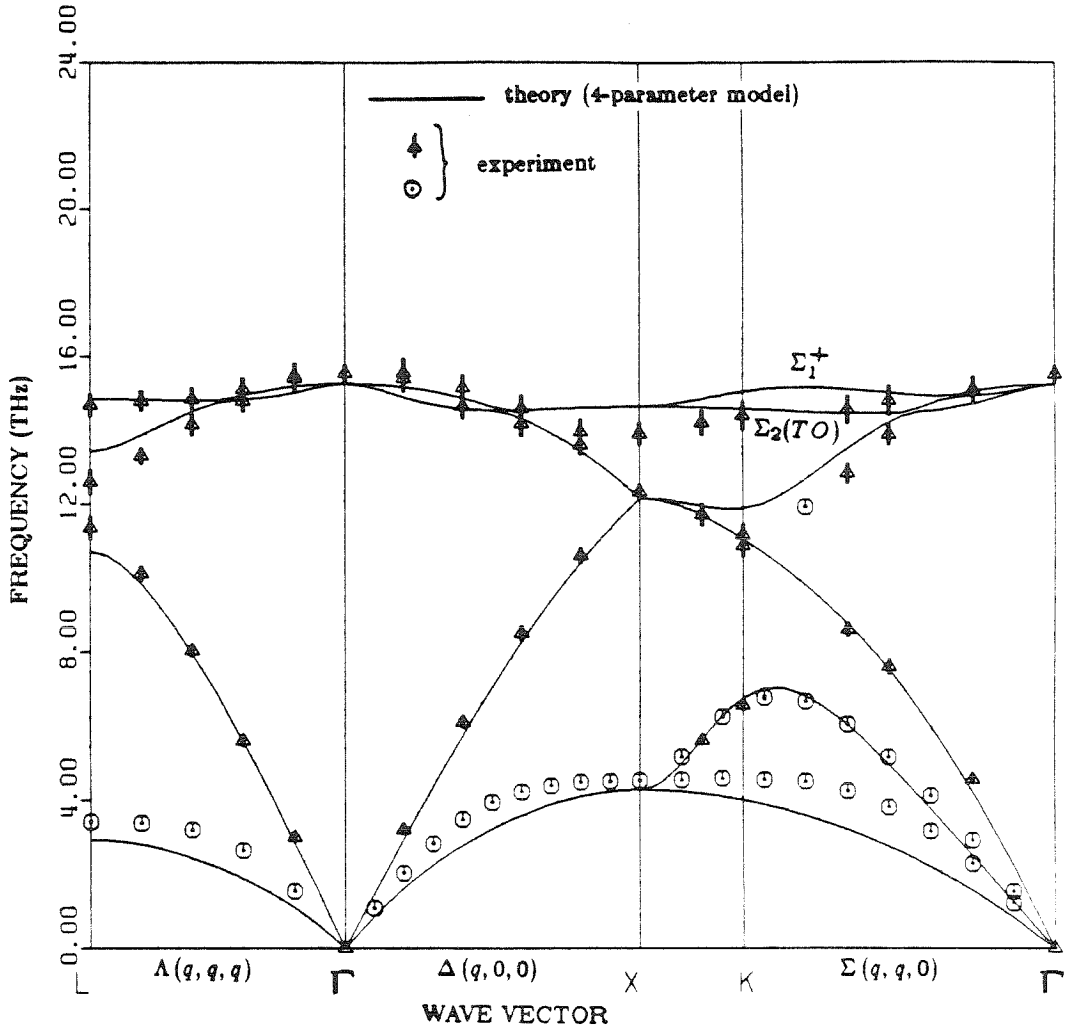

Fig. 3.9. Phonon band structure of silicon. The solid lines are theoretical predictions of Vasil'ev's model, using parameters obtained from ab-initio cluster calculations. The triangles and circles are experimental frequencies, obtained from neutron scattering experiments of Dolling (triangles) and Nilsson and Nellin (circles).

Comparison of the different models

In Table 3.10 we compare the phonon band structure as predicted by all the different models with experimental results. The parameters of the models were obtained from ab-initio cluster calculations using the GVB-CI method. The models appearing in Table 3.10 were the simple bond-bending and-stretching model with two parameters; the Singh-Dayal model with three parameters and Vasil'ev's model with four parameters. The five-parameter model of Musgrave and Pople does not appear in this table, since it predicts a band structure which is almost identical to that of the Singh-Dayal model. Regarding Vasil'ev's model, we have seen before that only three out of its four parameters could be calculated from our clusters, and the fourth parameter, A, can vary in the range $0.25 < A < 0.5$. In Table 3.10, we compare two values of A, which are near the edges of this range. As one can see, only the TA branch changes significantly.

In Table 3.3.11, we compare the static elastic constants, predicted by the various models, with experimental results. The elastic constants diasplayed are c_{11}, c_{12} and c_{44}, as well as two linear combinations of the first two. These two linear combinations are the bulk modulus B which satisfies $B = (c_{11} + 2c_{12})/3$, and $c_{11} - c_{12}$. These two particular linear combinations were chosen because B involves only bond stretching, while $c_{11} - c_{12}$ involves only bond bending. One can see that the agreement between the models and the experiment is reasonable for c_{11} and B, which involve mainly bond stretching, while it is poor for c_{12}, c_{44} and $c_{11} - c_{22}$, in which the bond bending contribution is more significant.

TABLE 3.10. Phonon frequencies in THz at the Γ, X, L, $\Delta(1/2)$ and $\Sigma(1/2)$ points. The predictions of the models used in this chapter are compared to experimental results. The models tabulated below are the simple bond-bending-and-stretching (SBBS) with two parameters, the Singh-Dayal (S+D) model with three parameters, and the model of Vasil'ev *et al.* with four parameters. A, the torque parameter of Vasil'ev's model, was not obtained from first principles. It may vary in the range $0.25 < A < 0.5$, and the predictions of the model near the two end points of this range are given in this table.

special point	SBBS	S+D	Vasil'ev (A=0.26)	Vasil'ev (A=0.49)	Experiment
$\Gamma_{25'}(LO,TO)$	17.4	15.3	15.2	15.0	15.53 ± 0.23[a]
X_3(TA)	5.44	5.39	4.13	5.25	4.51 ± 0.02[b]
X_1(LA,LO)	12.6	11.8	12.0	11.9	12.44 ± 0.03[b]
X_4(TO)	15.9	15.3	14.7	14.8	13.90 ± 0.30[a]
L_3(TA)	3.85	3.81	2.84	3.56	3.41 ± 0.02[b]
$L_{2'}$(LA)	10.7	9.85	10.4	10.2	11.35 ± 0.30[a]
L_1(LO)	13.7	13.6	13.5	13.5	12.60 ± 0.32[a]
L_3(TO)	16.7	15.3	14.8	14.8	14.68 ± 0.30[a]
$\Delta_5(1/2)$(TA)	3.65	3.78	3.09	3.67	3.94 ± 0.02[b]
$\Delta_1(1/2)$(LA)	6.89	6.75	6.96	6.91	7.3[c]
$\Delta_{2'}(1/2)$(LO)	16.2	14.5	14.5	14.4	14.87[c]
$\Delta_5(1/2)$(TO)	16.7	15.3	14.6	14.9	14.41[c]

TABLE 3.10. (Continued)

sp. point	SBBS	S+D	Vasil'ev (A=0.26)	Vasil'ev (A=0.49)	Experiment
$\Sigma_4(1/2)$(TA)	3.85	3.81	3.07	3.57	4.24 ± 0.01[b]
$\Sigma_3^-(1/2)$	5.66	5.74	5.70	5.49	6.03 ± 0.02[b]
$\Sigma_1^-(1/2)$	8.98	8.54	8.68	8.87	8.60 ± 0.18[a]
$\Sigma_3^+(1/2)$	14.5	13.5	13.5	13.4	12.83 ± 0.27[a]
$\Sigma_1^+(1/2)$	16.5	15.6	15.1	15.1	14.55 ± 0.38[d]
$\Sigma_2(1/2)$(TO)	16.7	15.3	14.5	14.8	14.55 ± 0.38[d]

(a) Dolling, Ref. 1.

(b) Nilsson and Nellin, Ref. 2.

(c) Dolling, (op. cit.). The frequencies for q=0.5 were interpolated between q=0.4 and q=0.6.

(d) Dolling, (op. cit.). It is not known whether the frequency of 14.55 ± 0.38 belongs to the Σ_2 or to the Σ_1^+ branch.

TABLE 3.11. Static elastic constants of silicon (in units of 10^{11} J·m^{-3}) The predictions of the models used in this chapter are compared to experimental results. The models tabulated below are the simple bond-bending-and-stretching (SBBS) with two parameters, the Singh-Dayal (S+D) model with three parameters, and the model of Vasil'ev *et al.* with four parameters. A, the torque parameter of Vasil'ev's model, was not obtained from first principles. It may vary in the range $0.25 < A < 0.5$, and the predictions of the model near the two end points of this range are given in this table.

	SBBS	S+D	Vasil'ev (A=0.26)	Vasil'ev (A=0.49)	Experiment[(a)]
c_{11}	1.40	1.39	1.73	1.66	1.675
c_{12}	0.90	0.89	1.05	1.06	0.650
c_{44}	0.42	0.48	0.49	0.45	0.801
B	1.06	1.05	1.28	1.26	0.992
$c_{11} - c_{12}$	0.51	0.50	0.67	0.60	1.025

(a) McSkimin (Ref.3.), at 77 K.

3.4. Summary and conclusions

We have performed the first calculation of the elastic properties of bulk silicon from ab-initio small cluster calculations.

Four levels of ab-initio quantum-chemistry methods were used to obtain elastic properties of silicon clusters. The clusters were $Si(SiH_3)_4$ molecules, with hydrogen atoms that were inflated to mimic silicon electronegativity. An improvement (softening) of up to 15% was achieved by going from the simplest (HF) to the most complicated (GVB-CI) method of calculation. Most of this improvement was obtained between the HF and the GVB methods, but a slight further improvement could usually be achieved by using GVB-CI instead of GVB.

Using the elastic properties of the cluster, we have calculated the phonon band structure of bulk silicon by utilizing four different models. In three of these models, the elastic energy could be expressed in terms of the atomic positions, i.e., there were no hidden coordinates. These models included the simple bond-bending-and-stretching, with two parameters, its modification by Singh and Dayal, with three parameters, and the valence force field of Musgrave and Pople, with five parameters. Models with more adjustable parameters were not treated in this work since they require larger clusters to calculate their parameters. The fourth model treated in this work was the one by Vasil'ev *et al.* It had four parameters and involved some hidden coordinates that were calculated separately. These hidden coordinates made the model both powerful and tedious.

The silicon phonon band structures obtained by these four models, were in qualitative agreement with experiment. Some features of the band structure, especially the LA branch, agreed quite well with experiment for all the four different models. The TA and TO branches improved from the two-parameter to the three-parameter to Vasil'ev's model. No significant change was observed on

going from the three-parameter (Singh and Dayal) to the five-parameter (Musgrave and Pople) model. The slope of the TO branch was best approximated by the two-parameter model, while Vasil'ev's model described best the slope of the TA branch.

The parameters for all the above models were calculated from first principles, using small-cluster calculations. In the case of the two- and three-parameter models, these parameters result in band structures that are at least as accurate as any other set of parameters for the same model. However, in the case of the five-parameter model of Musgrave and Pople, one can fit the experimental band structure better than it is possible from ab-initio calculations.

All the four different models described rather poorly the slopes of the TA branch near the Γ point, which determines some sound velocities and static elastic properties. In all the different models the predicted sound velocities associated with the TA branch are smaller than those observed experimentally.

In general, short-wave phonon frequencies were in better agreement with experiment than static elastic constants, and among the static elastic constants, those dominated by bond stretching were in better agreement than those dominated by bond bending.

In conclusion, we can apply the method described in this chapter to obtain the spectrum of evanescent vibrations from first principles. Using models that involve only nearest-neighbours interaction, we can expect reasonable accuracy for the vibrational frequencies (10%–20%). We can expect even better accuracy for vibrational modes involving stretching of bonds. On the other hand, we cannot expect to be so accurate in predicting static elastic properties, especially when the strain involves only bending of bonds. In that case, errors of the order of 50% may occur. In order to properly account for bond bending in the static

limit, one should take into account longer-range interactions; larger clusters are needed to calculate these interactions from first principles, requiring a much larger computational effort.

References for Chapter 3

1. G. Dolling, *Inelastic Scattering of Neutrons in Solids and Liquids* **Vol. 2**, Vienna (1963), p.37.
2. G. Nilsson and G. Nelin, *Phys. Rev.* **B6**, 3777 (1972).
3. H. J. McSkimin, *J. Appl. Phys.* **24**, 988 (1953).
4. B. D. Singh and B. Dayal, *Phys. Stat. Sol.* **38**, 141 (1970).
5. M. J. P. Musgrave and J. A. Pople, *Proc. Roy. Soc. (London)* **A268**, 474 (1962).
6. H. L. McMurry, A. W. Solbrig Jr., J. K. Boyter and C. Noble, *J. Phys. Chem. Solids* **28**, 2359 (1967).
7. A. W. Solbrig, *J. Phys. Chem. Solids*, 1761 (1971).
8. L. N. Vasil'ev, Yu. A. Logachev, B. Ya Moizhes and M. S. Yur'ev, *Fiz. Tver. Tela* **13**, 450 (1971). (English translation in Sov. Phys. Solid State 3, 685).
9. I was not able to reproduce the band structure of Vasil'ev *et al.* (op. cit.), by using their parameters.
10. L. J. Sham in *Dynamical Properties of Solids*, **V-1**, ed. G. K. Horton and A. A. Maradudin, North-Holland, Amsterdam (1974) pp323-325.
11. W. A. Goddard and T. C. McGill, J. Vac. Sci. Technol. 16, 1308 (1979).
12. F. W. Bobrowicz and W. A. Goddard III, *in Modern Theoretical Chemistry: Methods of Electronic Structure Theory*, edited by H. F. Schaefer III (Plenum, New York, 1977), Vol. III, pp. 79-128 .
13. A. Redondo, W. A. Goddard, III, and T. C. McGill, *Phys. Rev.* **B15**, 5038 (1977).
14. A. Redondo, W. A. Goddard, III, C. A. Swarts, and T. C. McGill, *J. Vac. Sci. Technol.* **19**, 498 (1981).
15. M. Lax, *Symmetry Principles in Solid State and Molecular Physics*,

Wiley, New York (1974) ,Chapter 12.

Appendix A-1.1. Statistics of carriers in bulk semiconductors.

In this appendix, the statistics of carriers in semiconductors is presented, and a formula for the space charge in a semi infinite semiconductor is derived. This material may be found in most textbooks dealing with physics of semiconductors, for example Sze[1] pp16-27. It is repeated here for convenience.

The density of the electrons in the conduction band is given by

$$n = \frac{2}{\sqrt{\pi}} N_c \mathcal{F}\left(\frac{\mu - E_c}{k_B T}\right) \qquad (A-1.1.1)$$

where N_c is the effective density of states,

$$N_c = 2\left(\frac{2\pi m_e^* k_B T}{h^2}\right)^{3/2}.$$

(If the conduction band minimum has more than one equivalent valley, $(m_e^*)^{3/2}$ is multiplied by the number of valleys). Similarly,

$$p = \frac{2}{\sqrt{\pi}} N_v \mathcal{F}\left(\frac{E_v - \mu}{k_B T}\right) \qquad (A-1.1.2)$$

The Fermi–Dirac integral $\mathcal{F}$ is given by

$$\mathcal{F}(\zeta) = \int_0^\infty \frac{\sqrt{\zeta'}\, d\zeta'}{1 + \exp(\zeta' - \zeta)}$$

If the Fermi level is well within the band gap, then $\zeta = (\mu - E_c)/k_B T$ is very negative, and $\mathcal{F}$ can be evaluated analytically.

$$\frac{2}{\sqrt{\pi}} \mathcal{F}(\zeta) \approx \exp\left(\frac{\mu - E_c}{k_B T}\right).$$

The density of excited donors is given by

$$N_D^+ = \frac{N_D}{1 + g_D \exp\left(\frac{\mu - E_D}{k_B T}\right)}. \qquad (A - 1.1.3)$$

where g_D is the degeneracy factor. Similarly, the density of ionized acceptors is

$$N_A^- = \frac{N_A}{1 + g_A \exp\left(\frac{E_A - \mu}{k_B T}\right)}. \qquad (A - 1.1.4)$$

The position of the Fermi level in the bulk is given by charge neutrality:

$$n + N_A^- - p - N_D^+ = 0. \qquad (A - 1.1.5)$$

Given a semi infinite semiconductor, then deep inside the bulk the Fermi level has to satisfy (A-1.1.5), otherwise the semiconductor will be charged by an infinite amount of charge. Near the surface, however, charge neutrality does not necessarily hold, and there could be some excess charge near the surface. If $\mathcal{Q}_s(x)$ is the total charge per unit area between x and ∞, i.e.,

$$\mathcal{Q}_s(x) = \int_x^\infty \left(p - n + N_D^+ - N_A^-\right) dx$$

then there is a one to one relation between $\mathcal{Q}_s(x)$ and the Fermi level at x. Denote by $\eta(x) = \mu - E_c(x)$, the relative fermi level with respect to the conduction band, then

$$\begin{aligned} \frac{d\eta}{dx} &= \frac{q^2}{\epsilon\epsilon_0}\mathcal{Q}_s(x) \qquad \eta = (\mu - E_c) \\ \frac{d\mathcal{Q}_s}{dx} &= n(\eta) + \begin{pmatrix} -N_D^+(\eta) \\ +N_A^-(\eta) \end{pmatrix} - p(\eta) \end{aligned}, \qquad (A - 1.1.6)$$

Dividing these two equations by each other we obtain,

$$\left[n(\eta) + \begin{pmatrix} -N_D^+(\eta) \\ +N_A^-(\eta) \end{pmatrix} - p(\eta)\right] d\eta = \frac{q^2}{\epsilon\epsilon_0}\mathcal{Q}_s d\mathcal{Q}_s$$

which can be reduced to an integral:

$$\mathcal{Q}_s(\eta) = \pm\sqrt{\frac{2\epsilon\epsilon_0}{q^2}\int_{\eta(\infty)}^{\eta}\left[n(\eta') + \begin{pmatrix} -N_D^+(\eta') \\ +N_A^-(\eta') \end{pmatrix} - p(\eta')\right] d\eta'} \qquad \begin{matrix} \text{n-type} \\ \text{p-type} \end{matrix}$$

References

1. S. M. Sze, *Physics of Semiconductor Devices*, 2nd ed. Wiley–Interscience (1981).

Appendix A-1.2. The density functional formalism

The spatial arrangement of charge near a jellium surface, as well as the conventions for energy levels were given in Fig.1.1 in section 1.3. The electrons are subject to an effective potential v_{eff}, which is the sum of the electrostatic potential energy, as well as the exchange-correlation energy. The charge density was calculated by solving the one-dimensional Schrödinger equation with the effective potential v_{eff}, to obtain the wavefunctions $\psi_k(x)$. Summing $|\psi_k(x)|^2$ over all the k-vectors in the Fermi sphere gave us the charge density $n(x)$ as a function of position.

In order to close the cycle and calculate the effective potential from the charge density, we have to use the density-functional formalism [1] of Hohenberg and Kohn[2] and Kohn and Sham[3]. According to this formalism, the total energy of the ground state of the electron gas is given by

$$E[n] = \int \phi(\vec{\mathbf{r}}) n(\vec{\mathbf{r}})\, d\vec{\mathbf{r}} + G[n], \qquad (A - 1.2.1)$$

where $G[n]$ is a universal functional of the local density $n(\vec{\mathbf{r}})$, including average kinetic energy, exchange and correlation interactions, and

$$\phi(\vec{\mathbf{r}}) = \int \frac{n(\vec{\mathbf{r}}') - n^{+}(\vec{\mathbf{r}}')}{|\vec{\mathbf{r}} - \vec{\mathbf{r}}'|} d\vec{\mathbf{r}},$$

is the long range Coulomb interaction of both the positive background and the electron gas. Hohenberg and Kohn were able to prove the existence of such functional, but the problem of actually finding this functional is still unsolved for a rapidly-changing charge density. In order to proceed we have to use further approximations. The most common of these approximations is the Local Density Approximation, in which we assume that the electron density is slowly varying (on

a characteristic length of $1/k_f$). This assumption clearly does not hold near metal surfaces and interfaces, but it is nevertheless often used, for want of a better formalism. Under the Local Density Approximation, we can write $G[n]$ as a sum of kinetic, exchange and correlation energies.

$$G[n] \doteq n \cdot \epsilon[n] = n \cdot (t(n) + \epsilon_x(n) + \epsilon_c(n)). \qquad (A - 1.2.2)$$

Expressions for the kinetic and exchange parts are well known[4] and are given, in atomic units (Hartrees and Bohrs), by

$$t(n) = \frac{3}{10}(3\pi^2 n)^{2/3} = \frac{1.105}{r_s^2}$$

and

$$\epsilon_x(n) = -\frac{3}{4}(3n/\pi)^{1/3} = -\frac{0.458}{r_s}.$$

Expressions for the correlation energy are more complicated, and there are several interpolation schemes to obtain good correlation expressions between the limits of very high and very low densities. The asymptotic expression for high densities was obtained by Gell-Mann and Brueckner[5]

$$\epsilon_c^{GB} = 0.031 \log r_s - 0.048 + O(r_s).$$

Other expressions more suitable to metallic densities are given by Wigner (cf. Pines[4] eq. (3.58)), Pines and Nozières[6] and Vashista and Singwi[7]

$$\epsilon_c^{W} = \frac{-0.44}{r_s + 7.8}, \qquad (A - 1.2.3)$$

$$\epsilon_c^{PN} = 0.0155 \log r_s - 0.0575, \qquad (A - 1.2.4)$$

$$\epsilon_c^{VS} = 0.01675 \log r_s - 0.056. \qquad (A - 1.2.5)$$

The chemical potential μ, of the electrons in the jellium model is given by the Lagrange multiplier in the variational equation for n($\vec{r}$)

$$\delta(E[n] - \mu N) = 0, \qquad N = \int n(\vec{r})\, d\vec{r}. \qquad (A - 1.2.6)$$

The meaning of this equation is that $E[n]$ given by (A-1.2.1) is a minimum with respect to any small change in n that conserves the number of particles. Therefore, for the corect density n, that is, the density satisfying (A-1.2.6), the chemical potential is given by

$$\mu = \phi(\vec{r}) + \frac{\delta G[n]}{\delta n(\vec{r})}$$

under the local density approximation, this last equation becomes,

$$\mu = \phi(\vec{r}) + \left(\frac{\partial G}{\partial n}\right)_{n=n(\vec{r})} = \phi(\vec{r}) + \frac{\partial n\epsilon(n)}{\partial n} = \phi(\vec{r}) + \frac{1}{2}k_f^2 + \mu_{xc}(n).$$

References

1. N. D. Lang, *Solid State Physics, Advances in Research and Applications,* edited by H. Ehrenreich, F. Seitz, and D. Turnbull (Academic, New York, 1973) Vol. 28.
2. P. Hohenberg and W. Kohn, *Phys. Rev.* **136,**, B864 (1964) .
3. W. Kohn and L. J. Sham, *Phys. Rev.* **140,** A1133 (1965) .
4. D. Pines, *Elementary Excitations in Solids,* Chapter 3. Benjamin, New York, (1963).
5. M. Gell-Mann and K. A. Brueckner, *Phys. Rev.***106,** 364 (1957).
6. D. Pines and P. Nozières, *The Theory of Quantum Liquids,* (Benjamin, New York, 1966) p.330.
7. P. Vashista and K. S. Singwi, *Phys. Rev.***B6,** 875 (1972).

Appendix A-1.3. Sugiyama's sum rule.

One of the most useful sum rules applicable for jellium surface calculations is the conservation of charge. Sugiyama's sum rule expresses conservation of charge in terms of the phase of the wave functions deep inside the jellium. This sum rule is used in calculating the parameters of a non-self-consistent effective potential.

Non-self-consistent calculations are performed in the following way. We assume a general form for an effective potential, solve Schrödinger's equation to obtain wave functions, and sum up the square of the wave functions with wave vectors in the Fermi sphere to obtain the electronic charge density. The total charge density (i.e., the electronic plus the background densities) from $-\infty$ to $+\infty$ should sum up to zero, if the system is electrically neutral. If the jellium is not electrically neutral, the total charge density has some prescribed value. This requirement forms a constraint on the shape of the effective potential. Alternatively, it is very convenient to assume a certain shape of the effective potential and to reposition the jellium surface with respect to it, so as to obtain overall charge neutrality or some other surface charge density.

The Sugiyama's sum rule, extended to non-neutral surfaces states that

$$\frac{k_f^3 a}{3\pi^2} + \frac{1}{\pi^2}\int_0^{k_f} k\gamma\, dk - \frac{k_f^2}{8\pi} - \sigma = 0.$$

Here k_f is the Fermi wave number, a is the position of the jellium surface, $\gamma(k)$ is the asymptotic phase shift of the wave function associated with the wave number k, and σ is the number of excess charges per unit surface area. We shall now define all this terms precisely, and prove the sum rule.

The effective potential is assumed to vanishes deep inside the jellium. Therefore, the wave functions have an asymptotic form:

$$\psi_k(x) \approx -\sqrt{\frac{2}{L}} \cdot \sin[kx - \gamma(k)], \qquad x \ll 0. \qquad (A - 1.3.1)$$

Here $-\sqrt{2/L}$ is the normalization factor, assumming that the wavefunctions extends only to $x = -L$, rather than to $-\infty$, and taking the limit $L \to \infty$. $\gamma(k)$ is a phase shift satisfying

$$\lim_{k \to 0} \gamma(k) = 0.$$

It is worth noting that the effective potential, v_{eff}, enters the asymptotic form of ψ_k for $x \to -\infty$ only via this phase shift γ. Sugiyama[1] was the first to formulate the charge neutrality condition using these phase shifts. His original proof is quite complicated, and instead, an alternative proof by Langreth[2] is presented here and extended to non-neutral surfaces and arbitrary surface position. In essence, the Sugiyama sum rule is analogous to the Friedel sum rule[3] developed for a spherically symmetric effective potential.

In the derivation below, we assume that the wave function $\psi_k(x)$ satisfies the Schrödinger equation,

$$-\frac{\hbar^2}{2m}\frac{\partial^2 \psi_k(x)}{\partial x^2} + v_{\text{eff}}(x)\psi_k(x) = \frac{\hbar^2 k^2}{2m}\psi_k(x) \qquad (A - 1.3.2)$$

One can calculate the electron number density by integrating $|\psi|^2$ inside the Fermi sphere. Recalling the spherical symmetry of the Fermi sphere, and the fact that the wave functions are plane waves in the y and z directions, this integral becomes,

$$n(x) = \frac{L}{2\pi^2}\int_0^{k_f} (k_f^2 - k^2)|\psi_k(x)|^2 \, dk.$$

One can show that

$$\lim_{x \to -\infty} n(x) = \frac{k_f^3}{3\pi^2} = n^+.$$

The positive background extends from $-\infty$ to $x = a$, i.e., the total charge density (in atomic units) is

$$n_t(x) = \begin{cases} -n(x), & x > a, \\ \frac{k_f^3}{3\pi^2} - n(x), & x \leq a. \end{cases}$$

and the total surface charge is

$$\sigma = \int_{-\infty}^{\infty} n_t(x)\, dx.$$

In his paper, Sugiyama required $\sigma = 0$, i.e. the whole system is overall neutral. Langreth proof, however, extends very easily to an arbitrary σ.

Multiply (A-1.3.2) by $\psi_{k'}$ and subtract from a similar expression with k and k' interchanged, to get

$$\psi_k \frac{\partial^2 \psi_{k'}}{\partial x^2} - \psi_{k'} \frac{\partial^2 \psi_k}{\partial x^2} = (k^2 - k'^2)\psi_k \psi_{k'}$$

or,

$$\frac{\partial}{\partial x}\left(\psi_k \frac{\partial \psi_{k'}}{\partial x} - \psi_{k'} \frac{\partial \psi_k}{\partial x}\right) = (k^2 - k'^2)\psi_k \psi_{k'}.$$

Integrating from x to ∞,

$$-\int_x^{\infty} \psi_k \psi_{k'}\, dx = \frac{1}{k^2 - k'^2}\left(\psi_k \frac{\partial \psi_{k'}}{\partial x} - \psi_{k'} \frac{\partial \psi_k}{\partial x}\right) \qquad (A - 1.3.3)$$

This integral was derived using $\psi_k(\infty) = 0$. Now let $k' = k + \Delta k$, where Δk is very small. Then,

$$\psi_{k'}(x) \approx \psi_k(x) + \Delta k \frac{\partial \psi_k(x)}{\partial k},$$

so by taking the limit of (A-1.3.3) when $k' \to k$, we obtain

$$\int_x^{\infty} |\psi_k(x)|^2\, dx = -\frac{1}{2k}\left(\frac{\partial \psi_k}{\partial k}\frac{\partial \psi_k}{\partial x} - \psi_k \frac{\partial^2 \psi_k}{\partial k \partial x}\right)$$

Define $\mathcal{Q}^*(x)$ to be the charge per unit area from x to ∞,

$$\begin{aligned}
\mathcal{Q}^*(x) &= \int_x^{\infty} n_t(x')\, dx' \\
&= \frac{k_f^3}{3\pi^2}(a - x)\Theta(a - x) - \frac{L}{2\pi^2}\int_x^{\infty}\int_0^{k_f} (k_f^2 - k^2)|\psi_k(x)|^2\, dk\, dx \\
&= \frac{k_f^3}{3\pi^2}(a - x)\Theta(a - x) + \frac{L}{2\pi^2}\int_0^{k_f} \frac{k_f^2 - k^2}{2k}\left(\frac{\partial \psi_k}{\partial k}\frac{\partial \psi_k}{\partial x} - \psi_k \frac{\partial^2 \psi_k}{\partial k \partial x}\right)
\end{aligned}$$

and for $x \ll 0$, we can take the asymptotic form of $\psi_k(x)$,

$$\psi_k(x) \approx -\sqrt{\frac{2}{L}} \sin(kx - \gamma).$$

$$\begin{aligned} \mathcal{Q}^*(x) &\approx \frac{k_f^3}{3\pi^2}(a-x) + \frac{1}{2\pi^2}\int_0^{k_f} \frac{k_f^2 - k^2}{k}\left(kx - k\frac{\partial\gamma}{\partial k} - \frac{1}{2}\sin(2kx - 2\gamma)\right) dk \\ &= \frac{k_f^3 a}{3\pi^2} + \frac{1}{2\pi^2}\int_0^{k_f}(k_f^2 - k^2)\frac{\partial\gamma}{\partial k}\, dk - \frac{1}{4\pi^2}\int_0^{k_f}\frac{k_f^2 - k^2}{k}\sin(2kx - 2\gamma)\, dx \end{aligned}$$

Now let $x \to -\infty$, and we obtain Sugiyama sum rule

$$\sigma = \mathcal{Q}^*(-\infty) = \frac{k_f^3 a}{3\pi^2} + \frac{1}{\pi^2}\int_0^{k_f} k\gamma\, dk - \frac{k_f^2}{8\pi} \qquad (A - 1.3.4)$$

using

$$\int_0^{k_f}(k_f^2 - k^2)\frac{\partial\gamma}{\partial k}\, dk = (k_f^2 - k^2)\gamma\Big]_0^{k_f} + \int_0^{k_f} 2k\gamma\, dk = 2\int_0^{k_f} k\gamma\, dk$$

and

$$\lim_{x\to-\infty}\int_0^{k_f}\frac{k_f^2 - k^2}{k}\sin(2kx - 2\gamma)\, dk = k_f^2 \cdot Si(0) = \frac{k_f^2\pi}{2}.$$

References

1. A. Sugiyama, *J. Phys. Soc. Japan* **15**, 965 (1960).

2. D. C. Langreth, *Phys. Rev.* **B5**, 2842 (1972).

3. J. Friedel, *Phil. Mag.* **43**, 153 (1952).

idea is to evaluate $\int_{-\infty}^{\infty} \phi(x)\frac{dn(x)}{dx}\,dx$, writing the electronic charge density as the difference between the positive charge density and the total charge density. In the first term, the positive background density is a step function, whose derivative is a delta-function. The second term we integrate by parts, recalling that the derivative of the potential is related to the integral of the total charge density by the Poisson equation.

$$\begin{aligned}\int_{-\infty}^{\infty} \phi(x)\frac{dn(x)}{dx}\,dx &= n^{+}\int_{-\infty}^{\infty} \phi(x)\frac{d\Theta(a-x)}{dx}\,dx - \int_{-\infty}^{\infty} \phi(x)\frac{dn_t(x)}{dx}\,dx \\ &= -n^{+}\int_{-\infty}^{\infty} \phi(x)\delta(x-a)\,dx - \int_{-\infty}^{\infty} \phi(x)\frac{dn_t(x)}{dx}\,dx \\ &= -n^{+}\phi(a) - \int_{-\infty}^{\infty} \phi(x)\frac{dn_t(x)}{dx}\,dx\end{aligned}$$

Now

$$\begin{aligned}\int_{-\infty}^{\infty} \phi(x)\frac{dn_t(x)}{dx}\,dx &= [\phi\cdot n_t]_{-\infty}^{\infty} - \int_{-\infty}^{\infty} \frac{d\phi}{dx}n_t(x)\,dx \\ &= -\int_{-\infty}^{\infty} \frac{d\phi}{dx}n_t(x)\,dx \\ &= -\frac{q}{\epsilon_0}\int_{-\infty}^{\infty} n_t(x)\int_{-\infty}^{x} n_t(x')\,dx'\,dx \\ &= -\frac{q}{2\epsilon_0}\left(\int_{-\infty}^{\infty} n_t(x)\,dx\right)^2\end{aligned}$$

The last equation follows from exchange of variables:

$$\int_{-\infty}^{\infty} n_t(x)\int_{-\infty}^{x} n_t(x')\,dx'\,dx = \int_{-\infty}^{\infty} n_t(x')\int_{x'}^{\infty} n_t(x)\,dx\,dx',$$

and then taking the average of both sides. Therefore,

$$\begin{aligned}\int_{-\infty}^{\infty} \phi(x)\frac{dn(x)}{dx}\,dx &= \frac{q}{2\epsilon_0}\left(\int_{-\infty}^{\infty} n_t(x)\,dx\right)^2 - n^{+}\phi(a) \\ &= \frac{q\sigma^2}{2\epsilon_0} - n^{+}\phi(a)\end{aligned}$$

Recall that in equilibrium, assumming the local density formalism,

$$\mu = \left(\frac{d(n\epsilon[n])}{dn} + q\phi \right)$$

is constant throughout space (the potential ϕ is assumed to be zero at $x = -\infty$).

Recall also that

$$\int_{-\infty}^{\infty} \frac{dn}{dx}\, dx = -n^{+}$$

Thus,

$$\begin{aligned}
\mu &= -\frac{1}{n^{+}} \int_{-\infty}^{\infty} \left(\frac{d(n\epsilon[n])}{dn} + q\phi \right) \frac{dn}{dx}\, dx \\
&= -\frac{1}{n^{+}} \int_{-\infty}^{\infty} \frac{d(n\epsilon[n])}{dn} \frac{dn}{dx}\, dx - \frac{1}{n^{+}} \int_{-\infty}^{\infty} q\phi(x) \frac{dn}{dx}\, dx \\
&= -\frac{1}{n^{+}} [n\epsilon[n]]_{-\infty}^{\infty} + \frac{1}{n^{+}} \left[-\frac{q^2\sigma^2}{2\epsilon_0} + n^{+} \cdot q\phi(a) \right]
\end{aligned}$$

and thus,

$$\mu = \epsilon[n(-\infty)] - \frac{q^2\sigma^2}{2n^{+}\epsilon_0} + q\phi(a). \qquad (A-1.4.3)$$

But

$$\mu = \frac{\partial n(\epsilon[n])}{\partial n} + q\phi = \epsilon[n] + n\frac{\partial \epsilon[n]}{\partial n} + q\phi. \qquad (A-1.4.4)$$

Substituting (A-1.4.4) with $n = n^{+} = n(-\infty)$, we obtain the modified Budd – Vannimenus theorem

$$q\phi(a) = n^{+} \left(\frac{\partial \epsilon[n]}{\partial n} \right)_{n=n^{+}} + \frac{q^2\sigma^2}{2n^{+}\epsilon_0} \qquad (A-1.4.5)$$

References

1. H. F. Budd and J. Vannimenus, *Phys. Rev. Lett.* **31**, 1218 (1973).
2. G. D. Mahan and W. L. Schaich, *Phys. Rev.* **B10**, 2647 (1974)

A-2.1. Crystallographic Appendix

Special care should be taken in order to have a set of consistent crystallographic notations. Confusion might occur when two sets of notations are possible at the same time. This happens for rhombohedral crystals, in which one often appends three unit cells to obtain hexagonal structure, and also for face and body centered structures, in which it is common to refer to the simple structure unit cell, which is twice or four times larger.

It is always recommended to work with the smallest possible unit cell when it comes to lattice match, i.e., one should work with rhombohedral rather than hexagonal, and face-, one-face-, or body-centered structures rather than the simple one when both are applicable. On the other hand, one should be able to report the results in hexagonal rather than rhombohedral, and in simple structure rather than body- or face-centered structure notation. In this appendix, the transformations from one set of notations to the other will be clarified.

Rombohedral and Hexagonal notations.

When one works with rhombohedral materials like sapphire, it is sometimes convenient to transform to hexagonal notations. We follow here the conventions of M. L. Kronberg.[1]

Three rhombohedral unit cells are joined to give a hexagonal unit cell. If $\vec{a}_1$, $\vec{a}_2$, and $\vec{a}_3$ are the rhombohedral primitive vectors, one can form a set of hexagonal vectors $\vec{A}_1$, $\vec{A}_2$, $\vec{A}_3$, and $\vec{C}$ such that,

$$\vec{A}_1 = \vec{a}_1 - \vec{a}_2,$$

$$\vec{A}_2 = \vec{a}_2 - \vec{a}_3,$$

$$\vec{A}_3 = \vec{a}_3 - \vec{a}_1,$$

$$\vec{C} = \vec{a}_1 + \vec{a}_2 + \vec{a}_3.$$

The inverse of this transformation is given by,

$$\vec{a}_1 = \frac{2\vec{A}_1 + \vec{A}_2 + \vec{C}}{3},$$

$$\vec{a}_2 = \frac{-\vec{A}_1 + \vec{A}_2 + \vec{C}}{3},$$

$$\vec{a}_3 = \frac{-\vec{A}_1 - 2\vec{A}_2 + \vec{C}}{3}.$$

If $\vec{v} = \alpha\vec{a}_1 + \beta\vec{a}_2 + \gamma\vec{a}_3$, is a vector in rhombohedral coordinates, then the hexagonal representation is:

$$\vec{v} = \frac{2\alpha - \beta - \gamma}{3}\vec{A}_1 + \frac{\alpha + \beta - 2\gamma}{3}\vec{A}_2 + \frac{\alpha + \beta + \gamma}{3}\vec{C}.$$

Therefore, the transformation from rhombohedral to hexagonal with three indices is given by $[\alpha, \beta, \gamma](R) = [U, V, W](H)$, where

$$U = \frac{2\alpha - \beta - \gamma}{3}, \qquad V = \frac{\alpha + \beta - 2\gamma}{3}, \qquad W = \frac{\alpha + \beta + \gamma}{3}.$$

It is left to transform from hexagonal three-indices [UVW] to four-indices [uvtw] notation. This transformation is given by[2]

$$U = u - t, \qquad V = v - t, \qquad W = w,$$

$$u = \frac{2U - V}{3}, \qquad v = \frac{2V - U}{3}, \qquad t = -u - v, \qquad w = W.$$

Thus,

$$[\alpha, \beta, \gamma](R) = [\frac{\alpha - \beta}{3}, \frac{\beta - \gamma}{3}, \frac{\gamma - \alpha}{3}, \frac{\alpha + \beta + \gamma}{3}](H).$$

(e.g., [1,1,0](R)=[0,1,$\bar{1}$,2](H).)

Similarly for reciprocal lattices, the transformations from rhombohedral (HKL) to hexagonal-four-indices (hkil) are given by[2]

$$H = \frac{2h + k + l}{3}, \qquad K = \frac{h - k + l}{3}, \qquad L = \frac{-2k - h + l}{3},$$

$$h = H - K, \qquad k = K - L, \qquad i = L - H, \qquad l = H + K + L.$$

e.g., (110)(R)=(01$\bar{1}$2)(H), (411)(R)=(30$\bar{3}$6)=(10$\bar{1}$2)(H).

The relationships between the hexagonal parameters (a_h, c) and the rhombohedral parameters (a_r, α) are given by[3]

$$a_r = \sqrt{a_h^2/3 + c^2/9} \qquad \cos\alpha = \frac{-a_h^2/2 + c^2/3}{a_h^2 + c^2/3}$$

$$a_h = 2a_r \sin\frac{\alpha}{2} \qquad c = 3\sqrt{a_r^2 - a_h^2/3}.$$

Simple and face-, body-, and one-face-centered notations.

Crystal structures fall into fourteen Bravais types: triclinic, simple monoclinic, one face centered monoclinic, simple orthorhombic, face centered orthorhombic, body centered orthorhombic, one face centered orthorhombic, simple tetragonal, body centerd tetragonal, hexagonal, rhombohedral, simple cubic, face centered cubic, and body centered cubic.

Out of these fourteen structures, seven are simple and seven are either face centered, body centered or one face centered. Usually, when it comes to designations of fasces and directions, it is more common to refer to the axes defined by the corresponding simple structures. For example, the face centered cubic structure has a standard set of primitive translations, namely, [0,1/2,1/2], [1/2,0,1/2], and [1/2,1/2,0], but directions and planes are referred to the simple cubic directions,

i.e., to [1,0,0], [0,1,0] and [0,0,1], which are not even primitive. In this appendix, the transformations from one set of notations to the other are described.

Let $\vec{u}_1$, $\vec{u}_2$, and $\vec{u}_3$ be the simple basis, for example (100), (010) and (001) for cubic crystals. Let $\vec{v}_1$, $\vec{v}_2$, and $\vec{v}_3$ be the standard basis for the face- or body- or one-face-centered structure. Then

$$\begin{bmatrix} \vec{v}_1 \\ \vec{v}_2 \\ \vec{v}_3 \end{bmatrix} = B \begin{bmatrix} \vec{u}_1 \\ \vec{u}_2 \\ \vec{u}_3 \end{bmatrix},$$

where the transformation matrices B for face-centered, body-centered and one-face-centered structures are given by

$$B_{fc} = \begin{bmatrix} 0 & 1/2 & 1/2 \\ 1/2 & 0 & 1/2 \\ 1/2 & 1/2 & 0 \end{bmatrix}, \qquad B_{bc} = \begin{bmatrix} -1/2 & 1/2 & 1/2 \\ 1/2 & -1/2 & 1/2 \\ 1/2 & 1/2 & -1/2 \end{bmatrix},$$

and

$$B_{ofc} = \begin{bmatrix} 1/2 & -1/2 & 0 \\ 1/2 & 1/2 & 0 \\ 0 & 0 & 1 \end{bmatrix}.$$

Let $\vec{r}_1$, $\vec{r}_2$ and $\vec{r}_3$ be the reciprocal basis of the simple structure, and $\vec{s}_1$, $\vec{s}_2$, and $\vec{s}_3$ be the reciprocal basis of the face-centered, body-centered or one-face-centered structure.

$$\begin{bmatrix} \vec{u}_1 \\ \vec{u}_2 \\ \vec{u}_3 \end{bmatrix} (\vec{r}_1, \vec{r}_2, \vec{r}_3) = \begin{bmatrix} 1 & 0 & 0 \\ 0 & 1 & 0 \\ 0 & 0 & 1 \end{bmatrix} = \begin{bmatrix} \vec{v}_1 \\ \vec{v}_2 \\ \vec{v}_3 \end{bmatrix} (\vec{s}_1, \vec{s}_2, \vec{s}_3).$$

then,

$$\begin{bmatrix} 1 & 0 & 0 \\ 0 & 1 & 0 \\ 0 & 0 & 1 \end{bmatrix} = B \begin{bmatrix} \vec{u}_1 \\ \vec{u}_2 \\ \vec{u}_3 \end{bmatrix} (\vec{r}_1, \vec{r}_2, \vec{r}_3) B^{-1},$$

and, therefore,

$$(\vec{\mathbf{s}}_1, \vec{\mathbf{s}}_2, \vec{\mathbf{s}}_3) = (\vec{\mathbf{r}}_1, \vec{\mathbf{r}}_2, \vec{\mathbf{r}}_3)B^{-1}.$$

Transformations of planes

A plane is determined by the reciprocal vector. If a plane is written as (n_1, n_2, n_3) in the simple structure notation, and as (m_1, m_2, m_3) in the fc, bc, or ofc notation, then these two triplets have to represent the same vector $\vec{\mathbf{r}}$.

$$\vec{\mathbf{r}} = (\vec{\mathbf{r}}_1, \vec{\mathbf{r}}_2, \vec{\mathbf{r}}_3)\begin{bmatrix} n_1 \\ n_2 \\ n_3 \end{bmatrix} = (\vec{\mathbf{s}}_1, \vec{\mathbf{s}}_2, \vec{\mathbf{s}}_3)B\begin{bmatrix} n_1 \\ n_2 \\ n_3 \end{bmatrix} = (\vec{\mathbf{s}}_1, \vec{\mathbf{s}}_2, \vec{\mathbf{s}}_3)\begin{bmatrix} m_1 \\ m_2 \\ m_3 \end{bmatrix}.$$

Therefore,

$$B\begin{bmatrix} n_1 \\ n_2 \\ n_3 \end{bmatrix} = \begin{bmatrix} m_1 \\ m_2 \\ m_3 \end{bmatrix},$$

and one has to multiply from the left by the B matrices in order to transform a plane from simple to centered notation.

Transformations of crystal directions

A direction is determined by a lattice vector. If this vector is written as (n_1, n_2, n_3) in the simple structure notation, and as (m_1, m_2, m_3) in the fc, bc, or ofc notation, then these two triplets have to represent the same vector $\vec{\mathbf{u}}$.

$$\vec{\mathbf{u}} = (n_1, n_2, n_3)\begin{bmatrix} \vec{\mathbf{u}}_1 \\ \vec{\mathbf{u}}_2 \\ \vec{\mathbf{u}}_3 \end{bmatrix} = (n_1, n_2, n_3)B^{-1}\begin{bmatrix} \vec{\mathbf{v}}_1 \\ \vec{\mathbf{v}}_2 \\ \vec{\mathbf{v}}_3 \end{bmatrix} = (m_1, m_2, m_3)\begin{bmatrix} \vec{\mathbf{v}}_1 \\ \vec{\mathbf{v}}_2 \\ \vec{\mathbf{v}}_3 \end{bmatrix}.$$

Therefore,

$$(n_1, n_2, n_3) = (m_1, m_2, m_3) \cdot B^{-1},$$

or by transposing,

$$\begin{bmatrix} n_1 \\ n_2 \\ n_3 \end{bmatrix} = (B^{-1})^T \begin{bmatrix} m_1 \\ m_2 \\ m_3 \end{bmatrix}.$$

In other words, one has to multiply from the left by the $(B^{-1})^T$, in order to transform a direction from simple to centered notation.

$$B_{fc}^{-1} = \begin{bmatrix} -1 & 1 & 1 \\ 1 & -1 & 1 \\ 1 & 1 & -1 \end{bmatrix} \qquad B_{bc}^{-1} = \begin{bmatrix} 0 & 1 & 1 \\ 1 & 0 & 1 \\ 1 & 1 & 0 \end{bmatrix},$$

and

$$B_{ofc}^{-1} = \begin{bmatrix} 1 & -1 & 0 \\ 1 & 1 & 0 \\ 0 & 0 & 1 \end{bmatrix}.$$

References for Appendix A-2.1.

1. M. L. Kronberg *Acta Met.* **5**, 507 (1957).

2. C. S. Barrett, *Structure of Metals* McGraw-Hill, New York (1952), pp12-15.

3. J. C. Slater, *Symmetry and Energy Bands in Crystals*, Dover 1972 p.21

A-2.2. Mathematical Appendix

In this appendix, we formulate the concepts of lattice match in a rigorous way, and prove all the results quoted without a proof in section 2.2. These include a proof that the reduction procedure described in Fig. 2.2 terminates after a finite number of steps, and results in a reduced basis, a proof of (2.2.3)-(2.2.6) regarding the construction of all the possible superlattices of a certain order, and a proof that there are at most $\sigma(n)$ distinct superlattices of order n.

Definition 1: Two 2-dimensional lattices will be called **congruent** if they are obtained from each other by a rigid transformation (translation, rotation or reflexion).

Definition 2: Two 2-dimensional lattices will be called **matched** if each one of them possesses a superlattice, such that the two superlattices are congruent.

With these two definitions in mind, one sees that the problem of lattice match between any two given 2-dimensional lattices, reduces to scanning over superlattices, and then for each pair of superlattices determining whether or not they are congruent. Lets treat the congruency problem first. The problem here is that while a lattice is uniquely determined by its basis, there are infinitely many bases that generate the same lattice. (A **basis** of a lattice is a set of two vectors $\vec{\mathbf{a}}$ and $\vec{\mathbf{b}}$, such that all the lattice points can be written as $n_1\vec{\mathbf{a}} + n_2\vec{\mathbf{b}}$, ($n_1$ and n_2 are integers). For a general treatment of lattices see for example Cassels.[1] The approach to the solution of the congruency problem is by using reduction, that is, finding a particular basis for any given lattice, in such a way that only intrinsic properties (lengths and angles) of the lattice would be involved, but not through any particular coordinate system.

Definition 3: Given a two dimensional lattice, a basis $(\vec{a},\vec{b})$ will be called **reduced** if it has the following properties:

$|\vec{a}|$ is the smallest possible length for a nonzero lattice vector. $(A-2.1)$

$|\vec{b}|$ is the smallest possible one for a lattice vector linearly independent of $\vec{a}$. $(A-2.2)$

$$\vec{a}\cdot\vec{b}\geq 0. \qquad (A-2.3)$$

This definition is very similar to the one given by Cassels[1] (p.27), except for (A-2.3) which was added to further reduce the number of "reduced" bases. Condition (A-2.3) can always be satisfyed by taking $-\vec{b}$ instead of $\vec{b}$ if necessary. For any given lattice, there exists at least one such reduced basis.[1] The existence of such reduced basis is not enough, since what one needs is a constructive way to obtain it. This is what theorem 1 and the conclusion following it are all about.

Theorem 1: Conditions (A-2.1) and (A-2.2) of the above definition can be replaced by the weaker condition:

$$|\vec{a}|\leq|\vec{b}|\leq \min(|\vec{b}-\vec{a}|,|\vec{b}+\vec{a}|) \qquad (A-2.4)$$

Therefore, if $(\vec{a},\vec{b})$ is a basis satisfying (A-2.4), then it will satisfy (A-2.1) and (A-2.2).

For the proof of theorem 1, we shall need an obvious proposition.

Proposition: Let $\vec{a}$ and $\vec{b}$ be any two vectors. Let

$$\vec{u} = \lambda\vec{a} + (1-\lambda)\vec{b}, \qquad (0 \leq \lambda \leq 1)$$

then:

If $|\vec{a}| < |\vec{b}|$, then $|\vec{u}| \leq |\vec{b}|$ with sharp inequality unless $\vec{u}=\vec{b}$ $\qquad (A-2.5)$

If $|\vec{a}| = |\vec{b}|$, then $|\vec{u}| \leq |\vec{b}|$ with sharp inequality unless $\vec{u}=\vec{b}$ or $\vec{u}=\vec{a}$. $\qquad (A-2.6)$

proof: Consider the circle C in Fig. A-2.1. This circle has a radius of $|\vec{b}|$; if $|\vec{a}| < |\vec{b}|$, then $\vec{a}$ must be entirely inside C. Since the circle is convex, all the segment connecting $\vec{a}$ and $\vec{b}$ must be entirely within C, with the exception of the end point $\vec{b}$. In particular, $\vec{u}$ lies on this segment; it must be, therefore, within C, which proves (A-2.5). By taking the limit as the end point $\vec{a}$ approaches the circle C, (A-2.6) is proved.

Proof of theorem 1: First, let us show that $\vec{a}$ satisfying (A-2.4) has the smallest possible absolute value. Suppose a nonzero lattice vector $\vec{c}$ satisfies

$$|\vec{c}| < |\vec{a}|. \qquad (A-2.7)$$

Since $(\vec{a},\vec{b})$ are a basis, one can write

$$\vec{c} = n_a\vec{a} + n_b\vec{b} \qquad (A-2.8)$$

with n_a, n_b integers. Neither n_a nor n_b can be zero, since $(\vec{a},\vec{b})$ are a basis; hence there is no lattice vector colinear with either one them but having smaller absolute

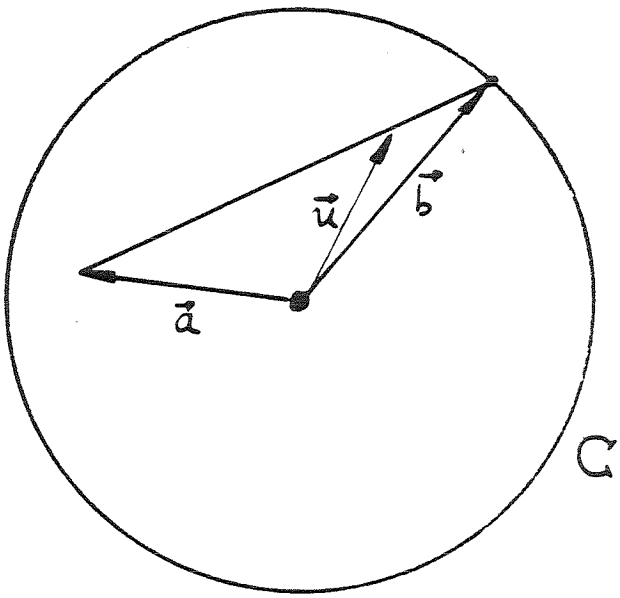

Fig. A-2.1. A demonstration that if $|\vec{a}| < |\vec{b}|$ and $\vec{u}$ lies on the segment connecting $\vec{a}$ and $\vec{b}$, then $|\vec{u}| \leqslant |\vec{b}|$ with sharp inequality unless $\vec{u}=\vec{b}$.

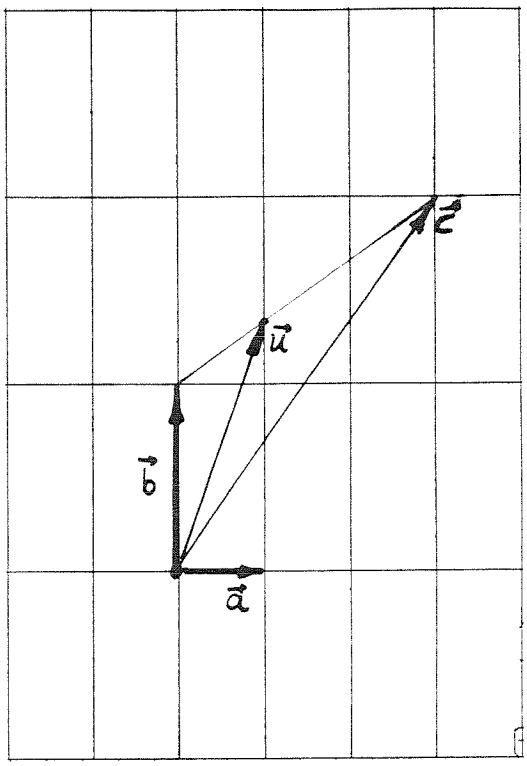

Fig. A-2.2. A construction used in the proof of theorem 1. $\vec{a}$ and $\vec{b}$ are two lattice vectors such that $|\vec{a}|$ is not larger than $|\vec{b}|$, and $\vec{b}$ does not shrink in size upon adding or subtracting $\vec{a}$. In that case $\vec{a}$ will have to be the smallest non-zero lattice vector, and $\vec{b}$ is the smallest lattice vector not colinear with $\vec{a}$.

value. One can assume without loss of generality that both n_a and n_b are positive. (replace $\vec{c}$ by $-\vec{c}$ if $n_b < 0$, and then substitute $\vec{b}-\vec{a}$ for $\vec{b}+\vec{a}$ in the rest of the proof if $n_a < 0$). Now look at the point $\vec{u}$ (not necessarily a lattice vector), defined as

$$\vec{u} = \left(1 - \frac{1}{n_a}\right)\vec{b} + \frac{1}{n_a}\vec{c} \qquad (A-2.9)$$

(see Fig.A-2.2) then, since $\vec{u}$ lies on the segment connecting $\vec{b}$ and $\vec{c}$, and since $|\vec{c}| < |\vec{a}| \leq |\vec{b}|$ by (A-2.4) and (A-2.7), it follows from (A-2.5) that $|\vec{u}| \leq |\vec{b}|$ with a sharp inequality unless $\vec{u}=\vec{b}$, but $\vec{u}=\vec{b}$ is impossible, since by (A-2.8) and (A-2.9)

$$\vec{u} = \vec{a} + \frac{n_a + n_b - 1}{n_a}\vec{b},$$

and this representation is unique. Therefore $|\vec{u}| < |\vec{b}|$.

Now,

$$\vec{b} + \vec{a} = \left(1 - \frac{n_a}{n_a + n_b - 1}\right)\vec{a} + \frac{n_a}{n_a + n_b - 1}\vec{u}$$

$\vec{b}+\vec{a}$, therefore, lies on the segment connecting $\vec{a}$ and $\vec{u}$. Thus, by (A-2.6), either $|\vec{b} + \vec{a}| \leq |\vec{u}| < |\vec{b}|$ or $|\vec{b} + \vec{a}| \leq |\vec{a}| \leq |\vec{b}|$. In any case $|\vec{b} + \vec{a}| \leq |\vec{b}|$ with equality implying $\vec{b}+\vec{a}=\vec{a}$ which is impossible. Therefore one must conclude that $|\vec{b} + \vec{a}| < \vec{b}$, in contradiction to (A-2.4).

One must conclude, therefore, that $\vec{a}$ has indeed the smallest possible absolute value. It remains to show that $\vec{b}$ has the smallest possible absolute value among lattice vectors not co-linear with $\vec{a}$. Assume $\vec{c}$ is a lattice vector, not co-linear with $\vec{a}$, such that $|\vec{c}| < |\vec{b}|$. Once again, since $(\vec{a},\vec{b})$ form a basis, $\vec{c}$ can be written as $\vec{c} = n_a\vec{a} + n_b\vec{b}$ with n_a, n_b integers. This time $n_b \neq 0$ by the assumption that $\vec{c}$ is not colinear with $\vec{a}$. Now repeat the construction of $\vec{u}$ exactly as before, since $\vec{u}$ lies on the segment connecting $\vec{c}$ and $\vec{b}$, it follows that $|\vec{u}| < |\vec{b}|$. Equality in this case cannot hold by exactly the same arguments as before. Now $\vec{b}+\vec{a}$ lies on the

segment connecting $\vec{a}$ and $\vec{u}$, therefore $|\vec{b}+\vec{a}| \leq \max(|\vec{a}|, |\vec{u}|) \leq |\vec{b}|$ from (A-2.6). But we assumed that $\vec{b} \leq |\vec{b}+\vec{a}|$; one must have, therefore, $|\vec{b}+\vec{a}| = |\vec{a}| = |\vec{b}|$, but this equality together with (A-2.6) implies $\vec{a} = \vec{b}+\vec{a}$ which is impossible. Once again contradicting the assumption that $|\vec{c}| < \vec{b}$.

Conclusion: Given any basis $(\vec{a},\vec{b})$ one can reduce it by the following procedure:

$$\text{If } \vec{a}\cdot\vec{b} < 0 \text{ replace } \vec{b} \text{ by } -\vec{b}. \qquad (A-2.10)$$

$$\text{If } |\vec{a}| > |\vec{b}| \text{ interchange } \vec{a} \text{ and } \vec{b} \text{ and go to (A-2.10).} \qquad (A-2.11)$$

$$\text{If } |\vec{b}| > |\vec{b}+\vec{a}| \text{ replace } \vec{b} \text{ by } \vec{b}+\vec{a} \text{ and go to (A-2.10)} \qquad (A-2.12)$$

$$\text{If } |\vec{b}| > |\vec{b}-\vec{a}|) \text{ replace } \vec{b} \text{ by } \vec{b}-\vec{a} \text{ and go back to (A-2.10).} \qquad (A-2.13)$$

$$|\vec{a}| \leq |\vec{b}| \leq \min(|\vec{b}+\vec{a}|, |\vec{b}-\vec{a}|), \text{ the basis is reduced.} \qquad (A-2.14)$$

Proof: (A-2.14) follows from Theorem 1. It is left to prove that the process (A-2.10)-(A-2.14) ends after a finite number of steps. After applying each one of (A-2.10)-(A-2.14), it is still true that the new set of $(\vec{a},\vec{b})$ is a basis. While (A-2.11) in general may increase $|\vec{b}|$, every such interchange will decrease $|\vec{a}|$. Nowhere in (A-2.10)-(A-2.14) can $|\vec{a}|$ grow, and since there are only a finite number of lattice vectors with absolute value smaller than $|\vec{a}|$, it follows that (A-2.11) could be applied only a finite number of times. (A-2.12)-(A-2.13) then can also be applied only a finite number of times, since every time one goes through (A-2.12)-(A-2.13), $|\vec{b}|$ decreases, or if not, the procedure is terminated by (A-2.14).

It is worth mentioning here, that the reduced basis is **not unique**. For example,

if $(\vec{a},\vec{b})$ is a reduced basis, so is $(-\vec{a},-\vec{b})$, and there might be few others. We will show, however, that:

Theorem 2: If $(\vec{a},\vec{b})$ and $(\vec{c},\vec{d})$ are two reduced bases of the same lattice, then:

$$|\vec{a}| = |\vec{c}| \qquad (A-2.15)$$

$$|\vec{b}| = |\vec{d}| \qquad (A-2.16)$$

$$\vec{a}\cdot\vec{b} = \vec{c}\cdot\vec{d} \qquad (A-2.17)$$

Proof: (A-2.15) follows from (A-2.1). If $|\vec{a}|\neq|\vec{b}|$ then $\vec{c}$ has to be colinear with $\vec{a}$, otherwise $(\vec{a},\vec{b})$ is not reduced. (Replacing $\vec{b}$ by $\vec{c}$ will reduce it further). Therefore, condition (A-2.2) becomes the same for both $\vec{b}$ and $\vec{d}$, therefore $|\vec{b}| = |\vec{d}|$. The case when $|\vec{a}| = |\vec{b}|$ is equally simple. We have already showed that if $\vec{a}$ and $\vec{c}$ are colinear, then $|\vec{b}| = |\vec{d}|$, however $\vec{a}$ and $\vec{c}$ need not be colinear in this case. If they are not colinear, one must have $|\vec{b}| = |\vec{c}|$ for $(\vec{a},\vec{b})$ to be reduced, and similarly one must have $|\vec{d}| = |\vec{a}|$ for $(\vec{c},\vec{d})$ to be reduced, therefore, (A-2.16) follows from (A-2.15).

The last thing remained to be proved is (A-2.17). Consider first the case $|\vec{a}| < |\vec{b}|$. It was shown earlier that in this case one must have $\vec{a} = \pm\vec{c}$, and by taking $(-\vec{c},-\vec{d})$ instead of $(\vec{c},\vec{d})$ if necessary, one may assume without loss of generality that

$$\vec{c} = \vec{a}. \qquad (A-2.18)$$

We will next show that

$$\vec{d} = \pm\vec{b} \quad \text{or} \quad \vec{d} = \pm\vec{b}+\vec{a} \quad \text{or} \quad \vec{d} = \pm\vec{b}-\vec{a}. \qquad (A-2.19)$$

Write $\vec{d}$ as $\vec{d} = n_a\vec{a}+n_b\vec{b}$. n_b is non-zero since $\vec{d}$ and $\vec{c}$ are not colinear. If $n_a = 0$, then (A-2.16) implies $\vec{d} = \pm\vec{b}$, and then (A-2.3) guaranties (A-2.17). Therefore one

may assume that neither n_a nor n_b vanishes. Now we proceed by a construction similar to the one done in the proof of Theorem 1. Let $\vec{u}$ be one of the four

$$\vec{u} = \begin{cases} +\left(1-\frac{1}{n_b}\right)\vec{a}+\frac{1}{n_b}\vec{d} & (n_a \geq 1, \quad n_b \geq 1) \\ -\left(1-\frac{1}{n_b}\right)\vec{a}+\frac{1}{n_b}\vec{d} & (n_a \leq -1, \quad n_b \geq 1) \\ +\left(1+\frac{1}{n_b}\right)\vec{a}-\frac{1}{n_b}\vec{d} & (n_a \geq 1, \quad n_b \leq -1) \\ -\left(1+\frac{1}{n_b}\right)\vec{a}-\frac{1}{n_b}\vec{d} & (n_a \leq -1, \quad n_b \leq -1) \end{cases} \qquad (A-2.20)$$

and consider the appropriate one of

$$\begin{aligned} \vec{a}+\vec{b} &= \left(1-\frac{n_b}{n_a+n_b-1}\right)\vec{b}+\frac{n_b}{n_a+n_b-1}\vec{u}, & (n_a \geq 1, \quad n_b \geq 1) \\ -\vec{a}+\vec{b} &= \left(1-\frac{n_b}{-n_a+n_b-1}\right)\vec{b}+\frac{n_b}{-n_a+n_b-1}\vec{u}, & (n_a \leq -1, \quad n_b \geq 1) \\ \vec{a}-\vec{b} &= -\left(1-\frac{-n_b}{n_a-n_b-1}\right)\vec{b}+\frac{-n_b}{n_a-n_b-1}\vec{u}, & (n_a \geq 1, \quad n_b \leq -1) \\ -\vec{a}-\vec{b} &= -\left(1-\frac{-n_b}{-n_a-n_b-1}\right)\vec{b}+\frac{-n_b}{-n_a-n_b-1}\vec{u}, & (n_a \leq -1, \quad n_b \leq -1) \end{aligned}$$

Therefore, one of $\pm\vec{a}\pm\vec{b}$ lies on the segment connecting $\pm\vec{b}$ and $\vec{u}$, while $\vec{u}$ in turn, lies on the segment connecting $\pm\vec{a}$ and $\vec{d}$. Hence by (A-2.6), either

$$|\pm\vec{a}\pm\vec{b}| \leq |\vec{u}| \leq |\vec{b}| \qquad (A-2.21)$$

or

$$|\pm\vec{a}\pm\vec{b}| \leq |\vec{a}| \qquad (A-2.22)$$

in any case, since $\vec{u} \neq \pm\vec{a}$ by (A-2.20), it follows from (A-2.4) and (A-2.6) that,

$$|\pm\vec{a}\pm\vec{b}| = |\vec{b}|. \qquad (A-2.23)$$

and

$$\pm\vec{a}\pm\vec{b} = \vec{u} = \vec{d}. \qquad (A-2.24)$$

which proves (A-2.19) for the case $|\vec{a}| < |\vec{b}|$. (In (A-2.21)-(A-2.24) $\pm\vec{a}\pm\vec{b}$ means one of the four, according to (A-2.19).)

From (A-2.16),(A-2.18) and (A-2.19), one can easily see that

$$\vec{a} \cdot \vec{b} = \pm \vec{c} \cdot \vec{d}. \qquad (A - 2.25)$$

This is obvious if $\vec{d} = \pm \vec{b}$ in (A-2.19). If, say, $\vec{d}=\vec{b}+\vec{a}$ in (A-2.19), then from (A-2.16) $|\vec{b}| = |\vec{b} + \vec{a}|$, and by squaring both sides one obtains

$$\vec{b} \cdot \vec{b} = \vec{a} \cdot \vec{a} + 2\vec{a} \cdot \vec{b} + \vec{b} \cdot \vec{b}$$

or $\vec{a} \cdot \vec{b} = -|\vec{a}|^2/2$. Similarly,

$$\vec{c} \cdot \vec{d} = \vec{a} \cdot \vec{d} = \vec{a} \cdot (\vec{a} + \vec{b}) = \vec{a} \cdot \vec{b} + |\vec{a}|^2 = |\vec{a}|^2/2,$$

and in this case $\vec{a} \cdot \vec{b} = -\vec{c} \cdot \vec{d}$, which proves (A-2.25) and then (A-2.17) follows from (A-2.3).

The case $|\vec{a}| = |\vec{b}|$ is very similar, but this time one can repeat the same argument and show that both $\vec{c}$ and $\vec{d}$ must be equal to either $\pm\vec{a}$ or $\pm\vec{b}$ or $\pm\vec{a} \pm \vec{b}$. To show that, one uses the same construction that we have used for (A-2.19). Note, however, that only one of $(\vec{c}, \vec{d})$ can be equal to $\pm\vec{a} \pm \vec{b}$. The reason is that when $|\vec{a}| = |\vec{b}|$, the four vectors $\pm\vec{a} \pm \vec{b}$ are either parallel or orthogonal. $\vec{c}$ and $\vec{d}$ cannot be parallel since they form a basis. They cannot be orthogonal, since the reduced basis of the square lattice is unique up to sign and order of the basis vectors, and $(\vec{a}, \vec{b})$ is also a reduced basis. Since only one of $(\vec{c}, \vec{d})$ can be equal to $\pm\vec{a} \pm \vec{b}$, the other one has to be equal to either $\pm\vec{a}$ or $\pm\vec{b}$. There is no loss of generality in assuming that it is $\vec{c} = \vec{a}$, and the rest is just as before.

Theorem 2 enables one to verify that two lattices are congruent, that is, they are actually the same up to a rigid transformation, no matter in what bases these

lattices are given. The real problem one faces in determining lattice matches, is more complicated. According to definition 2, one considers two lattices as matching if each one of them has a superlattice, such that the two superlattices are congruent. It is well worth at this point to characterize all superlattices of a given order. This will be done in theorem 3.

Let Λ_0 be a two dimensional lattice, viewed as a discrete, two- dimensional group of vectors in the plane. (the group operation is normal vector addition). A subgroup Λ will be called a **superlattice** if it is two dimensional. Any superlattice has a basis. If $(\vec{\mathbf{a}}_0, \vec{\mathbf{b}}_0)$ is a basis of Λ_0, and $(\vec{\mathbf{a}}, \vec{\mathbf{b}})$ is a basis of its superlattice Λ, then

$$\begin{pmatrix} \vec{\mathbf{a}} \\ \vec{\mathbf{b}} \end{pmatrix} = \begin{pmatrix} \mathrm{i} & \mathrm{j} \\ \mathrm{l} & \mathrm{m} \end{pmatrix} \begin{pmatrix} \vec{\mathbf{a}}_0 \\ \vec{\mathbf{b}}_0 \end{pmatrix} \qquad (A-2.26)$$

where i,j,l,m are integers, and the determinant of this transformation,

$$n = im - jl$$

is called the **index** of Λ in Λ_0. Its geometric meaning is as follows: the area of any primitive cell of the superlattice, is n times larger than that of the original lattice. Equivalently, every primitive cell of Λ, contains n lattice points of Λ_0.

Theorem 3: Given a lattice Λ_0 with a basis $(\vec{\mathbf{a}}_0, \vec{\mathbf{b}}_0)$, and a superlattice Λ of index n in Λ_0, one can always choose a basis $(\vec{\mathbf{a}},\vec{\mathbf{b}})$ of Λ such that the integers (i,j,l,m) in (A-2.26) satisfy the following conditions:

$$l = 0 \qquad (A-2.27)$$

$$1 \leq m \leq n, \qquad m \mid n \qquad (A-2.28)$$

$$1 \leq j \leq m \qquad (A-2.29)$$

$$i = n/m \qquad (A-2.30)$$

Proof: (A-2.27) is a consequence of Theorem I in chapter-I of Cassels.[1] (A-2.28) follows from (A-2.27) and the fact that $n = im - jl = im$, therefore m must divide n, thus $-n \leq m \leq n$, and by choosing -m instead of m if necessary, one can guarantee $m \geq 1$. Choosing -m instead of m will merely reverse the sign of $\vec{\mathbf{b}}$, and if ($\vec{\mathbf{a}}$, $\vec{\mathbf{b}}$) is a basis, so is ($\vec{\mathbf{a}}$,-$\vec{\mathbf{b}}$). Now (A-2.30) follows directly, and it only remains to show (A-2.29). One can always find an integer k, such that

$$1 \leq j + km \leq m$$

and now the effect of replacing j by j+km in (A-2.26) will be to replace ($\vec{\mathbf{a}}$, $\vec{\mathbf{b}}$) by ($\vec{\mathbf{a}}$+k$\vec{\mathbf{b}}$,$\vec{\mathbf{b}}$), and if one of them is a basis, so is the other.

Conclusion: For a given lattice, the number of non-congruent superlattices of an index n cannot exceed,

$$\sigma(n) = \sum_{m|n} m.$$

Now it is easy to formulate the general algorithm for finding lattice matches.

Step (1): Given a pair of crystal structures, scan over various crystal directions for each one of the two crystals. Every such crystal direction will determine a two dimensional lattice; one has, therefore, two 2-dimensional lattices, Λ_1 and Λ_2. Pick any pair of bases ($\vec{\mathbf{a}}_1^0$, $\vec{\mathbf{b}}_1^0$) and ($\vec{\mathbf{a}}_2^0$, $\vec{\mathbf{b}}_2^0$) for these two lattices. Let A_1 and A_2 be the corresponding unit-cell areas, then

$$A_1 = |\vec{\mathbf{a}}_1^0 \times \vec{\mathbf{b}}_1^0|, \qquad A_2 = |\vec{\mathbf{a}}_2^0 \times \vec{\mathbf{b}}_2^0|.$$

Step (2): Now one wants to scan over superlattices M_1 and M_2 of index n_1 and n_2 in Λ_1 and Λ_2 respectively. One does not want, however, to scan over too many irrelevant superlattices. Since a necessary condition for M_1 and M_2 to be congruent is that they will have the same unit-cell area, it follows that a necessary condition for the match is

$$n_1 A_1 = n_2 A_2 \qquad (A - 2.31)$$

Therefore it suffices to scan over pairs of integers n_1 and n_2 satisfying

$$\frac{n_1}{n_2} \approx \frac{A_2}{A_1},$$

to within a prescribed precision. The scanning should end when n_1 and n_2 become too large. This upper bound is also prescribed, and I do not have at this stage any reasonable value for this upper bound, more than a general feeling that the higher n_1 and n_2 are, (that is the larger the unit-cell area of the congruent superlattices), the worse the match is. (In the limit when $n_1, n_2 \to \infty$, the interface becomes amorphous).

Step (3): Now given n_1 and n_2, one scans over all superlattices of index n_1 and n_2. In view of Theorem 3 this is equivalent to generating sets of (i_1, j_1, m_1) and (i_2, j_2, m_2), each satisfying (A-2.27)-(A-2.30), to be plugged into (A-2.26) in order to determine a pair of bases $(\vec{\mathbf{a}}_1, \vec{\mathbf{b}}_1)$ of M_1 and $(\vec{\mathbf{a}}_2, \vec{\mathbf{b}}_2)$ of M_2.

Step (4): Given M_1 and M_2 with their bases, one wants to compare them for congruency. If each one of the two bases is not reduced in the sense of definition 3, one applys the reduction procedure (A-2.10)-(A-2.14). Assuming the bases were reduced, one is left with two sets of lengths and angles, (a_1, b_1, α_1) and (a_2, b_2, α_2), where

$$a = |\vec{\mathbf{a}}|, \qquad b = |\vec{\mathbf{b}}|, \qquad \cos\alpha = \frac{\vec{\mathbf{a}} \cdot \vec{\mathbf{b}}}{|\vec{\mathbf{a}}| \cdot |\vec{\mathbf{b}}|}$$

with the appropriate index, 1 or 2. Now in view of theorem 2, M_1 and M_2 are congruent if,

$$(a_1, b_1, \alpha_1) = (a_2, b_2, \alpha_2).$$

One checks this condition to hold within a prescribed precision.

In actual use of this method for epitaxy, one often wants to hold the substrate orientation fixed, and scan over the possible orientations of the film. Such scan is done by holding A_1 fixed in (A-2.31), scanning on n_1 and then on all the possible film reciprocal vectors that satisfy (A-2.31) with some n_2. We will now show how this is done.

Let $(\vec{t}_1, \vec{t}_2, \vec{t}_3)$ be a basis of the second lattice (the film). What one wants is two integer triplets (r_1, r_2, r_3) and (s_1, s_2, s_3), such that the two lattice vectors

$$\vec{a}_2 = r_1\vec{t}_1 + r_2\vec{t}_2 + r_3\vec{t}_3 \qquad \text{and} \qquad \vec{b}_2 = s_1\vec{t}_1 + s_2\vec{t}_2 + r_3\vec{t}_3$$

are the basis of the second superlattice satisfying (A-2.26,31,32). For this to happen one must have

$$n_1 A_1 = |\vec{a}_2 \times \vec{b}_2|.$$

But

$$|\vec{a}_2 \times \vec{b}_2| = \left|\begin{matrix} r_1 & r_2 \\ s_1 & s_2 \end{matrix}\right| |(\vec{t}_1 \times \vec{t}_2) + \left|\begin{matrix} r_2 & r_3 \\ s_2 & s_3 \end{matrix}\right| |(\vec{t}_2 \times \vec{t}_3) + \left|\begin{matrix} r_3 & r_1 \\ s_3 & s_1 \end{matrix}\right| |(\vec{t}_3 \times \vec{t}_1),$$

and recall that the basis for the reciprocal basis $(\vec{r}_1, \vec{r}_2, \vec{r}_3)$ is related to the original basis by,

$$\vec{r}_1 = \frac{\vec{t}_2 \times \vec{t}_3}{|\vec{t}_1 \cdot (\vec{t}_2 \times \vec{t}_3)|}, \qquad \vec{r}_2 = \frac{\vec{t}_3 \times \vec{t}_1}{|\vec{t}_1 \cdot (\vec{t}_2 \times \vec{t}_3)|}, \qquad \vec{r}_3 = \frac{\vec{t}_1 \times \vec{t}_2}{|\vec{t}_1 \cdot (\vec{t}_2 \times \vec{t}_3)|}.$$

Therefore,

Theorem 4: A necessary condition for a lattice match with the (h, k, l) direction of the second material is

$$|h\vec{r}_1 + k\vec{r}_2 + l\vec{r}_3| = n_1 \frac{A_1}{U_2},$$

where $U_2 = |\vec{t}_1 \cdot (\vec{t}_2 \times \vec{t}_3)|$ is the unit-cell volume of the second lattice.

We now address the following question. Let,

$$F(x, y, z) = |x\vec{r}_1 + y\vec{r}_2 + z\vec{r}_3|.$$

What are the bounds for a search on h,k,l (integers) such that,

$$F(h, k, l) < A.$$

Fix h. Look for $min[F(h, y, z)]$. Suppose the minimum is F($\vec{t}$), where $\vec{t} = h\vec{r}_1 + y\vec{r}_2 + z\vec{r}_3$. Then,

$$0 = F_y(h, y, z) = \vec{r}_2 \cdot \vec{t}.$$

$$0 = F_z(h, y, z) = \vec{r}_3 \cdot \vec{t}.$$

Thus, $\vec{t}$ is perpendicular to both $\vec{r}_2$ and $\vec{r}_3$, i.e., $\vec{t}$ is parallel to $\vec{t}_1$. Now,

$$\vec{t}_1 = (\vec{t}_1 \cdot \vec{t}_1)\vec{r}_1 + (\vec{t}_1 \cdot \vec{t}_2)\vec{r}_2 + (\vec{t}_1 \cdot \vec{t}_3)\vec{r}_3,$$

therefore,

$$|h| < \frac{A(\vec{t}_1 \cdot \vec{t}_1)}{F[(\vec{t}_1 \cdot \vec{t}_1), (\vec{t}_1 \cdot \vec{t}_2), (\vec{t}_1 \cdot \vec{t}_3)]},$$

with similar expressions for k and l.

References for Appendix A-2.2.

1. J. W. S. Cassels, *An Introduction to the Geometry of Numbers*, Springer-Verlag (1959)

Appendix A-2.3

Lattice match between silicides and silicon

In this appendix we present the results of a systematic search for lattice match between binary-transition-metal silicides and silicon. The input parameters for this search were the crystal structures of the silicides, and the quality of the match. The crystal structures of the silicides used in this search are given in the next appendix (A-2.4); the crystal structure of silicon is face-centered cubic with a lattice parameter of 5.431Å. The quality of the match, as described in the introduction to Chapter 2, is given by two parameters: the mismatch and the common unit-cell area. In this appendix the allowed mismatch is 1%, and the common unit-cell area is restricted to $200\mathring{A}^2$. Further restrictions on the possible faces were imposed: for silicon, only the (111),(100) and (110) faces were considered; for the silicides we used only those faces whose two-dimensional translations form a lattice with a unit cell of $50\mathring{A}^2$ or less.

The results of our search is given as a set of 133 tables; each table corresponds to one silicide. Each table contains a caption and a body. The two materials (silicide/silicon), the common unit-cell area, and the matching precision are given in the first two lines in the caption; the crystal structure of the silicide is given in the third line of the caption; if several crystal structures are given in the literature for the same silicide, each one was considered as a different phase. The faces of both the silicide and the silicon that were checked for a possible match are given in the last few lines of the caption.

The body of each table contains twelve columns. For any possible match, the corresponding faces are given in the first column (labeled "Matching faces"). Only one face in a symmetry class is given; for example, the Si(100) face represents any one of (100), ($\bar{1}$00), (010), (0$\bar{1}$0), (001), or (00$\bar{1}$). A pair of matching crystal

directions are given in the second column (labeled "Orientation"). This pair is required to define the mutual orientation of one crystal with respect to the other. There are infinite number of such pairs of matching crystal directions, for any matching face; only one of them (the shortest) is given for any match. Each one of the two directions in this pair represents a symmetry class (Si[100] stands for one of [100], [$\bar{1}$00], [010], and so on). The direction on the left refers to the silicide; the one on the right refers to silicon. The common unit-cell area is given in the third column (labeled "Area"); this is actually the unit-cell area on the silicide side of the interface, and the corresponding area for the silicon is almost the same. The dimensions of the common unit cells, on both sides of the interface, are given in the next six columns (labeled "a_2", "b_2", ..., "α_1"). Here each unit cell is a parallelogram, whose short side is a, the long side is b, and the angle between them is α. The subscript 2 refers to the silicide, and the subscript 1 refers to silicon. All areas, lengths, and angles in these tables are given in units of square angstroms, angstroms, and degrees, respectively. The last three columns give the mismatch percentage, i.e.

$$\%_a = 100 \cdot |\frac{a_1 - a_2}{a_1}|, \quad \%_b = 100 \cdot |\frac{b_1 - b_2}{b_1}|, \quad \%_\alpha = 100 \cdot |\frac{\alpha_1 - \alpha_2}{\alpha_1}|.$$

An example of a typical match table, as well as a graphic explanation of the entries of that table are given in Fig. A-2.3.1. Following this figure, we list the 133 tables. Some tables do not include a body; in that case no match was found for that pair of crystals, under the restrictions mentioned above.

$PtSi/Si$ lattice match, using a matched unit cell not exceeding 200.$\mathring{A}^2$ and matching precision of 1.0%.
$PtSi$ is orthorhombic with a= 5.577, b= 5.916, c= 3.587;
Si (111), (100), and (110) compared to $PtSi$ (010), (100), (110), (001), (011), (101), (111), (120), and (210)

Matching faces	Orientation	Area	a_2	b_2	α_2	a_1	b_1	α_1	$\%_a$	$\%_b$	$\%_\alpha$
PtSi(110)/Si(100)	[001]||[001]	175.	10.76	16.26	90.00	10.86	16.29	90.00	0.9	0.2	0.0

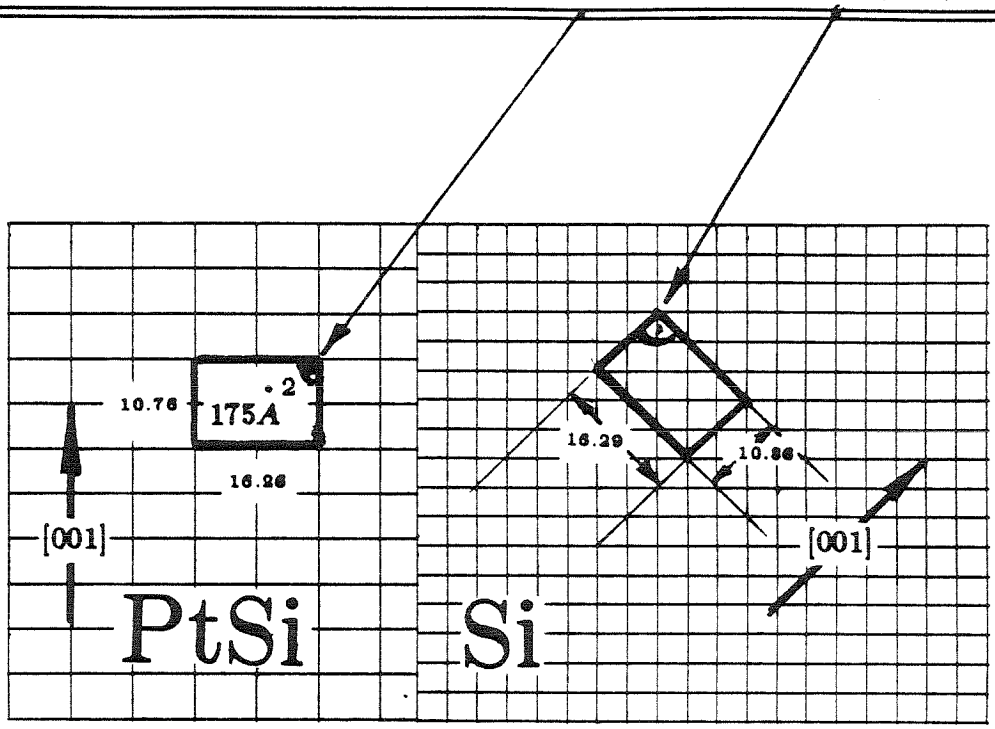

Fig. A-2.3.1. A sample of a match table and the meaning of each of its columns. The grids in this figure represent the translations parallel to the interface.

Sc_5Si_3/Si lattice match, using a matched unit cell not exceeding 200.$\mathring{A}^2$ and matching precision of 1.0%.
Sc_5Si_3 is hexagonal with a= 7.861, c= 5.812;
Si (111), (100), and (110) compared to Sc_5Si_3 $(10\bar{1}0)$

Matching faces	Orientation	Area	a_2	b_2	α_2	a_1	b_1	α_1	$\%_a$	$\%_b$	$\%_\alpha$

$ScSi/Si$ lattice match, using a matched unit cell not exceeding 200.$\mathring{A}^2$ and matching precision of 1.0%.
$ScSi$ is orthorhombic with a= 3.988, b= 9.882, c= 3.659;
Si (111), (100), and (110) compared to $ScSi$ (010), (100), (110), (001), (011), (120), and (021)

Matching faces	Orientation	Area	a_2	b_2	α_2	a_1	b_1	α_1	$\%_a$	$\%_b$	$\%_\alpha$

Sc_2Si_3/Si lattice match, using a matched unit cell not exceeding 200.$\mathring{A}^2$ and matching precision of 1.0%.
Sc_2Si_3 is hexagonal with a= 3.664, c= 3.877;
Si (111), (100), and (110) compared to Sc_2Si_3 (0001), $(10\bar{1}0)$, $(10\bar{1}1)$, $(11\bar{2}0)$, $(11\bar{2}1)$, $(10\bar{1}2)$, $(20\bar{2}1)$, $(11\bar{2}2)$, $(21\bar{3}0)$, $(10\bar{1}3)$, $(21\bar{3}1)$, $(11\bar{2}3)$, $(30\bar{3}1)$, $(21\bar{3}2)$, $(20\bar{2}3)$, $(30\bar{3}2)$, and $(10\bar{1}4)$

Matching faces	Orientation	Area	a_2	b_2	α_2	a_1	b_1	α_1	$\%_a$	$\%_b$	$\%_\alpha$
Sc_2Si_3 (0001)/Si(111)	[2$\bar{5}$70]‖[121]	151.	13.21	13.21	60.00	13.30	13.30	60.00	0.7	0.7	0.0
Sc_2Si_3 (10$\bar{1}$0)/Si(111)	[0001]‖[01$\bar{1}$]	128.	3.88	32.98	90.00	3.84	33.26	90.00	0.9	0.9	0.0
Sc_2Si_3 (21$\bar{3}$2)/Si(111)	[66$\bar{1}$]‖[121]	177.	13.27	13.75	75.69	13.30	13.85	76.10	0.2	0.7	0.5
Sc_2Si_3 (11$\bar{2}$0)/Si(100)	[0001]‖[011]	74.	3.88	19.04	90.00	3.84	19.20	90.00	0.9	0.9	0.0
Sc_2Si_3 (21$\bar{3}$0)/Si(100)	[0001]‖[011]	75.	3.88	19.39	90.00	3.84	19.20	90.00	0.9	1.0	0.0
Sc_2Si_3 (11$\bar{2}$0)/Si(110)	[0001]‖[1$\bar{1}$0]	148.	3.88	38.08	90.00	3.84	38.02	90.00	0.9	0.2	0.0
Sc_2Si_3 (21$\bar{3}$0)/Si(110)	[0001]‖[1$\bar{1}$0]	188.	3.88	48.47	90.00	3.84	48.88	90.00	0.9	0.8	0.0

Ti_5Si_3/Si lattice match, using a matched unit cell not exceeding 200.$\mathring{A}^2$ and matching precision of 1.0%.
Ti_5Si_3 is hexagonal with a= 7.429, c= 5.139;
Si (111), (100), and (110) compared to Ti_5Si_3 (10$\bar{1}$0) and (0001)

Matching faces	Orientation	Area	a_2	b_2	α_2	a_1	b_1	α_1	$\%_a$	$\%_b$	$\%_\alpha$

Ti_5Si_4/Si lattice match, using a matched unit cell not exceeding 200.$\mathring{A}^2$ and matching precision of 1.0%.
Ti_5Si_4 is orthorhombic with a= 6.645, b= 12.690, c= 6.506;
Si (111), (100), and (110) compared to Ti_5Si_4 (010)

Matching faces	Orientation	Area	a_2	b_2	α_2	a_1	b_1	α_1	$\%_a$	$\%_b$	$\%_\alpha$

Ti_5Si_4/Si lattice match, using a matched unit cell not exceeding 200.$\mathring{A}^2$ and matching precision of 1.0%.
Ti_5Si_4 is tetragonal with a= 6.702, c= 12.174;
Si (111), (100), and (110) compared to Ti_5Si_4 (001)

Matching faces	Orientation	Area	a_2	b_2	α_2	a_1	b_1	α_1	$\%_a$	$\%_b$	$\%_\alpha$
Ti_5Si_4 (001)/Si(111)	[010]‖[2$\bar{1}$1]	180.	6.70	26.81	90.00	6.65	26.88	90.00	0.8	0.3	0.0

$TiSi/Si$ lattice match, using a matched unit cell not exceeding 200.$\mathring{A}^2$ and matching precision of 1.0%.
$TiSi$ is orthorhombic with a= 3.618, b= 6.492, c= 4.973;
Si (111), (100), and (110) compared to $TiSi$ (010), (001), (011), (100), (110), (101), (021), (111), and (120)

Matching faces	Orientation	Area	a_2	b_2	α_2	a_1	b_1	α_1	$\%_a$	$\%_b$	$\%_\alpha$
TiSi(011)/Si(100)	[100]‖[010]	178.	10.85	16.36	90.00	10.86	16.29	90.00	0.1	0.4	0.0

$TiSi/Si$ lattice match, using a matched unit cell not exceeding 200.$\mathring{A}^2$ and matching precision of 1.0%.
$TiSi$ is orthorhombic with a= 3.638, b= 6.544, c= 4.997;
Si (111), (100), and (110) compared to $TiSi$ (010), (001), (011), (100), (110), (101), (021), (111), and (120)

Matching faces	Orientation	Area	a_2	b_2	α_2	a_1	b_1	α_1	$\%_a$	$\%_b$	$\%_\alpha$

$TiSi_2/Si$ lattice match, using a matched unit cell not exceeding 200.$\mathring{A}^2$ and matching precision of 1.0%.
$TiSi_2$ is face-centered orthorhombic with a= 8.267, b= 4.800, c= 8.550;
Si (111), (100), and (110) compared to $TiSi_2$ (001), (100), (111), (101), (010), (113), (311), (011), (110), (102), (201), and (313)

Matching faces	Orientation	Area	a_2	b_2	α_2	a_1	b_1	α_1	$\%_a$	$\%_b$	$\%_\alpha$

$TiSi_2/Si$ lattice match, using a matched unit cell not exceeding 200.$\mathring{A}^2$ and matching precision of 1.0%.
$TiSi_2$ is one-face-centered orthorhombic with a= 3.562, b= 13.531, c= 3.550;
Si (111), (100), and (110) compared to $TiSi_2$ (010), (001), (110), (021), (130), (150), (100), (011), (112), (132), (031), (152), and (012)

Matching faces	Orientation	Area	a_2	b_2	α_2	a_1	b_1	α_1	$\%_a$	$\%_b$	$\%_\alpha$

$TiSi_2/Si$ lattice match, using a matched unit cell not exceeding 200.$\mathring{A}^2$ and matching precision of 1.0%.
$TiSi_2$ is hexagonal with a= 4.712, c= 6.535;
Si (111), (100), and (110) compared to $TiSi_2$ (0001), (10$\bar{1}$0), (10$\bar{1}$1), and (10$\bar{1}$2)

Matching faces	Orientation	Area	a_2	b_2	α_2	a_1	b_1	α_1	$\%_a$	$\%_b$	$\%_\alpha$

V_3Si/Si lattice match, using a matched unit cell not exceeding 200.$\mathring{A}^2$ and matching precision of 1.0%.
V_3Si is simple cubic with a= 4.726;
Si (111), (100), and (110) compared to V_3Si (001), (011), (111), and (012)

Matching faces	Orientation	Area	a_2	b_2	α_2	a_1	b_1	α_1	$\%_a$	$\%_b$	$\%_\alpha$
V_3 Si(001)/Si(111)	[110]‖[12$\bar{1}$]	179.	6.68	26.73	90.00	6.65	26.88	90.00	0.5	0.6	0.0
V_3 Si(111)/Si(111)	[10$\bar{1}$]‖[1$\bar{2}$1]	39.	6.68	6.68	60.00	6.65	6.65	60.00	0.5	0.5	0.0
V_3 Si(011)/Si(110)	[01$\bar{1}$]‖[1$\bar{1}$2]	63.	6.68	9.45	90.00	6.65	9.41	90.00	0.5	0.5	0.0
V_3 Si(011)/Si(110)	[100]‖[1$\bar{1}$1]	126.	9.45	13.37	90.00	9.41	13.30	90.00	0.5	0.5	0.0
V_3 Si(011)/Si(110)	[21$\bar{1}$]‖[1$\bar{1}$0]	126.	11.58	11.58	70.53	11.52	11.52	70.53	0.5	0.5	0.0
V_3 Si(011)/Si(110)	[21$\bar{1}$]‖[1$\bar{1}$4]	190.	11.58	16.37	90.00	11.52	16.29	90.00	0.5	0.5	0.0
V_3 Si(011)/Si(110)	[2$\bar{1}$1]‖[1$\bar{1}$0]	190.	11.58	16.37	90.00	11.52	16.29	90.00	0.5	0.5	0.0

V_5SI_3/Si lattice match, using a matched unit cell not exceeding 200.$\mathring{A}^2$ and matching precision of 1.0%.
V_5SI_3 is body-centered tetragonal with a= 9.410, c= 4.747;
Si (111), (100), and (110) compared to V_5SI_3 (110), (100), and (101)

Matching faces	Orientation	Area	a_2	b_2	α_2	a_1	b_1	α_1	$\%_a$	$\%_b$	$\%_\alpha$
V_5 SI_3 (110)/Si(110)	[001]‖[1$\bar{1}$1]	126.	9.49	13.31	90.00	9.41	13.30	90.00	0.9	0.0	0.0

V_5Si_3/Si lattice match, using a matched unit cell not exceeding 200.$\mathring{A}^2$ and matching precision of 1.0%.
V_5Si_3 is hexagonal with a= 7.121, c= 4.832;
Si (111), (100), and (110) compared to V_5Si_3 (10$\bar{1}$0) and (0001)

Matching faces	Orientation	Area	a_2	b_2	α_2	a_1	b_1	α_1	$\%_a$	$\%_b$	$\%_\alpha$

V_6Si_5/Si lattice match, using a matched unit cell not exceeding 200.$\mathring{A}^2$ and matching precision of 1.0%.
V_6Si_5 is body-centered orthorhombic with a= 15.966, b= 7.501, c= 4.858;
Si (111), (100), and (110) compared to V_6Si_5 (100) and (110)

Matching faces	Orientation	Area	a_2	b_2	α_2	a_1	b_1	α_1	$\%_a$	$\%_b$	$\%_\alpha$

VSi_2/Si lattice match, using a matched unit cell not exceeding 200.$\mathring{A}^2$ and matching precision of 1.0%.
VSi_2 is hexagonal with a= 4.571, c= 6.372;
Si (111), (100), and (110) compared to VSi_2 (0001), (10$\bar{1}$0), (10$\bar{1}$1), and (10$\bar{1}$2)

Matching faces	Orientation	Area	a_2	b_2	α_2	a_1	b_1	α_1	$\%_a$	$\%_b$	$\%_\alpha$
VSi_2 (0001)/Si(111)	[2$\bar{1}$10]‖[31$\bar{4}$]	163.	13.71	13.71	60.00	13.85	13.85	60.00	1.0	1.0	0.0

Cr_3Si/Si lattice match, using a matched unit cell not exceeding 200.$\mathring{A}^2$ and matching precision of 1.0%.
Cr_3Si is simple cubic with a= 4.555;
Si (111), (100), and (110) compared to Cr_3Si (001), (011), (111), and (012)

Matching faces	Orientation	Area	a_2	b_2	α_2	a_1	b_1	α_1	$\%_a$	$\%_b$	$\%_\alpha$

Cr_5Si_3/Si lattice match, using a matched unit cell not exceeding 200.$\mathring{A}^2$ and matching precision of 1.0%.
Cr_5Si_3 is body-centered tetragonal with a= 9.150, c= 4.639;
Si (111), (100), and (110) compared to Cr_5Si_3 (110), (100), and (101)

Matching faces	Orientation	Area	a_2	b_2	α_2	a_1	b_1	α_1	$\%_a$	$\%_b$	$\%_\alpha$

$CrSi/Si$ lattice match, using a matched unit cell not exceeding 200.$\mathring{A}^2$ and matching precision of 1.0%.
$CrSi$ is simple cubic with a= 4.622;
Si (111), (100), and (110) compared to $CrSi$ (001), (011), (111), and (012)

Matching faces	Orientation	Area	a_2	b_2	α_2	a_1	b_1	α_1	$\%_a$	$\%_b$	$\%_\alpha$
CrSi(001)/Si(100)	[100]||[051]	192.	13.87	13.87	90.00	13.85	13.85	90.00	0.1	0.1	0.0

$CrSi_2/Si$ lattice match, using a matched unit cell not exceeding 200.$\mathring{A}^2$ and matching precision of 1.0%.
$CrSi_2$ is hexagonal with a= 4.430, c= 6.365;
Si (111), (100), and (110) compared to $CrSi_2$ (0001), (10$\bar{1}$0), (10$\bar{1}$1), (10$\bar{1}$2), and (11$\bar{2}$0)

Matching faces	Orientation	Area	a_2	b_2	α_2	a_1	b_1	α_1	$\%_a$	$\%_b$	$\%_\alpha$
$CrSi_2$ (0001)/Si(111)	[03$\bar{3}$0]‖[1$\bar{1}$0]	51.	7.67	7.67	60.00	7.68	7.68	60.00	0.1	0.1	0.0
$CrSi_2$ (0001)/Si(100)	[33$\bar{0}$0]‖[01$\bar{1}$]	119.	7.67	15.97	76.10	7.68	15.83	75.96	0.1	0.9	0.2
$CrSi_2$ (11$\bar{2}$0)/Si(100)	[3$\bar{3}$00]‖[01$\bar{1}$]	147.	7.67	19.09	90.00	7.68	19.20	90.00	0.1	0.6	0.0
$CrSi_2$ (10$\bar{1}$0)/Si(110)	[12$\bar{1}$1]‖[1$\bar{1}$0]	85.	7.75	10.91	89.14	7.68	10.86	90.00	1.0	0.4	1.0
$CrSi_2$ (10$\bar{1}$0)/Si(110)	[242$\bar{1}$]‖[001]	169.	10.91	15.51	89.14	10.86	15.36	90.00	0.4	1.0	1.0

Mn_3Si/Si lattice match, using a matched unit cell not exceeding 200.$\mathring{A}^2$ and matching precision of 1.0%.
Mn_3Si is simple cubic with a= 5.722;
Si (111), (100), and (110) compared to Mn_3Si (001) and (011)

Matching faces	Orientation	Area	a_2	b_2	α_2	a_1	b_1	α_1	$\%_a$	$\%_b$	$\%_\alpha$
Mn_3 Si(001)/Si(100)	[100]‖[011]	131.	11.44	11.44	90.00	11.52	11.52	90.00	0.7	0.7	0.0
Mn_3 Si(011)/Si(110)	[100]‖[1$\bar{1}$0]	185.	11.44	16.18	90.00	11.52	16.29	90.00	0.7	0.7	0.0
Mn_3 Si(011)/Si(110)	[100]‖[11$\bar{4}$]	185.	11.44	16.18	90.00	11.52	16.29	90.00	0.7	0.7	0.0

Mn_5Si_3/Si lattice match, using a matched unit cell not exceeding 200.$\mathring{A}^2$ and matching precision of 1.0%.
Mn_5Si_3 is hexagonal with a= 6.910, c= 4.814;
Si (111), (100), and (110) compared to Mn_5Si_3 (10$\bar{1}$0) and (0001)

Matching faces	Orientation	Area	a_2	b_2	α_2	a_1	b_1	α_1	$\%_a$	$\%_b$	$\%_\alpha$
Mn_5 Si_3 (0001)/Si(111)	[2$\bar{1}\bar{1}$0]‖[31$\bar{4}$]	165.	13.82	13.82	60.00	13.85	13.85	60.00	0.2	0.2	0.0

$MnSi/Si$ lattice match, using a matched unit cell not exceeding 200.$\mathring{A}^2$ and matching precision of 1.0%.
$MnSi$ is simple cubic with a= 4.558;
Si (111), (100), and (110) compared to $MnSi$ (001), (011), (111), and (012)

Matching faces	Orientation	Area	a_2	b_2	α_2	a_1	b_1	α_1	$\%_a$	$\%_b$	$\%_\alpha$

Mn_4Si_7/Si lattice match, using a matched unit cell not exceeding 200.$\mathring{A}^2$ and matching precision of 1.0%.
Mn_4Si_7 is tetragonal with a= 5.506, c= 17.522;
Si (111), (100), and (110) compared to Mn_4Si_7 (001)

Matching faces	Orientation	Area	a_2	b_2	α_2	a_1	b_1	α_1	$\%_a$	$\%_b$	$\%_\alpha$

Fe_3Si/Si lattice match, using a matched unit cell not exceeding 200.$\mathring{A}^2$ and matching precision of 1.0%.
Fe_3Si is simple cubic with a= 5.651;
Si (111), (100), and (110) compared to Fe_3Si (001) and (011)

Matching faces	Orientation	Area	a_2	b_2	α_2	a_1	b_1	α_1	$\%_a$	$\%_b$	$\%_\alpha$

Fe_5Si_3/Si lattice match, using a matched unit cell not exceeding 200.$\mathring{A}^2$ and matching precision of 1.0%.
Fe_5Si_3 is hexagonal with a= 6.741, c= 4.715;
Si (111), (100), and (110) compared to Fe_5Si_3 $(10\bar{1}0)$ and (0001)

Matching faces	Orientation	Area	a_2	b_2	α_2	a_1	b_1	α_1	$\%_a$	$\%_b$	$\%_\alpha$
Fe_5Si_3 $(10\bar{1}0)$/Si(110)	$[\bar{1}2\bar{1}2]\|\|[1\bar{1}0]$	127.	11.59	11.59	71.12	11.52	11.52	70.53	0.6	0.6	0.8
Fe_5Si_3 $(10\bar{1}0)$/Si(110)	$[\bar{1}2\bar{1}2]\|\|[1\bar{1}\bar{4}]$	191.	11.59	16.45	89.41	11.52	16.29	90.00	0.6	1.0	0.7

$FeSi/Si$ lattice match, using a matched unit cell not exceeding 200.$\mathring{A}^2$ and matching precision of 1.0%.
$FeSi$ is simple cubic with a= 4.489;
Si (111), (100), and (110) compared to $FeSi$ (001), (011), (111), (012), and (112)

Matching faces	Orientation	Area	a_2	b_2	α_2	a_1	b_1	α_1	$\%_a$	$\%_b$	$\%_\alpha$

$FeSi_2/Si$ lattice match, using a matched unit cell not exceeding 200.$\mathring{A}^2$ and matching precision of 1.0%.
$FeSi_2$ is tetragonal with a= 2.690, c= 5.134;
Si (111), (100), and (110) compared to $FeSi_2$ (001), (010), (011), (110), (012), (111), (112), (013), (021), (113), (120), (121), (014), (122), (114), (023), (123), (015), (221), (115), (031), (124), (130), (032), (131), (223), (025), (016), (132), (125), (116), (133), and (230)

Matching faces	Orientation	Area	a_2	b_2	α_2	a_1	b_1	α_1	$\%_a$	$\%_b$	$\%_\alpha$
$FeSi_2$ (001)/Si(111)	[110]‖[01$\bar{1}$]	101.	3.80	26.63	90.00	3.84	26.61	90.00	0.9	0.1	0.0
$FeSi_2$ (110)/Si(111)	[1$\bar{1}$0]‖[01$\bar{1}$]	176.	3.80	46.21	90.00	3.84	46.56	90.00	0.9	0.8	0.0
$FeSi_2$ (223)/Si(111)	[1$\bar{1}$0]‖[01$\bar{1}$]	179.	3.80	46.99	90.00	3.84	46.56	90.00	0.9	0.9	0.0
$FeSi_2$ (001)/Si(100)	[110]‖[011]	14.	3.80	3.80	90.00	3.84	3.84	90.00	0.9	0.9	0.0
$FeSi_2$ (110)/Si(100)	[1$\bar{1}$0]‖[01$\bar{1}$]	59.	3.80	15.40	90.00	3.84	15.36	90.00	0.9	0.3	0.0
$FeSi_2$ (012)/Si(100)	[100]‖[001]	160.	5.38	29.87	84.83	5.43	29.99	84.81	0.9	0.4	0.0
$FeSi_2$ (112)/Si(100)	[1$\bar{1}$0]‖[01$\bar{1}$]	73.	3.80	19.17	90.00	3.84	19.20	90.00	0.9	0.2	0.0
$FeSi_2$ (013)/Si(100)	[100]‖[001]	103.	5.38	19.32	82.00	5.43	19.20	81.87	0.9	0.6	0.2
$FeSi_2$ (113)/Si(100)	[1$\bar{1}$0]‖[01$\bar{1}$]	58.	3.80	15.35	90.00	3.84	15.36	90.00	0.9	0.1	0.0
$FeSi_2$ (121)/Si(100)	[2$\bar{1}$0]‖[012]	190.	12.03	15.86	85.65	12.14	15.83	85.60	0.9	0.2	0.1
$FeSi_2$ (114)/Si(100)	[1$\bar{1}$0]‖[01$\bar{1}$]	175.	3.80	45.89	90.00	3.84	46.08	90.00	0.9	0.4	0.0
$FeSi_2$ (032)/Si(100)	[100]‖[001]	88.	5.38	16.31	90.00	5.43	16.29	90.00	0.9	0.1	0.0
$FeSi_2$ (131)/Si(100)	[3$\bar{1}$0]‖[013]	89.	8.51	10.95	71.90	8.59	10.86	71.57	0.9	0.8	0.5
$FeSi_2$ (131)/Si(100)	[1$\bar{1}$2]‖[001]	177.	10.95	17.01	71.90	10.86	17.17	71.57	0.8	0.9	0.5
$FeSi_2$ (116)/Si(100)	[1$\bar{1}$0]‖[01$\bar{1}$]	190.	3.80	50.06	90.00	3.84	49.92	90.00	0.9	0.3	0.0

$FeSi_2$ (Continued)

Matching faces	Orientation	Area	a_2	b_2	α_2	a_1	b_1	α_1	$\%_a$	$\%_b$	$\%_\alpha$
$FeSi_2$ (001)/Si(110)	[010]‖[001]	145.	5.38	26.90	90.00	5.43	26.88	90.00	0.9	0.1	0.0
$FeSi_2$ (001)/Si(110)	[110]‖[1$\bar{1}$0]	145.	3.80	38.04	90.00	3.84	38.02	90.00	0.9	0.1	0.0
$FeSi_2$ (010)/Si(110)	[100]‖[001]	83.	5.38	15.40	90.00	5.43	15.36	90.00	0.9	0.3	0.0
$FeSi_2$ (011)/Si(110)	[100]‖[001]	62.	5.38	11.59	90.00	5.43	11.52	90.00	0.9	0.6	0.0
$FeSi_2$ (011)/Si(110)	[01$\bar{1}$]‖[1$\bar{1}$0]	187.	11.59	16.14	90.00	11.52	16.29	90.00	0.6	0.9	0.0
$FeSi_2$ (011)/Si(110)	[011]‖[1$\bar{1}\bar{4}$]	187.	11.59	16.14	90.00	11.52	16.29	90.00	0.6	0.9	0.0
$FeSi_2$ (111)/Si(110)	[1$\bar{1}$0]‖[1$\bar{1}$0]	42.	3.80	10.95	90.00	3.84	10.86	90.00	0.9	0.8	0.0
$FeSi_2$ (111)/Si(110)	[112]‖[001]	125.	10.95	11.41	90.00	10.86	11.52	90.00	0.8	0.9	0.0
$FeSi_2$ (111)/Si(110)	[01$\bar{1}$]‖[1$\bar{1}\bar{4}$]	167.	11.59	15.22	70.84	11.52	15.36	70.53	0.6	0.9	0.4
$FeSi_2$ (112)/Si(110)	[1$\bar{1}$0]‖[1$\bar{1}$0]	146.	3.80	38.34	90.00	3.84	38.02	90.00	0.9	0.8	0.0
$FeSi_2$ (013)/Si(110)	[100]‖[001]	103.	5.38	19.13	90.00	5.43	19.20	90.00	0.9	0.4	0.0
$FeSi_2$ (115)/Si(110)	[1$\bar{1}$0]‖[1$\bar{1}$0]	82.	3.80	21.62	90.00	3.84	21.72	90.00	0.9	0.5	0.0

$FeSi_2/Si$ lattice match, using a matched unit cell not exceeding 200.$\mathring{A}^2$ and matching precision of 1.0%.
$FeSi_2$ is one-face-centered orthorhombic with a= 9.879, b= 7.799, c= 7.839;
Si (111), (100), and (110) compared to $FeSi_2$ (001) and (110)

Matching faces	Orientation	Area	a_2	b_2	α_2	a_1	b_1	α_1	$\%_a$	$\%_b$	$\%_\alpha$

$Fe11Si_5/Si$ lattice match, using a matched unit cell not exceeding 200.$\mathring{A}^2$ and matching precision of 1.0%.
$Fe11Si_5$ is simple cubic with a= 5.629;
Si (111), (100), and (110) compared to $Fe11Si_5$ (001) and (011)

Matching faces	Orientation	Area	a_2	b_2	α_2	a_1	b_1	α_1	$\%_a$	$\%_b$	$\%_\alpha$

Co_2Si/Si lattice match, using a matched unit cell not exceeding 200.$\mathring{A}^2$ and matching precision of 1.0%.
Co_2Si is orthorhombic with a= 4.918, b= 3.737, c= 7.109;
Si (111), (100), and (110) compared to Co_2Si (001), (100), (101), (010), (011), (110), (102), and (111)

Matching faces	Orientation	Area	a_2	b_2	α_2	a_1	b_1	α_1	$\%_a$	$\%_b$	$\%_\alpha$

$CoSi/Si$ lattice match, using a matched unit cell not exceeding 200.$\mathring{A}^2$ and matching precision of 1.0%.
$CoSi$ is simple cubic with a= 4.447;
Si (111), (100), and (110) compared to $CoSi$ (001), (011), (111), (012), and (112)

Matching faces	Orientation	Area	a_2	b_2	α_2	a_1	b_1	α_1	$\%_a$	$\%_b$	$\%_\alpha$
CoSi(011)/Si(110)	[11$\bar{1}$]||[1$\bar{1}$0]	84.	7.70	10.89	90.00	7.68	10.86	90.00	0.3	0.3	0.0
CoSi(011)/Si(110)	[21$\bar{1}$]||[001]	168.	10.89	15.40	90.00	10.86	15.36	90.00	0.3	0.3	0.0
CoSi(011)/Si(110)	[122]||[1$\bar{1}$2]	168.	13.34	13.34	70.53	13.30	13.30	70.53	0.3	0.3	0.0

$CoSi_2/Si$ lattice match, using a matched unit cell not exceeding 200.$\mathring{A}^2$ and matching precision of 1.0%.
$CoSi_2$ is face-centered cubic with a= 5.367;
Si (111), (100), and (110) compared to $CoSi_2$ (111), (100), (110), (311), (331), (210), (211), (511), (531), (221), (310), and (533)

Matching faces	Orientation	Area	a_2	b_2	α_2	a_1	b_1	α_1	$\%_a$	$\%_b$	$\%_\alpha$

Ni_3Si/Si lattice match, using a matched unit cell not exceeding 200.$\mathring{A}^2$ and matching precision of 1.0%.
Ni_3Si is simple cubic with a= 3.504;
Si (111), (100), and (110) compared to Ni_3Si (001), (011), (111), (012), (112), (122), (013), (113), (023), and (123)

Matching faces	Orientation	Area	a_2	b_2	α_2	a_1	b_1	α_1	$\%_a$	$\%_b$	$\%_\alpha$
Ni_3 Si(012)/Si(100)	[12$\bar{1}$]||[013]	192.	8.58	22.44	86.34	8.59	22.39	85.60	0.0	0.2	0.9
Ni_3 Si(011)/Si(110)	[31$\bar{1}$]||[1$\bar{1}$0]	191.	11.62	16.44	90.00	11.52	16.29	90.00	0.9	0.9	0.0
Ni_3 Si(011)/Si(110)	[31$\bar{1}$]||[1$\bar{1}\bar{4}$]	191.	11.62	16.44	90.00	11.52	16.29	90.00	0.9	0.9	0.0

Ni_5Si_2/Si lattice match, using a matched unit cell not exceeding 200.$\mathring{A}^2$ and matching precision of 1.0%.
Ni_5Si_2 is trigonal with a= 5.617, α=72.833;
Si (111), (100), and (110) compared to Ni_5Si_2 (001), (011), and (111)

Matching faces	Orientation	Area	a_2	b_2	α_2	a_1	b_1	α_1	$\%_a$	$\%_b$	$\%_\alpha$
Ni_5 Si_2 (001)/Si(111)	[1$\bar{1}$0]\|\|[1$\bar{2}$1]	90.	6.67	13.96	76.18	6.65	13.85	76.10	0.3	0.8	0.1
Ni_5 Si_2 (111)/Si(111)	[1$\bar{1}$0]||[121]	39.	6.67	6.67	60.00	6.65	6.65	60.00	0.3	0.3	0.0
Ni_5 Si_2 (011)/Si(110)	[01$\bar{1}$]||[1$\bar{1}$2]	187.	6.67	28.09	90.00	6.65	28.22	90.00	0.3	0.5	0.0

Ni_2Si/Si lattice match, using a matched unit cell not exceeding 200.$\mathring{A}^2$ and matching precision of 1.0%.
Ni_2Si is orthorhombic with a= 5.000, b= 7.030, c= 3.730;
Si (111), (100), and (110) compared to Ni_2Si (010), (100), (110), (001), (011), (101), (120), and (111)

Matching faces	Orientation	Area	a_2	b_2	α_2	a_1	b_1	α_1	$\%_a$	$\%_b$	$\%_\alpha$

$NiSi/Si$ lattice match, using a matched unit cell not exceeding 200.$\mathring{A}^2$ and matching precision of 1.0%.
$NiSi$ is orthorhombic with a= 5.180, b= 5.620, c= 3.340;
Si (111), (100), and (110) compared to $NiSi$ (010), (100), (110), (001), (011), (101), (111), (120), (210), (021), (201), and (121)

Matching faces	Orientation	Area	a_2	b_2	α_2	a_1	b_1	α_1	$\%_a$	$\%_b$	$\%_\alpha$
NiSi(110)/Si(111)	[001]‖[2$\bar{1}$1]	51.	6.68	7.64	90.00	6.65	7.68	90.00	0.4	0.5	0.0
NiSi(110)/Si(111)	[1$\bar{1}$0]‖[01$\bar{1}$]	102.	7.64	13.36	90.00	7.68	13.30	90.00	0.5	0.4	0.0
NiSi(110)/Si(111)	[1$\bar{1}$2]‖[231]	102.	10.15	10.15	82.31	10.16	10.16	81.79	0.1	0.1	0.6
NiSi(210)/Si(111)	[001]‖[1$\bar{2}$1]	165.	6.68	24.98	82.32	6.65	25.18	82.41	0.4	0.8	0.1
NiSi(100)/Si(110)	[001]‖[11$\bar{2}$]	188.	6.68	28.10	90.00	6.65	28.22	90.00	0.4	0.4	0.0

$NiSi/Si$ lattice match, using a matched unit cell not exceeding 200.$\mathring{A}^2$ and matching precision of 1.0%.
$NiSi$ is simple cubic with a= 4.446;
Si (111), (100), and (110) compared to $NiSi$ (001), (011), (111), (012), and (112)

Matching faces	Orientation	Area	a_2	b_2	α_2	a_1	b_1	α_1	$\%_a$	$\%_b$	$\%_\alpha$
NiSi(011)/Si(110)	[11$\bar{1}$]‖[1$\bar{1}$0]	84.	7.70	10.89	90.00	7.68	10.86	90.00	0.3	0.3	0.0
NiSi(011)/Si(110)	[21$\bar{1}$]‖[001]	168.	10.89	15.40	90.00	10.86	15.36	90.00	0.3	0.3	0.0
NiSi(011)/Si(110)	[122]‖[1$\bar{1}$2]	168.	13.34	13.34	70.53	13.30	13.30	70.53	0.3	0.3	0.0

$NiSi_2/Si$ lattice match, using a matched unit cell not exceeding 200.$\mathring{A}^2$ and matching precision of 1.0%.
$NiSi_2$ is face-centered cubic with a= 5.407;
Si (111), (100), and (110) compared to $NiSi_2$ (111), (100), (110), (311), (331), (210), (211), (511), (531), (221), (310), and (533)

Matching faces	Orientation	Area	a_2	b_2	α_2	a_1	b_1	α_1	$\%_a$	$\%_b$	$\%_\alpha$
$NiSi_2$ (111)/Si(111)	[1$\bar{1}$0]‖[1$\bar{1}$0]	13.	3.82	3.82	60.00	3.84	3.84	60.00	0.4	0.4	0.0
$NiSi_2$ (100)/Si(111)	[01$\bar{1}$]‖[01$\bar{1}$]	102.	3.82	26.76	90.00	3.84	26.61	90.00	0.4	0.6	0.0
$NiSi_2$ (331)/Si(111)	[1$\bar{1}$0]‖[01$\bar{1}$]	127.	3.82	33.33	90.00	3.84	33.26	90.00	0.4	0.2	0.0
$NiSi_2$ (211)/Si(111)	[01$\bar{1}$]‖[01$\bar{1}$]	179.	3.82	46.83	90.00	3.84	46.56	90.00	0.4	0.6	0.0
$NiSi_2$ (511)/Si(111)	[01$\bar{1}$]‖[01$\bar{1}$]	38.	3.82	10.12	79.11	3.84	10.16	79.11	0.4	0.4	0.0
$NiSi_2$ (511)/Si(111)	[1$\bar{1}$4]‖[01$\bar{1}$]	152.	11.47	13.79	73.90	11.52	13.85	73.90	0.4	0.4	0.0
$NiSi_2$ (511)/Si(111)	[10$\bar{5}$]‖[3$\bar{4}$1]	190.	13.79	13.79	87.80	13.85	13.85	87.80	0.4	0.4	0.0
$NiSi_2$ (111)/Si(100)	[01$\bar{1}$]‖[01$\bar{1}$]	177.	3.82	46.36	90.00	3.84	46.08	90.00	0.4	0.6	0.0
$NiSi_2$ (100)/Si(100)	[011]‖[011]	15.	3.82	3.82	90.00	3.84	3.84	90.00	0.4	0.4	0.0
$NiSi_2$ (110)/Si(100)	[1$\bar{1}$0]‖[01$\bar{1}$]	103.	3.82	27.04	90.00	3.84	26.88	90.00	0.4	0.6	0.0
$NiSi_2$ (311)/Si(100)	[01$\bar{1}$]‖[01$\bar{1}$]	145.	3.82	38.04	90.00	3.84	38.40	90.00	0.4	0.9	0.0
$NiSi_2$ (331)/Si(100)	[1$\bar{1}$0]‖[01$\bar{1}$]	191.	3.82	50.00	90.00	3.84	49.92	90.00	0.4	0.1	0.0
$NiSi_2$ (221)/Si(100)	[1$\bar{1}$0]‖[01$\bar{1}$]	44.	3.82	11.47	90.00	3.84	11.52	90.00	0.4	0.4	0.0
$NiSi_2$ (221)/Si(100)	[11$\bar{4}$]‖[011]	132.	11.47	11.47	90.00	11.52	11.52	90.00	0.4	0.4	0.0
$NiSi_2$ (221)/Si(100)	[3$\bar{1}$4]‖[015]	175.	13.79	13.79	67.38	13.85	13.85	67.38	0.4	0.4	0.0
$NiSi_2$ (221)/Si(100)	[01$\bar{2}$]‖[012]	175.	12.09	15.29	71.57	12.14	15.36	71.57	0.4	0.4	0.0
$NiSi_2$ (533)/Si(100)	[01$\bar{1}$]‖[01$\bar{1}$]	192.	3.82	50.14	90.00	3.84	49.92	90.00	0.4	0.4	0.0
$NiSi_2$ (100)/Si(110)	[01$\bar{1}$]‖[1$\bar{1}$0]	146.	3.82	38.23	90.00	3.84	38.02	90.00	0.4	0.6	0.0
$NiSi_2$ (110)/Si(110)	[1$\bar{1}$0]‖[1$\bar{1}$0]	21.	3.82	5.41	90.00	3.84	5.43	90.00	0.4	0.4	0.0
$NiSi_2$ (110)/Si(110)	[1$\bar{1}$0]‖[1$\bar{1}$4]	186.	11.47	16.22	90.00	11.52	16.29	90.00	0.4	0.4	0.0
$NiSi_2$ (110)/Si(110)	[1$\bar{1}$4]‖[1$\bar{1}$0]	186.	11.47	16.22	90.00	11.52	16.29	90.00	0.4	0.4	0.0
$NiSi_2$ (311)/Si(110)	[01$\bar{1}$]‖[1$\bar{1}$0]	145.	3.82	38.04	90.00	3.84	38.02	90.00	0.4	0.1	0.0

Cu_5Si/Si lattice match, using a matched unit cell not exceeding 200.$\mathring{A}^2$ and matching precision of 1.0%.
Cu_5Si is simple cubic with a= 6.224;
Si (111), (100), and (110) compared to Cu_5Si (001)

Matching faces	Orientation	Area	a_2	b_2	α_2	a_1	b_1	α_1	$\%_a$	$\%_b$	$\%_\alpha$
Cu_5 Si(001)/Si(100)	[120]‖[05I]	194.	13.92	13.92	90.00	13.85	13.85	90.00	0.5	0.5	0.0

Cu_3Si/Si lattice match, using a matched unit cell not exceeding 200.$\mathring{A}^2$ and matching precision of 1.0%.
Cu_3Si is hexagonal with a= 7.045, c= 21.950;
Si (111), (100), and (110) compared to Cu_3Si (0001)

Matching faces	Orientation	Area	a_2	b_2	α_2	a_1	b_1	α_1	$\%_a$	$\%_b$	$\%_\alpha$

YSi/Si lattice match, using a matched unit cell not exceeding 200.$\mathring{A}^2$ and matching precision of 1.0%.
YSi is one-face-centered orthorhombic with a= 4.257, b= 10.527, c= 3.839;
Si (111), (100), and (110) compared to YSi (010), (110), (001), (021), (111), (130), (100), (150), (011), (112), (132), (101), (012), and (114)

Matching faces	Orientation	Area	a_2	b_2	α_2	a_1	b_1	α_1	$\%_a$	$\%_b$	$\%_\alpha$
YSi(010)/Si(111)	[001]‖[01$\bar{1}$]	180.	3.84	46.83	90.00	3.84	46.56	90.00	0.0	0.6	0.0
YSi(110)/Si(111)	[001]‖[01$\bar{1}$]	153.	3.84	39.74	90.00	3.84	39.91	90.00	0.0	0.4	0.0
YSi(130)/Si(111)	[001]‖[01$\bar{1}$]	127.	3.84	33.10	90.00	3.84	33.26	90.00	0.0	0.5	0.0
YSi(010)/Si(100)	[001]‖[011]	147.	3.84	38.31	90.00	3.84	38.40	90.00	0.0	0.2	0.0
YSi(130)/Si(100)	[001]‖[011]	191.	3.84	49.65	90.00	3.84	49.92	90.00	0.0	0.5	0.0
YSi(100)/Si(100)	[001]‖[011]	162.	3.84	42.11	90.00	3.84	42.24	90.00	0.0	0.3	0.0
YSi(010)/Si(110)	[001]‖[1$\bar{1}$0]	147.	3.84	38.31	90.00	3.84	38.02	90.00	0.0	0.8	0.0

Y_3Si_5/Si lattice match, using a matched unit cell not exceeding 200.$\mathring{A}^2$ and matching precision of 1.0%.
Y_3Si_5 is one-face-centered orthorhombic with a= 4.052, b= 3.954, c= 13.360;
Si (111), (100), and (110) compared to Y_3Si_5 (001), (110), (112), (114), (116), and (118)

Matching faces	Orientation	Area	a_2	b_2	α_2	a_1	b_1	α_1	$\%_a$	$\%_b$	$\%_\alpha$
Y_3Si_5 (001)/Si(111)	[5$\bar{1}$0]‖[3$\bar{1}$2]	152.	10.09	15.37	78.89	10.16	15.36	79.11	0.7	0.1	0.3

Y_3Si_5/Si lattice match, using a matched unit cell not exceeding 200.$\mathring{A}^2$ and matching precision of 1.0%.
Y_3Si_5 is hexagonal with a= 3.836, c= 4.139;
Si (111), (100), and (110) compared to Y_3Si_5 (0001), (10$\bar{1}$0), (10$\bar{1}$1), (11$\bar{2}$0), (10$\bar{1}$2), (11$\bar{2}$1), (20$\bar{2}$1), (11$\bar{2}$2), (10$\bar{1}$3), (21$\bar{3}$0), (21$\bar{3}$1), (11$\bar{2}$3), (21$\bar{3}$2), (30$\bar{3}$1), and (20$\bar{2}$3)

Matching faces	Orientation	Area	a_2	b_2	α_2	a_1	b_1	α_1	$\%_a$	$\%_b$	$\%_\alpha$
Y_3Si_5 (0001)/Si(111)	[2$\bar{1}$10]‖[1$\bar{1}$0]	13.	3.84	3.84	60.00	3.84	3.84	60.00	0.1	0.1	0.0
Y_3Si_5 (0001)/Si(111)	[4$\bar{5}$10]‖[23$\bar{1}$]	89.	10.15	10.15	60.00	10.16	10.16	60.00	0.1	0.1	0.0
Y_3Si_5 (0001)/Si(111)	[7$\bar{5}$20]‖[4$\bar{1}$3]	166.	13.83	13.83	60.00	13.85	13.85	60.00	0.1	0.1	0.0
Y_3Si_5 (10$\bar{1}$0)/Si(111)	[$\bar{1}$2$\bar{1}$0]‖[10$\bar{1}$]	127.	3.84	33.11	90.00	3.84	33.26	90.00	0.1	0.4	0.0
Y_3Si_5 (10$\bar{1}$2)/Si(111)	[$\bar{1}$2$\bar{1}$0]‖[01$\bar{1}$]	180.	3.84	46.97	90.00	3.84	46.56	90.00	0.1	0.9	0.0
Y_3Si_5 (11$\bar{2}$3)/Si(111)	[3300]‖[12$\bar{1}$]	141.	6.64	21.52	81.12	6.65	21.38	81.05	0.1	0.7	0.1
Y_3Si_5 (0001)/Si(100)	[$\bar{1}$2$\bar{1}$0]‖[01$\bar{1}$]	178.	3.84	46.51	90.00	3.84	46.08	90.00	0.1	0.9	0.0
Y_3Si_5 (10$\bar{1}$0)/Si(100)	[$\bar{1}$2$\bar{1}$0]‖[01$\bar{1}$]	191.	3.84	49.67	90.00	3.84	49.92	90.00	0.1	0.5	0.0
Y_3Si_5 (10$\bar{1}$1)/Si(100)	[$\bar{1}$2$\bar{1}$0]‖[01$\bar{1}$]	163.	3.84	42.46	90.00	3.84	42.24	90.00	0.1	0.5	0.0
Y_3Si_5 (11$\bar{2}$2)/Si(110)	[3$\bar{3}$00]‖[1$\bar{1}$$\bar{2}$]	187.	6.64	28.22	90.00	6.65	28.22	90.00	0.1	0.0	0.0
Y_3Si_5 (10$\bar{1}$3)/Si(110)	[$\bar{1}$2$\bar{1}$0]‖[1$\bar{1}$0]	83.	3.84	21.58	90.00	3.84	21.72	90.00	0.1	0.7	0.0
Y_3Si_5 (11$\bar{2}$3)/Si(110)	[3$\bar{3}$00]‖[1$\bar{1}$$\bar{2}$]	188.	6.64	28.35	90.00	6.65	28.22	90.00	0.1	0.5	0.0

Zr_2Si/Si lattice match, using a matched unit cell not exceeding 200.$\mathring{A}^2$ and matching precision of 1.0%.
Zr_2Si is body-centered tetragonal with a= 6.609, c= 5.298;
Si (111), (100), and (110) compared to Zr_2Si (110), (101), (100), (001), and (211)

Matching faces	Orientation	Area	a_2	b_2	α_2	a_1	b_1	α_1	$\%_a$	$\%_b$	$\%_\alpha$
Zr_2 Si(101)/Si(111)	[010]‖[112]	140.	6.61	21.43	81.13	6.65	21.38	81.05	0.6	0.2	0.1

Zr_5Si_3/Si lattice match, using a matched unit cell not exceeding 200.$\mathring{A}^2$ and matching precision of 1.0%.
Zr_5Si_3 is hexagonal with a= 7.886, c= 5.558;
Si (111), (100), and (110) compared to Zr_5Si_3 ($10\bar{1}0$)

Matching faces	Orientation	Area	a_2	b_2	α_2	a_1	b_1	α_1	$\%_a$	$\%_b$	$\%_\alpha$

Zr_3Si_2/Si lattice match, using a matched unit cell not exceeding 200.$\mathring{A}^2$ and matching precision of 1.0%.
Zr_3Si_2 is tetragonal with a= 7.082, c= 3.715;
Si (111), (100), and (110) compared to Zr_3Si_2 (010) and (110)

Matching faces	Orientation	Area	a_2	b_2	α_2	a_1	b_1	α_1	$\%_a$	$\%_b$	$\%_\alpha$

Zr_6Si_5/Si lattice match, using a matched unit cell not exceeding 200.$\mathring{A}^2$ and matching precision of 1.0%.
Zr_6Si_5 is orthorhombic with a= 3.761, b= 9.912, c= 3.753;
Si (111), (100), and (110) compared to Zr_6Si_5 (010), (100), (001), (110), (011), (120), and (021)

Matching faces	Orientation	Area	a_2	b_2	α_2	a_1	b_1	α_1	$\%_a$	$\%_b$	$\%_\alpha$

$ZrSi/Si$ lattice match, using a matched unit cell not exceeding 200.$\mathring{A}^2$ and matching precision of 1.0%.
$ZrSi$ is orthorhombic with a= 5.296, b= 6.995, c= 3.786;
Si (111), (100), and (110) compared to $ZrSi$ (010), (100), (110), (001), (011), (101), (120), and (111)

Matching faces	Orientation	Area	a_2	b_2	α_2	a_1	b_1	α_1	$\%_a$	$\%_b$	$\%_\alpha$

$ZrSi/Si$ lattice match, using a matched unit cell not exceeding 200.$\mathring{A}^2$ and matching precision of 1.0%.
$ZrSi$ is hexagonal with a= 7.005, c= 12.772;
Si (111), (100), and (110) compared to $ZrSi$ (0001)

Matching faces	Orientation	Area	a_2	b_2	α_2	a_1	b_1	α_1	$\%_a$	$\%_b$	$\%_\alpha$

$ZrSi_2/Si$ lattice match, using a matched unit cell not exceeding 200.$\mathring{A}^2$ and matching precision of 1.0%.
$ZrSi_2$ is one-face-centered orthorhombic with a= 3.720, b= 14.690, c= 3.660;
Si (111), (100), and (110) compared to $ZrSi_2$ (010), (001), (110), (021), (130), (150), (011), (112), (132), and (031)

Matching faces	Orientation	Area	a_2	b_2	α_2	a_1	b_1	α_1	$\%_a$	$\%_b$	$\%_\alpha$

Nb_4Si/Si lattice match, using a matched unit cell not exceeding 200.$\mathring{A}^2$ and matching precision of 1.0%.
Nb_4Si is hexagonal with a= 3.590, c= 4.460;
Si (111), (100), and (110) compared to Nb_4Si (0001), (10$\bar{1}$0), (10$\bar{1}$1), (10$\bar{1}$2), (11$\bar{2}$0), (11$\bar{2}$1), (20$\bar{2}$1), (11$\bar{2}$2), (10$\bar{1}$3), (21$\bar{3}$0), (11$\bar{2}$3), (21$\bar{3}$1), (20$\bar{2}$3), (10$\bar{1}$4), (21$\bar{3}$2), and (30$\bar{3}$1)

Matching faces	Orientation	Area	a_2	b_2	α_2	a_1	b_1	α_1	$\%_a$	$\%_b$	$\%_\alpha$
Nb_4 Si(10$\bar{1}$0)/Si(111)	[$\bar{1}$2$\bar{1}$]‖[01$\bar{1}$]	192.	11.45	16.90	83.02	11.52	16.74	83.41	0.6	1.0	0.5
Nb_4 Si(10$\bar{1}$1)/Si(100)	[3$\bar{3}$0$\bar{1}$]‖[011]	59.	7.65	7.65	89.45	7.68	7.68	90.00	0.4	0.4	0.6
Nb_4 Si(10$\bar{1}$1)/Si(100)	[$\bar{1}$2$\bar{1}$0]‖[001]	117.	10.77	10.87	90.00	10.86	10.86	90.00	0.9	0.1	0.0
Nb_4 Si(10$\bar{1}$1)/Si(100)	[3032]‖[001]	176.	10.87	17.05	71.40	10.86	17.17	71.57	0.1	0.8	0.2
Nb_4 Si(21$\bar{3}$1)/Si(100)	[33$\bar{0}$1]‖[01$\bar{1}$]	88.	7.65	11.45	89.27	7.68	11.52	90.00	0.4	0.6	0.8
Nb_4 Si(0001)/Si(110)	[$\bar{1}$2$\bar{1}$0]‖[001]	167.	10.77	16.45	70.89	10.86	16.29	70.53	0.9	1.0	0.5
Nb_4 Si(10$\bar{1}$2)/Si(110)	[303$\bar{1}$]‖[1$\bar{1}$0]	82.	7.65	10.77	90.00	7.68	10.86	90.00	0.4	0.9	0.0
Nb_4 Si(11$\bar{2}$0)/Si(110)	[33$\bar{0}$1]‖[1$\bar{1}$0]	83.	7.65	10.87	89.23	7.68	10.86	90.00	0.4	0.1	0.9
Nb_4 Si(1120)/Si(110)	[6601]‖[1$\bar{1}$2]	166.	13.21	13.38	70.27	13.30	13.30	70.53	0.7	0.6	0.4
Nb_4 Si(1120)/Si(110)	[3302]‖[001]	166.	10.87	15.30	89.23	10.86	15.36	90.00	0.1	0.4	0.9
Nb_4 Si(21$\bar{3}$0)/Si(110)	[45$\bar{1}$0]‖[1$\bar{1}$1]	127.	9.50	13.38	90.00	9.41	13.30	90.00	1.0	0.6	0.0

Nb_3Si/Si lattice match, using a matched unit cell not exceeding 200.$\mathring{A}^2$ and matching precision of 1.0%.
Nb_3Si is simple cubic with a= 4.211;
Si (111), (100), and (110) compared to Nb_3Si (001), (011), (111), (012), and (112)

Matching faces	Orientation	Area	a_2	b_2	α_2	a_1	b_1	α_1	$\%_a$	$\%_b$	$\%_\alpha$

Nb_5Si_3/Si lattice match, using a matched unit cell not exceeding 200.$\mathring{A}^2$ and matching precision of 1.0%.
Nb_5Si_3 is body-centered tetragonal with a= 6.570, c= 11.880;
Si (111), (100), and (110) compared to Nb_5Si_3 (001) and (101)

Matching faces	Orientation	Area	a_2	b_2	α_2	a_1	b_1	α_1	$\%_a$	$\%_b$	$\%_\alpha$

Nb_5Si_3/Si lattice match, using a matched unit cell not exceeding 200.$\mathring{A}^2$ and matching precision of 1.0%.
Nb_5Si_3 is hexagonal with a= 7.536, c= 5.248;
Si (111), (100), and (110) compared to Nb_5Si_3 (10$\bar{1}$0) and (0001)

Matching faces	Orientation	Area	a_2	b_2	α_2	a_1	b_1	α_1	$\%_a$	$\%_b$	$\%_\alpha$

$NbSi_2/Si$ lattice match, using a matched unit cell not exceeding 200.$\mathring{A}^2$ and matching precision of 1.0%.
$NbSi_2$ is hexagonal with a= 4.797, c= 6.592;
Si (111), (100), and (110) compared to $NbSi_2$ (0001), (10$\bar{1}$0), and (10$\bar{1}$1)

Matching faces	Orientation	Area	a_2	b_2	α_2	a_1	b_1	α_1	$\%_a$	$\%_b$	$\%_\alpha$
$NbSi_2$ (10$\bar{1}$0)/Si(111)	[0001]‖[112]	126.	6.59	19.19	90.00	6.65	19.20	90.00	0.9	0.1	0.0

Mo_3Si/Si lattice match, using a matched unit cell not exceeding 200.$\mathring{A}^2$ and matching precision of 1.0%.
Mo_3Si is simple cubic with a= 4.890;
Si (111), (100), and (110) compared to Mo_3Si (001), (011), and (111)

Matching faces	Orientation	Area	a_2	b_2	α_2	a_1	b_1	α_1	$\%_a$	$\%_b$	$\%_\alpha$
Mo_3 Si(111)/Si(111)	[1$\bar{1}$0]\|\|[31$\bar{4}$]	166.	13.83	13.83	60.00	13.85	13.85	60.00	0.1	0.1	0.0
Mo_3 Si(001)/Si(100)	[120]||[001]	120.	10.93	10.93	90.00	10.86	10.86	90.00	0.7	0.7	0.0
Mo_3 Si(001)/Si(100)	[110]||[05$\bar{1}$]	191.	13.83	13.83	90.00	13.85	13.85	90.00	0.1	0.1	0.0

Mo_5Si_3/Si lattice match, using a matched unit cell not exceeding 200.$\mathring{A}^2$ and matching precision of 1.0%.
Mo_5Si_3 is body-centered tetragonal with a= 9.620, c= 4.900;
Si (111), (100), and (110) compared to Mo_5Si_3 (110) and (100)

Matching faces	Orientation	Area	a_2	b_2	α_2	a_1	b_1	α_1	$\%_a$	$\%_b$	$\%_\alpha$

Mo_5Si_3/Si lattice match, using a matched unit cell not exceeding 200.$\mathring{A}^2$ and matching precision of 1.0%.
Mo_5Si_3 is hexagonal with a= 7.286, c= 5.000;
Si (111), (100), and (110) compared to Mo_5Si_3 (10$\bar{1}$0) and (0001)

Matching faces	Orientation	Area	a_2	b_2	α_2	a_1	b_1	α_1	$\%_a$	$\%_b$	$\%_\alpha$

$MoSi_2/Si$ lattice match, using a matched unit cell not exceeding 200.$\mathring{A}^2$ and matching precision of 1.0%.
$MoSi_2$ is body-centered tetragonal with a= 3.203, c= 7.887;
Si (111), (100), and (110) compared to $MoSi_2$ (001), (101), (110), (103), (112), (100), (114), (105), (211), (213), (102), (116), (111), (107), (215), (301), (310), (312), (118), (314), (217), (305), (321), (113), (109), (323), and (104)

Matching faces	Orientation	Area	a_2	b_2	α_2	a_1	b_1	α_1	$\%_a$	$\%_b$	$\%_\alpha$
$MoSi_2$ (001)/Si(100)	[320]‖[011]	133.	11.55	11.55	90.00	11.52	11.52	90.00	0.2	0.2	0.0

$MoSi_2/Si$ lattice match, using a matched unit cell not exceeding 200.$\mathring{A}^2$ and matching precision of 1.0%.
$MoSi_2$ is hexagonal with a= 4.605, c= 6.559;
Si (111), (100), and (110) compared to $MoSi_2$ (0001), (10$\bar{1}$0), (10$\bar{1}$1), and (10$\bar{1}$2)

Matching faces	Orientation	Area	a_2	b_2	α_2	a_1	b_1	α_1	$\%_a$	$\%_b$	$\%_\alpha$
$MoSi_2$ (0001)/Si(111)	[2$\bar{1}$10]‖[31$\bar{4}$]	165.	13.82	13.82	60.00	13.85	13.85	60.00	0.2	0.2	0.0
$MoSi_2$ (10$\bar{1}$1)/Si(100)	[15$\bar{4}$1]‖[015]	177.	13.84	13.84	67.39	13.85	13.85	67.38	0.1	0.1	0.0

Tc_4Si/Si lattice match, using a matched unit cell not exceeding 200.$\mathring{A}^2$ and matching precision of 1.0%.
Tc_4Si is body-centered cubic with a= 3.009;
Si (111), (100), and (110) compared to Tc_4Si (110), (100), (211), (310), (111), (321), (411), (210), (332), (431), (510), (521), (530), (433), (221), (611), (532), (541), (311), (631), (543), (710), (320), (721), (552), (730), (651), (732), (554), (741), (811), (410), (322), (653), (831), (750), (743), (331), (752), (910), (833), (421), (655), (761), (921), (754), (851), (763), (932), (853), (941), (430), (772), (943), (950), (511), (765), (952), (774), (871), (855), (432), (520), and (961)

Matching faces	Orientation	Area	a_2	b_2	α_2	a_1	b_1	α_1	$\%_a$	$\%_b$	$\%_\alpha$
Tc_4 Si(100)/Si(100)	[01$\bar{1}$]||[013]	72.	8.51	8.51	90.00	8.59	8.59	90.00	0.9	0.9	0.0
Tc_4 Si(100)/Si(100)	[032]||[001]	118.	10.85	10.85	90.00	10.86	10.86	90.00	0.1	0.1	0.0
Tc_4 Si(100)/Si(100)	[001]||[012]	145.	12.04	12.04	90.00	12.14	12.14	90.00	0.9	0.9	0.0
Tc_4 Si(100)/Si(100)	[01$\bar{1}$]||[013]	145.	8.51	17.02	90.00	8.59	17.17	90.00	0.9	0.9	0.0
Tc_4 Si(554)/Si(100)	[1$\bar{1}$0]||[013]	147.	8.51	17.29	90.00	8.59	17.17	90.00	0.9	0.6	0.0
Tc_4 Si(943)/Si(110)	[137]||[1$\bar{1}$0]	186.	11.56	16.13	89.30	11.52	16.29	90.00	0.3	1.0	0.8
Tc_4 Si(943)/Si(110)	[137]||[1$\bar{1}$4]	186.	11.56	16.13	89.30	11.52	16.29	90.00	0.3	1.0	0.8

Tc_5Si_3/Si lattice match, using a matched unit cell not exceeding 200.$\mathring{A}^2$ and matching precision of 1.0%.
Tc_5Si_3 is body-centered tetragonal with a= 9.403, c= 4.849;
Si (111), (100), and (110) compared to Tc_5Si_3 (110), (100), and (101)

Matching faces	Orientation	Area	a_2	b_2	α_2	a_1	b_1	α_1	$\%_a$	$\%_b$	$\%_\alpha$

$TcSi/Si$ lattice match, using a matched unit cell not exceeding 200.$\mathring{A}^2$ and matching precision of 1.0%.
$TcSi$ is simple cubic with a= 4.755;
Si (111), (100), and (110) compared to $TcSi$ (001), (011), and (111)

Matching faces	Orientation	Area	a_2	b_2	α_2	a_1	b_1	α_1	$\%_a$	$\%_b$	$\%_\alpha$

Tc_4Si_7/Si lattice match, using a matched unit cell not exceeding 200.$\mathring{A}^2$ and matching precision of 1.0%.
Tc_4Si_7 is tetragonal with a= 5.737, c= 18.099;
Si (111), (100), and (110) compared to Tc_4Si_7 (001)

Matching faces	Orientation	Area	a_2	b_2	α_2	a_1	b_1	α_1	$\%_a$	$\%_b$	$\%_\alpha$
Tc_4Si_7 (001)/Si(100)	[100]‖[011]	132.	11.47	11.47	90.00	11.52	11.52	90.00	0.4	0.4	0.0

Ru_2Si/Si lattice match, using a matched unit cell not exceeding 200.$\mathring{A}^2$ and matching precision of 1.0%.
Ru_2Si is orthorhombic with a= 5.279, b= 4.005, c= 7.418;
Si (111), (100), and (110) compared to Ru_2Si (001), (100), (101), (010), (011), and (110)

Matching faces	Orientation	Area	a_2	b_2	α_2	a_1	b_1	α_1	$\%_a$	$\%_b$	$\%_\alpha$

Ru_5Si_3/Si lattice match, using a matched unit cell not exceeding 200.$\mathring{A}^2$ and matching precision of 1.0%.
Ru_5Si_3 is orthorhombic with a= 5.246, b= 9.815, c= 4.023;
Si (111), (100), and (110) compared to Ru_5Si_3 (010), (100), and (110)

Matching faces	Orientation	Area	a_2	b_2	α_2	a_1	b_1	α_1	$\%_a$	$\%_b$	$\%_\alpha$

Ru_4Si_3/Si lattice match, using a matched unit cell not exceeding 200.$\mathring{A}^2$ and matching precision of 1.0%.
Ru_4Si_3 is orthorhombic with a= 5.194, b= 4.022, c= 17.134;
Si (111), (100), and (110) compared to Ru_4Si_3 (001)

Matching faces	Orientation	Area	a_2	b_2	α_2	a_1	b_1	α_1	$\%_a$	$\%_b$	$\%_\alpha$

$RuSi/Si$ lattice match, using a matched unit cell not exceeding 200.$\mathring{A}^2$ and matching precision of 1.0%.
$RuSi$ is simple cubic with a= 2.909;
Si (111), (100), and (110) compared to $RuSi$ (001), (011), (111), (012), (112), (122), (013), (113), (023), (123), (223), (014), (114), (133), (124), (233), (034), (015), (134), (115), (234), (025), (125), (225), (144), (334), and (035)

Matching faces	Orientation	Area	a_2	b_2	α_2	a_1	b_1	α_1	$\%_a$	$\%_b$	$\%_\alpha$
RuSi(011)/Si(111)	[100]‖[01$\bar{1}$]	191.	11.64	17.45	70.53	11.52	17.60	70.89	1.0	0.8	0.5
RuSi(001)/Si(100)	[100]‖[011]	135.	11.64	11.64	90.00	11.52	11.52	90.00	1.0	1.0	0.0
RuSi(011)/Si(110)	[100]‖[1$\bar{1}$0]	191.	11.64	16.46	90.00	11.52	16.29	90.00	1.0	1.0	0.0
RuSi(011)/Si(110)	[100]‖[1$\bar{1}$4]	191.	11.64	16.46	90.00	11.52	16.29	90.00	1.0	1.0	0.0

$RuSi/Si$ lattice match, using a matched unit cell not exceeding 200.$\mathring{A}^2$ and matching precision of 1.0%.
$RuSi$ is simple cubic with a= 4.703;
Si (111), (100), and (110) compared to $RuSi$ (001), (011), (111), and (012)

Matching faces	Orientation	Area	a_2	b_2	α_2	a_1	b_1	α_1	$\%_a$	$\%_b$	$\%_\alpha$
RuSi(111)/Si(111)	[10$\bar{1}$]‖[12$\bar{1}$]	38.	6.65	6.65	60.00	6.65	6.65	60.00	0.0	0.0	0.0
RuSi(011)/Si(110)	[01$\bar{1}$]‖[1$\bar{1}$2]	63.	6.65	9.41	90.00	6.65	9.41	90.00	0.0	0.0	0.0
RuSi(011)/Si(110)	[100]‖[1$\bar{1}$1]	125.	9.41	13.30	90.00	9.41	13.30	90.00	0.0	0.0	0.0
RuSi(011)/Si(110)	[21$\bar{1}$]‖[1$\bar{1}$0]	125.	11.52	11.52	70.53	11.52	11.52	70.53	0.0	0.0	0.0
RuSi(011)/Si(110)	[21$\bar{1}$]‖[1$\bar{1}$4]	188.	11.52	16.29	90.00	11.52	16.29	90.00	0.0	0.0	0.0

Ru_2Si_3/Si lattice match, using a matched unit cell not exceeding 200.$\mathring{A}^2$ and matching precision of 1.0%.
Ru_2Si_3 is tetragonal with a= 5.531, c= 4.469;
Si (111), (100), and (110) compared to Ru_2Si_3 (010), (001), (110), (011), and (111)

Matching faces	Orientation	Area	a_2	b_2	α_2	a_1	b_1	α_1	$\%_a$	$\%_b$	$\%_\alpha$

Ru_2Si_3/Si lattice match, using a matched unit cell not exceeding 200.$\mathring{A}^2$ and matching precision of 1.0%.
Ru_2Si_3 is orthorhombic with a= 11.057, b= 8.934, c= 5.533;
Si (111), (100), and (110) compared to Ru_2Si_3 (100)

Matching faces	Orientation	Area	a_2	b_2	α_2	a_1	b_1	α_1	$\%_a$	$\%_b$	$\%_\alpha$

Rh_2Si/Si lattice match, using a matched unit cell not exceeding 200.$\mathring{A}^2$ and matching precision of 1.0%.
Rh_2Si is orthorhombic with a= 5.408, b= 7.383, c= 3.930;
Si (111), (100), and (110) compared to Rh_2Si (010), (100), (110), (001), (011), and (101)

Matching faces	Orientation	Area	a_2	b_2	α_2	a_1	b_1	α_1	$\%_a$	$\%_b$	$\%_\alpha$

Rh_5Si_3/Si lattice match, using a matched unit cell not exceeding 200.$\mathring{A}^2$ and matching precision of 1.0%.
Rh_5Si_3 is orthorhombic with a= 5.317, b= 10.131, c= 3.895;
Si (111), (100), and (110) compared to Rh_5Si_3 (010), (100), and (110)

Matching faces	Orientation	Area	a_2	b_2	α_2	a_1	b_1	α_1	$\%_a$	$\%_b$	$\%_\alpha$

Rh_3Si_2/Si lattice match, using a matched unit cell not exceeding 200.$\mathring{A}^2$ and matching precision of 1.0%.
Rh_3Si_2 is hexagonal with a= 11.851, c= 3.623;
Si (111), (100), and (110) compared to Rh_3Si_2 ($10\bar{1}0$)

Matching faces	Orientation	Area	a_2	b_2	α_2	a_1	b_1	α_1	$\%_a$	$\%_b$	$\%_\alpha$

Rh_3Si2+/Si lattice match, using a matched unit cell not exceeding 200.$\mathring{A}^2$ and matching precision of 1.0%.
Rh_3Si2+ is hexagonal with a= 3.949, c= 5.047;
Si (111), (100), and (110) compared to Rh_3Si2+ (0001), ($10\bar{1}0$), ($10\bar{1}1$), ($10\bar{1}2$), ($11\bar{2}0$), ($11\bar{2}1$), ($20\bar{2}1$), ($11\bar{2}2$), and ($10\bar{1}3$)

Matching faces	Orientation	Area	a_2	b_2	α_2	a_1	b_1	α_1	$\%_a$	$\%_b$	$\%_\alpha$

$RhSi/Si$ lattice match, using a matched unit cell not exceeding 200.$\mathring{A}^2$ and matching precision of 1.0%.
$RhSi$ is orthorhombic with a= 5.531, b= 6.362, c= 3.063;
Si (111), (100), and (110) compared to $RhSi$ (010), (100), (110), (001), (011), (120), (101), (210), (111), and (021)

Matching faces	Orientation	Area	a_2	b_2	α_2	a_1	b_1	α_1	$\%_a$	$\%_b$	$\%_\alpha$

$RhSi/Si$ lattice match, using a matched unit cell not exceeding 200.$\mathring{A}^2$ and matching precision of 1.0%.
$RhSi$ is simple cubic with a= 2.963;
Si (111), (100), and (110) compared to $RhSi$ (001), (011), (111), (012), (112), (122), (013), (113), (023), (123), (223), (014), (114), (133), (124), (233), (034), (015), (134), (115), (025), (234), and (125)

Matching faces	Orientation	Area	a_2	b_2	α_2	a_1	b_1	α_1	$\%_a$	$\%_b$	$\%_\alpha$
RhSi(012)/Si(111)	[021]||[21I]	177.	6.63	26.67	90.00	6.65	26.88	90.00	0.4	0.8	0.0
RhSi(001)/Si(100)	[140]||[012]	149.	12.22	12.22	90.00	12.14	12.14	90.00	0.6	0.6	0.0

$RhSi/Si$ lattice match, using a matched unit cell not exceeding 200.$\mathring{A}^2$ and matching precision of 1.0%.
$RhSi$ is simple cubic with a= 4.674;
Si (111), (100), and (110) compared to $RhSi$ (001), (011), (111), and (012)

Matching faces	Orientation	Area	a_2	b_2	α_2	a_1	b_1	α_1	$\%_a$	$\%_b$	$\%_\alpha$
RhSi(111)/Si(111)	[1I0]||[121]	38.	6.61	6.61	60.00	6.65	6.65	60.00	0.6	0.6	0.0
RhSi(011)/Si(110)	[01I]||[1I2]	62.	6.61	9.35	90.00	6.65	9.41	90.00	0.6	0.6	0.0
RhSi(011)/Si(110)	[21I]||[1I4]	185.	11.45	16.19	90.00	11.52	16.29	90.00	0.6	0.6	0.0

Rh_4Si_5/Si lattice match, using a matched unit cell not exceeding 200.$\mathring{A}^2$ and matching precision of 1.0%.
Rh_4Si_5 is monoclinic with a= 12.335, b= 5.924, c= 3.508, γ==100.181 ;
Si (111), (100), and (110) compared to Rh_4Si_5 ($\bar{1}00$), (100), ($0\bar{1}0$), (010), ($1\bar{1}0$), and ($\bar{1}10$)

Matching faces	Orientation	Area	a_2	b_2	α_2	a_1	b_1	α_1	$\%_a$	$\%_b$	$\%_\alpha$

Rh_3Si_4/Si lattice match, using a matched unit cell not exceeding 200.$\mathring{A}^2$ and matching precision of 1.0%.
Rh_3Si_4 is orthorhombic with a= 18.810, b= 3.614, c= 5.813;
Si (111), (100), and (110) compared to Rh_3Si_4 (100)

Matching faces	Orientation	Area	a_2	b_2	α_2	a_1	b_1	α_1	$\%_a$	$\%_b$	$\%_\alpha$
Rh_3Si_4 (100)/Si(110)	[010]‖[001]	126.	10.84	11.63	90.00	10.86	11.52	90.00	0.2	0.9	0.0

$RhSi_2/Si$ lattice match, using a matched unit cell not exceeding 200.$\mathring{A}^2$ and matching precision of 1.0%.
$RhSi_2$ is simple cubic with a= 2.963;
Si (111), (100), and (110) compared to $RhSi_2$ (001), (011), (111), (012), (112), (122), (013), (113), (023), (123), (223), (014), (114), (133), (124), (233), (034), (015), (134), (115), (025), (234), and (125)

Matching faces	Orientation	Area	a_2	b_2	α_2	a_1	b_1	α_1	$\%_a$	$\%_b$	$\%_\alpha$
$RhSi_2$ (012)/Si(111)	[02$\bar{1}$]‖[1$\bar{2}$1]	177.	6.63	26.67	90.00	6.65	26.88	90.00	0.4	0.8	0.0
$RhSi_2$ (001)/Si(100)	[140]‖[012]	149.	12.22	12.22	90.00	12.14	12.14	90.00	0.6	0.6	0.0

Pd_4Si/Si lattice match, using a matched unit cell not exceeding 200.$\mathring{A}^2$ and matching precision of 1.0%.
Pd_4Si is triclinic with a= 4.402, b= 7.700, c= 8.990, α==111.02, β=96.520, γ=89.150;
Si (111), (100), and (110) compared to Pd_4Si (001), (0$\bar{1}$0), (010), and (0$\bar{1}$1)

Matching faces	Orientation	Area	a_2	b_2	α_2	a_1	b_1	α_1	$\%_a$	$\%_b$	$\%_\alpha$
Pd_4 Si(001)/Si(111)	[010]||[01$\bar{1}$]	102.	7.70	13.21	89.15	7.68	13.30	90.00	0.3	0.7	1.0

Pd_3Si/Si lattice match, using a matched unit cell not exceeding 200.$\mathring{A}^2$ and matching precision of 1.0%.
Pd_3Si is orthorhombic with a= 5.735, b= 7.555, c= 5.260;
Si (111), (100), and (110) compared to Pd_3Si (010), (100), (001), and (110)

Matching faces	Orientation	Area	a_2	b_2	α_2	a_1	b_1	α_1	$\%_a$	$\%_b$	$\%_\alpha$

Pd_9Si_4/Si lattice match, using a matched unit cell not exceeding 200.$\mathring{A}^2$ and matching precision of 1.0%.
Pd_9Si_4 is tetragonal with a= 4.700, c= 6.870;
Si (111), (100), and (110) compared to Pd_9Si_4 (001), (010), (011), and (110)

Matching faces	Orientation	Area	a_2	b_2	α_2	a_1	b_1	α_1	$\%_a$	$\%_b$	$\%_\alpha$

Pd_2Si/Si lattice match, using a matched unit cell not exceeding 200.$\mathring{A}^2$ and matching precision of 1.0%.
Pd_2Si is hexagonal with a= 6.496, c= 3.433;
Si (111), (100), and (110) compared to Pd_2Si (10$\bar{1}$0), (0001), (11$\bar{2}$0), and (10$\bar{1}$1)

Matching faces	Orientation	Area	a_2	b_2	α_2	a_1	b_1	α_1	$\%_a$	$\%_b$	$\%_\alpha$

$PdSi/Si$ lattice match, using a matched unit cell not exceeding 200.$\mathring{A}^2$ and matching precision of 1.0%.
$PdSi$ is orthorhombic with a= 5.617, b= 6.153, c= 3.391;
Si (111), (100), and (110) compared to $PdSi$ (010), (100), (110), (001), (011), (101), (120), (111), and (210)

Matching faces	Orientation	Area	a_2	b_2	α_2	a_1	b_1	α_1	$\%_a$	$\%_b$	$\%_\alpha$

La_3Si_2/Si lattice match, using a matched unit cell not exceeding 200.$\mathring{A}^2$ and matching precision of 1.0%.
La_3Si_2 is tetragonal with a= 7.885, c= 4.434;
Si (111), (100), and (110) compared to La_3Si_2 (010) and (110)

Matching faces	Orientation	Area	a_2	b_2	α_2	a_1	b_1	α_1	$\%_a$	$\%_b$	$\%_\alpha$

$LaSi/Si$ lattice match, using a matched unit cell not exceeding 200.$\mathring{A}^2$ and matching precision of 1.0%.
$LaSi$ is orthorhombic with a= 6.059, b= 8.404, c= 4.010;
Si (111), (100), and (110) compared to $LaSi$ (010), (100), and (110)

Matching faces	Orientation	Area	a_2	b_2	α_2	a_1	b_1	α_1	$\%_a$	$\%_b$	$\%_\alpha$
LaSi(010)/Si(100)	[001]||[012]	146.	12.03	12.12	90.00	12.14	12.14	90.00	0.9	0.2	0.0

La_3Si_5/Si lattice match, using a matched unit cell not exceeding 200.$\mathring{A}^2$ and matching precision of 1.0%.
La_3Si_5 is orthorhombic with a= 4.250, b= 4.170, c= 14.050;
Si (111), (100), and (110) compared to La_3Si_5 (001)

Matching faces	Orientation	Area	a_2	b_2	α_2	a_1	b_1	α_1	$\%_a$	$\%_b$	$\%_\alpha$

$LaSi_2/Si$ lattice match, using a matched unit cell not exceeding 200.$\mathring{A}^2$ and matching precision of 1.0%.
$LaSi_2$ is body-centered tetragonal with a= 4.281, c= 13.750;
Si (111), (100), and (110) compared to $LaSi_2$ (001), (101), (103), (110), and (112)

Matching faces	Orientation	Area	a_2	b_2	α_2	a_1	b_1	α_1	$\%_a$	$\%_b$	$\%_\alpha$
$LaSi_2$ (001)/Si(100)	[100]||[013]	73.	8.56	8.56	90.00	8.59	8.59	90.00	0.3	0.3	0.0
$LaSi_2$ (001)/Si(100)	[110]||[012]	147.	12.11	12.11	90.00	12.14	12.14	90.00	0.3	0.3	0.0

Hf_2Si/Si lattice match, using a matched unit cell not exceeding 200.$\mathring{A}^2$ and matching precision of 1.0%.
Hf_2Si is body-centered tetragonal with a= 6.553, c= 5.186;
Si (111), (100), and (110) compared to Hf_2Si (110), (101), (100), (001), (211), and (112)

Matching faces	Orientation	Area	a_2	b_2	α_2	a_1	b_1	α_1	$\%_a$	$\%_b$	$\%_\alpha$

Hf_5Si_3/Si lattice match, using a matched unit cell not exceeding 200.$\mathring{A}^2$ and matching precision of 1.0%.
Hf_5Si_3 is hexagonal with a= 7.890, c= 5.558;
Si (111), (100), and (110) compared to Hf_5Si_3 ($10\bar{1}0$)

Matching faces	Orientation	Area	a_2	b_2	α_2	a_1	b_1	α_1	$\%_a$	$\%_b$	$\%_\alpha$

Hf_3Si_2/Si lattice match, using a matched unit cell not exceeding 200.$\mathring{A}^2$ and matching precision of 1.0%.
Hf_3Si_2 is tetragonal with a= 7.000, c= 3.671;
Si (111), (100), and (110) compared to Hf_3Si_2 (010), (110), and (001)

Matching faces	Orientation	Area	a_2	b_2	α_2	a_1	b_1	α_1	$\%_a$	$\%_b$	$\%_\alpha$

Hf_5Si_4/Si lattice match, using a matched unit cell not exceeding 200.$\mathring{A}^2$ and matching precision of 1.0%.
Hf_5Si_4 is tetragonal with a= 7.039, c= 12.826;
Si (111), (100), and (110) compared to Hf_5Si_4 (001)

Matching faces	Orientation	Area	a_2	b_2	α_2	a_1	b_1	α_1	$\%_a$	$\%_b$	$\%_\alpha$

$HfSi/Si$ lattice match, using a matched unit cell not exceeding 200.$\mathring{A}^2$ and matching precision of 1.0%.
$HfSi$ is orthorhombic with a= 6.855, b= 3.753, c= 5.191;
Si (111), (100), and (110) compared to $HfSi$ (100), (001), (101), (010), (110), (011), (201), and (111)

Matching faces	Orientation	Area	a_2	b_2	α_2	a_1	b_1	α_1	$\%_a$	$\%_b$	$\%_\alpha$
HfSi(010)/Si(100)	[101]‖[013]	178.	8.60	20.75	85.78	8.59	20.68	85.24	0.1	0.3	0.6

$HfSi/Si$ lattice match, using a matched unit cell not exceeding 200.$\mathring{A}^2$ and matching precision of 1.0%.
$HfSi$ is hexagonal with a= 6.860, c= 12.600;
Si (111), (100), and (110) compared to $HfSi$ (0001)

Matching faces	Orientation	Area	a_2	b_2	α_2	a_1	b_1	α_1	$\%_a$	$\%_b$	$\%_\alpha$
HfSi(0001)/Si(111)	[2$\bar{1}$10]‖[3$\bar{1}$4]	163.	13.72	13.72	60.00	13.85	13.85	60.00	0.9	0.9	0.0

$HfSi_2/Si$ lattice match, using a matched unit cell not exceeding 200.$\mathring{A}^2$ and matching precision of 1.0%.
$HfSi_2$ is one-face-centered orthorhombic with a= 3.677, b= 14.550, c= 3.649;
Si (111), (100), and (110) compared to $HfSi_2$ (010), (001), (110), (021), (130), (150), (011), (112), (132), and (031)

Matching faces	Orientation	Area	a_2	b_2	α_2	a_1	b_1	α_1	$\%_a$	$\%_b$	$\%_\alpha$
$HfSi_2$ (010)/Si(100)	[023]‖[011]	134.	11.55	11.62	89.74	11.52	11.52	90.00	0.2	0.8	0.3

Ta_9Si_2/Si lattice match, using a matched unit cell not exceeding 200.$\mathring{A}^2$ and matching precision of 1.0%.
Ta_9Si_2 is hexagonal with a= 6.105, c= 4.919;
Si (111), (100), and (110) compared to Ta_9Si_2 (10$\bar{1}$0), (0001), and (10$\bar{1}$1)

Matching faces	Orientation	Area	a_2	b_2	α_2	a_1	b_1	α_1	$\%_a$	$\%_b$	$\%_\alpha$

Ta_2Si/Si lattice match, using a matched unit cell not exceeding 200.$\mathring{A}^2$ and matching precision of 1.0%.
Ta_2Si is body-centered tetragonal with a= 6.160, c= 5.056;
Si (111), (100), and (110) compared to Ta_2Si (110), (101), (100), (001), (211), (112), and (310)

Matching faces	Orientation	Area	a_2	b_2	α_2	a_1	b_1	α_1	$\%_a$	$\%_b$	$\%_\alpha$
Ta_2 Si(110)/Si(111)	[1$\bar{1}$1]‖[132]	88.	10.07	10.07	60.26	10.16	10.16	60.00	0.9	0.9	0.4
Ta_2 Si(110)/Si(111)	[331]‖[12$\bar{1}$]	154.	13.31	13.35	60.20	13.30	13.30	60.00	0.0	0.3	0.3
Ta_2 Si(112)/Si(111)	[13$\bar{1}$]‖[13$\bar{2}$]	88.	10.06	10.06	60.07	10.16	10.16	60.00	1.0	1.0	0.1
Ta_2 Si(001)/Si(100)	[120]‖[051]	190.	13.77	13.77	90.00	13.85	13.85	90.00	0.5	0.5	0.0

Ta_5Si_3/Si lattice match, using a matched unit cell not exceeding 200.$\mathring{A}^2$ and matching precision of 1.0%.
Ta_5Si_3 is hexagonal with a= 7.484, c= 5.223;
Si (111), (100), and (110) compared to Ta_5Si_3 (10$\bar{1}$0) and (0001)

Matching faces	Orientation	Area	a_2	b_2	α_2	a_1	b_1	α_1	$\%_a$	$\%_b$	$\%_\alpha$

Ta_5Si_3/Si lattice match, using a matched unit cell not exceeding 200.$\mathring{A}^2$ and matching precision of 1.0%.
Ta_5Si_3 is body-centered tetragonal with a= 9.880, c= 5.060;
Si (111), (100), and (110) compared to Ta_5Si_3 (110) and (100)

Matching faces	Orientation	Area	a_2	b_2	α_2	a_1	b_1	α_1	$\%_a$	$\%_b$	$\%_\alpha$

Ta_5Si_3/Si lattice match, using a matched unit cell not exceeding 200.$\mathring{A}^2$ and matching precision of 1.0%.
Ta_5Si_3 is body-centered tetragonal with a= 6.516, c= 11.873;
Si (111), (100), and (110) compared to Ta_5Si_3 (001) and (101)

Matching faces	Orientation	Area	a_2	b_2	α_2	a_1	b_1	α_1	$\%_a$	$\%_b$	$\%_\alpha$

$TaSi_2/Si$ lattice match, using a matched unit cell not exceeding 200.$\mathring{A}^2$ and matching precision of 1.0%.
$TaSi_2$ is hexagonal with a= 4.782, c= 6.569;
Si (111), (100), and (110) compared to $TaSi_2$ (0001), (10$\bar{1}$0), and (10$\bar{1}$1)

Matching faces	Orientation	Area	a_2	b_2	α_2	a_1	b_1	α_1	$\%_a$	$\%_b$	$\%_\alpha$

W_3Si/Si lattice match, using a matched unit cell not exceeding 200.$\mathring{A}^2$ and matching precision of 1.0%.
W_3Si is simple cubic with a= 4.910;
Si (111), (100), and (110) compared to W_3Si (001), (011), and (111)

Matching faces	Orientation	Area	a_2	b_2	α_2	a_1	b_1	α_1	$\%_a$	$\%_b$	$\%_\alpha$
W_3 Si(111)/Si(111)	[1$\bar{1}$0]‖[31$\bar{4}$]	167.	13.89	13.89	60.00	13.85	13.85	60.00	0.3	0.3	0.0
W_3 Si(001)/Si(100)	[110]‖[051]	193.	13.89	13.89	90.00	13.85	13.85	90.00	0.3	0.3	0.0

W_5Si_3/Si lattice match, using a matched unit cell not exceeding 200.$\mathring{A}^2$ and matching precision of 1.0%.
W_5Si_3 is body-centered tetragonal with a= 9.645, c= 4.970;
Si (111), (100), and (110) compared to W_5Si_3 (110) and (100)

Matching faces	Orientation	Area	a_2	b_2	α_2	a_1	b_1	α_1	$\%_a$	$\%_b$	$\%_\alpha$
W_5 Si_3 (100)/Si(111)	[012]‖[3$\bar{4}$1]	192.	13.85	13.85	88.27	13.85	13.85	87.80	0.0	0.0	0.5

W_5Si_3/Si lattice match, using a matched unit cell not exceeding 200.$\mathring{A}^2$ and matching precision of 1.0%.
W_5Si_3 is hexagonal with a= 7.190, c= 4.850;
Si (111), (100), and (110) compared to W_5Si_3 (10$\bar{1}$0) and (0001)

Matching faces	Orientation	Area	a_2	b_2	α_2	a_1	b_1	α_1	$\%_a$	$\%_b$	$\%_\alpha$

WSi_2/Si lattice match, using a matched unit cell not exceeding 200.$\mathring{A}^2$ and matching precision of 1.0%.
WSi_2 is body-centered tetragonal with a= 3.210, c= 7.829;
Si (111), (100), and (110) compared to WSi_2 (001), (101), (110), (103), (112), (100), (114), (211), (105), (213), (102), (116), (111), (301), (215), (107), (310), (312), (314), (118), (321), (305), (217), (113), (323), (109), and (104)

Matching faces	Orientation	Area	a_2	b_2	α_2	a_1	b_1	α_1	$\%_a$	$\%_b$	$\%_\alpha$
WSi_2 (102)/Si(111)	[23$\bar{1}$]‖[3$\bar{4}$1]	195.	13.97	13.97	87.13	13.85	13.85	87.80	0.9	0.9	0.8
WSi_2 (001)/Si(100)	[230]‖[011]	134.	11.57	11.57	90.00	11.52	11.52	90.00	0.5	0.5	0.0

Re_5Si_3/Si lattice match, using a matched unit cell not exceeding 200.$\mathring{A}^2$ and *matching precision of* 1.0%.
Re_5Si_3 is body-centered tetragonal with a= 9.530, c= 4.810;
Si (111), (100), and (110) compared to Re_5Si_3 (110) and (100)

Matching faces	Orientation	Area	a_2	b_2	α_2	a_1	b_1	α_1	$\%_a$	$\%_b$	$\%_\alpha$

Re_5Si_3/Si lattice match, using a matched unit cell not exceeding 200.$\mathring{A}^2$ and matching precision of 1.0%.
Re_5Si_3 is monoclinic with a= 6.451, b= 5.394, c= 9.601, γ=94.203;
Si (111), (100), and (110) compared to Re_5Si_3 (001)

Matching faces	Orientation	Area	a_2	b_2	α_2	a_1	b_1	α_1	$\%_a$	$\%_b$	$\%_\alpha$

$ReSi/Si$ *lattice* match, using a matched unit cell not exceeding 200.$\mathring{A}^2$ and matching precision of 1.0%.
$ReSi$ is simple cubic with a= 4.774;
Si (111), (100), and (110) compared to $ReSi$ (001), (011), and (111)

Matching faces	Orientation	Area	a_2	b_2	α_2	a_1	b_1	α_1	$\%_a$	$\%_b$	$\%_\alpha$

$ReSi_2/Si$ lattice match, using a matched unit cell not exceeding 200.$\mathring{A}^2$ and matching precision of 1.0%.
$ReSi_2$ is body-centered tetragonal with a= 3.138, c= 7.666;
Si (111), (100), and (110) compared to $ReSi_2$ (001), (101), (110), (103), (112), (100), (114), (211), (105), (213), (102), (116), (111), (301), (215), (107), (310), (312), (314), (118), (321), (305), (217), (113), (323), (109), (104), (316), (201), (411), (325), and (307)

Matching faces	Orientation	Area	a_2	b_2	α_2	a_1	b_1	α_1	$\%_a$	$\%_b$	$\%_\alpha$
$ReSi_2$ (110)/Si(111)	[001]‖[1$\bar{1}$0]	51.	7.67	7.68	60.07	7.68	7.68	60.00	0.2	0.0	0.1
$ReSi_2$ (110)/Si(111)	[3$\bar{3}$1]‖[01$\bar{1}$]	102.	7.68	13.29	89.87	7.68	13.30	90.00	0.0	0.1	0.1
$ReSi_2$ (110)/Si(111)	[1$\bar{1}$1]‖[12$\bar{1}$]	153.	13.29	13.29	60.13	13.30	13.30	60.00	0.1	0.1	0.2
$ReSi_2$ (103)/Si(111)	[33$\bar{1}$]‖[01$\bar{1}$]	152.	7.68	19.84	89.94	7.68	19.95	90.00	0.0	0.6	0.1
$ReSi_2$ (116)/Si(111)	[33$\bar{1}$]‖[01$\bar{1}$]	102.	7.68	13.31	90.00	7.68	13.30	90.00	0.0	0.1	0.0
$ReSi_2$ (310)/Si(111)	[001]‖[01$\bar{1}$]	152.	7.67	19.85	90.00	7.68	19.95	90.00	0.2	0.5	0.0
$ReSi_2$ (110)/Si(100)	[3$\bar{3}$1]‖[011]	119.	7.68	15.96	76.21	7.68	15.83	75.96	0.0	0.8	0.3
$ReSi_2$ (102)/Si(110)	[010]‖[1$\bar{1}$1]	187.	9.41	19.81	90.00	9.41	19.95	90.00	0.1	0.7	0.0
$ReSi_2$ (201)/Si(110)	[010]‖[1$\bar{1}$1]	147.	9.41	15.96	78.66	9.41	15.83	78.58	0.1	0.8	0.1

$OsSi/Si$ lattice match, using a matched unit cell not exceeding 200.$\mathring{A}^2$ and matching precision of 1.0%.
$OsSi$ is simple cubic with a= 4.729;
Si (111), (100), and (110) compared to $OsSi$ (001), (011), and (111)

Matching faces	Orientation	Area	a_2	b_2	α_2	a_1	b_1	α_1	$\%_a$	$\%_b$	$\%_\alpha$
OsSi(001)/Si(111)	[110]‖[2$\bar{1}$$\bar{1}$]	179.	6.69	26.75	90.00	6.65	26.88	90.00	0.5	0.5	0.0
OsSi(111)/Si(111)	[1$\bar{1}$0]‖[1$\bar{2}$1]	39.	6.69	6.69	60.00	6.65	6.65	60.00	0.5	0.5	0.0
OsSi(011)/Si(110)	[01$\bar{1}$]‖[1$\bar{1}$2]	63.	6.69	9.46	90.00	6.65	9.41	90.00	0.5	0.5	0.0
OsSi(011)/Si(110)	[100]‖[1$\bar{1}$1]	127.	9.46	13.38	90.00	9.41	13.30	90.00	0.5	0.5	0.0
OsSi(011)/Si(110)	[21$\bar{1}$]‖[1$\bar{1}$0]	127.	11.58	11.58	70.53	11.52	11.52	70.53	0.5	0.5	0.0
OsSi(011)/Si(110)	[21$\bar{1}$]‖[1$\bar{1}$4]	190.	11.58	16.38	90.00	11.52	16.29	90.00	0.5	0.5	0.0

$OsSi/Si$ lattice match, using a matched unit cell not exceeding 200.$\mathring{A}^2$ and matching precision of 1.0%.
$OsSi$ is simple cubic with a= 2.963;
Si (111), (100), and (110) compared to $OsSi$ (001), (011), (111), (012), (112), (122), (013), (113), (023), (123), (223), (014), (114), (133), (124), (233), (034), (015), (134), (115), (025), (234), and (125)

Matching faces	Orientation	Area	a_2	b_2	α_2	a_1	b_1	α_1	$\%_a$	$\%_b$	$\%_\alpha$
OsSi(012)/Si(111)	[02$\bar{1}$]‖[2$\bar{1}$$\bar{1}$]	177.	6.63	26.67	90.00	6.65	26.88	90.00	0.4	0.8	0.0
OsSi(001)/Si(100)	[140]‖[012]	149.	12.22	12.22	90.00	12.14	12.14	90.00	0.6	0.6	0.0

Os_2Si_3/Si lattice match, using a matched unit cell not exceeding 200.$\mathring{A}^2$ and matching precision of 1.0%.
Os_2Si_3 is tetragonal with a= 5.580, c= 4.480;
Si (111), (100), and (110) compared to Os_2Si_3 (010), (001), (110), (011), and (111)

Matching faces	Orientation	Area	a_2	b_2	α_2	a_1	b_1	α_1	$\%_a$	$\%_b$	$\%_\alpha$

$OsSi2.4/Si$ lattice match, using a matched unit cell not exceeding 200.$\mathring{A}^2$ and matching precision of 1.0%.
$OsSi2.4$ is monoclinic with a= 8.770, b= 7.380, c= 3.000, γ==118.5;
Si (111), (100), and (110) compared to $OsSi2.4$ ($\bar{1}00$), (100), ($1\bar{1}0$), ($\bar{1}10$), ($0\bar{1}0$), (010), ($2\bar{1}0$), ($\bar{2}10$), ($\bar{1}\bar{1}0$), (110), ($1\bar{2}0$), and ($\bar{1}20$)

Matching faces	Orientation	Area	a_2	b_2	α_2	a_1	b_1	α_1	$\%_a$	$\%_b$	$\%_\alpha$

$OsSi_2/Si$ lattice match, using a matched unit cell not exceeding 200.$\mathring{A}^2$ and matching precision of 1.0%.
$OsSi_2$ is one-face-centered orthorhombic with a= 10.150, b= 8.117, c= 8.223;
Si (111), (100), and (110) compared to $OsSi_2$ (001)

Matching faces	Orientation	Area	a_2	b_2	α_2	a_1	b_1	α_1	$\%_a$	$\%_b$	$\%_\alpha$

Ir_3Si/Si lattice match, using a matched unit cell not exceeding 200.$\mathring{A}^2$ and matching precision of 1.0%.
Ir_3Si is body-centered tetragonal with a= 5.222, c= 7.954;
Si (111), (100), and (110) compared to Ir_3Si (101), (001), (110), (112), (100), (103), and (211)

Matching faces	Orientation	Area	a_2	b_2	α_2	a_1	b_1	α_1	$\%_a$	$\%_b$	$\%_\alpha$
Ir_3 Si(211)/Si(100)	[1$\bar{1}$1]‖[010]	194.	5.43	35.75	86.13	5.43	35.41	85.60	0.1	1.0	0.6

Ir_3Si/Si lattice match, using a matched unit cell not exceeding 200.$\mathring{A}^2$ and matching precision of 1.0%.
Ir_3Si is hexagonal with a= 4.350, c= 6.630;
Si (111), (100), and (110) compared to Ir_3Si (0001), (10$\bar{1}$0), (10$\bar{1}$1), (10$\bar{1}$2), and (11$\bar{2}$0)

Matching faces	Orientation	Area	a_2	b_2	α_2	a_1	b_1	α_1	$\%_a$	$\%_b$	$\%_\alpha$
Ir_3 Si(0001)/Si(111)	[4150]‖[1$\bar{1}$0]	115.	11.51	11.51	60.00	11.52	11.52	60.00	0.1	0.1	0.0
Ir_3 Si(10$\bar{1}$1)/Si(110)	[451$\bar{1}$]‖[11$\bar{2}$]	166.	13.28	13.28	70.08	13.30	13.30	70.53	0.2	0.2	0.6

Ir_2Si/Si lattice match, using a matched unit cell not exceeding 200.$\mathring{A}^2$ and matching precision of 1.0%.
Ir_2Si is orthorhombic with a= 5.284, b= 3.989, c= 7.615;
Si (111), (100), and (110) compared to Ir_2Si (001), (100), (101), (010), and (011)

Matching faces	Orientation	Area	a_2	b_2	α_2	a_1	b_1	α_1	$\%_a$	$\%_b$	$\%_\alpha$
Ir_2 Si(100)/Si(111)	[001]‖[01$\bar{1}$]	152.	7.61	19.94	90.00	7.68	19.95	90.00	0.9	0.0	0.0

$IrSi/Si$ lattice match, using a matched unit cell not exceeding 200.$\mathring{A}^2$ and matching precision of 1.0%.
$IrSi$ is orthorhombic with a= 5.558, b= 6.273, c= 3.211;
Si (111), (100), and (110) compared to $IrSi$ (010), (100), (110), (001), (011), (101), (120), (111), (210), and (021)

Matching faces	Orientation	Area	a_2	b_2	α_2	a_1	b_1	α_1	$\%_a$	$\%_b$	$\%_\alpha$

Ir_4Si_5/Si lattice match, using a matched unit cell not exceeding 200.$\mathring{A}^2$ and matching precision of 1.0%.
Ir_4Si_5 is monoclinic with a= 12.354, b= 5.881, c= 3.618, γ=100.14;
Si (111), (100), and (110) compared to Ir_4Si_5 ($\bar{1}00$), (100), ($0\bar{1}0$), (010), ($1\bar{1}0$), and ($\bar{1}10$)

Matching faces	Orientation	Area	a_2	b_2	α_2	a_1	b_1	α_1	$\%_a$	$\%_b$	$\%_\alpha$

Ir_3Si_4/Si lattice match, using a matched unit cell not exceeding 200.$\mathring{A}^2$ and matching precision of 1.0%.
Ir_3Si_4 is orthorhombic with a= 18.870, b= 3.679, c= 5.774;
Si (111), (100), and (110) compared to Ir_3Si_4 (100)

Matching faces	Orientation	Area	a_2	b_2	α_2	a_1	b_1	α_1	$\%_a$	$\%_b$	$\%_\alpha$
Ir_3Si_4 (100)/Si(100)	[012]‖[012]	191.	12.12	15.81	86.25	12.14	15.83	85.60	0.2	0.2	0.7

$IrSi_3/Si$ lattice match, using a matched unit cell not exceeding 200.$\mathring{A}^2$ and matching precision of 1.0%.
$IrSi_3$ is hexagonal with a= 4.351, c= 6.622;
Si (111), (100), and (110) compared to $IrSi_3$ (0001), (10$\bar{1}$0), (10$\bar{1}$1), (10$\bar{1}$2), and (11$\bar{2}$0)

Matching faces	Orientation	Area	a_2	b_2	α_2	a_1	b_1	α_1	$\%_a$	$\%_b$	$\%_\alpha$
$IrSi_3$ (0001)/Si(111)	[4$\bar{5}$10]‖[1$\bar{1}$0]	115.	11.51	11.51	60.00	11.52	11.52	60.00	0.1	0.1	0.0
$IrSi_3$ (10$\bar{1}$1)/Si(110)	[15$\bar{4}$1]‖[1$\bar{1}$2]	166.	13.28	13.28	70.02	13.30	13.30	70.53	0.2	0.2	0.7

Pt_3Si/Si lattice match, using a matched unit cell not exceeding 200.$\mathring{A}^2$ and matching precision of 1.0%.
Pt_3Si is monoclinic with a= 5.566, b= 5.389, c= 7.773, γ=90.466;
Si (111), (100), and (110) compared to Pt_3Si (001), ($\bar{1}$00), (100), (0$\bar{1}$0), and (010)

Matching faces	Orientation	Area	a_2	b_2	α_2	a_1	b_1	α_1	$\%_a$	$\%_b$	$\%_\alpha$
Pt_3 Si(100)/Si(110)	[010]‖[001]	168.	10.78	16.45	70.88	10.86	16.29	70.53	0.8	1.0	0.5

Pt_3Si/Si lattice match, using a matched unit cell not exceeding 200.$\mathring{A}^2$ and matching precision of 1.0%.
Pt_3Si is monoclinic with a= 7.702, b= 5.378, c= 7.765, γ=46.190;
Si (111), (100), and (110) compared to Pt_3Si (001), ($\bar{1}$00), (100), ($\bar{1}\bar{1}$0), and (110)

Matching faces	Orientation	Area	a_2	b_2	α_2	a_1	b_1	α_1	$\%_a$	$\%_b$	$\%_\alpha$
Pt_3 Si(100)/Si(110)	[010]‖[001]	167.	10.76	16.43	70.90	10.86	16.29	70.53	1.0	0.9	0.5

Pt_2Si/Si lattice match, using a matched unit cell not exceeding 200.$\mathring{A}^2$ and matching precision of 1.0%.
Pt_2Si is tetragonal with a= 5.554, c= 5.923;
Si (111), (100), and (110) compared to Pt_2Si (001), (010), (011), and (110)

Matching faces	Orientation	Area	a_2	b_2	α_2	a_1	b_1	α_1	$\%_a$	$\%_b$	$\%_\alpha$

Pt_2Si/Si lattice match, using a matched unit cell not exceeding 200.$\mathring{A}^2$ and matching precision of 1.0%.
Pt_2Si is simple cubic with a= 5.630;
Si (111), (100), and (110) compared to Pt_2Si (001) and (011)

Matching faces	Orientation	Area	a_2	b_2	α_2	a_1	b_1	α_1	$\%_a$	$\%_b$	$\%_\alpha$

Pt_2Si/Si lattice match, using a matched unit cell not exceeding 200.$\mathring{A}^2$ and matching precision of 1.0%.
Pt_2Si is tetragonal with a= 3.933, c= 5.910;
Si (111), (100), and (110) compared to Pt_2Si (001), (010), (011), (110), (111), (012), (112), and (021)

Matching faces	Orientation	Area	a_2	b_2	α_2	a_1	b_1	α_1	$\%_a$	$\%_b$	$\%_\alpha$

Pt_6Si_5/Si lattice match, using a matched unit cell not exceeding 200.$\mathring{A}^2$ and matching precision of 1.0%.
Pt_6Si_5 is monoclinic with a= 15.462, b= 6.169, c= 3.499, γ=86.880;
Si (111), (100), and (110) compared to Pt_6Si_5 ($\bar{1}$00) and (100)

Matching faces	Orientation	Area	a_2	b_2	α_2	a_1	b_1	α_1	$\%_a$	$\%_b$	$\%_\alpha$

Pt_6Si_5/Si lattice match, using a matched unit cell not exceeding 200.$\mathring{A}^2$ and matching precision of 1.0%.
Pt_6Si_5 is monoclinic with a= 15.308, b= 6.120, c= 3.480, γ=86.600;
Si (111), (100), and (110) compared to Pt_6Si_5 ($\bar{1}$00) and (100)

Matching faces	Orientation	Area	a_2	b_2	α_2	a_1	b_1	α_1	$\%_a$	$\%_b$	$\%_\alpha$

$PtSi/Si$ lattice match, using a matched unit cell not exceeding 200.$\mathring{A}^2$ and matching precision of 1.0%.
$PtSi$ is orthorhombic with a= 5.577, b= 5.916, c= 3.587;
Si (111), (100), and (110) compared to $PtSi$ (010), (100), (110), (001), (011), (101), (111), (120), and (210)

Matching faces	Orientation	Area	a_2	b_2	α_2	a_1	b_1	α_1	$\%_a$	$\%_b$	$\%_\alpha$
PtSi(110)/Si(100)	[001]||[001]	175.	10.76	16.26	90.00	10.86	16.29	90.00	0.9	0.2	0.0

Pt_3Si_2/Si lattice match, using a matched unit cell not exceeding 200.$\mathring{A}^2$ and matching precision of 1.0%.
Pt_3Si_2 is tetragonal with a= 2.780, c= 2.960;
Si (111), (100), and (110) compared to Pt_3Si_2 (001), (010), (011), (110), (111), (012), (021), (120), (112), (121), (122), (221), (013), (031), (113), (130), (131), (023), (032), (123), (230), (132), (231), (014), (223), (114), (232), (041), (140), (141), (133), (331), (124), (142), (241), (233), (332), (015), (034), (043), (115), (134), (143), (340), (051), (341), (150), (025), (151), (125), (234), (243), (052), (342), (250), (152), (251), (225), (035), (144), (135), (334), (252), (016), (441), (053), (343), (116), (153), (350), (351), (235), (126), and (061)

Matching faces	Orientation	Area	a_2	b_2	α_2	a_1	b_1	α_1	$\%_a$	$\%_b$	$\%_\alpha$
Pt_3Si_2 (001)/Si(100)	[140]||[011]	131.	11.46	11.46	90.00	11.52	11.52	90.00	0.5	0.5	0.0
Pt_3Si_2 (001)/Si(100)	[100]||[051]	193.	13.90	13.90	90.00	13.85	13.85	90.00	0.4	0.4	0.0
Pt_3Si_2 (001)/Si(100)	[430]||[051]	193.	13.90	13.90	90.00	13.85	13.85	90.00	0.4	0.4	0.0
Pt_3Si_2 (121)/Si(100)	[10$\bar{1}$]||[012]	180.	12.18	15.51	71.88	12.14	15.36	71.57	0.3	1.0	0.4
Pt_3Si_2 (223)/Si(100)	[122]||[013]	131.	8.58	15.73	76.76	8.59	15.83	77.47	0.0	0.7	0.9
Pt_3Si_2 (120)/Si(110)	[2$\bar{1}$3]||[001]	166.	10.84	15.28	89.46	10.86	15.36	90.00	0.2	0.5	0.6
Pt_3Si_2 (142)/Si(110)	[4$\bar{1}$0]\|\|[1$\bar{1}$0]	186.	11.46	16.76	76.03	11.52	16.74	76.74	0.5	0.1	0.9
Pt_3Si_2 (252)/Si(110)	[421]||[332]	188.	12.78	15.81	68.30	12.74	15.83	68.55	0.3	0.2	0.4

Appendix A-2.4

Crystal structures of binary transition-metal silicides

The compilation of crystal structures in this appendix was used as input data for lattice match calculations described in Chapter 2; the results of these calculations were presented in the previous appendix (A-2.3). The material presented in this appendix was gathered from Donnay and Ondik[1] (Volumes II and IV), the periodical "Structure Reports", Kim,[2] and Samsonov and Vinitskii.[3] We did not try to assess the quality of the data in these sources; in case of a disagreement between various authors, we list all the different structures proposed.

The tables are ordered by increasing atomic number of the transition metal. The silicides are given in the first column of each table. Phases that are known to be either high- or low-temperature phases are denoted by "(H.T.)" or "(L.T.)", correspondingly. When a phase is known to be stabilized by impurities, it is mentioned specifically. The Bravais systems of the silicides as well as their space group (if known) are given in the second column. The structure type and its Strukturberichte notation are given in the third and fourth columns. The structure type was not used in the lattice-match calculations, but it may be useful in determining the actual positions of the atoms. The lattice parameters are given in the next three columns (labeled "a", "b", and "c"); lengths are given in units of angstroms, angles are given in degrees. The number of formula units ("Z") are given in the eighth column; sometimes only the average number of atoms per unit cell is known, and then it is said explicitely. The references are given in the last three column. Because of the importance of "Structure Reports" and Donnay and Ondik[1] as general references for crystal structures, we list the volume and page number in which the silicide appears in these two sources; for example, an entry 29-79 in the column "Structure

Reports" means volume 29, page 79 in that source. Reference to Donnay and Ondik usually refers to volume II; references to volume IV are designated by "(IV)" in the next to last column. In the last column we give the original reference. Various comments are given below the tables.

1. J. D. H. Donnay and H. M. Ondik, *Crystal Data, Determinative Tables,* (U. S. Department of Commerce, National Bureau of Standards and Joint Commission on Powder Diffraction Standards, Washington, 1973), Volumes II and IV.
2. M. A. Nicolet and S. S. Lau, *Formation and Characterization of Transition-Metal Silicides*; S. J. Kim, *Appendix A: Silicide Tables,* in *ELECTRONICS: MICROSTRUCTURE SCIENCE,* N. Einspruch, Series Editor, *SUPPLEMENT A - MATERIALS AND PROCESS CHARACTERIZATION,* G. Larrabee, Guest Editor (Academic, New York, in press).
3. G. V. Samsonov and I. M. Vinitskii, *Hqandbook of Refractory Compounds,* (Plenum, New York, 1980)

Silicide	Bravais system (sp. group)	structure type	Strukturberichte	a	b	c	Z	Structure Reports	Donnay-Ondik	Reference
Sc_5Si_3	Hexag. ($P6_3/mcm$)	Mn_5Si_3	$D8_8$	7.861		5.812	2	27-341	H-0.7393	Arbuckle, Parthé: Acta Cryst. 15, 1205, (1962)
ScSi	o.f.c.-Orthor. (Cmcm)	CrB	B_f	3.988	9.882	3.659	4	-	O-0.4036	Schob, Parthé. Acta Cryst. 19, 214 (1965)
Sc_2Si_3	Hexag.	defect AlB_2	defect C32	3.664		3.877	2		H-1.0581	Schob, Parthé: Monatsh. Chem. 95, 1466 (1964)
Sc_3Si_5	Hexag. (P6/mmm)	defect AlB_2	defect C32	3.66		3.87	1/3	-	H-1.0574	Gladishevskii, Emes-Misenko: Zh. Strukt. Khim. 4, 861 (1963)

Silicide	Bravais system (sp. group)	structure type	Strukturberichte	a	b	c	Z	Structure Reports	Donnay-Ondik	Reference
Ti_3Si	Tetrag. ($P4_2/n$)	Ti_3P		10.39		5.17	8		T-0.4976(IV)	Schubert et al., Naturwissenschaften 51, 506 (1964)
Ti_5Si_3	Hexag. ($P6_3/mcm$)	Mn_5Si_3	$D8_8$	7.429		5.1392	2	23-236	H-0.6918	Swanson et al.,Natl. Bur. Std. Circ. 539, 8, 64 (1959)
				7.448		5.114		23-238	H-0.6867	Nowotny et al., Monatsh. Chem. 90, 15, (1959)
				7.40		5.14		-	H-0.6918	Freundlich et al., Compt. Rend. 239, 1141 (1954)
				7.465		5.162		15-72	H-0.6918	Pietrokowsky, Duwez: J. Metals 3, 191, 772 (1951)
Ti_5Si_4 (H.T.)	Orthor. (Pc*n)	Ti_5Si_4		6.645	12.69	6.506			O-0.5236(IV)	Nickl, Sprenger: Z. Metallk. 60, 136 (1969)
	Tetrag. ($P4_{1,3}2_12$)	Zr_5Si_4		6.702		12.174	4		T-1.8165(IV)	Nickl, Sprenger: Z. Metallk. 60, 136 (1969)
	Tetrag.			6.713		12.171			T-1.8165(IV)	Sprenger, Nickl: Naturwissenschaften 54, 645 (1967)
	Tetrag.	Zr_5Si_4		7.133		12.997	4			Svechnikov et al, Dokl. Akad. Nauk SSSR 193, 393 (1970)
TiSi	Orthor. (P2mm)			3.618	6.492	4.973	4	23-255 21-172	O-0.7654	Ageev, Samsonov: Zh. Neorgan. Khim. 4, 1590 (1959); Dokl. Akad. Nauk SSSR , 112, 853 (1957)
	(Pnma)	ZrSi, FeB		3.638	6.544	4.997		26-18	O-0.7636	Brukl et al., Monatsh. Chem. 92, 781 (1961)

Silicide	Bravais system (sp. group)	structure type	Strukturberichte	a	b	c	Z	Structure Reports	Donnay-Ondik	Reference
$TiSi_2$	f.c. Orthor. (Fddd)	$TiSi_2$	C54	8.236	4.773	8.523	8	7-95	O-0.9663	Laves, Wallbaum: Z. Krist. 101, 78 (1939)
				8.523	4.773	2.746		-	O-0.5600	Laves, Wallbaum: Z. Krist. 101, 78 (1939)
				8.2671	4.8000	8.5505	8	43A-96		Jeitschko: Acta Cryst. B33, 2347 (1977)
(Re stabilized)	Orthor.		C54	8.279	8.568	4.819	24		O-0.9663(IV)	Duffin et al., Acta Cryst. 17, 450 (1964); up to 0.8 Re
	o.f.c.-Orthor.	$ZrSi_2$	C49	3.62	13.76	3.605	4	20-116	O-0.2631	Cotter et al., J. Am. Ceram. Soc. 39, 11 (1956)
(Cu stabilized)	o.f.c-Orthor. (Cmcm)	$ZrSi_2$	C49	3.562	13.531	3.550	4		O-0.2632(IV)	Nickl, Sprenger: Z. Metallk. 60, 136 (1969)
(Re stabilized)	Hexag. ($P6_222$)	$CrSi_2$	C40	4.712		6.535			O-0.9663(IV)	Duffin et al.

Silicide	Bravais system (sp. group)	structure type	Strukturberichte	a	b	c	Z	Structure Reports	Donnay-Ondik	Reference
V_3Si	Cubic (Pm3n)	β-W	A15	4.722			2	7-3	C-4.722	Wallbaum, Z. Metallk. 31, 362 (1939)
				4.721				18-278		Nowotny et al., Monatsh. Chem. 85, 241 (1954)
				4.7240				16-137		Pearson, Christian: Acta Cryst. 5, 157 (1952)
(Co,Ga-stabilized)				4.7253					C-4.7253(IV)	Zegler, Downey: Trans. AIME. 227, 1407 (1963); solid solution up to 0.3 Co; 0.9 Ga
(Al-stabilized)				4.724					C-4.724(IV)	Müller, Z.Naturforsch. A, 24, 1134 (1969); Al-V-Si alloys. Superconductors.
				4.726				38A-101		Spinat et al., Bull. Soc. Fr. Minér. Crist. 93, 23 (1970)
	Tetrag.			4.715		4.725		31A-64	(at 4.2K)	Batterman, Barrett: Phys. Rev. 145, 296 (1966); Phys. Rev. Letters , 13, 390 (1964)
	Tetrag.			4.715		4.727		42A-126 45A-111	(at 13.5K)	Staudenmann: Solid State Comm. 19, 29 (1976); Solid State Comm. 26, 461 (1978)
V_5Si_3	b.c.-Tetrag. (I42m)	W_5Si_3	$D8_m$(T1)	9.429		4.756	4	-	T-0.5044	Parthé et al., Monatsh. Chem. 86, 385 (1955)
				9.410		4.747		38A-101		Spinat et al., Bull. Soc. Fr. Minér. Crist. 93, 23 (1970)
V_5Si_3 (C stab.)	Hexag. ($P6_3/mcm$)	Mn_5Si_3	$D8_8$	7.135		4.842	2	18-239	-	Schachner et al., Monatsh. Chem. 85, 245 (1954)
				7.121		4.832		38A-101		Spinat et al., Bull. Soc. Fr. Minér. Crist. 93, 23 (1970)
V_6Si_5	b.c.-Orthor. (Ibam)	$Cr_4Nb_2Si_5$		15.966	7.501	4.858	4	38A-101	O-0.4698	Spinat et al., Bull. Soc. Fr. Minér. Crist. 93, 23 (1970); Hallais: Ann. Chim. 6, 321 (1971); Herpin et al., C. R. Acad. Sci. Ser. C, 268, 1750 (1969)
VSi_2	Hexag. ($P6_222$)	$CrSi_2$	C40	4.571		6.372	3	8-102		Wallbaum: Z. Metallk. 33, 378 (1941)

SR-19-245: Kieffer et al., Plansee Proc., (Pergamon) p154 (1955) - phase diagram.
SR-19-245: Rostoker, Yamamoto: Trans. Amer. Soc. Metals 46, 1136 (1954) - phase diagram.
Samsonov: VSi_2 : a and c interchanged.
V_5Si_3: Space group determined by Parthe et al. to be I42m. It is different from W_5Si_3

Silicide	Bravais system (sp. group)	structure type	Strukturberichte	a	b	c	Z	Structure Reports	Donnay-Ondik	Reference
$Cr_3Si(\beta)$	Cubic (Pm3n)	β-W	A15	4.564			2	3-628	C-4.564	Borén, Arkiv Kemi Mineral. Geol. 11A, no.10, 1-28 (1933)
				4.5578			2	20-78		Swanson et al., Natl. Bur. Std. Circ. , 539, V-6, 29 (1956)
				4.559				17-117	C-4.559	Nowotny et al., Monatsh. Chem. 84, 579 (1953)
				4.557				18-278		Nowotny et al., Monatsh. Chem. 85, 241 (1954)
				4.550				17-123		Kieffer et al., Z. Metallk. 44, 437 (1953)
				4.555			2		C-4.555(IV)	Chang: Trans. AIME. 242, 1509 (1968)
Cr_5Si_3	b.c.-Tetrag. ($I\bar{4}2m$)	W_5Si_3	$D8_m$(T1)	9.170		4.636	4	20-78	T-0.5056	Dauben et al., J. Phys. Chem. 60, 443 (1956)
	Tetrag.		$D8_m$	9.18		4.65		19-278		Parthé et al., Monatsh. Chem. 86, 182 (1955)
α-Cr_5Si_3 (L.T.)				9.15		4.639			T-0.5070(IV)	Chang: Trans. AIME. 242, 1509 (1968)
Cr_3Si_2	Tetrag.			9.18		4.65		-		Parthé et al., Monatsh. Chem. 86, 182 (1955)
$CrSi(\epsilon)$	Cubic ($P2_13$)	FeSi	B20	4.607			4	17-122	C-4.607	Kieffer et al., Z. Metallk. 44, 437 (1953)
		FeSi	B28	4.629				3-628	C-4.629	Borén, Arkiv Kemi Mineral. Geol. 11A, no.10, 1 (1933)
				4.622			4		C-4.622(IV)	Chang: Trans. AIME. 242, 1509 (1968)

Silicide	Bravais system (sp. group)	structure type	Struktur-berichte	a	b	c	Z	Structure Reports	Donnay-Ondik	Reference
$CrSi_2(\gamma)$	Hexag. ($P6_222$)	$CrSi_2$	C40	4.429		6.362	3	17-118	H-1.4362	Nowotny et al., Monatsh. Chem. 84, 579 (1953); solid solution data with TiSi2 and TaSi2
				4.420				17-123		Kieffer et al., Z. Metallk. 44, 437 (1953)
				4.422		6.351		3-628	H-1.4362	Borén, Arkiv Kemi Mineral. Geol. 11A no.10 (1933)
				4.430		6.36		-	H-1.4362	Trusova et al., Zh. Neorgan. Khim. 5, 1119 (1960); Si. to Cr ratio of 1.99-2.99
				4.430		6.365	3		H-1.4368(IV)	Chang: Trans. AIME. 242, 1509 (1968)
				4.43		6.37	3		H-1.4379(IV)	Gurin et al., Izv. Akad. Nauk SSSR Neorg. Mater. 5, 1995 (1969)
				4.431		6.364			H-1.4379(IV)	Verkhorobin, Matyushenko: Poroshk. Metall. 6, 51 (1963)

SR-17-122: phase diagram.
Cr_3Si_2 is probably Cr_5Si_3.

Silicide	Bravais system (sp. group)	structure type	Strukturberichte	a	b	c	Z	Structure Reports	Donnay-Ondik	Reference
Mn_6Si	Hexag.	R-phase		10.874		19.177		-	H-1.7636	Kuz'ma, Gladyshevskii, Zh. Neorgan. Khim. 9, 674 (1964)
$Mn_3Si(\beta)$	Cubic	BiF_3	DO_3	5.722			4	24-78	C-5.722	Aronsson, Acta Chem. Scand. 14, 1414 (1960)
		α-Fe	A2	2.85			2	3-629		Laves: Z. Krist. 89, 189 (1934)
				2.857					C-5.722	Amark et al., Svensk Kem. Tidskr. 48, 273 (1936)
				2.864				20-82	C-2.864	Gladyshevskii et al., Fiz. Metal. i Metalloved. 2, 454 (1956)
	Hexag.			6.898		4.802	4	3-629	-	Boren: Arkiv Kemi Mineral. Geol. 11a, no.10, 1-28 (1933)
Mn_5Si_2	Tetrag.			8.910		8.716	8	-	T-0.9782	Sénateur, Fruchart, Compt. Rend. 258, 1524 (1964); a=8.866, c=8.655 for (Mn.66,Fe.34)5Si2
				8.9097		8.7153		42A-109	-	Shoemaker, Shoemaker: Acta Cryst. B32, 2306 (1976)
Mn_5Si_3	Hexag. ($P6_3/mcm$)	Mn_5Si_3	$D8_8$	6.910		4.814	2	24-78	H-0.6967	Aronsson, Acta Chem. Scand. 14, 1414 (1960)
				6.898		4.802		4-24	H-0.6967(II)	Åmark et al., Svensk Kem. Tidskr. 48, 273 (1936)
				6.912		4.812			H-0.6967(IV)	Åmark et al., Svensk Kem. Tidskr. 48, 273 (1936)
				elec.	dens.	dist.			H-0.6967(IV)	Lander, Brown: Phil. Mag. 16, 521 (1967)
$MnSi(\epsilon)$	Cubic ($P2_13$)	FeSi	B28	4.558			4	3-629	C-4.557	Borén, Arkiv Kemi Mineral. Geol. 11A, no.10, 1 (1933)

Silicide	Bravais system (sp. group)	structure type	Strukturberichte	a	b	c	Z	Structure Reports	Donnay-Ondik	Reference
Mn_4Si_7	Tetrag. ($P\bar{4}c2$)	chimney-ladder		5.506		17.522	4	-	T-3.1823	Mueller, Knott, Am. Cryst. Assoc. meeting abstracts, 73 (1965)
				5.534		17.550			T-3.1713(IV)	Knott et al., Acta Cryst. 23, 549 (1967) (subcell?)
				5.525		17.463		34A-101	T-3.1607(IV)	Karpinskij, Evseev: Izv. Akad. Nauk SSSR Neorg. Mater. 5, 525 (1969)
$MnSi_{1.72}$	Tetrag.			5.526		17.455			T-3.1587(IV)	Fujino et al., Jap. J. Appl. Phys. 3, 431 (1964)
$Mn_{11}Si_{19}$	Tetrag.	chimney-ladder		5.518		48.136			T-8.7235	Schwomma et al., Monatsh. Chem. 94, 681 (1963); 95, 1527 (1964); Wittmann, Nowotny, J. Less Com. Metals 9, 303 (1965); Völlenkle et al., Z. Krist. 124, 9 (1967)
				5.524		17.457			T-8.7235	Borén Arkiv Kemi Mineral. Geol. 11A, no.10 (1933)
				5.52		48.2	4	29-64		Schwomma et al., Monatsh. Chem. 95, 1527 (1964)
	Tetrag. ($P\bar{4}n2$)	chimney-ladder		5.530		47.763			T-8.6371(IV)	Knott et al., Acta Cryst. 23, 549 (1967) (subcell?)
				5.518		48.136			T-8.7235(IV)	Flieher et al., Monatsh. Chem. 98, 2173 (1967)
$Mn_{15}Si_{26}$	b.c.-Tetrag. ($I\bar{4}2d$)	chimney-ladder		5.531		65.311	4	32A-99	-	Knott et al., Acta Cryst. 23, 549 (1967)
				5.525		65.55	4	32A-99		Flieher et al., Monatsh. Chem. 98, 2173 (1967)
$Mn_{26}Si_{45}$	Tetrag.	chimney-ladder		5.515		113.36			T-20.5549(IV)	Flieher et al., Monatsh. Chem. 98, 2173 (1967)
$Mn_{27}Si_{47}$	Tetrag.	chimney-ladder		5.53		117.9		39A-83	-	Zwilling, Nowotny: Monatsh. Chem. 104, 668 (1973)
				5.530		117.94			T-21.3273(IV)	Flieher et al., Monatsh. Chem. 98, 2173 (1967)

Silicide	Bravais system (sp. group)	structure type	Strukturberichte	a	b	c	Z	Structure Reports	Donnay-Ondik	Reference
$MnSi_2(\gamma)$	Tetrag.			5.513		17.422	16	3-629		Borén, Arkiv Kemi Mineral. Geol. , 11A, 1 (1933)
$Mn_{81.5}Si_{18.5}(\nu)$	Orthor.			16.992	28.634	4.6556	4	37A-111	-	Shoemaker, Shoemaker: Acta Cryst. B27, 227 (1971)

Silicide	Bravais system (sp. group)	structure type	Strukturberichte	a	b	c	Z	Structure Reports	Donnay-Ondik	Reference
$Fe_3Si(\alpha')$	Cubic	Cu_2MnAl		2.824				-	C2.824	Gladyshevskii et al., Fiz. Metal. i Metalloved., 2, 454 (1956); 2.829 for(Fe2.5Mn.5); 2.832 for (Fe2Mn); 2.835 for (1.5,1.5)
		BiF_3	DO_3	5.6554			4	-	-	Farquhar et al., J. Iron Steel Inst., 152, 457 (1945)
		BiF_3	DO_3	5.651			4	-	-	Piton, Fay: Compt. Rend. 266C, 514 (1968)
Fe_2Si (H.T.)	Cubic	(CsCl)		2.81				8-87	-	Osawa, Murata: Nippon Kinzoku Gakkai-Si 4, 228 (1940)
				2.81				40A-82		Khalaff, Schubert: J. Less Com. Metals 35, 341 (1974)
								44A-76		
$Fe_{11}Si_5$	Cubic	$Fe_{11}Si_5$		5.629					-	Khalaff, Schubert: J. Less Com. Metals 35, 341 (1974)
$Fe_{11}Si_5$				2.80-2.82				8-87	-	Osawa, Murata: Nippon Kinzoku Gakkai-Si 4, 228 (1940)
$Fe_5Si_3(\eta)$	Hexag. ($P6_3/mcm$)	Mn_5Si_3	$D8_8$	6.7552		4.7174	2	-	-	Weill: Nature, 152, 413 (1943)
				6.7411		4.7151		10-63	-	Farquhar et al., J. Iron Steel Inst., 152, 457 (1945)
				6.7411		9.4302		8-87	-	Osawa, Murata: Nippon Kinzoku Gakkai-Si 4, 228 (1940)

Silicide	Bravais system (sp. group)	structure type	Strukturberichte	a	b	c	Z	Structure Reports	Donnay-Ondik	Reference
FeSi(ϵ)	Cubic ($P2_13$)	FeSi	B28	4.487			4	-	C-4.487	Bor' en, Arkiv Kemi Mineral. Geol. , 11A, no.10 (1933)
				4.476				-	C-4.487	Wever, Möller: Z. Krist. 75, 362 (1930)
				4.489				11-146	C-4.487	Pauling, Soldate: Acta Cryst. 1, 212 (1948)
				4.493	at 77K					
				4.500	at 298K					Watanabe et al., J. Phys. Soc. Japan, 18, 995 (1963)
				4.517	at 573K			28-28	-	
				4.4881			4	10-63	-	Farquhar et al., J. Iron Steel Inst., 152, 457 (1945)
				4.480			4		C-4.480(IV)	Gevork'yan: Dokl. Akad. Nauk SSSR 185, 416 (1969)
$FeSi_2$(ζ)	Tetrag.			2.6901		5.134	1	23-168	-	Seybolt: Trans. AIME. 212, 161 (1958); Guttman: Trans. AIME. 215, 169 (1959); Siderenko et al., Fiz. Metal. i Metalloved. 8 (3), 465 (1959); 8(5), 735
	(P4/mmm)			2.684		5.128		24-77	T-1.9106	Aronsson, Acta Chem. Scand. 14, 1414 (1960)
				2.6910		5.1262	3	8-87	-	Osawa, Murata: Nippon Kinzoku Gakkai-Si 4, 228 (1940)
	Tetrag.			2.690		5.08	1		T-1.8885(IV)	Gevork'yan: Dokl. Akad. Nauk SSSR 185, 416 (1969)
($Fe_{.87}Si$?)	Tetrag.	Lebeauite		2.69		5.13			-	Corre, Genin: Phys. Status Solidi, 51 K85 (1972)
β-$FeSi_2$	o.f.c.-Orthor. (Cmca)	$FeSi_2$		9.863	7.791	7.833	16	37A-101	-	Glaser, Ivanick: Trans. AIME. 206, 1290; 209, 529 (1956); Gel'd, Serebrenikov: Dokl. Akad. Nauk SSSR 97, 827, 695 (1954); Corre, Genin: Phys. Status Solid. 51, K85 (1972); Dusausoy et al.: Acta Cryst. 27, 1209 (1971)
	Orthor.			9.8792	7.7991	7.8388	16		O-0.7935(IV)	Bucksch: Z. Naturforsch. A, 22, 2124 (1967)
	Orthor.			9.863	7.791	7.833	16		O-0.7942(IV)	Wandji et al., C. R. Acad. Sci. Ser. C, 267, 1587 (1968); 269, 907 (1969)

SR-37A-101: β-$FeSi_2$ is a semiconductor.

Silicide	Bravais system (sp. group)	structure type	Strukturberichte	a	b	c	Z	Structure Reports	Donnay-Ondik	Reference
Co_3Si	Hexag.	Ni_3Sn						-	-	Koster, Gödecke: Z. Metallk. 64, 399 (1973)
$Co_2Si(\vartheta)$	Orthor. (Pnma)	$PbCl_2$	C23	4.918	3.737	7.109	4	19-124	O-0.6918	Geller, Wolonits: Acta Cryst. 8, 83 (1955)
				4.908	3.730	7.095		3-626	O-0.6918	Borén, Arkiv Kemi Mineral. Geol. , 11A, no. 10, 1 (1933); Borén et al., Z. Physik. Chem. Leipzig, 29, 231 (1935)
				4.87	3.76	7.14			O-0.6821	Panteleimonov et al., Vestn. Mosk. Univ. Khim. 22, 87 (1967)
$CoSi(\epsilon)$	Cubic ($P2_13$)	FeSi	B20	4.4426			4	-	-	Zelenin et al., (1964) quoted by Pearson.
				4.447				3-626	C-4.447	Borén, Arkiv Kemi Mineral. Geol. , 11A, no.10, 1 (1933)
				4.4445						Gladyshevskii: Crystal Chemistry of Silicides and Germanides, Moscow (1971)
$CoSi_2$	f.c.-Cubic (Fm3m)	CaF_2	C1	5.365			4	13-90		Bertaut, Blum: C.R. Acad. Sci. Paris, 231, 626 (1950)
				5.367			4	13-90	C-5.356	Schubert, Pfisterer: Z. Metallk. , 41, 433 (1950)
				5.3627						Gladyshevskii: Crystal Chemistry of Silicides and Germanides, Moscow (1971)

DO-C-5.356: probably kX instead of Å.
Samsonov: Co_3Si exists between 1193-1214 °C.

Silicide	Bravais system (sp. group)	structure type	Strukturberichte	a	b	c	Z	Structure Reports	Donnay-Ondik	Reference
$Ni_3Si(\beta_1)$	Cubic	$AuCu_3$	$L1_2$	3.5040			1	-	-	Ôsawa, Okamoto: Sci. Rep. Tôhoku Imp. Univ. 27, 326 (1939)
				3.51				23-194 15-108	C-3.51	Lashko, Sorokina: Zh. Neorgan. Khim. , 4, 1613 (1959); Lashko, Dokl. Akad. Nauk SSSR , 81, 605 (1951)
$Ni_5Si_2(\gamma)$	Hexag.			6.68		12.28	6	-	H-1.8383	Saini et al., Can. J. Chem. 42, 1511 (1964)
	Trigonal			5.617 6.670	$\alpha=72^{\circ}50'$ (hex.)	12.267		26-211	H-1.8383	Pilström, Acta Chem. Scand. 15, 893 (1961)
	Hexag.	-	-	7.688		9.771		23-194	H-1.2708	Lashko, Sorokina: Zh. Neorgan. Khim. , 4, 1613 (1959)
$Ni_{31}Si_{12}$	Trigonal	Ni_5Si_2		6.671		12.288	1	37A-114	-	Frank, Schubert: Acta Cryst. B27, 916 (1971)
$Ni_2Si(\delta)$ (L.T.)	Orthor. (Pnma)	$PbCl_2$	C23	4.99	7.03	3.72	4		O-0.7098	Toman, Acta Cryst. 5, 329 (1952)
				4.99	7.06	3.72	4	16-123	-	Toman, Acta Cryst. 5, 329 (1952)
				7.40	9.92	7.05		23-194	O-0.7465	Lashko, Sorokina: Zh. Neorgan. Khim. , 4, 1613 (1959)
	Orthor.	anti-$PbCl_2$	anti-C23	5.00	7.03	3.73	4		O-0.7112(IV)	Schulz et al., Z. Anorg. Allg. Chem. 357, 299 (1968)
$Ni_2Si(\vartheta)$ (H.T.)	Hexag. ($P6_3/mmc$)	Ni_2In	B8	3.805		4.890	2	16-123	H-1.2852	Toman, Acta Cryst. 5, 329 (1952)
Ni_3Si_2	o.f.c.-Orthor. ($Ccm2_1$)			10.805	12.229	6.924	16	26-211	O-0.8836	Pilström, Acta Chem. Scand. 15, 893 (1961)

Silicide	Bravais system (sp. group)	structure type	Strukturberichte	a	b	c	Z	Structure Reports	Donnay-Ondik	Reference
NiSi(ϵ)	Orthor. (Pnma)	MnP or deformed NiAs	B31	5.18	5.62	3.34	4	15-107	O-0.9217	Toman, Acta Cryst. 4, 462 (1951)
	Cubic	FeSi	B28	4.446			4		C-4.446	Borén, Arkiv Kemi Mineral. Geol. , 11A, no.10, 1 (1933)
α-$NiSi_2$	f.c.-Cubic (Fm3m)	CaF_2	C1	5.406			4	13-90	C-5.395	Schubert, Pflsterer: Z. Metallk. , 41, 433 (1950); Naturwissenschaften , 77, 112 (1950)
				5.407					C-5.407(IV)	Panday, Schubert: J. Less Com. Metals 18, 175 (1969)
$Ni_{1.04}Si_{1.93}$				5.407					C-5.407(IV)	Sidorenko et al., Zh. Neorgan. Khim. 13, 1475 (1968)
ζ-$NiSi_2$	Trig.			8.881	α=90°23'					Dvorina, Popova: Neorg. Mater. 6, 1969 (1970)

DO-C-5.395: $NiSi_2$. a given in kX instead of Å?

Silicide	Bravais system (sp. group)	structure type	Struktur-berichte	a	b	c	Z	Structure Reports	Donnay-Ondik	Reference
$CuSi_x(\iota)$	Hexag.	Mg	A3	2.559		4.185	2 atoms	s-	-	Taylor and Kogle, Crystallographic Data on Metal and Alloy Structures, (Dover, New York, 1963)
(H.T.)	Cubic	W(?)	A2	2.854						Taylor and Kogle, Crystallographic Data on Metal and Alloy Structures, (Dover, New York, 1963)
$Cu_5Si(\gamma)$	Cubic ($P4_{1,3}32$)	β-Mn	A13	6.224			20 atoms	3-332	C-6.224	Fagerberg, Westgren: Metallwirtschaft, 14,265 (1935)
				6.198						Isawa: Nippon Kink. Gakk. 4, 398 (1940)
$Cu_{31}Si_8$	Cubic		$D8_{1-3}$	8.506						Isawa: Nippon Kink. Gakk. 2, 400 (1938)
$Cu_{15}Si_4(\epsilon)$	b.c.-Cubic ($I\bar{4}3d$)		$D8_6$	9.713			4	3-366	C-9.713	Morral, Westgren: Arkiv Kemi Mineral. Geol. , 11B, no.37, 1 (1934)
$Cu_3Si(\eta)$	Cubic	Cu_3Ge	$D8_2$						-	Schubert, Brandauer: Z. Metallk. 43, 267 (1952)
	Hexag.			7.045		21.95	18		H-3.1157	Krylov et al., Kristallografiya, 11, 822 (1966)
	Hexag. /Trig.			25.4		44.2	2000 atoms		H-1.7402(IV)	Kolster: Acta Cryst. 19, 1049 (1965)

Silicide	Bravais system (sp. group)	structure type	Strukturberichte	a	b	c	Z	Structure Reports	Donnay-Ondik	Reference
Y_5Si_3	Hexag. ($P6_3/mcm$)	Mn_5Si_3	$D8_8$	8.418		6.337	2	-	-	Lundin: The Rare Earths (John Wiley 1961) p.264
	Hexag.	Mn_5Si_3	$D8_8$	8.403		6.303	2	24-147	H-0.7501(IV)	Parthé: Acta Cryst. 13, 868 (1960)
		Mn_5Si_3	$D8_8$	8.42		6.32	2		H-0.7506(IV)	Mayer, Shidlovsky: Inorg. Chem. 8, 1240 (1969)
Y_5Si_4	Orthor. ($Pn2_1a$)	Ge_4Sm_5		7.39	14.52	7.64	4	-	O-0.5261	Smith et al., Nature, 210, 1148 (1966); Acta Cryst. 22, 940 (1967)
		Ge_4Sm_5		7.390	14.52	7.640	4		O-0.5262(IV)	Raman, Trans. Indian Inst. Metals, 21, 5 (1968)
YSi	o.f.c.-Orthor. (Cmcm)	CrB	B_f	4.251	10.526	3.826	4	23-146	O-0.4039	Parthé, Acta Cryst. 12, 559 (1959)
		TlI		4.257	10.527	3.839				Hohnke, Parthé: Acta Cryst. 20(4), 572 (1966)

Silicide	Bravais system (sp. group)	structure type	Strukturberichte	a	b	c	Z	Structure Reports	Donnay-Ondik	Reference
α-Y_3Si_5 (L.T.)	Orthor.	($GdSi_2$)		4.052	3.954	13.360			-	Lundin: The Rare Earths (John Wiley 1961) p.264
YSi_2				4.04	13.33	3.95		24-226	-	Binder: j. Amer. Ceram. Soc., 43, 287 (1960)
YSi_2				4.04	13.33	3.95	4	23-220	O-0.3031	Perri et al., J. Phys. Chem. 63, 2073 (1959)
β-Y_3Si_5 (H.T.)	b.c.-Tetrag. (I4/amd)	$ThSi_2$	C_c	4.04		13.42	3	-	-	Perri et al., J. Phys. Chem. 63, 616 (1959)
YSi_2(H.T.)	b.c.-Tetrag. ($I4_1$/amd)	$ThSi_2$	C_c	4.04	(at 545C)	13.42	4	23-220	T-3.3218	Perri et al., J. Phys. Chem. 63, 2073 (1959); Brauer, Haag: Z. Anorg. Allgem. Chem. 267, 198 (1952)
γ-Y_3Si_5	Hexag.			3.836		4.139		-	-	Baglin et al., J. Appl. Phys. 52, 2841 (1981)
		defect AlB_2	defect C32	3.842		4.140	1/3	-	H-1.0776	Gladyshevskii, Emes-Misenko, Zh. Strukt. Khim 4, 861 (1963)
YSi_2		AlB_2	C32					38A-171	-	Mayer, Felner: J. Less Com. Metals 29 25-31
(L.T., $<$ 1600C)		AlB_2	C32	3.83		4.14	1		H-1.0809	Mayer et al., Inorg. Chem. 6, 842 (1967)

Y_3Si_5 and YSi_2 are probably the same phases.

Silicide	Bravais system (sp. group)	structure type	Strukturberichte	a	b	c	Z	Structure Reports	Donnay-Ondik	Reference
Zr_4Si?	Hexag.	Mg	A3					17-262		Lundin et al., Trans. Am. Soc. Metals, 45, 901 (1953)
Zr_3Si	Tetrag. ($P4_2/n$)	Ti_3P		11.01		5.45	8		T-0.4950(IV)	Schubert et al., Naturwissenschaften 51, 506 (1964)
Zr_2Si	b.c.-Tetrag. ($I4/mcm$)	Al_2Cu	C16	6.6120		5.2943	4	18-281	T-0.8007	Pietrokowsky, Acta Cryst. 7, 435 (1954)
(Zr rich)			C16	6.581		5.372	4	17-263	T-0.8162	Schachner et al., Monatsh. Chem. 84, 677 (1953)
				6.609		5.298		38A-6	-	Havinga et al., J. Less Com. Metals 27, 169,269 (1972)
Zr_5Si_3 C stabilized	Hexag. ($P6_3/mcm$)	Mn_5Si_3	$D8_8$	7.886		5.558	2	17-263	H-0.7048	Schachner et al., Monatsh. Chem. 84, 677 (1953)
		Mn_5Si_3	$D8_8$	8.13		5.78		-	(H-0.7109)	Nowotny et al., Monatsh. Chem. 90, 15 (1959)
Zr_3Si_2	Tetrag. ($P4/mbm$)	U_3Si_2		7.082		3.715	2	17-263	-	Lundin et al., Trans. Am. Soc. Metals, 45, 901 (1953)
		U_3Si_2		7.082		3.714	2	26-11	T-0.5244	Schob et al., Monatsh. Chem. 92, 1218 (1961)
Zr_5Si_4	Tetrag. ($P4_{1,3}2_12$)	Zr_5Si_4		7.1225		13.000	4	31A-65	T-1.8252	Pfeifer, Schubert: Z. Metallk. 57, 884 (1966)
				7.123		13.002	4	33A-144	T-1.8252	Karpinskij, Evseev: Acta Cryst. 21, A82 (1966); Izv. Akad. Nauk SSSR Neorg. Mater. 4, 1248 (1968)
Zr_6Si_5	Orthor.	(CrB)		3.761	9.912	3.753		-	-	Lundin et al., Trans. Am. Soc. Metals, 45, 901 (1953)

Silicide	Bravais system (sp. group)	structure type	Strukturberichte	a	b	c	Z	Structure Reports	Donnay-Ondik	Reference
ZrSi	Orthor. (Pnma)	USi		5.302	6.711	3.786	4	-	O-0.7905	Schachner et al., Monatsh. Chem. 85, 1140 (1954)
	Orthor. (P2mm)	FeB	B27	5.302	6.982	3.786		18-280	-	Schachner et al., Monatsh. Chem. 85, 1140 (1954)
		FeB	B27	5.296	6.995	3.786		30A-97	-	Karpinskij, Evseev: Izv. Akad. Nauk SSSR Neorg. Mater. 1, 337 (1965)
	(Cmcm)	CrB	B_f	3.764	9.917	3.748	4		O-0.3796(IV)	Karpinskij, Shamrai: Izv. Akad. Nauk SSSR Metal. 209, 1969
		CrB	B_f	3.762	9.912	3.754	4		O-0.3795(IV)	Schob et al., Monatsh. Chem. 92, 1218 (1961)
	Orthor.			7.04	3.75	5.32			O-0.7557	Gurin et al., Izv. Akad. Nauk SSSR Neorg. Mater. 5, 1995 (1969)
				6.69	3.77	5.29			O-0.7557	Samsonov, quoted by Gurin et al.
	Hexag.			7.005		12.772		17-263	H-1.8233	Lundin et al., Trans. Amer. Soc. Metals 45, 901 (1953)
$ZrSi_2$	o.f.c.-Orthor. (Cmcm)	$ZrSi_2$	C49	3.72	14.61	3.67	4	5-5,53	O-0.2546	Náray-Szabó, Z. Krist. 97, 223 (1937)
				3.72	14.76	3.67		18-280	-	Schachner et al., Monatsh. Chem. 85, 1140 (1954)
				3.72	14.73	3.67			O-0.2546	Schachner et al., Monatsh. Chem. 85, 1140 (1954)
				3.72	14.69	3.66		20-116	O-0.2546	Cotter et al., J. Am. Ceram. Soc. 39, 11 (1956)
				3.721	14.68	3.683		19-285	O-0.2546	Vaughan, Bracuti: Am. Cryst. Assoc. Meeting, Abstr. 8 (1955)

Remark: H-0.7109 is changed in Corrections and Additions (3rd ed.). It is Al_3Zr_5 rather than Si_3Zr_5

SR-17-263: Phase diag. by Lundin et al.

SR-17-263: (Schachner et al.) Zr_5Si_6, Zr_4Si_3, Zr_3Si_2 of Lundin et al. were not found; probably supressed by traces of carbon.

SR-18-279: Phase diagram. (Kieffer et al., Z. Metallk. 45, 493 (1954))

Silicide	Bravais system (sp. group)	structure type	Strukturberichte	a	b	c	Z	Structure Reports	Donnay-Ondik	Reference
Nb_4Si	Hexag.	ϵ-Fe_3N		3.59		4.46	2		H-1.2423	Samsonov et al., Zh. Neorgan. Khim. 3, 868 (1958)
Nb_3Si	Tetrag. ($P4_2/n$)	Ti_3P		10.23		5.19	8	30A-157	-	Rossteutscher, Schubert: Z. Metallk. 56, 813 (1965)
		Ti_3P		10.23		5.19	8		T-0.5073(IV)	Schubert et al., Naturwissenschaften 51, 506 (1964)
		Ti_3P		10.224		5.189	8	41A-23		Waterstrat et al., Acta Cryst. B31, 2765 (1975)
	Cubic	$AuCu_3$	$L1_2$	4.211	at 22C			28-48	C-4.211	Galasso, Pyle: Acta cryst. 16, 228
α-Nb_5Si_3 (L.T.)	b.c.-Tetrag. (I4/mcm)	Cr_5B_3(T2)	$D8_l$	6.56		11.86	4		T-1.8079	Samsonov et al., Zh. Neorgan. Khim. 3, 868 (1958)
				6.57		11.88				Dokukina et al., Zh. Neorgan. Khim. 9, 1905 (1964)
			T2	6.570		11.884		19-279		Parthé et al., Monatsh. Chem. 86, 385,859 (1955)
β-Nb_5Si_3 (H.T.)	b.c.-Tetrag. ($I\bar{4}2m$)	W_5Si_3	$D8_m$(T1)	10.018		5.072	4	19-277	T-0.5070	Parthé et al., Monatsh. Chem. 86, 385 (1955)
				10.00		5.07			T-0.5070	Samsonov et al., Zh. Neorgan. Khim. 3, 868 (1958)
				10.04		5.07			T-0.5070	Dokukina et al., Zh. Neorgan. Khim. 9, 1905 (1964); Alyamovskii et al. Zh. Neorgan. Khim. 7, 1968 (1962)
γ-Nb_5Si_3	Hexag. ($P6_3/mcm$)	Mn_5Si_3	$D8_8$	7.536		5.248	2	18-239	H-0.6964	Schachner et al., Monatsh. Chem. 85, 245 (1954)
				7.52		5.24			H-0.6968	Samsonov et al., Zh. Neorgan. Khim. 3, 868 (1958)

Silicide	Bravais system (sp. group)	structure type	Strukturberichte	a	b	c	Z	Structure Reports	Donnay-Ondik	Reference
$NbSi_2$	Hexag. ($P6_222$)	$CrSi_2$	C40	4.78		6.56	3		H-1.3724	Samsonov et al., Zh. Neorgan. Khim. 3, 868 (1958)
				4.80		6.56			H-1.3724	Dokukina et al., Zh. Neorgan. Khim. 9, 1905 (1964); Alyamovskii et al. Zh. Neorgan. Khim. 7, 1968 (1962)
									H-1.3724	Dokukina et al., Izv. Akad. Nauk SSSR Otd. Tekhn. Nauk Met. i Toplivo, 6,102 (1959); data for solid solution (Nb,W)Si2
				4.7971		6.592	3		H-1.3742	Swanson et al., Natl. Bur. Std. Circ. 539, 8, 39 (1959)
				4.785		6.576		8-102	H-1.3742	Wallbaum, Z. Metallk. 33, 378 (1941)
				4.819		6.592		38A-98		Kubiak et al., Bull. Acad. Polon. Sci. Ser. Sci. Chim. 20,429 (1972)
				4.794		6.589		19-28		Parthé et al., Monatsh. Chem. 86, 385 (1955)
				4.803		6.604				Gladyshevskii: Crystal Chemistry of Silicides and Germanides, Moscow (1971)

SR-19-244: Phase diagram (Knapton: Nature, 175, 730 (1955))
SR-19-244: Kieffer et al., Plansee Proc. (Pergamon press 1956) p.156 gives a phase diagram.

Silicide	Bravais system (sp. group)	structure type	Strukturberichte	a	b	c	Z	Structure Reports	Donnay-Ondik	Reference
Mo_3Si	Cubic (Pm3n)	β-W	A15	4.890			2	12-111	C-4.890	Templeton, Dauben: Acta Cryst. 3, 261 (1950)
				4.878	(kX?)			16-117		Kieffer, Cerwenka: Z. Metallk. 43, 101 (1952)
				4.889				17-117		Nowotny et al., Monatsh. Chem. 84, 579 (1953)
				4.886				18-278		Nowotny et al., Monatsh. Chem. 85, 241 (1954)
Mo_5Si_3	b.c.-Tetrag. (I42m)	W_5Si_3	$D8_m$(T1)	9.62		4.90	4		T-0.5094	Aronsson: Acta Chem. Scand. 9, 1107 (1955)
				9.66		4.99	4	19-278		Parthé et al., Monatsh. Chem. 86, 182 (1955)
				9.642		4.905		20-155		Dauben et al., J. Phys. Chem. 60, 443 (1956)
				9.617		4.899	4	19-278		Aronsson: Acta Chem. Scand. 9, 137 (1955)
(C-stabilized)	Hexag. ($P6_3/mcm$)	Mn_5Si_3	$D8_8$	7.286		5.00				Schachner et al., Monatsh. Chem. 85, 245
Mo_3Si_2										Brewer et al., J. Am. Ceram. Soc. 33,291 (1950)
$MoSi_2$	b.c.-Tetrag. (I4/mmm)	$MoSi_2$	$C11_b$	3.200		7.861	2	1-784	T-2.4566	Zachariasen: Z. Physik. Chem. Leipzig, 128, 39 (1927); Norsk Geol. Tidsskr. B9, 337 (1927)
				3.203		7.887		16-117	T-2.4566	Kieffer, Cerwenka: Z. Metallk. 43, 101 (1952)
				3.202		7.852	(2)	16-118	T-2.4522	Nowotny et al., Monatsh. Chem. 83, 1243 (1952)
				3.203		7.855				Matyushenko: Poroshk. Metall. 20, 22 (1964)
	Hexag. ($P6_222$)	$CrSi_2$	C40	4.605		6.559			H-1.4243	Aubry et al., Compt. rend. 261, 2665 (1965)

Silicide	Bravais system (sp. group)	structure type	Strukturberichte	a	b	c	Z	Structure Reports	Donnay-Ondik	Reference
Tc_4Si	Cubic (Im3m)	α-Fe		3.009						Gladyshevskii: Crystal Chemistry of Silicides and Germanides, Metalurgiya, Moscow (1971)
Tc_3Si	Cubic (I43m)	Fe_3Zn_{10}		9.014						Gladyshevskii: Crystal Chemistry of Silicides and Germanides, Metalurgiya, Moscow (1971)
Tc_5Si_3	Tetrag. (I4/mcm)	W_5Si_3(T1)		9.403		4.849				Gladyshevskii: Crystal Chemistry of Silicides and Germanides, Metalurgiya, Moscow (1971)
TcSi	Cubic ($P2_13$)	FeSi		4.755						Gladyshevskii: Crystal Chemistry of Silicides and Germanides, Metalurgiya, Moscow (1971)
Tc_4Si_7	Tetrag.			5.737		18.099			T-3.1548	Wittmann, Nowotny: J. Less Com. Metals , 9, 303 (1965)

Silicide	Bravais system (sp. group)	structure type	Strukturberichte	a	b	c	Z	Structure Reports	Donnay-Ondik	Reference
Ru_2Si	Orthor. (Pnma)	$PbCl_2$	C23	5.279	4.005	7.418	4	26-243		Aronsson, Åselius: Acta Chem. Scand. 15, 1571 (1961)
				"	"	"		23-57,59		Aronsson et al., Nature, 183 1318 (1959)
Ru_5Si_3	Orthor. (Pbam)	Rh_5Ge_3		5.2462	9.8152	4.0231	2	35A-86		Engström: Acta Chem. Scand. 24, 1466 (1970)
Ru_4Si_3	Orthor. (Pnma)			5.1936	4.0216	17.1343	4	34A-125	O-0.3031(IV)	Engström, Johnsson: Ark. Kemi. 30, 141 (1969)
α-RuSi	Cubic (Pm3m)	CsCl	B2	2.909			1	21-169		Korst et al., J. Phys. Chem. 61, 1541 (1957)
				2.91				15-24	C-2.91	Buddery, Welch: Nature, 167, 362 (1951)
β-RuSi	Cubic ($P2_13$)	FeSi	B20	4.703			4			Finnie: J. Less Com. Metals 4, 24 (1962)
			B20?	4.73				21-169		Korst et al., J. Phys. Chem. 61, 1541 (1957)
				4.71				15-24,25	C-4.71	Buddery, Welch: Nature, 167, 362 (1951)
Ru_2Si_3	Tetrag.			11.075		8.954	16		T-0.8085	Schomma et al., Monatsh. Chem. 94, 681 (1963)
				5.53		4.47		15-24,25	T-0.8085	Buddery, Welch: Nature, 167, 32 (1951)
				5.531		4.469			T-0.8085	Raub, Fritzsche: Z. Metallk. 53, 779 (1962)
	Orthor.			11.057	8.934	5.533		40A-75		Poutcharovsky, Parthé: Acta Cryst. B30, 2692 (1974)
				11.06	8.94	5.53	8	40A-75		Völlenkle: Monatsh. Chem. 105, 1217 (1974); Israiloff, Völlenkle: Monatsh. Chem. 105, 1313 (1974)
$RuSi_{1.8}$										Finnie: J. Less Com. Metals 4, 24 (1962)

Silicide	Bravais system (sp. group)	structure type	Strukturberichte	a	b	c	Z	Structure Reports	Donnay-Ondik	Reference
Rh_2Si	Orthor. (Pnma)	$PbCl_2$	C23	5.408	7.383	3.930	4	23-57,60	O-0.7325	Engström: Acta Chem. Scand. 17, 775 (1963)
				5.41	7.38	3.93	4	28-40		Aronsson et al., Nature, 183, 1318 (1959)
	Orthor.	anti-$PbCl_2$	anti-C23	5.41	7.39	3.93	4		O-0.7321(IV)	Schulz et al., Z. Anorg. Allg. Chem. 357, 299 (1968)
Rh_5Si_3	Orthor. (Pbam)	Rh_5Ge_3		5.317	10.131	3.895	2		O-0.5248	Engström: Acta Chem. Scand. 17, 775 (1963)
				5.309	10.074	3.888			O-0.5248	Schubert et al., Naturwissenschaften 47, 303 (1960)
				5.32	10.13	3.90	2	28-40		Engström: Acta Chem. Scand. 17, 775 (1963)
$Rh_{20}Si_{13}$	Hexag. ($P6_3/m$)	$Rh_{20}Si_{13}$		11.851		3.623	1	30A-88		Engström Acta Chem. Scand. 19, 1924 (1965)
Rh_3Si_2	Hexag. ($P6_3/mmc$)			11.851		3.623			H-0.3057	Engström: Acta Chem. Scand. 17, 775 (1963)
Rh_3Si_{2+}	Hexag. ($P6_3/mmc$)	Ni_2In	B8	3.949		5.047			H-1.2780(IV)	Schubert et al., Naturwissenschaften 47, 303 (1960); Bahn, Schubert: Z. Metallk. 51, 327 (1960)
RhSi	Orthor. (Pnma)	MnP	B31	5.531	6.362	3.063	4		O-0.8694(IV)	Schubert et al., Naturwissenschaften 47, 303 (1960); Bhan, Schubert: Z. Metallk. 51, 327 (1960)
	Cubic (Pm3m)	CsCl	B2	2.9630			1	23-227	C-2.9630	Finnie, Searcy: Acta Cryst. 12, 260 (1959)
	Cubic ($P2_13$)	FeSi	B20	4.675			4	18-271	C-4.675	Geller, Wood: Acta Cryst. 7, 441 (1954)
				4.674			4	30A-89	C-4.675	Engström, Johnson: Acta Chem. Scand. 19, 1508 (1965)

Silicide	Bravais system (sp. group)	structure type	Strukturberichte	a	b	c	Z	Structure Reports	Donnay-Ondik	Reference
Rh_4Si_5	Monocl. ($P2_1m$)			12.335	100.181° 3.508	5.924	2	33A-137	M-3.5162	Engström: Acta Chem. Scand. 22, 3127 (1968)
Rh_3Si_4	Orthor. (Pnma)	Rh_3Si_4		18.810	3.614	5.813	4	33A-136	O-0.3090(IV)	Engström, Persson: Acta Chem. Scand. 22, 3120 (1968)
$RhSi_2$	Cubic	(CsCl)	(B2)	2.963						Goldschmidt, Interstitial Alloys, (Plenum, New York, 1967)

Remark: DO-H-1.2780(IV) Rh_3Si_{2+} (nominal composition $Rh_{48}Si_{52}$) replaces DO-H-1.2780(II) $Rh_{58}Si_{42}$.

Silicide	Bravais system (sp. group)	structure type	Strukturberichte	a	b	c	Z	Structure Reports	Donnay-Ondik	Reference
Pd_9Si_2	Orthor.			9.048	9.396	7.418	4	31A-56	O-0.9630	Nylund: Acta Chem. Scand. 20, 2381 (1966)
Pd_4Si	Tricl.			111.02° 4.402	96.52° 7.700	89.15° 8.990	4			Canali et al., J. Appl. Phys. 50, 5768 (1979)
Pd_3Si	Orthor. (Pnma)	Fe_3C	DO_{11}	5.735	7.555	5.260	4	24-205	O-0.7591	Aronsson, Nylund: Acta Chem. Scand. 14, 1011 (1960)
Pd_9Si_4	Tetrag.			4.73-4.67		6.87				Saviteky, Dolyakova, Gorina and Roshan: Physical Metallurgy of Platinum Metals (MIR, Moscow, 1978)
Pd_2Si	Hexag. (P62m)	Fe_2P	C22	6.49		3.43	3	17-254	H-0.5278	Andreko, Schubert: Z. Metallk. 44, 307 (1953)
				6.49		3.45			H-0.5278	Schubert, Andreko: Naturwissenschaften 39, 351 (1952)
				6.53		3.43			H-0.5278	Buddery, Welch: Nature, 167, 362 (1951)
				6.497 6.528	Si poor Si rich	3.432 3.437	3	24-206	H-0.5278	Aronsson et al., Acta Chem. Scand. 14, 1011 (1960)
				6.4960		3.4330		31A-56	H-0.5285	Nylund: Acta Chem. Scand. 20, 2381 (1966)
				13.055	Si rich	27.490	96	31A-56	H-2.1057	Nylund: Acta Chem. Scand. 20, 2381 (1966)
		Fe_2P		6.491		3.431	3		H-0.5286(IV)	Schulz et al., Z. Anorg. Allg. Chem. 357, 299 (1968)
PdSi	Orthor. (Pnma)	MnP	B31	5.599	6.133	3.381	4	13-28	O-0.9129	Pfisterer, Schubert: Z. Metallk. 41, 358 (1950); Naturwissenschaften 37, 112 (1950)
				5.6173	6.1534	3.3909		35A-86		Engström: Acta Chem. Scand. 24, 1466 (1970)

Silicide	Bravais system (sp. group)	structure type	Strukturberichte	a	b	c	Z	Structure Reports	Donnay-Ondik	Reference
La_5Si_3	b.c.-Tetrag. (I4/mcm)	Cr_5B_3	$D8_l$(T2)	7.96		14.14	4		T-1.7764(IV)	Mayer, Shidlovsky: Inorg. Chem. 8, 1240 (1969)
		Cr_5B_3	$D8_l$(T2)	7.949 7.950	La rich Si rich	14.07 14.04	4		T-1.7700(IV)	Raman: Trans. Indian Inst. Metals, 21, 5 (1968)
		Cr_5B_3		7.953		14.04	4		T-1.7654(IV)	Smith et al., Acta Cryst. 22, 940 (1967)
La_5Si_3	Hexag.			9.75		7.06				Grinthal: WADC Tech. Rept. 53-190 pt.VI(1958)
La_3Si_2	Tetrag. (P4/mbm)	U_3Si_2		7.885		4.434	2		T-0.5623	Raman: Trans. Indian Inst. Metals, 21, 5 (1968)
La_5Si_4	Tetrag. ($P4_{1,3}2_12$)	Zr_5Si_4		8.04		15.43	4		T-1.9192(IV)	Smith et al., Acta Cryst. 22, 940 (1967)
LaSi	Orthor. (P2mm)	FeB	B27	6.04	8.48	4.02	4		O-0.7123	Gladyshevskii, Kripyakevich: Zh. Strukt. Khim. 5, 853 (1964)
			B27	6.059	8.404	4.010	4		O-0.7210	Hohnke, Parthé: Acta Cryst. 20, 572 (1966)
	Orthor.	FeB	B27	6.024	8.380	3.990	4		O-0.7189(IV)	Raman: Trans. Indian Inst. Metals, 21, 5 (1968)
	Orthor.	FeB	B27	6.02	8.38	3.99	4		O-0.7184	Raman, Steinfink: Acta Cryst. 22, 688 (1967)

Silicide	Bravais system (sp. group)	structure type	Strukturberichte	a	b	c	Z	Structure Reports	Donnay-Ondik	Reference
La_3Si_5	Orthor.	$GdSi_2$		4.250	4.170	14.05			O-0.3025(IV)	Raman: Trans. Indian Inst. Metals, 21, 5 (1968)
$LaSi_2$	b.c.-Tetrag. (I4/amd)	$ThSi_2$	C_c	4.281		13.75	4	16-105	T-3.2116	Brauer, Haag: Z. Anorg. Allgem. Chem. 267, 198 (1952); Naturwissenschaften 37, 210 (1950)
				4.374		13.565			T-3.2116	Bertaut, Blum: Acta Cryst. 3, 319 (1950)
				4.31		13.80			T-3.2116	Perri et al., J. Phys. Chem. 63, 616 (1959)
	Tetrag.	$ThSi_2$	C_c	4.305		13.84	4		T-3.2149(IV)	Raman, Steinfink: Inorg. Chem. 6, 1789 (1967); Raman: Trans. Indian Inst. Metals, 21, 5 (1968)
	b.c.-Orthor. (Imma)	$GdSi_2$		4.27	4.19	13.94	4		O-0.3063(IV)	Mayer et al., Inorg. Chem. 6, 842 (1967)
$LaSi_2$ (H.T.)	Orthor.	$GdSi_2$		4.27	4.18	14.05	4			Gladyshevskii, Kripyakevich: Zh. Strukt. Khim. 5, 853 (1964)

Other references:

SR-27-336: Mayer et al., J. Phys. Chem. 66, 693 (1962); Tharp: J. Phys. Chem. 66, 758 (1962); give structures for MSi_2, where M is Tb,Ho,Y,Er,Tm,Yb,Lu.

SR-28-48: Dop. Akad. Nauk Ukrain. RSR, 886 (1963); gives structures of MSi_{2-x} having AlB_2 structure.

Silicide	Bravais system (sp. group)	structure type	Strukturberichte	a	b	c	Z	Structure Reports	Donnay-Ondik	Reference
Hf_2Si	b.c.-Tetrag. (I4/mcm)	Al_2Cu	C16	6.48		5.21	4	22-134	H-0.8037	Nowotny et al., Monatsh. Chem. 89, 701 (1958)
	Tetrag.		C16	6.553		5.186		38A-6		Havinga et al., J. Less Com. Metals 27, 169,269 (1972)
Hf_5Si_3 (C-stabilized)	Hexag. ($P6_3/mcm$)	Mn_5Si_3	$D8_8$	7.890		5.558	2	22-134	H-0.7045	Nowotny et al., Monatsh. Chem. 89, 701 (1958)
Hf_3Si_2	Tetrag. (P4/mbm)	U_3Si_2		7.000		3.671	2	26-11	T-0.5244(IV)	Schob et al., Monatsh. Chem. 92, 1218 (1961)
				7.000		3.714				Gladyshevskii: Crystal Chemistry of Silicides and Germanides, Moscow (1971)
Hf_5Si_4	Tetrag. ($P4_{1,3}2_12$)	Zr_5Si_4		7.039		12.826	4		T-1.8221	Pfeifer, Schubert: Z. Metallk. 57, 884 (1966)
HfSi	Orthor. (P2mm)	FeB	B27	6.855	3.753	5.191	4	22-134	O-0.7573	Nowotny et al., Monatsh. Chem. 89, 701 (1958)
	Hexag.			6.86		12.60		18-166	H-1.8367	Post et al., J. Chem. Phys. 22, 1264 (1954)
$HfSi_2$	o.f.c.-Orthor.	$ZrSi_2$	C49	3.677	14.550	3.649	4	21-124	O-0.2527	Smith, Bailey: Acta Cryst. 10, 341 (1957)
			C49	3.67	14.56	3.64	2	18-167	O-0.2527	Post et al., J. Chem. Phys. 22, 1264 (1954)
				3.69	14.46	3.64		20-116	O-0.2527	Cotter et al., J. Am. Ceram. Soc. 39, 11 (1956)

DO-H-0.8037: Hf_2Si is considered hexagonal by mistake?

Silicide	Bravais system (sp. group)	structure type	Strukturberichte	a	b	c	Z	Structure Reports	Donnay-Ondik	Reference
$Ta_3(Ta_{.28}Si_{.72})$	Hexag.	Ni_3Sn	DO_{19}	6.105		4.919	2	17-259	H-0.8057	Nowotny et al., Monatsh. Chem. 84, 1 (1953)
$Ta_4Si(\sigma)$	Tetrag.			10.18		5.19			T-0.5098	Ganglberger et al., Monatsh. Chem. 96, 242 (1965)
Ta_3Si	Tetrag. ($P4_2/n$)	Ti_3P		10.19		5.17	8		T-0.5098 T-0.5074(IV)	Schubert et al., Naturwissenschaften 51, 506 (1964)
Ta_2Si	b.c.-Tetrag. ($I4/mcm$)	Al_2Cu	C16	6.157		5.039	4	17-259	T-0.8184	Kieffer et al., Z. Metallk. 44, 242 (1953); Nowotny et al., Monatsh. Chem. 84, 1 (1953)
	"	"	"	6.160		5.056		38A-6		Havinga et al., J. Less Com. Metals 27, 169,269 (1972)
γ-Ta_5Si_3 (C-stabilized)	Hexag. ($P6_3/mcm$)	Mn_5Si_3	$D8_8$	7.474		5.226	2	17-259	H-0.6992	Nowotny et al., Monatsh. Chem. 84, 1 (1953)
				7.484		5.223				Nowotny, Laube: Planseeber. Pulvermet. 9, 54 (1961)
α-Ta_5Si_3	b.c.-Tetrag. ($I\bar{4}2m$)	W_5Si_3	$D8_m$(T1)	9.88		5.06	4	19-278		Parthé et al., Monatsh. Chem. 86, 385 (1955)
β-Ta_5Si_3	b.c.-Tetrag. ($I4/mcm$)	Cr_5B_3	$D8_l$(T2)	6.516		11.873	4	19-279	T-1.8221	Parthé et al., Monatsh. Chem. 86, 859 (1955)
$TaSi_2$	Hexag. ($P6_222$)	$CrSi_2$	C40	4.7821		6.5695	3	23-236	H-1.3738	Swanson et al., Natl. Bur. Std. Circ. 539, 8, 59 (1959)
				4.781		6.564		17-118	H-1.3738	Nowotny et al., Monatsh. Chem. 84, 579 (1953)
				4.783		6.565		8-102	H-1.3738	Wallbaum: Z. Metallk. 33, 378 (1941)
								26-246		

DO-H-1.3738: Wallbaum ($TaSi_2$) gives a=4,773, c=6.552. kX?

Silicide	Bravais system (sp. group)	structure type	Strukturberichte	a	b	c	Z	Structure Reports	Donnay-Ondik	Reference
W_3Si	Cubic (Pm3n)	β-W	A15	4.910			2	23-239	C-4.910	Matyushenko et al., Fiz. Metal. i Metalloved. 8, 878 (1959)
W_5Si_3	b.c.-Tetrag. (I42m)	W_5Si_3	$D8_m$(T1)	9.645		4.97	4		T-0.5153	Aronsson: Acta Chem. Scand. 9, 1107 (1955)
				9.605		4.964		20-155		Dauben et al., J. Phys. Chem. 60, 443 (1956)
				9.645		4.969		19-277		Aronsson: Acta Chem. Scand. 9, 137 (1955)
				9.56		4.94		19-278		Parthé et al., Monatsh. Chem. 86, 182 (1955)
W_5Si_3 (C-stabilized)	Hexag. ($P6_3/mcm$)	Mn_5Si_3	$D8_8$	7.19		4.85	2	19-280		Parthé et al., Monatsh. Chem. 86, 182 (1955)
WSi_2	Tetrag.	WSi_2	C11	3.212		7.880	2	1-219,783	T-2.4533	Zachariasen: Z. Physik. Chem. Leipzig 128, 39 (1927); Norsk Geol. Tidsskr. B9, 337 (1927)
	b.c.-Tetrag. (I4/mmm)	$MoSi_2$	$C11_b$	3.21		7.84			T-2.4533	Alyamovskii et al., Zh. Neorgan. Khim. 7, 1678 (1962); Dokukina et al., Zh. Neorgan. Khim. 9, 1905 (1964)
		$MoSi_2$	$C11_b$	3.212		7.835				Matyushenko: Poroshk. Metall. 20, 22 (1964)
				3.217		7.884		16-137	T-2.4533	Kieffer et al., Z. Metallk. 43, 284 (1952)
				3.210		7.829		16-118	T-2.4533	Nowotny et al., Monatsh. Chem. 83, 1243 (1952); complete solid soln. to $MoSi_2$

The phase W_3Si_2 (Aronsson: Acta Chem. Scand. 9, 137 (1955)) was later identified as W_5Si_3.

Silicide	Bravais system (sp. group)	structure type	Strukturberichte	a	b	c	Z	Structure Reports	Donnay-Ondik	Reference
Re_5Si_3	b.c.-Tetrag. (I42m)	W_5Si_3	$D8_m$(T1)	9.53		4.81	4			Knapton: J. Inst. Met. 87, 28 (1958-9)
				9.53		4.81		23-223		Knapton: Plansec Proc. 412 (1959) (phase diag.)
	Monocl.			6.4511	5.3938	γ=94.203 9.6012		45A-107		Pecarskij et al., Kristalografija 24, 945 (1979)
ReSi	Cubic ($P2_13$)	FeSi	B20	4.774			4	19-267 23-223	C-4.775	McNees, Searcy: J. Amer. Chem. Soc. 77, 5290 (1955)
$ReSi_2$	b.c.-Tetrag. (I4/mmm)	$MoSi_2$	$C11_b$	3.131		7.676	2	8-102		Knapton: J. Inst. Met. 87, 28 (1958-9)
				3.131		7.676		23-223		Buddery, Thesis, Imperial College, London (1951)
				3.129		7.674				Aronsson: Ark. Kemi. 16, 379 (1960)
	Tetrag.		C11	3.138		7.666	2		T-2.4430	Duffin et al., Acta Cryst. 17, 450 (1964)

DO-T-2.4430: $ReSi_2$ forms solid solution with up to 0.7 Ti.

Silicide	Bravais system (sp. group)	structure type	Strukturberichte	a	b	c	Z	Structure Reports	Donnay-Ondik	Reference
OsSi	Cubic ($P2_13$)	FeSi	B20	4.729			4	21-161		Korst et al., J. Phys. Chem. 61, 1541 (1957)
	Cubic ($Pm3m$)	CsCl	B2	2.963						Finnie: J. Less Com. Metals 4, 24 (1962)
Os_2Si_3	Tetrag.	Ru_2Si_3		11.158		8.962	8		T-0.8032	Schwomma et al., Monatsh. Chem. 94, 924 (1963)
				5.58		4.48		15-25	T-0.8032	Buddery, Welch: Nature, 167, 362 (1951)
$OsSi_{2.4}$	Monocl.	$OsGe_2$ or As_2Nb		8.77	β=118.5 3.00	7.38	4	27-372		Finnie: J. Less Com. Metals 4, 24 (1962)
$OsSi_2$	o.f.c.-Orthor. (Cmca)	β-$FeSi_2$		10.1496	8.1168	8.2230	16	35A-84		Engström: Acta Chem. Scand. 24, 2117 (1970)
$OsSi_{1.8}$ $OsSi_3$								27-372		Finnie: J. Less Com. Metals 4, 24 (1962)

The monoclinic form of $OsSi_2$ is stabilized by Al or O. Probably not a pure form.

Silicide	Bravais system (sp. group)	structure type	Strukturberichte	a	b	c	Z	Structure Reports	Donnay-Ondik	Reference
Ir_3Si	b.c.-Tetrag. (I4/mcm)	U_3Si		5.222		7.954	4	24-113	T-1.5232(IV)	Schubert et al., Naturwissenschaften 47, 303 (1960); Bahn, Schubert: Z. Metallk. 51, 327 (1960)
	Tetrag.	U_3Si		5.222		7.954		45A-85		Kimmel J. Less Com. Metals 59, 83 (1978)
	Hexag.	Na_3As	DO_{18}	4.350		6.630	2	27-373		Finnie: J. Less Com. Metals 4, 24 (1962)
Ir_2Si	Orthor. (Pnma)	$PbCl_2$	C23	5.284	3.989	7.615	4	24-113	O-0.6939(IV	Schubert et al., Naturwissenschaften 47, 303 (1960); Bahn, Schubert: Z. Metallk. 51, 327 (1960)
Ir_3Si_2(H.T.)	Hexag. ($P6_3/mmc$)	Ni_2In	$B8_2$	3.963		5.126			H-1.2922(IV)	Schubert et al., Naturwissenschaften 47, 303 (1960)
				3.968		5.126	1	24-113	H-1.2922(IV)	Bahn, Schubert: Z. Metallk. 51, 327 (1960)
				3.97		5.13		15-25	H-1.2922(IV)	Buddery, Welch: Nature, 167, 362 (1951)
IrSi	Orthor. (Pnma)	MnP	B31	5.558	6.273	3.211	4	21-136	O-0.8860	Korst et al., J. Phys. Chem. 61,1541 (1957)
		MnP		5.56	6.27	3.22	4		O-0.8868(IV	Schulz et al., Z. Anorg. Allg. Chem. 357, 299 (1968)
Ir_4Si_5	Monocl. ($P2_1/m$)	Rh_4Si_5		α=100 12.354	14 3.618	5.881				Engström: Acta Univ. Upsala, p54 (1970)
Ir_3Si_4	Orthor. (Pnma)	Rh_3Si_4		18.8701	3.6967	5.7742	4	35A-70		Engström, Zackrisson Acta Chem. Scand. 24, 2109 (1970)
Ir_3Si_4	Orthor.	Rh_3Si_4		18.8741	3.6979	5.7717	4	35A-70		Engström, Zackrisson Acta Chem. Scand. 24, 2109 (1970)

Silicide	Bravais system (sp. group)	structure type	Strukturberichte	a	b	c	Z	Structure Reports	Donnay-Ondik	Reference
Ir_2Si_3										Bahn, Schubert: Z. Metallk. 51, 327 (1960)
								27-373		Finnie: J. Less Com. Metals 4, 24 (1962)
$IrSi_{1.75}$	Monocl.			5.542	β=120.61 14.166	12.426				Petersson et al., J. Apl. Phys. 50, 3357 (1979)
$IrSi_2$								27-373		Finnie: J. Less Com. Metals 4, 24 (1962)
										Bahn, Schubert: Z. Metallk. 51, 327 (1960)
$IrSi_3$	Hexag.	$AsNa_3$	DO_{18}	4.350		6.630	2			Finnie: J. Less Com. Metals 4, 24 (1962)
				4.351		6.622		37A-100		White, Hockings: Inorg. Chem. 10, 1934 (1971)
				4.350		6.610	2	24-113	H-1.5195(IV)	Bahn, Schubert: Z. Metallk. 51, 327 (1960)

Silicide	Bravais system (sp. group)	structure type	Strukturberichte	a	b	c	Z	Structure Reports	Donnay-Ondik	Reference
Pt_4Si?										Gohle, Schubert: Z. Metallk. 55, 503 (1964)
Pt_3Si	Monocl.	Pt_3Ge		5.566	$\beta=90^{\circ}28'$ 7.773	5.389	4		M-0.7161	Schubert et al., Naturwissenschaften 47, 303 (1960)
				7.715	$\beta=88^{\circ}15'$ 7.773	7.778		24-117		Schubert et al., Naturwissenschaften 47, 303 (1960)
(L.T.)	Monocl.	Pt_3Ge		7.702	$\beta=88^{\circ}18'$ 7.765	7.765	8	29-129	M-0.7161	Gohle, Schubert: Z. Metallk. 55, 503 (1964)
				7.702	$\beta=46.19$ 7.765	5.378	4	29-129		Gohle, Schubert: Z. Metallk. 55, 503 (1964)
				7.072	$\beta=135.19$ 7.765	5.558	4			Engström: Acta Univ. Upsala, p54 (1970)
(H.T.)	b.c.-Tetrag. (I4/mcm)	U_3Si		5.46		7.86	4	29-129		Gohle, Schubert: Z. Metallk. 55, 503 (1964)
Pt_5Si_2										Voronov: Izvest. Sektora Platiny B 145, (1936)
$Pt_{12}Si_5$ (H.T.)	Tetrag.	$Pt_{12}Si_5$		13.404		5.451	4		T-0.4067(IV)	Gold, Schubert Z. Krist. 128, 406 (1969)
Pt_7Si_3	Tetrag.			13.395		5.54		29-129		Gohle, Schubert: Z. Metallk. 55, 503 (1964)

Silicide	Bravais system (sp. group)	structure type	Strukturberichte	a	b	c	Z	Structure Reports	Donnay-Ondik	Reference
Pt_2Si	Tetrag.		deformed C1	5.554		5.923			T-1.0664	Schubert et al., Naturwissenschaften 47, 303 (1960)
α-Pt_2Si(L.T.)	Tetrag.	ZrH_2		3.933		5.910	2			Gohle, Schubert: Z. Metallk. 55, 503 (1964)
β-Pt_2Si(H.T.)	Hexag. (P62m)	Fe_2P	C22	6.436		3.569	3		H-0.5545	Schubert et al., Naturwissenschaften 47, 303 (1960)
				6.440		3.573		29-129		Gohle, Schubert: Z. Metallk. 55, 503 (1964)
Pt_6Si_5	Monocl.		Quinier phot.	15.462	β=86°53' 3.499	6.169	2	29-79		Gohle, Schubert: Z. Metallk. 55, 503 (1964)
			Weissenberg phot.	15.308	β=86.6 3.48	6.120	2	29-79		Gohle, Schubert: Z. Metallk. 55, 503 (1964)
PtSi	Orthor. (Pnma)	MnP	B31	5.595	5.932	3.603	4	13-28	O-0.9432	Pfisterer, Schubert: Z. Metallk. 41, 358 (1950); Naturwissenschaften 37, 112 (1950)
				5.577	5.916	3.587		39A-66		Graber et al., Acta Cryst. B29, 1991 (1973)
Pt_3Si_2 or Pt_2Si	Tetrag.	Pt_3B_2?		2.78		2.96		15-25		Buddery, Welch: Nature 167, 362 (1951)

Pt_4Si H.T. form; O - stabilized.

Appendix A-3.1.

The geometric models used in chapter 3 and their static elastic properties

Four models were used in chapter 3. Three of these models are geometric in nature, i.e., they do not have any hidden coordinates, and the elastic energy can be written in terms of interatomic distances and angles. In this appendix, these models are described, and their predictions for the static elastic properties of the bulk silicon are given. The dynamic elastic properties, i.e., various points on the phonon band structure, are given in Appendix A-3.2.

The models that will be described are the simple bond-bending and-stretching model, its modification by Singh and Dayal[1], and the Valence Force Field model of Musgrave and Pople[2]. The calculation of the static elastic properties for the first model will be described in detail. For the other models only the final results will be given, since the calculations are very similar.

Simple bond bending and stretching model

In the diamond structure, every atom has four nearest neighbors. Considering the straight line segment connecting nearest neighbors as 'the bond', all the bonds have equal length r_0, and the angle between two adjacent bonds is always the same, θ_0. $r_0 = 2.3517\mathring{A}$ for silicon at 0°K, and θ_0 is the tetrahedral angle, i.e., $\cos\theta_0 = -1/3$, or $\theta_0 = 109.471°$. The interatomic distance r_0 is related to the lattice parameter a of the cubic structure by

$$r_0 = a\frac{\sqrt{3}}{4}. \qquad (A-3.1.1)$$

According to this simple model, every bond resists a change in its length by the same amount, regardless of the other bonds, and every two adjacent bonds resist a change in the angle between them by the same amount. Therefore, the total ground state energy of a deformed cluster or solid can be written as

$$E = E_0 + \frac{1}{2}k_r \sum_{\text{bonds}} (r - r_0)^2 + r_0^2 \frac{k_\theta}{2} \sum_{\substack{\text{adjacent} \\ \text{bonds}}} (\theta - \theta_0)^2.$$

Here E_0 is the ground state energy of the undeformed cluster or solid and will be taken to be zero throughout this chapter; r is a bond length, and θ is the angle between a pair of adjacent bonds.

Using this model, there is a very simple expression for the bulk modulus of a solid. The bulk modulus is defined as

$$B = V\left(\frac{\partial^2 E}{\partial V^2}\right)_{r=r_0}$$

under a uniform pressure. Such pressure will change only the interatomic distance, but not the bond-bond angles. Thus, one can calculate the change in volume as a function of a change in interatomic distance, using (A-3.1.1), then calculate the change in energy as a function of volume change, to obtain the bulk modulus.

$$B = V\left(\frac{\partial^2 E}{\partial V^2}\right)_{r=r_0} = V \cdot \frac{r}{3V}\frac{\partial}{\partial r}\left(\frac{r}{3V}\frac{\partial E}{\partial r}\right)_{r=r_0} = \left(\frac{r^2}{9V}\frac{\partial^2 E}{\partial r^2}\right)_{r=r_0}.$$

A cubic unit cell has a volume of $V = a^3$. It contains eight atoms, hence sixteen bonds. Therefore,

$$B = \left(\frac{r^2}{9a^3}\right)_{r=r_0} \cdot 16k_r = \frac{k_r}{3a} = \frac{k_r}{4\sqrt{3}r_0}. \qquad (A-3.1.2)$$

Calculating the Poisson ratios and the stiffness coefficients c_{11}, c_{12} and c_{44} is somewhat more complicated. Consider a uniaxial pressure along the [001] direction

(cf. Fig. A-3.1.). As a result of this pressure, both the bond lengths and the angle between the bonds will change. The ratio of the change in bond length to the change in bond-bond angles will be such as to minimize the energy gain for the given strain. For this particular strain, symmetry dictates that all the bonds will have the same length, $r_0 - \Delta r$, all the angles pointing along the z-axis will be the same, $\theta_0 + \Delta\theta$, and all the angles pointing perpendicular to the z-axis will be the same. These angles are between adjacent bonds, and they are said to point in the direction of their bisector. In the diamond structure they all point either along the x-, y-, or z- axes. As there are four bonds to each atom, there are six such angles with an apex on each atom. These six angles are not independent, and there is one relation connecting them. This relation has quite a complicated form, but, if the angles are all almost tetrahedral, then their deviations from tetrahedral sum up to zero, to first order. Quantitatively put, if

$$\theta_i = \theta_0 + \left(\frac{\partial\theta_i}{\partial t}\right)_0 \cdot t + O(t^2), \qquad i = 1, \ldots, 6$$

then

$$\sum_{i=1}^{6} \left(\frac{\partial\theta_i}{\partial t}\right)_0 = 0.$$

Each atom has two angles pointing along the z-axis, and four angles pointing perpendicular to it. Therefore, if the angles pointing along the z-axis increase by $\Delta\theta$, then the angles perpendicular to the z-axis should decrease by $\Delta\theta/2$, to within first order in $\Delta\theta$. There are two bonds and six angles per atom, therefore, the total energy change per atom is

$$\Delta E/\text{atom} = k_r \cdot \Delta r^2 + \frac{3}{2} r_0^2 k_\theta \Delta\theta^2. \qquad (A - 3.1.3)$$

The axial strain is given by $\Delta Z/Z$, where $Z = r_0 \cos(\theta_0/2)$.

$$\frac{\Delta Z}{Z} = -\frac{\Delta r}{r_0} - \frac{1}{2}\tan\frac{\theta_0}{2}\Delta\theta = -\frac{\Delta r}{r_0} - \frac{\sqrt{2}}{2}\Delta\theta.$$

Since the axial strain is given, we now use a Lagrange multiplier λ, to minimize $(\Delta E/\text{atom}) - \lambda(\Delta Z/Z)$. Differentiating with respect to Δr and $\Delta\theta$, one obtains,

$$2k_r \cdot \Delta r + \frac{\lambda}{r_0} = 0.$$

$$3r_0^2 k_\theta \cdot \Delta\theta + \frac{\lambda\sqrt{2}}{2} = 0.$$

Therefore,

$$\lambda = -2r_0 k_r \Delta r = -\frac{6r_0^2 k_\theta \Delta\theta}{\sqrt{2}},$$

and

$$\frac{\Delta\theta}{\Delta r} = \frac{\sqrt{2}k_r}{3r_0 k_\theta}.$$

We can now calculate the axial strain as a function of λ and the spring constants:

$$\frac{\Delta Z}{Z} = -\frac{\Delta r}{r_0} - \frac{\sqrt{2}}{2}\Delta\theta = \lambda\left(\frac{1}{2r_0^2 k_r} + \frac{1}{6r_0^2 k_\theta}\right).$$

and similarly, for $X = r_0 \sin(\theta_0/2)$, one can calculate the perpendicular $\Delta X/X$:

$$\frac{\Delta X}{X} = -\frac{\Delta r}{r_0} + \cot\frac{\theta_0}{2}\cdot\frac{\Delta\theta}{2} = -\frac{\Delta r}{r_0} + \frac{\Delta\theta}{2\sqrt{2}} = \lambda\left(\frac{1}{2r_0^2 k_r} - \frac{1}{12r_0 k_\theta}\right)$$

One should notice that the quantity X appearing here and in Fig. A-3.1 is not directed along the x-axis, but rather along the [110] direction. The Poisson ratio is defined as the ratio of the perpendicular to the axial strains:

$$P.R. = \frac{s_{12}}{s_{11}} = \frac{\Delta X/X}{\Delta Z/Z} = \frac{6k_\theta - k_r}{6k_\theta + 2k_r}. \qquad (A-3.1.4)$$

Equations (A-3.1.2) and (A-3.1.4) relate k_r and k_θ to experimentally measurable quantities. Other such quantities are the elastic constants c_{ij} and the elastic moduli s_{ij}. To calculate them, one may recall that for cubic crystals

$$B = \frac{c_{11} + 2c_{12}}{3} = \frac{1}{3(s_{11} + 2s_{12})},$$

and using (A-3.1.2), obtain

$$s_{11} + 2s_{12} = \frac{4\sqrt{3}}{3} \cdot \frac{r_0}{k_r}. \qquad (A-3.1.5)$$

From equations (A-3.1.4) and (A-3.1.5), one can extract s_{11} and s_{12}:

$$s_{11} = \frac{4r_0}{3\sqrt{3}}\left(\frac{1}{k_r} + \frac{1}{3k_\theta}\right) \qquad s_{12} = \frac{4r_0}{3\sqrt{3}}\left(\frac{1}{k_r} - \frac{1}{6k_\theta}\right)$$

and

$$c_{11} = \frac{s_{11} + s_{12}}{(s_{11} - s_{12})(s_{11} + 2s_{12})} = \frac{\sqrt{3}}{r_0}\left(k_\theta + \frac{k_r}{12}\right)$$

$$c_{12} = \frac{-s_{12}}{(s_{11} - s_{12})(s_{11} + 2s_{12})} = \frac{\sqrt{3}}{r_0}\left(-\frac{k_\theta}{2} + \frac{k_r}{12}\right)$$

The shear modulus is obtained in a similar way. In Fig. A-3.1 one can see a model of a shear stress in the [110] direction. Neglecting quadratic and higher order terms, the angles pointing along the [001] and [00$\bar{1}$] direction remain unchanged, the angles pointing in the [100] and [010] directions decrease by $\Delta\theta$, the angles pointing along the [$\bar{1}$00] and [0$\bar{1}$0] directions increase by $\Delta\theta$, the bonds along the [1$\bar{1}$1] and [$\bar{1}$11] directions remain unchanged, the bonds along the [111] direction increase by Δr and the bonds along the [11$\bar{1}$] direction decrease by Δr.

The shear strain is given by $\Delta X/Z$. To calculate ΔX, note that the angles in the (1$\bar{1}$0) plane (the plane in which Fig. A-3.1 is drawn) do not change magnitude to first order, but they rotate around the [1$\bar{1}$0] direction (perpendicular to the page). The same is true for the angles that are initially in the (110) plane. They also maintain the same magnitude, up to first order, but they rotate around the [1$\bar{1}$0] direction, away from the (110) plane. ΔX is due to these two rotations. It is convenient, therefore, to split ΔX into its two contributions, and write

$$\Delta X = r_0 \cdot (\xi_1 + \xi_2).$$

Here ξ_1 is the contribution due to the rotation of an angle away from the (110) plane, and ξ_2 is the contribution due to the rotation of an angle in the $(1\bar{1}0)$ plane. Introducing a coordinate system in Fig. A-3.1, such that the x-axis is along the crystal [110] direction, and the y-axis is along the $[1\bar{1}0]$ direction, one can write the relative coordinates of the nearest neighbors as:

$$\vec{r}_1 = r_0\left(\xi_1, \sqrt{\frac{2}{3}}, \sqrt{\frac{1}{3}}\right),$$
$$\vec{r}_2 = r_0\left(\xi_1, -\sqrt{\frac{2}{3}}, \sqrt{\frac{1}{3}}\right),$$
$$\vec{r}_3 = r_0\left(-\sqrt{\frac{2}{3}} - \xi_2, 0, -\sqrt{\frac{1}{3}}\right),$$

and

$$\vec{r}_4 = r_0\left(\sqrt{\frac{2}{3}} - \xi_2, 0, -\sqrt{\frac{1}{3}}\right).$$

Expanding only to first order in ξ_1 and ξ_2:

$$|\vec{r}_1| = r_0, \quad |\vec{r}_2| = r_0, \quad |\vec{r}_3| = r_0 + \Delta r, \quad |\vec{r}_4| = r_0 - \Delta r$$

and

$$\theta_{12} = \theta_{34} = \theta_0, \quad \theta_{13} = \theta_{23} = \theta_0 + \Delta\theta, \quad \theta_{14} = \theta_{24} = \theta_0 - \Delta\theta,$$

where

$$\Delta r = \sqrt{2/3}\xi_2 r_0, \qquad \Delta\theta = \frac{\sqrt{3}\xi_1}{2} - \frac{\sqrt{3}\xi_2}{6}.$$

Now, analogous to (A-3.1.3), one can write the elastic energy per atom due to this shear stress.

$$\Delta E/\text{atom} = \frac{1}{2}k_r \cdot \Delta r^2 + 2r_0^2 k_\theta \Delta\theta^2,$$

and try to minimize $(\Delta E/\text{atom}) - \lambda(\Delta X/Z)$. The resulting expression to minimize is

$$\frac{\Delta E}{\text{atom}} - \lambda\left(\frac{\Delta X}{Z}\right) = \frac{1}{3}k_r r_0^2 \xi_2^2 + \frac{3}{2}r_0^2 k_\theta \left(\xi_1 - \frac{\xi_2}{3}\right)^2 - \frac{\sqrt{3}}{2}\lambda(\xi_1 + \xi_2).$$

Differentiating with respect to ξ_1 and ξ_2 one obtains,

$$3r_0^2 k_\theta \left(\xi_1 - \frac{\xi_2}{3}\right) - \frac{\sqrt{3}\lambda}{2} = 0, \qquad (A - 3.1.6)$$

$$\frac{2}{3}k_r r_0^2 \xi_2 - r_0^2 k_\theta \left(\xi_1 - \frac{\xi_2}{3}\right) - \frac{\sqrt{3}\lambda}{2} = 0. \qquad (A - 3.1.7)$$

From these two equations it is easy to extract the ratio ξ_1/ξ_2.

$$\frac{\xi_1}{\xi_2} = \frac{1}{3} + \frac{1}{6}\frac{k_r}{k_\theta}.$$

The fact that $\xi_1/\xi_2 > 1/3$ guarantees that $\Delta\theta > 0$.

Now one has to calculate the energy per unit volume, to find c_{44}:

$$\frac{\Delta E}{\text{volume}} = \frac{1}{2}c_{44}u_4^2.$$

This is done by calculating the ξ_1 and ξ_2 in terms of the Lagrange multiplier λ, then expressing the shear strain $\Delta X/Z$ in terms of λ, and finally, the energy per unit volume is the energy per atom divided by the atomic volume. From (A-3.1.6) and (A-3.1.7),

$$\xi_1 = \frac{\sqrt{3}}{3}\left(\frac{1}{2r_0^2 k_\theta} + \frac{1}{k_r r_0^2}\right)\lambda, \qquad \xi_2 = \frac{\sqrt{3}\lambda}{k_r r_0^2};$$

therefore,

$$u_4 = \frac{\Delta X}{Z} = \frac{\sqrt{3}}{2}(\xi_1 + \xi_2) = \left(\frac{1}{4r_0^2 k_\theta} + \frac{2}{k_r r_0^2}\right)\lambda$$

and

$$\frac{\Delta E}{\text{volume}} = \frac{\Delta E}{\text{atom}} \cdot \frac{3^{3/2}}{8r_0^3} = \frac{3^{3/2}}{4r_0} \cdot \frac{1}{\frac{1}{k_\theta} + \frac{8}{k_r}} \cdot u_4^2.$$

Thus,

$$c_{44} = \frac{3^{3/2}}{2r_0} \cdot \frac{1}{\frac{1}{k_\theta} + \frac{8}{k_r}} = \frac{6}{a} \cdot \frac{1}{\frac{1}{k_\theta} + \frac{8}{k_r}}.$$

The Singh - Dayal and the Valence Force Field models

The Valence Force Field model of Musgrave and Pople[2] can account for the most general form of direct interaction between an atom and its nearest neighbors. The elements contributing to the interaction are the same as in the previous model, i.e., the four bonds between any given atom and its nearest neighbors, as well as the six angles between them. The most general form of interaction involves bond-bond, bond-angle, and angle-angle interactions. As there are ten coordinates to describe the neighborhood of each atom (four bond lengths and six angles), one might expect as many as $10(10+1)/2=55$ spring constants. Fortunately, the symmetry of the problem enables one to express all these 55 elements of the dynamical matrix in terms of only five independent quantities.

All the four bonds are equivalent. Therefore, the bond-bond interactions are described by only two spring constants: k_r for the interaction of a bond with itself, and k_{rr} for the interaction of adjacent bonds. All the six angles are equivalent. Moreover, as was explained for the previous model, they are not independent, and there is one relation between them. If all the angles are almost tetrahedral, with small corrections, then these small corrections add up to zero, to within first order in the corrections. Angle pairs may fall in one of three inequivalent classes. Either the two angles are the same one, or they are adjacent, sharing a bond, or they are opposite to each other. Three spring constants are, therefore, necessary: k_θ to describe the interaction of an angle with itself, $k_{\theta\prime}$ to describe the interaction of two adjacent angles, and $k_{\theta\prime\prime}$ to describe the interaction of two opposite angles. Since there is one relation between the angles, there will also be one relation between the spring constants, and one may arbitrarily take one of these to be zero. Similarly, a bond and an angle can fall in two classes: either the angle touches the bond, or it does not. This will bring about two spring constants, one of which can be taken to

be zero, by the relation between the angles. The total elastic energy can be written, following Musgrave and Pople,

$$\frac{\Delta E}{\text{atom}} = \frac{1}{4}k_r \sum_{1}^{4}(\Delta r_i)^2 + k_{rr} \sum_{1\le i<j\le 4} (\Delta r_i)(\Delta r_j)$$
$$+ \frac{r_0}{\sqrt{2}}k_{r\theta} \sum_{i\neq j}(\Delta r_i)(\Delta\theta_{ij}) + \frac{r_0^2}{2}k_\theta \sum_{6 \text{ angles}} (\Delta\theta_{ij})^2$$
$$+ r_0^2 k_{\theta\theta}{}' \sum_{3 \text{ pairs}} (\Delta\theta_{ij})(\Delta\theta_{kl}).$$

The factor (1/4) in front of k_r takes care of double counting, as each bond is counted on two atoms. The factors $r_0/\sqrt{2}$ and r_0^2 in front of the bond-angle and angle-angle terms was introduced so that all the different spring constants will have the same dimensions.

Using this formalism, one can now write the elastic constants of the diamond structure:

$$c_{11} = \frac{1}{3a}[k_r + 6k_{rr} + 12k_\theta + 12k_{\theta\theta}{}']$$
$$c_{12} = \frac{1}{3a}[k_r + 6k_{rr} - 6k_\theta - 6k_{\theta\theta}{}']$$
$$c_{44} = \frac{6}{a}\left[\frac{(k_r - 2k_{rr})(k_\theta - k_{\theta\theta}{}') - 2k_{r\theta}^2}{(k_r - 2k_{rr}) + 8(k_\theta - k_{\theta\theta}{}' - k_{r\theta})}\right].$$

The Singh – Dayal model is a sub-model of the Valence Force Field model with

$$k_{rr} = k_{\theta\theta}{}' = 0.$$

Using this model, the elastic constants of the diamond structure can be written as:

$$c_{11} = \frac{1}{3a}[k_r + 12k_\theta]$$
$$c_{12} = \frac{1}{3a}[k_r - 6k_\theta]$$
$$c_{44} = \frac{6}{a}\left[\frac{k_r k_\theta - 2k_{r\theta}^2}{k_r + 8k_\theta - 8k_{r\theta}}\right].$$

References to Appendix A-3.1

1. B. D. Singh and B. Dayal, *Phys. Stat. Sol.* **38**, 141 (1970).

2. M. J. P. Musgrave and J. A. Pople, *Proc. Roy. Soc. (London)* **A268**, 474 (1962).

Appendix A-3.2. Phonon calculations for the geometrical models.

The general formalism of phonon calculations is given by Maradudin[1] . Out of this general formalism, we present here only the parts relevant to bulk silicon, i.e., the case of diamond structure with two equivalent atoms per unit cell.

The three geometrical models, described in the introduction to Chapter 3 and in Appendix A-3.1, express the elastic energy in terms of the local geometry of the crystal. The first step in calculating phonon modes is to be able to find the local geometry, i.e., bond lengthes and angles. Consider a configuration of two atoms in a diamond-structure unit cell, together with their six neighbors. This configuration suffices to describe the interaction in the simple bond bending and stretching model, the Singh – Dayal model[2] and the Valence Force Field of Musgrave and Pople[3] . The first two models are sub-models of the Valence Force Field model. Therefore, only the latter model will be treated.

For a specific phonon mode, the displacement of two atoms separated by a lattice vector is related by a phase factor.

$$\vec{r}_1 = (0,0,0) + (w_{11}, w_{21}, w_{31})\exp(-i\omega t)$$

$$\vec{r}_2 = (\frac{a}{4}, \frac{a}{4}, \frac{a}{4}) + (w_{12}, w_{22}, w_{32})\exp(-i\omega t)$$

$$\vec{r}_3 = (0, \frac{a}{2}, \frac{a}{2}) + (w_{11}, w_{21}, w_{31})\exp\left(\frac{iak_2}{2} + \frac{iak_3}{2} - i\omega t\right)$$

$$\vec{r}_4 = (\frac{a}{2}, 0, \frac{a}{2}) + (w_{11}, w_{21}, w_{31})\exp\left(\frac{iak_1}{2} + \frac{iak_3}{2} - i\omega t\right)$$

$$\vec{r}_5 = (\frac{a}{2}, \frac{a}{2}, 0) + (w_{11}, w_{21}, w_{31})\exp\left(\frac{iak_1}{2} + \frac{iak_2}{2} - i\omega t\right)$$

$$\vec{r}_6 = (\frac{a}{4}, -\frac{a}{4}, -\frac{a}{4}) + (w_{12}, w_{22}, w_{32})\exp\left(\frac{-iak_2}{2} + \frac{-iak_3}{2} - i\omega t\right)$$

$$\vec{r}_7 = (-\frac{a}{4}, \frac{a}{4}, -\frac{a}{4}) + (w_{12}, w_{22}, w_{32})\exp\left(\frac{-iak_1}{2} + \frac{-iak_3}{2} - i\omega t\right)$$

$$\vec{r}_8 = (-\frac{a}{4}, -\frac{a}{4}, \frac{a}{4}) + (w_{12}, w_{22}, w_{32})\exp\left(\frac{-iak_1}{2} + \frac{-iak_2}{2} - i\omega t\right)$$

Using these expressions for $\vec{r}_1, \ldots, \vec{r}_8$, one can calculate the differential change in bond lengthes and angles to first order in $w_{11}, \ldots, w_{32}$. While $\vec{r}_1$ and $\vec{r}_2$ have the same coordinates, $\vec{r}_3, \ldots, \vec{r}_8$ depend on the $\vec{k}$ of the particular phonon mode. In the following set of tables, the bond lengths and angles are given to first order in $w_{11}, \ldots, w_{32}$ for the Γ, X, $\Delta_{1/2}$, L, K, and $\Sigma_{1/2}$ points. In general, $w_{11}, \ldots, w_{32}$ are complex; however, for the Γ, X and L points, they can be taken as real. For other special points we write

$$w_{ij} = u_{ij} + i \cdot v_{ij}.$$

Having calculated the bond lengths and angles to first order, one can use them in any energy expression involving bond lengths and angles. The resulting expression is a quadratic polynomial in the local coordinates. Its eigenvalues and eigenvectors are the natural frequencies and the phonon modes for that particular $\vec{k}$.

The local displacements w_{ij} satisfy the equations of motion

$$\omega^2 w_{\alpha\kappa} = \sum_{\kappa'\beta} D^{(\vec{k})}_{\alpha\beta\kappa\kappa'} w_{\beta\kappa'}, \qquad \alpha\beta = 1,2,3, \quad \kappa,\kappa' = 1,2$$

where

$$D^{(\vec{\mathbf{k}})}_{\alpha\beta\kappa\kappa'} = \frac{1}{M}\left(\frac{\partial^2\Phi}{\partial w_{\alpha\kappa}\partial w^{*}_{\beta\kappa'}}\right).$$

	$\Gamma = \frac{2\pi}{a}(0,0,0)$	$X = \frac{2\pi}{a}(1,0,0)$
$\lvert\vec{v}_1\text{-}\vec{v}_2\rvert - r_0$	$\frac{-u_{11}+u_{12}-u_{21}+u_{22}-u_{31}+u_{32}}{\sqrt{3}}$	$\frac{-u_{11}+u_{12}-u_{21}+u_{22}-u_{31}+u_{32}}{\sqrt{3}}$
$\lvert\vec{v}_1\text{-}\vec{v}_6\rvert - r_0$	$\frac{-u_{11}+u_{12}+u_{21}-u_{22}+u_{31}-u_{32}}{\sqrt{3}}$	$\frac{-u_{11}+u_{12}+u_{21}-u_{22}+u_{31}-u_{32}}{\sqrt{3}}$
$\lvert\vec{v}_1\text{-}\vec{v}_7\rvert - r_0$	$\frac{+u_{11}-u_{12}-u_{21}+u_{22}+u_{31}-u_{32}}{\sqrt{3}}$	$\frac{+u_{11}+u_{12}-u_{21}-u_{22}+u_{31}+u_{32}}{\sqrt{3}}$
$\lvert\vec{v}_1\text{-}\vec{v}_8\rvert - r_0$	$\frac{+u_{11}-u_{12}+u_{21}-u_{22}-u_{31}+u_{32}}{\sqrt{3}}$	$\frac{+u_{11}+u_{12}+u_{21}+u_{22}-u_{31}-u_{32}}{\sqrt{3}}$
$\lvert\vec{v}_2\text{-}\vec{v}_3\rvert - r_0$	$\frac{-u_{11}+u_{12}+u_{21}-u_{22}+u_{31}-u_{32}}{\sqrt{3}}$	$\frac{-u_{11}+u_{12}+u_{21}-u_{22}+u_{31}-u_{32}}{\sqrt{3}}$
$\lvert\vec{v}_2\text{-}\vec{v}_4\rvert - r_0$	$\frac{+u_{11}-u_{12}-u_{21}+u_{22}+u_{31}-u_{32}}{\sqrt{3}}$	$\frac{-u_{11}-u_{12}+u_{21}+u_{22}-u_{31}-u_{32}}{\sqrt{3}}$
$\lvert\vec{v}_2\text{-}\vec{v}_5\rvert - r_0$	$\frac{+u_{11}-u_{12}+u_{21}-u_{22}-u_{31}+u_{32}}{\sqrt{3}}$	$\frac{-u_{11}-u_{12}-u_{21}-u_{22}+u_{31}+u_{32}}{\sqrt{3}}$
$\angle 216 - \theta_0$	$\frac{16}{3\sqrt{2}a}(+u_{11}-u_{12})$	$\frac{16}{3\sqrt{2}a}(+u_{11}-u_{12})$
$\angle 217 - \theta_0$	$\frac{16}{3\sqrt{2}a}(+u_{21}-u_{22})$	$\frac{16}{3\sqrt{2}a}(+u_{21}+\frac{u_{12}}{2}+\frac{u_{32}}{2})$
$\angle 218 - \theta_0$	$\frac{16}{3\sqrt{2}a}(+u_{31}-u_{32})$	$\frac{16}{3\sqrt{2}a}(+u_{31}+\frac{u_{12}}{2}+\frac{u_{22}}{2})$
$\angle 617 - \theta_0$	$\frac{16}{3\sqrt{2}a}(-u_{31}+u_{32})$	$\frac{16}{3\sqrt{2}a}(-u_{31}+\frac{u_{12}}{2}-\frac{u_{22}}{2})$
$\angle 618 - \theta_0$	$\frac{16}{3\sqrt{2}a}(-u_{21}+u_{22})$	$\frac{16}{3\sqrt{2}a}(-u_{21}+\frac{u_{12}}{2}-\frac{u_{32}}{2})$
$\angle 718 - \theta_0$	$\frac{16}{3\sqrt{2}a}(-u_{11}+u_{12})$	$\frac{16}{3\sqrt{2}a}(-u_{11}-u_{12})$
$\angle 123 - \theta_0$	$\frac{16}{3\sqrt{2}a}(+u_{11}-u_{12})$	$\frac{16}{3\sqrt{2}a}(+u_{11}-u_{12})$
$\angle 124 - \theta_0$	$\frac{16}{3\sqrt{2}a}(+u_{21}-u_{22})$	$\frac{16}{3\sqrt{2}a}(-\frac{u_{11}}{2}-\frac{u_{31}}{2}-u_{22})$
$\angle 125 - \theta_0$	$\frac{16}{3\sqrt{2}a}(+u_{31}-u_{32})$	$\frac{16}{3\sqrt{2}a}(-\frac{u_{11}}{2}-\frac{u_{21}}{2}-u_{32})$
$\angle 324 - \theta_0$	$\frac{16}{3\sqrt{2}a}(-u_{31}+u_{32})$	$\frac{16}{3\sqrt{2}a}(-\frac{u_{11}}{2}+\frac{u_{21}}{2}+u_{32})$
$\angle 325 - \theta_0$	$\frac{16}{3\sqrt{2}a}(-u_{21}+u_{22})$	$\frac{16}{3\sqrt{2}a}(-\frac{u_{11}}{2}+\frac{u_{31}}{2}+u_{22})$
$\angle 425 - \theta_0$	$\frac{16}{3\sqrt{2}a}(-u_{11}+u_{12})$	$\frac{16}{3\sqrt{2}a}(+u_{11}+u_{12})$

	$L = \frac{2\pi}{a}(\frac{1}{2}, \frac{1}{2}, \frac{1}{2})$	
$\lvert\vec{v}_1\text{-}\vec{v}_2\rvert - r_0$	$\frac{-u_{11}+u_{12}-u_{21}+u_{22}-u_{31}+u_{32}}{\sqrt{3}}$	
$\lvert\vec{v}_1\text{-}\vec{v}_6\rvert - r_0$	$\frac{-u_{11}-u_{12}+u_{21}+u_{22}+u_{31}+u_{32}}{\sqrt{3}}$	
$\lvert\vec{v}_1\text{-}\vec{v}_7\rvert - r_0$	$\frac{+u_{11}+u_{12}-u_{21}-u_{22}+u_{31}+u_{32}}{\sqrt{3}}$	
$\lvert\vec{v}_1\text{-}\vec{v}_8\rvert - r_0$	$\frac{+u_{11}+u_{12}+u_{21}+u_{22}-u_{31}-u_{32}}{\sqrt{3}}$	
$\lvert\vec{v}_2\text{-}\vec{v}_3\rvert - r_0$	$\frac{+u_{11}+u_{12}-u_{21}-u_{22}-u_{31}-u_{32}}{\sqrt{3}}$	
$\lvert\vec{v}_2\text{-}\vec{v}_4\rvert - r_0$	$\frac{-u_{11}-u_{12}+u_{21}+u_{22}-u_{31}-u_{32}}{\sqrt{3}}$	
$\lvert\vec{v}_2\text{-}\vec{v}_5\rvert - r_0$	$\frac{-u_{11}-u_{12}-u_{21}-u_{22}+u_{31}+u_{32}}{\sqrt{3}}$	
$\angle 216 - \theta_0$	$\frac{16}{3\sqrt{2}a}(+u_{11} + \frac{u_{22}}{2} + \frac{u_{32}}{2})$	
$\angle 217 - \theta_0$	$\frac{16}{3\sqrt{2}a}(+u_{21} + \frac{u_{12}}{2} + \frac{u_{32}}{2})$	
$\angle 218 - \theta_0$	$\frac{16}{3\sqrt{2}a}(+u_{31} + \frac{u_{12}}{2} + \frac{u_{22}}{2})$	
$\angle 617 - \theta_0$	$\frac{16}{3\sqrt{2}a}(-u_{31} - u_{32})$	
$\angle 618 - \theta_0$	$\frac{16}{3\sqrt{2}a}(-u_{21} - u_{22})$	
$\angle 718 - \theta_0$	$\frac{16}{3\sqrt{2}a}(-u_{11} - u_{12})$	
$\angle 123 - \theta_0$	$\frac{16}{3\sqrt{2}a}(-\frac{u_{21}}{2} - \frac{u_{31}}{2} - u_{12})$	
$\angle 124 - \theta_0$	$\frac{16}{3\sqrt{2}a}(-\frac{u_{11}}{2} - \frac{u_{31}}{2} - u_{22})$	
$\angle 125 - \theta_0$	$\frac{16}{3\sqrt{2}a}(-\frac{u_{11}}{2} - \frac{u_{21}}{2} - u_{32})$	
$\angle 324 - \theta_0$	$\frac{16}{3\sqrt{2}a}(+u_{31} + u_{32})$	
$\angle 325 - \theta_0$	$\frac{16}{3\sqrt{2}a}(+u_{21} + u_{22})$	
$\angle 425 - \theta_0$	$\frac{16}{3\sqrt{2}a}(+u_{11} + u_{12})$	

	$K = \frac{2\pi}{a}(\frac{3}{4}, \frac{3}{4}, 0)$
	$s = \sqrt{2}/2$
$\lvert\vec{v}_1\text{-}\vec{v}_2\rvert - r_0$	$\frac{-u_{11}+u_{12}-u_{21}+u_{22}-u_{31}+u_{32}}{\sqrt{3}}$
$\lvert\vec{v}_1\text{-}\vec{v}_6\rvert - r_0$	$\frac{-u_{11}-su_{12}+u_{21}+su_{22}+u_{31}+su_{32}+sv_{12}-sv_{22}-sv_{32}}{\sqrt{3}}$
$\lvert\vec{v}_1\text{-}\vec{v}_7\rvert - r_0$	$\frac{+u_{11}+su_{12}-u_{21}-su_{22}+u_{31}+su_{32}-sv_{12}+sv_{22}-sv_{32}}{\sqrt{3}}$
$\lvert\vec{v}_1\text{-}\vec{v}_8\rvert - r_0$	$\frac{+u_{11}+u_{21}-u_{31}+v_{12}+v_{22}-v_{32}}{\sqrt{3}}$
$\lvert\vec{v}_2\text{-}\vec{v}_3\rvert - r_0$	$\frac{+su_{11}+u_{12}-su_{21}-u_{22}-su_{31}-u_{32}+sv_{11}-sv_{21}-sv_{31}}{\sqrt{3}}$
$\lvert\vec{v}_2\text{-}\vec{v}_4\rvert - r_0$	$\frac{-su_{11}-u_{12}+su_{21}+u_{22}-su_{31}-u_{32}-sv_{11}+sv_{21}-sv_{31}}{\sqrt{3}}$
$\lvert\vec{v}_2\text{-}\vec{v}_5\rvert - r_0$	$\frac{-u_{12}-u_{22}+u_{32}+v_{11}+v_{21}-v_{31}}{\sqrt{3}}$
$\angle 216 - \theta_0$	$\frac{16}{3\sqrt{2}a}\frac{+4u_{11}-2(1-s)u_{12}+(1+s)u_{22}+(1+s)u_{32}-2sv_{12}-sv_{22}-sv_{32}}{4}$
$\angle 217 - \theta_0$	$\frac{16}{3\sqrt{2}a}\frac{+4u_{21}+(1+s)u_{12}-2(1-s)u_{22}+(1+s)u_{32}-sv_{12}-2sv_{22}-sv_{32}}{4}$
$\angle 218 - \theta_0$	$\frac{16}{3\sqrt{2}a}\frac{+4u_{31}+u_{12}+u_{22}-2u_{32}+v_{12}+v_{22}+2v_{32}}{4}$
$\angle 617 - \theta_0$	$\frac{16}{3\sqrt{2}a}\frac{-4u_{31}-4su_{32}+4sv_{32}}{4}$
$\angle 618 - \theta_0$	$\frac{16}{3\sqrt{2}a}\frac{-4u_{21}-su_{12}-2su_{22}+su_{32}+(1+s)v_{12}-2(1-s)v_{22}-(1+s)v_{32}}{4}$
$\angle 718 - \theta_0$	$\frac{16}{3\sqrt{2}a}\frac{-4u_{11}-2su_{12}-su_{22}+su_{32}-2(1-s)v_{12}+(1+s)v_{22}-(1+s)v_{32}}{4}$
$\angle 123 - \theta_0$	$\frac{16}{3\sqrt{2}a}\frac{+2(1-s)u_{11}-(1+s)u_{21}-(1+s)u_{31}-4u_{12}-2sv_{11}-sv_{21}-sv_{31}}{4}$
$\angle 124 - \theta_0$	$\frac{16}{3\sqrt{2}a}\frac{-(1+s)u_{11}+2(1-s)u_{21}-(1+s)u_{31}-4u_{22}-sv_{11}-2sv_{21}-sv_{31}}{4}$
$\angle 125 - \theta_0$	$\frac{16}{3\sqrt{2}a}\frac{-u_{11}-u_{21}+2u_{31}-4u_{32}+v_{11}-v_{21}+2v_{31}}{4}$
$\angle 324 - \theta_0$	$\frac{16}{3\sqrt{2}a}\frac{+4su_{31}+4u_{32}+4sv_{31}}{4}$
$\angle 325 - \theta_0$	$\frac{16}{3\sqrt{2}a}\frac{+su_{11}+2su_{21}-su_{31}+4u_{22}+(1+s)v_{11}-2(1-s)v_{21}-(1+s)v_{31}}{4}$
$\angle 425 - \theta_0$	$\frac{16}{3\sqrt{2}a}\frac{+2su_{11}+su_{21}-su_{31}+4u_{12}-2(1-s)v_{11}+(1+s)v_{21}-(1+s)v_{22}}{4}$

	$\Delta_{1/2} = \frac{2\pi}{a}(\frac{1}{2}, 0, 0)$
$\lvert\vec{\nu}_1\text{-}\vec{\nu}_2\rvert - r_0$	$\frac{-u_{11}+u_{12}-u_{21}+u_{22}-u_{31}+u_{32}}{\sqrt{3}}$
$\lvert\vec{\nu}_1\text{-}\vec{\nu}_6\rvert - r_0$	$\frac{-u_{11}+u_{12}+u_{21}-u_{22}+u_{31}-u_{32}}{\sqrt{3}}$
$\lvert\vec{\nu}_1\text{-}\vec{\nu}_7\rvert - r_0$	$\frac{+u_{11}-u_{21}+u_{31}}{\sqrt{3}} + \frac{-v_{12}+v_{22}-v_{32}}{\sqrt{3}}$
$\lvert\vec{\nu}_1\text{-}\vec{\nu}_8\rvert - r_0$	$\frac{+u_{11}+u_{21}-u_{31}}{\sqrt{3}} + \frac{-v_{12}-v_{22}+v_{32}}{\sqrt{3}}$
$\lvert\vec{\nu}_2\text{-}\vec{\nu}_3\rvert - r_0$	$\frac{-u_{11}+u_{12}+u_{21}-u_{22}+u_{31}-u_{32}}{\sqrt{3}}$
$\lvert\vec{\nu}_2\text{-}\vec{\nu}_4\rvert - r_0$	$\frac{-u_{12}+u_{22}-u_{32}}{\sqrt{3}} + \frac{-v_{11}+v_{21}-v_{31}}{\sqrt{3}}$
$\lvert\vec{\nu}_2\text{-}\vec{\nu}_5\rvert - r_0$	$\frac{-u_{12}-u_{22}+u_{32}}{\sqrt{3}} + \frac{-v_{11}-v_{21}+v_{31}}{\sqrt{3}}$
$\angle 216 - \theta_0$	$\frac{16}{3\sqrt{2}a}(+u_{11} - u_{12})$
$\angle 217 - \theta_0$	$\frac{16}{3\sqrt{2}a}(+u_{21} + \frac{u_{12}}{4} - \frac{u_{22}}{2} + \frac{u_{32}}{4} - \frac{v_{12}}{4} - \frac{v_{22}}{2} - \frac{v_{32}}{4})$
$\angle 218 - \theta_0$	$\frac{16}{3\sqrt{2}a}(+u_{31} + \frac{u_{12}}{4} + \frac{u_{22}}{4} - \frac{u_{32}}{2} - \frac{v_{12}}{4} - \frac{v_{22}}{4} - \frac{v_{32}}{2})$
$\angle 617 - \theta_0$	$\frac{16}{3\sqrt{2}a}(-u_{31} + \frac{u_{12}}{4} - \frac{u_{22}}{4} + \frac{u_{32}}{2} - \frac{v_{12}}{4} + \frac{v_{22}}{4} + \frac{v_{32}}{2})$
$\angle 618 - \theta_0$	$\frac{16}{3\sqrt{2}a}(-u_{21} + \frac{u_{12}}{4} + \frac{u_{22}}{2} - \frac{u_{32}}{4} - \frac{v_{12}}{4} + \frac{v_{22}}{2} + \frac{v_{32}}{4})$
$\angle 718 - \theta_0$	$\frac{16}{3\sqrt{2}a}(-u_{11} + v_{12})$
$\angle 123 - \theta_0$	$\frac{16}{3\sqrt{2}a}(+u_{11} - u_{12})$
$\angle 124 - \theta_0$	$\frac{16}{3\sqrt{2}a}(-\frac{u_{11}}{4} + \frac{u_{21}}{2} - \frac{u_{31}}{4} - u_{22} - \frac{v_{11}}{4} - \frac{v_{21}}{2} - \frac{v_{31}}{4})$
$\angle 125 - \theta_0$	$\frac{16}{3\sqrt{2}a}(-\frac{u_{11}}{4} - \frac{u_{21}}{4} + \frac{u_{31}}{2} - u_{32} - \frac{v_{11}}{4} - \frac{v_{21}}{4} - \frac{v_{31}}{2})$
$\angle 324 - \theta_0$	$\frac{16}{3\sqrt{2}a}(-\frac{u_{11}}{4} + \frac{u_{21}}{4} - \frac{u_{31}}{2} + u_{32} - \frac{v_{11}}{4} + \frac{v_{21}}{4} + \frac{v_{31}}{2})$
$\angle 325 - \theta_0$	$\frac{16}{3\sqrt{2}a}(-\frac{u_{11}}{4} - \frac{u_{21}}{2} + \frac{u_{31}}{4} + u_{22} - \frac{v_{11}}{4} + \frac{v_{21}}{2} + \frac{v_{31}}{4})$
$\angle 425 - \theta_0$	$\frac{16}{3\sqrt{2}a}(+u_{12} + v_{11})$

	$\Sigma_{1/2} = \frac{2\pi}{a}(\frac{1}{2}, \frac{1}{2}, 0)$
$\lvert\vec{v}_1\text{-}\vec{v}_2\rvert - r_0$	$\frac{-u_{11}+u_{12}-u_{21}+u_{22}-u_{31}+u_{32}}{\sqrt{3}}$
$\lvert\vec{v}_1\text{-}\vec{v}_6\rvert - r_0$	$\frac{-u_{11}+u_{21}+u_{31}}{\sqrt{3}} + \frac{v_{12}-v_{22}-v_{32}}{\sqrt{3}}$
$\lvert\vec{v}_1\text{-}\vec{v}_7\rvert - r_0$	$\frac{+u_{11}-u_{21}+u_{31}}{\sqrt{3}} + \frac{-v_{12}+v_{22}-v_{32}}{\sqrt{3}}$
$\lvert\vec{v}_1\text{-}\vec{v}_8\rvert - r_0$	$\frac{+u_{11}+u_{12}+u_{21}+u_{22}-u_{31}-u_{32}}{\sqrt{3}}$
$\lvert\vec{v}_2\text{-}\vec{v}_3\rvert - r_0$	$\frac{+u_{12}-u_{22}-u_{32}}{\sqrt{3}} + \frac{v_{11}-v_{21}-v_{31}}{\sqrt{3}}$
$\lvert\vec{v}_2\text{-}\vec{v}_4\rvert - r_0$	$\frac{-u_{12}+u_{22}-u_{32}}{\sqrt{3}} + \frac{-v_{11}+v_{21}-v_{31}}{\sqrt{3}}$
$\lvert\vec{v}_2\text{-}\vec{v}_5\rvert - r_0$	$\frac{-u_{11}-u_{12}-u_{21}-u_{22}+u_{31}+u_{32}}{\sqrt{3}}$
$\angle 216 - \theta_0$	$\frac{16}{3\sqrt{2}a}(+u_{11} + \frac{-2u_{12}+u_{22}+u_{32}}{4} + \frac{-2v_{12}-v_{22}-v_{32}}{4})$
$\angle 217 - \theta_0$	$\frac{16}{3\sqrt{2}a}(+u_{21} + \frac{+u_{12}-2u_{22}+u_{32}}{4} + \frac{-v_{12}-2v_{22}-v_{32}}{4})$
$\angle 218 - \theta_0$	$\frac{16}{3\sqrt{2}a}(+u_{31} + \frac{+2u_{12}+2u_{22}}{4}))$
$\angle 617 - \theta_0$	$\frac{16}{3\sqrt{2}a}(-u_{31} + v_{32}))$
$\angle 618 - \theta_0$	$\frac{16}{3\sqrt{2}a}(-u_{21} + \frac{+u_{12}-2u_{22}-u_{32}}{4} + \frac{+v_{12}+2v_{22}-v_{32}}{4})$
$\angle 718 - \theta_0$	$\frac{16}{3\sqrt{2}a}(-u_{11} + \frac{-2u_{12}+u_{22}-u_{32}}{4} + \frac{+2v_{12}+v_{22}-v_{32}}{4})$
$\angle 123 - \theta_0$	$\frac{16}{3\sqrt{2}a}(\frac{+2u_{11}-u_{21}-u_{31}}{4} - u_{12} + \frac{-2v_{11}-v_{21}-v_{31}}{4})$
$\angle 124 - \theta_0$	$\frac{16}{3\sqrt{2}a}(\frac{-u_{11}+2u_{21}-u_{31}}{4} - u_{22} + \frac{-v_{11}-2v_{21}-v_{31}}{4})$
$\angle 125 - \theta_0$	$\frac{16}{3\sqrt{2}a}(+\frac{-2u_{11}-2u_{21}}{4} - u_{32})$
$\angle 324 - \theta_0$	$\frac{16}{3\sqrt{2}a}(+u_{32} + v_{31})$
$\angle 325 - \theta_0$	$\frac{16}{3\sqrt{2}a}(\frac{-u_{11}+2u_{21}+u_{31}}{4} + u_{22} + \frac{+v_{11}+2v_{21}-v_{31}}{4})$
$\angle 425 - \theta_0$	$\frac{16}{3\sqrt{2}a}(\frac{+2u_{11}-u_{21}+u_{31}}{4} + u_{12} + \frac{+2v_{11}+v_{21}-v_{31}}{4})$

Now one can use these geometries in the energy expression to obtain the dynamical matrix in terms of the coordinates $(u_{11}, u_{21}, u_{31}, u_{12}, u_{22}, u_{32})$. The dynamical matrix conveniently splits into a k_r part, k_θ part, etc. The potential energy per unit cell is given by

$$\frac{\Delta E}{\text{unit cell}} = \frac{1}{2}\vec{\mathbf{u}} \cdot D \cdot \vec{\mathbf{u}}^T$$

where $\vec{\mathbf{u}} = (u_{11}, u_{21}, u_{31}, u_{12}, u_{22}, u_{32})$.

The Γ point

$$MD^{(\Gamma)} = \begin{matrix} A & 0 & 0 & -A & 0 & 0 \\ 0 & A & 0 & 0 & -A & 0 \\ 0 & 0 & A & 0 & 0 & -A \\ -A & 0 & 0 & A & 0 & 0 \\ 0 & -A & 0 & 0 & A & 0 \\ 0 & 0 & -A & 0 & 0 & A \end{matrix}$$

The eigenvalues and eigenvectors of this matrix are 0 (acoustic) and 2A (optical, Raman), each three-fold degenerate.

For this model

$$A = \frac{4}{3}k_r - \frac{8}{3}k_{rr} - \frac{32}{3}k_{r\theta} + \frac{32}{3}k_\theta - \frac{32}{3}k_\theta''.$$

The X point

$$MD^{(X)} = \begin{matrix} A & 0 & 0 & 0 & 0 & 0 \\ 0 & B & 0 & 0 & 0 & C \\ 0 & 0 & B & 0 & C & 0 \\ 0 & 0 & 0 & A & 0 & 0 \\ 0 & 0 & C & 0 & B & 0 \\ 0 & C & 0 & 0 & 0 & B \end{matrix}$$

The eigenvalues and eigenvectors of this matrix are

$$(LA+LO): \qquad A \qquad (100000),(000100),$$

$$(TO): \qquad B-C \qquad (010000\bar{1}),(0010\bar{1}0),$$

$$(TA): \qquad B+C \qquad (010001),(001010).$$

For this model,

$$A = \frac{4}{3}k_r + \frac{8}{3}k_{rr} - \frac{16}{3}k_{r\theta} + \frac{40}{3}k_\theta + \frac{8}{3}k_\theta'',$$

$$B = \frac{4}{3}k_r - \frac{8}{3}k_{rr} - \frac{8}{3}k_{r\theta} + \frac{20}{3}k_\theta - \frac{20}{3}k_\theta'',$$

$$C = \frac{-4}{3}k_r + \frac{8}{3}k_{rr} + \frac{8}{3}k_{r\theta} + \frac{16}{3}k_\theta - \frac{16}{3}k_\theta'',$$

therefore, the spring constants for the phonons are

$$k_{LA,LO} = \frac{4}{3}k_r + \frac{8}{3}k_{rr} - \frac{16}{3}k_{r\theta} + \frac{40}{3}k_\theta + \frac{8}{3}k_\theta'',$$

$$k_{TO} = \frac{8}{3}k_r - \frac{16}{3}k_{rr} - \frac{16}{3}k_{r\theta} + \frac{4}{3}k_\theta - \frac{4}{3}k_\theta'',$$

$$k_{TA} = \qquad 12k_\theta - 12k_\theta''.$$

The $\Delta_{1/2}$ point

$$MD^{(\Delta_{1/2})} = \begin{matrix} A & 0 & 0 & C(1-i) & 0 & 0 \\ 0 & B & 0 & 0 & C(1-i) & D(1+i) \\ 0 & 0 & B & 0 & D(1+i) & C(1-i) \\ C(1+i) & 0 & 0 & A & 0 & 0 \\ 0 & C(1+i) & D(1-i) & 0 & B & 0 \\ 0 & D(1-i) & C(1+i) & 0 & 0 & B \end{matrix}$$

The eigenvalues and eigenvectors of this matrix are:

$$(LA): \qquad A + C\sqrt{2} \qquad , \left(1, 0, 0, \frac{\sqrt{2}}{2}(1+i), 0, 0\right)$$

$$(LO): \qquad A - C\sqrt{2} \qquad , \left(1, 0, 0, \frac{-\sqrt{2}}{2}(1+i), 0, 0\right)$$

$$(TO, TA): \qquad B \pm \sqrt{2C^2 + 2D^2} \qquad , (0, 1, 0, 0, \alpha, \beta) \quad (0, 0, 1, 0, \beta, \alpha)$$

where

$$\alpha = \pm\frac{C(1+i)}{\sqrt{2C^2 + 2D^2}}, \qquad \beta = \pm\frac{D(1-i)}{\sqrt{2C^2 + 2D^2}}. \qquad (+ : TO, \quad - : TA)$$

For this model,

$$A = \frac{4}{3}k_r \qquad - 8k_{r\theta} + 12k_\theta - 4k''_\theta,$$

$$B = \frac{4}{3}k_r - \frac{8}{3}k_{rr} - \frac{20}{3}k_{r\theta} + \frac{26}{3}k_\theta - \frac{26}{3}k''_\theta,$$

$$C = \frac{-2}{3}k_r + \frac{4}{3}k_{rr} + \frac{16}{3}k_{r\theta} - \frac{16}{3}k_\theta + \frac{16}{3}k''_\theta,$$

$$D = \frac{-2}{3}k_r + \frac{4}{3}k_{rr} + \frac{4}{3}k_{r\theta} + \frac{8}{3}k_\theta - \frac{8}{3}k''_\theta$$

The L point

$$MD^{(L)} = \begin{matrix} A & B & B & C & D & D \\ B & A & B & D & C & D \\ B & B & A & D & D & C \\ C & D & D & A & B & B \\ D & C & D & B & A & B \\ D & D & C & B & B & A \end{matrix}$$

The eigenvalues and eigenvectors are:

$$LA: \quad A+2B+C+2D \quad (111111),$$

$$LO: \quad A+2B-C-2D \quad (111\bar{1}\bar{1}\bar{1}),$$

$$TO: \quad A-B+C-D \quad (1\bar{1}01\bar{1}0), (10\bar{1}10\bar{1}),$$

$$TA: \quad A-B-C+D \quad (1\bar{1}0\bar{1}10), (10\bar{1}\bar{1}01).$$

For this model,

$$A = \frac{4}{3}k_\tau - \frac{4}{3}k_{\tau\tau} - \frac{16}{3}k_{\tau\theta} + \frac{28}{3}k_\theta - \frac{16}{3}k_\theta'',$$

$$B = +\frac{4}{3}k_{\tau\tau} + \frac{4}{3}k_{\tau\theta} + \frac{2}{3}k_\theta - \frac{8}{3}k_\theta'',$$

$$C = \frac{2}{3}k_\tau - \frac{4}{3}k_{\tau\tau} - \frac{16}{3}k_{\tau\theta} + \frac{16}{3}k_\theta - \frac{16}{3}k_\theta'',$$

$$D = \frac{-2}{3}k_\tau + \frac{4}{3}k_{\tau\tau} + \frac{4}{3}k_{\tau\theta} + \frac{8}{3}k_\theta - \frac{8}{3}k_\theta'',$$

therefore,

$$k_{TO} = \frac{8}{3}k_\tau - \frac{16}{3}k_{\tau\tau} - \frac{40}{3}k_{\tau\theta} + \frac{34}{3}k_\theta - \frac{16}{3}k_\theta'',$$

$$k_{LO} = 2k_\tau,$$

$$k_{LA} = \frac{2}{3}k_\tau + \frac{8}{3}k_{\tau\tau} - \frac{16}{3}k_{\tau\theta} + \frac{64}{3}k_\theta - \frac{64}{3}k_\theta'',$$

$$k_{TA} = 6k_\theta.$$

The $\Sigma_{1/2}$ point

$$MD^{(\Sigma_{1/2})} = \begin{matrix} A & B & -Ci & -Di & -Ei & -E \\ B & A & -Ci & -Ei & -Di & -E \\ Ci & Ci & A & -E & -E & -Di \\ Di & Ei & -E & A & B & Ci \\ Ei & Di & -E & B & A & Ci \\ -E & -E & Di & -Ci & -Ci & A \end{matrix}$$

The eigenvalues and eigenvectors are

$$\text{TO:} \qquad \lambda = A - B - D + E, \qquad (1, -1, 0, -i, i, 0)$$

$$\text{TA:} \qquad \lambda = A - B + D - E, \qquad (1, -1, 0, i, -i, 0)$$

$$\lambda = A + B - D - E + \alpha(E + C), \qquad (1, 1, \alpha i, -i, -i, -\alpha)$$

$$\lambda = A + B + D + E + \beta(C - E), \qquad (1, 1, \beta i, i, i, \beta)$$

$$\alpha = \frac{x \pm \sqrt{x^2 + 8}}{2}, \quad x = \frac{-B + 2D + E}{C + E},$$

$$\beta = \frac{y \pm \sqrt{y^2 + 8}}{2}, \quad y = \frac{B + 2D + E}{E - C}.$$

For this model,

$$A = \frac{4}{3}k_r - \frac{4}{3}k_{rr} - \frac{16}{3}k_{r\theta} + \frac{28}{3}k_\theta - \frac{16}{3}k''_\theta,$$

$$B = \frac{4}{3}k_{rr} + \frac{4}{3}k_{r\theta} + \frac{2}{3}k_\theta - \frac{8}{3}k''_\theta,$$

$$C = \frac{4}{3}k_{rr} - \frac{2}{3}k_{r\theta} - \frac{4}{3}k_\theta - \frac{2}{3}k''_\theta,$$

$$D = -\frac{2}{3}k_r + \frac{4}{3}k_{rr} + \frac{16}{3}k_{r\theta} - \frac{16}{3}k_\theta + \frac{16}{3}k''_\theta,$$

$$E = \frac{2}{3}k_r - \frac{4}{3}k_{rr} - \frac{4}{3}k_{r\theta} - \frac{8}{3}k_\theta + \frac{8}{3}k_\theta''.$$

therefore,

$$k_{TO} = \frac{8}{3}k_r - \frac{16}{3}k_{rr} - \frac{40}{3}k_{r\theta} + \frac{34}{3}k_\theta - \frac{16}{3}k_\theta'',$$

$$k_{TA} = 6k_\theta.$$

References for Appendix A-3.2

1. A. A. Maradudin in *Dynamical Properties of Solids*, Vol. 1, edited by G. K. Horton and A. A. Maradudin, (North-Holland, Amsterdam, 1974).

2. B. D. Singh and B. Dayal, *Phys. Stat. Sol.* **38**, 141 (1970).

3. M. J. P. Musgrave and J. A. Pople, *Proc. Roy. Soc. (London)* **A268**, 474 (1962).

Appendix A–3.3. The broken bond model of Vasil'ev et al.

An interesting model was proposed by Vasil'ev *et al*[1]. This model does not assume that the bond is the straight line segment between the nuclei. Instead, each bond is made of two lobes centered on neighboring atoms. The four lobes centered on the same atom and participating in the four bonds were assumed by Vasil'ev *et al.* to form rigid tetrahedral angles. This introduces a non-central force trying to maximize the overlap between two adjacent lobes.

One may view the four lobes on each atom as an internal coordinate system for this atom. The non-central force, therefore, comes from two origins: shear and rotation. The shear motion is described by a parallel motion of two atomic coordinate systems, but perpendicular to the straight line connecting the two atoms. The other force is due to rotation of the atomic coordinate system without moving the atom. The shear force operating on atom 1 due to its own displacement from equilibrium position, $\vec{u}_1$ and that of one of its nearest neighbors, $\vec{u}_2$, is proportional to the component of $\vec{u}_2 - \vec{u}_1$ perpendicular to $\vec{r}_{12}$:

$$\vec{F}_s^{(21)} = \beta_1 \left[\vec{u}_2 - \vec{u}_1 - \left(\frac{(\vec{u}_2 - \vec{u}_1) \cdot \vec{r}_{12}}{|\vec{r}_{12}|} \right) \frac{\vec{r}_{12}}{|\vec{r}_{12}|} \right].$$

Here $\vec{r}_{12}$ is the vector from atom 1 to atom 2, and β_1 is the proportionality factor. In general, β_1 may be a function of direction perpendicular to $\vec{r}_{12}$, but Vasil'ev *et al.* took it to be a constant.

The rotational restoring force acting on atom 1 due to a rotation of its own coordinate system by an angle $\vec{\omega}_1$, and that of one of its neighbors by $\vec{\omega}_2$, is given by

$$\vec{F}_r^{(21)} = -\frac{\beta_2}{2}(\vec{\omega}_2 + \vec{\omega}_1) \times \vec{r}_{12}.$$

The requirement of rotational invariance introduces a relation between β_1 and β_2. One has to assume that no net force is introduced by rigidly rotating the whole crystal by an angle $\vec{w}$. That means that the shear force introduced by $\vec{u}_2 - \vec{u}_1 = \vec{w} \times \vec{r}_{12}$ is exactly canceled by the rotational restoring force introduced by $\vec{w}_2 = \vec{w}_1 = \vec{w}$. In other words,

$$\beta_1 = \beta_2 \equiv \beta.$$

In addition to the non central force constant β Vasil'ev *et al.* introduced two central force constants α_1 and α_2 operating between nearest- and second-nearest neighbors. There are, therefore, three force constants to describe the interaction, two central and one non-central.

$$\vec{F}_{c1}^{(1)} = \alpha_1 \sum_{\substack{\text{nearest} \\ \text{neighbors}}} \left(\frac{(\vec{u}_j - \vec{u}_1) \cdot \vec{r}_{1j}}{|\vec{r}_{1j}|} \right) \frac{\vec{r}_{1j}}{|\vec{r}_{1j}|}, \qquad (A - 3.3.1)$$

$$\vec{F}_{c2}^{(1)} = \alpha_2 \sum_{\substack{\text{second} \\ \text{nearest} \\ \text{neighbors}}} \left(\frac{(\vec{u}_j - \vec{u}_1) \cdot \vec{r}_{1j}}{|\vec{r}_{1j}|} \right) \frac{\vec{r}_{1j}}{|\vec{r}_{1j}|}, \qquad (A - 3.3.2)$$

$$\vec{F}_{nc}^{(1)} = \beta \sum_{\substack{\text{nearest} \\ \text{neighbors}}} \left[\vec{u}_j - \vec{u}_1 - \left(\frac{(\vec{u}_j - \vec{u}_1) \cdot \vec{r}_{1j}}{|\vec{r}_{1j}|} \right) \frac{\vec{r}_{1j}}{|\vec{r}_{1j}|} - \frac{(\vec{w}_j + \vec{w}_1) \times \vec{r}_{1j}}{2} \right]. \qquad (A - 3.3.3)$$

These three forces are not enough, however. The introduction of atomic coordinate systems, which are assumed to be massless, requires that there will be no net torque operating on each atomic coordinate system. To calculate the torque, one has to know where the force is acting on each lobe. Vasil'ev *et al.* assumed a model in which the torque is due to two equal springs connecting two adjacent lobes at g and (1-g) times the bond length, where g is an adjustable parameter. The torque component at atom 1, due to both shear of $\vec{u}_2 - \vec{u}_1$ and rotations of $\vec{w}_1$ and $\vec{w}_2$,

is given by:

$$\vec{\tau}^{(21)} = \beta\Bigg[\frac{g\vec{r}_{12}+(1-g)\vec{r}_{12}}{2}\times(\vec{u}_2-\vec{u}_1) - \frac{g\vec{r}_{12}\times(\vec{w}_1\times g\vec{r}_{12})+(1-g)\vec{r}_{12}\times(\vec{w}_1\times(1-g)\vec{r}_{12})}{2} - \frac{g\vec{r}_{12}\times(\vec{w}_2\times(1-g)\vec{r}_{12})+(1-g)\vec{r}_{12}\times(\vec{w}_1\times g\vec{r}_{12})}{2}\Bigg]$$

$$= \beta\Bigg[\frac{\vec{r}_{12}\times(\vec{u}_2-\vec{u}_1)}{2} - A\vec{r}_{12}\times(\vec{w}_1\times\vec{r}_{12}) - B\vec{r}_{12}\times(\vec{w}_2\times\vec{r}_{12})\Bigg] .$$

The two parameters, A and B, introduced here, are given by

$$A = \frac{1}{2} - g(1-g), \qquad B = g(1-g)$$

for Vasil'ev's model. In general, A and B could be any two adjustable parameters that obey

$$A + B = \frac{1}{2}, \quad A > B \geq 0.$$

The first of these two constrains comes from a rotational invariance requirement, and the second from stability of the phonon band structure, to be proved later (A-3.3.38). With these two adjustable parameters, the general condition for no net torque on the atomic coordinate system at atom κ is

$$\sum_{\substack{\text{nearest}\\ \text{neighbors}}}\Bigg[\frac{\vec{r}_{\kappa j}\times(\vec{u}_j-\vec{u}_\kappa)}{2} - A\vec{r}_{\kappa j}\times(\vec{w}_\kappa\times\vec{r}_{\kappa j}) - B\vec{r}_{\kappa j}\times(\vec{w}_j\times\vec{r}_{\kappa j})\Bigg] = 0.$$

One can further simplify this formula by summing up all the terms involving the central atom. If $\vec{w}$ is any small vector, and one may neglect any quadratic or higher order terms in $\vec{w}$, then

$$\sum_{\substack{\text{nearest}\\ \text{neighbors}}}\vec{r}_{\kappa j}\times(\vec{w}\times\vec{r}_{\kappa j}) \approx \frac{a^2}{2}\vec{w}, \qquad (A-3.3.4)$$

$$\sum_{\substack{\text{nearest}\\ \text{neighbors}}} \mathbf{r}_{\kappa j} \times \mathbf{w} \approx 0, \qquad (A-3.3.5)$$

and

$$\sum_{\substack{\text{nearest}\\ \text{neighbors}}} \frac{(\mathbf{r}_{\kappa j}\cdot\mathbf{w})\mathbf{r}_{\kappa j}}{|\mathbf{r}_{\kappa j}|^2} \approx \frac{4}{3}\mathbf{w}, \qquad \sum_{\substack{\text{second}\\ \text{nearest}\\ \text{neighbors}}} \frac{(\mathbf{r}_{\kappa j}\cdot\mathbf{w})\mathbf{r}_{\kappa j}}{|\mathbf{r}_{\kappa j}|^2} \approx 4\mathbf{w} \qquad (A-3.3.6)$$

to within first order in $\mathbf{w}$, so

$$\mathbf{w}_\kappa \approx \frac{2}{Aa^2} \sum_{\substack{\text{nearest}\\ \text{neighbors}}} \left[\frac{\mathbf{r}_{\kappa j}\times\mathbf{u}_j}{2} - B\mathbf{r}_{\kappa j}\times(\mathbf{w}_j\times\mathbf{r}_{\kappa j})\right]. \qquad (A-3.3.7)$$

The expressions derived by Vasil'ev et al. for the elastic constants, using this model, are

$$c_{11} = \frac{1}{a}\left[4\alpha_2 + \frac{1}{3}(\alpha_1+2\beta)\right], \qquad (A-3.3.8)$$

$$c_{12} = \frac{1}{a}\left[2\alpha_2 + \frac{1}{3}(\alpha_1-\beta)\right], \qquad (A-3.3.9)$$

$$c_{44} = \frac{1}{a}\left[2\alpha_2 + \frac{1}{3}(\alpha_1+\frac{1}{2}\beta) - \frac{1}{3}\frac{(\alpha_1-\beta)^2}{\alpha_1+2\beta}\right]. \qquad (A-3.3.10)$$

Clearly, they do not depend on the adjustable parameters A and B.

It is important to notice that the formalism described here is actually much more general than the original model described by Vasil'ev *et al.* Their description of four lobes maintaining constant tetrahedral angles with each other enters the formalism only through the factor g, which is an adjustable parameter anyway.

Phonon calculations

When calculating phonon modes, one may take

$$\vec{u}_{\kappa l} = \vec{u}_\kappa \, e^{i(\vec{k}\cdot\vec{r}_l - \omega t)}, \qquad \vec{w}_{\kappa l} = \vec{w}_\kappa \, e^{i(\vec{k}\cdot\vec{r}_l - \omega t)}, \qquad \kappa = 1, 2. \quad (A - 3.3.11)$$

Here $\vec{u}_{\kappa l}$ is the deviation from equilibrium position, and $\vec{w}_{\kappa l}$ the rotation of the atomic coordinate system of the κ-th atom in the l-th unit cell. $\vec{k}$ is the reciprocal vector labeling a particular phonon mode. $2\pi\omega$ is the frequency associated with this mode.

To find the phonon modes, we first express the interactions (A-3.3.1), (A-3.3.2), (A-3.3.3) and (A-3.3.7) in matrix form using (A-3.3.11). We assume that the equilibrium position of atom 2 with respect to atom 1 is $(a/4)(1, 1, 1)$. Therefore, atom 1 has four nearest neighbors, whose equilibrium positions can be obtained from that of atom 2 by displacement of

$$(a/2)(000), \quad (a/2)(0\bar{1}\bar{1}), \quad (a/2)(\bar{1}0\bar{1}), \quad (a/2)(\bar{1}\bar{1}0).$$

Using (A-3.3.11), the relative deviations from equilibrium of these four nearest neighbors can all be expressed as $\vec{u}_2$ multiplied by some phase factor:

$$\vec{u}_2, \quad e^{\frac{-ia(k_2+k_3)}{2}}\vec{u}_2, \quad e^{\frac{-ia(k_3+k_1)}{2}}\vec{u}_2, \quad e^{\frac{-ia(k_1+k_2)}{2}}\vec{u}_2.$$

We can now write a typical term in the sum in (A-3.3.1) as

$$\left(\frac{\vec{u}_2\cdot\vec{r}_{12}}{|\vec{r}_{12}|}\right)\frac{\vec{r}_{12}}{|\vec{r}_{12}|} \approx \left(\frac{\vec{u}_2\cdot(1,1,1)}{3}\right)\begin{pmatrix}1\\1\\1\end{pmatrix} = \frac{1}{3}\begin{pmatrix}1&1&1\\1&1&1\\1&1&1\end{pmatrix}\vec{u}_2.$$

Since we calculate only to first order in $\vec{u}_\kappa$, there is no need to consider first order corrections to $\vec{r}_{1j}$, and they can be taken at their equilibrium values. Writing similar

expressions for the other three terms in (A-3.3.1) and using (A-3.3.6), we obtain

$$\begin{aligned}\vec{\mathbf{F}}_{c1}^{(1)} &= \alpha_1 \sum_{\substack{\text{nearest}\\ \text{neighbors}}} \left(\frac{(\vec{\mathbf{u}}_j - \vec{\mathbf{u}}_1)\cdot \vec{\mathbf{r}}_{1j}}{|\vec{\mathbf{r}}_{1j}|}\right)\frac{\vec{\mathbf{r}}_{1j}}{|\vec{\mathbf{r}}_{1j}|} \\ &\approx \alpha_1 \sum_{\substack{\text{nearest}\\ \text{neighbors}}} \left(\frac{\vec{\mathbf{u}}_j \cdot \vec{\mathbf{r}}_{1j}}{|\vec{\mathbf{r}}_{1j}|}\right)\frac{\vec{\mathbf{r}}_{1j}}{|\vec{\mathbf{r}}_{1j}|} - \frac{4}{3}\vec{\mathbf{u}}_1 \\ &\approx \alpha_1\left(\frac{1}{3}B\,\vec{\mathbf{u}}_2 - \frac{4}{3}\vec{\mathbf{u}}_1\right).\end{aligned} \qquad (A-3.3.12)$$

Here,

$$\begin{aligned}B = &\begin{pmatrix} +1 & +1 & +1\\ +1 & +1 & +1\\ +1 & +1 & +1\end{pmatrix} + e^{\frac{-ik_2-ik_3}{2}}\begin{pmatrix} +1 & -1 & -1\\ -1 & +1 & +1\\ -1 & +1 & +1\end{pmatrix} \\ &+ e^{\frac{-ik_3-ik_1}{2}}\begin{pmatrix} +1 & -1 & +1\\ -1 & +1 & -1\\ +1 & -1 & +1\end{pmatrix} + e^{\frac{-ik_1-ik_2}{2}}\begin{pmatrix} +1 & +1 & -1\\ +1 & +1 & -1\\ -1 & -1 & +1\end{pmatrix}\end{aligned} \qquad (A-3.3.13)$$

Similarly

$$\begin{aligned}\vec{\mathbf{F}}_{c1}^{(2)} &= \alpha_1 \sum_{\substack{\text{nearest}\\ \text{neighbors}}} \left(\frac{(\vec{\mathbf{u}}_j - \vec{\mathbf{u}}_2)\cdot \vec{\mathbf{r}}_{2j}}{|\vec{\mathbf{r}}_{2j}|}\right)\frac{\vec{\mathbf{r}}_{2j}}{|\vec{\mathbf{r}}_{2j}|} \\ &\approx \alpha_1 \sum_{\substack{\text{nearest}\\ \text{neighbors}}} \left(\frac{\vec{\mathbf{u}}_j \cdot \vec{\mathbf{r}}_{2j}}{|\vec{\mathbf{r}}_{2j}|}\right)\frac{\vec{\mathbf{r}}_{2j}}{|\vec{\mathbf{r}}_{2j}|} - \frac{4}{3}\vec{\mathbf{u}}_2 \\ &\approx \alpha_1\left(\frac{1}{3}B^*\,\vec{\mathbf{u}}_1 - \frac{4}{3}\vec{\mathbf{u}}_2\right).\end{aligned} \qquad (A-3.3.14)$$

Inserting (A-3.3.11) into (A-3.3.2),

$$\begin{aligned}\vec{\mathbf{F}}_{c2}^{(\kappa)} &= \alpha_2 \sum_{\substack{\text{second}\\ \text{nearest}\\ \text{neighbors}}} \left(\frac{(\vec{\mathbf{u}}_j - \vec{\mathbf{u}}_\kappa)\cdot \vec{\mathbf{r}}_{\kappa j}}{|\vec{\mathbf{r}}_{\kappa j}|}\right)\frac{\vec{\mathbf{r}}_{\kappa j}}{|\vec{\mathbf{r}}_{\kappa j}|} \\ &\approx \alpha_2 \sum_{\substack{\text{second}\\ \text{nearest}\\ \text{neighbors}}} \left(\frac{\vec{\mathbf{u}}_j \cdot \vec{\mathbf{r}}_{\kappa j}}{|\vec{\mathbf{r}}_{\kappa j}|}\right)\frac{\vec{\mathbf{r}}_{\kappa j}}{|\vec{\mathbf{r}}_{\kappa j}|} - 4\vec{\mathbf{u}}_\kappa \\ &\approx \alpha_2(C\vec{\mathbf{u}}_\kappa - 4\vec{\mathbf{u}}_\kappa).\end{aligned} \qquad (A-3.3.15)$$

Here,

$$\begin{aligned}C = &\cos\left(\frac{ak_2+ak_3}{2}\right)\begin{pmatrix} 0 & 0 & 0\\ 0 & 1 & 1\\ 0 & 1 & 1\end{pmatrix} + \cos\left(\frac{ak_3+ak_1}{2}\right)\begin{pmatrix} 1 & 0 & 1\\ 0 & 0 & 0\\ 1 & 0 & 1\end{pmatrix} \\ &+ \cos\left(\frac{ak_1+ak_2}{2}\right)\begin{pmatrix} 1 & 1 & 0\\ 1 & 1 & 0\\ 0 & 0 & 0\end{pmatrix} + \cos\left(\frac{ak_2-ak_3}{2}\right)\begin{pmatrix} 0 & 0 & 0\\ 0 & +1 & -1\\ 0 & -1 & +1\end{pmatrix} \\ &+ \cos\left(\frac{ak_3-ak_1}{2}\right)\begin{pmatrix} +1 & 0 & -1\\ 0 & 0 & 0\\ -1 & 0 & +1\end{pmatrix} + \cos\left(\frac{ak_1-ak_2}{2}\right)\begin{pmatrix} +1 & -1 & 0\\ -1 & +1 & 0\\ 0 & 0 & 0\end{pmatrix}.\end{aligned} \qquad (A-3.3.16)$$

In a similar way one can sum the parts of (A-3.3.3).

$$\sum_{\substack{\text{nearest}\\ \text{neighbors}}} \frac{-(\vec{w}_j + \vec{w}_1) \times \vec{r}_{1j}}{2} \approx \frac{1}{2} \sum_{\substack{\text{nearest}\\ \text{neighbors}}} \vec{r}_{1j} \times \vec{w}_j \approx \frac{a}{8} D \vec{w}_2 \qquad (A-3.3.17)$$

where

$$D = \begin{pmatrix} 0 & -1 & +1 \\ +1 & 0 & -1 \\ -1 & +1 & 0 \end{pmatrix} + e^{\frac{-ika_2 - ika_3}{2}} \begin{pmatrix} 0 & +1 & -1 \\ -1 & 0 & -1 \\ +1 & +1 & 0 \end{pmatrix} + e^{\frac{-ika_3 - ika_1}{2}} \begin{pmatrix} 0 & +1 & +1 \\ -1 & 0 & +1 \\ -1 & -1 & 0 \end{pmatrix} + e^{\frac{-ika_1 - ika_2}{2}} \begin{pmatrix} 0 & -1 & -1 \\ +1 & 0 & +1 \\ +1 & -1 & 0 \end{pmatrix}, \qquad (A-3.3.18)$$

and similarly,

$$\sum_{\substack{\text{nearest}\\ \text{neighbors}}} \frac{-(\vec{w}_j + \vec{w}_2) \times \vec{r}_{2j}}{2} \approx \frac{1}{2} \sum_{\substack{\text{nearest}\\ \text{neighbors}}} \vec{r}_{2j} \times \vec{w}_j \approx \frac{a}{8} D^* \vec{w}_1. \qquad (A-3.3.19)$$

Therefore, (A-3.3.3) becomes

$$\vec{F}_{nc}^{(1)} \approx \beta \left[A \vec{u}_2 - 4\vec{u}_1 - \left(\frac{1}{3} B \vec{u}_2 - \frac{4}{3} \vec{u}_1 \right) + \frac{a}{8} D \vec{w}_2 \right] \qquad (A-3.3.20)$$

$$\vec{F}_{nc}^{(2)} \approx \beta \left[A^* \vec{u}_1 - 4\vec{u}_2 - \left(\frac{1}{3} B^* \vec{u}_1 - \frac{4}{3} \vec{u}_2 \right) + \frac{a}{8} D^* \vec{w}_1 \right] \qquad (A-3.3.21)$$

where

$$A = 1 + e^{\frac{-ika_2 - ika_3}{2}} + e^{\frac{-ika_3 - ika_1}{2}} + e^{\frac{-ika_1 - ika_2}{2}}. \qquad (A-3.3.22)$$

Now it remains only to express (A-3.3.7) in a similar form.

$$\vec{w}_1 \approx \frac{1}{4Aa} D \vec{u}_2 + \frac{B}{8A} \mathcal{E} \vec{w}_2 \qquad (A-3.3.23)$$

$$\vec{w}_2 \approx \frac{1}{4Aa} D^* \vec{u}_1 + \frac{B}{8A} \mathcal{E}^* \vec{w}_1 \qquad (A-3.3.24)$$

where

$$\mathcal{E} = \begin{pmatrix} -2 & +1 & +1 \\ +1 & -2 & +1 \\ +1 & +1 & -2 \end{pmatrix} + e^{\frac{-ika_2 - ika_3}{2}} \begin{pmatrix} -2 & -1 & -1 \\ -1 & -2 & +1 \\ -1 & +1 & -2 \end{pmatrix} + e^{\frac{-ika_3 - ika_1}{2}} \begin{pmatrix} -2 & -1 & +1 \\ -1 & -2 & -1 \\ +1 & -1 & -2 \end{pmatrix} + e^{\frac{-ika_1 - ika_2}{2}} \begin{pmatrix} -2 & +1 & -1 \\ +1 & -2 & -1 \\ -1 & -1 & -2 \end{pmatrix} \qquad (A-3.3.25)$$

Inserting (A-3.3.11) — (A-3.3.25) into the equations of motion

$$-M\omega^2\mathfrak{u}_\kappa = \mathfrak{F}_{c1}^{(\kappa)} + \mathfrak{F}_{c2}^{(\kappa)} + \mathfrak{F}_{nc}^{(\kappa)}, \qquad (A-3.3.26)$$

one obtains

$$\left(M\omega^2 - \frac{4}{3}\alpha_1 + \alpha_2(C-4) - \frac{8}{3}\beta\right)\mathfrak{u}_1 + \left(\frac{\alpha_1}{3}B + \beta(A - \frac{1}{3}B)\right)\mathfrak{u}_2 + \beta\frac{a}{8}D\mathfrak{w}_2 = 0 \qquad (A-3.3.27)$$

$$\left(\frac{\alpha_1}{3}B^* + \beta(A^* - \frac{1}{3}B^*)\right)\mathfrak{u}_1 + \left(M\omega^2 - \frac{4}{3}\alpha_1 + \alpha_2(C-4) - \frac{8}{3}\beta\right)\mathfrak{u}_2 + \beta\frac{a}{8}D^*\mathfrak{w}_1 = 0 \qquad (A-3.3.28)$$

$$\frac{1}{4Aa}D\mathfrak{u}_2 - \mathfrak{w}_1 + \frac{B}{8A}\mathcal{E}\mathfrak{w}_2 = 0 \qquad (A-3.3.29)$$

$$\frac{1}{4Aa}D^*\mathfrak{u}_1 + \frac{B}{8A}\mathcal{E}^*\mathfrak{w}_1 - \mathfrak{w}_2 = 0. \qquad (A-3.3.30)$$

Equations (A-3.3.29) and (A-3.3.30) can be inverted in order to express $\mathfrak{w}_\kappa$ in terms of $\mathfrak{u}_1$ and $\mathfrak{u}_2$.

$$\mathfrak{w}_1 = \left(1 - \frac{B^2}{64A^2}\mathcal{E}\mathcal{E}^*\right)^{-1}\left[\frac{B}{32A^2a}\mathcal{E}D^*\mathfrak{u}_1 + \frac{1}{4Aa}D\mathfrak{u}_2\right] \qquad (A-3.3.31)$$

$$\mathfrak{w}_2 = \left(1 - \frac{B^2}{64A^2}\mathcal{E}^*\mathcal{E}\right)^{-1}\left[\frac{1}{4Aa}D^*\mathfrak{u}_1 + \frac{B}{32A^2a}\mathcal{E}^*D\mathfrak{u}_2\right] \qquad (A-3.3.32)$$

Special points in the phonon band structure

The Γ point

At the Γ point, $\vec{k} = 0$ and all the matrices A, B, C, D and E defined in (A-3.3.22), (A-3.3.13), (A-3.3.16), (A-3.3.18), and (A-3.3.25), are scalars:

$$A = 4, \quad B = 4, \quad C = 4, \quad D = 0, \quad E = -8.$$

The characteristic equations (A-3.3.27—30) become

$$\left(M\omega^2 - \frac{4}{3}\alpha_1 - \frac{8}{3}\beta\right)\vec{u}_1 + \left(\frac{4}{3}\alpha_1 + \frac{8}{3}\beta\right)\vec{u}_2 = 0$$

$$\left(\frac{4}{3}\alpha_1 + \frac{8}{3}\beta\right)\vec{u}_1 + \left(M\omega^2 - \frac{4}{3}\alpha_1 - \frac{8}{3}\beta\right)\vec{u}_2 = 0$$

$$\vec{w}_1 + \frac{B}{A}\vec{w}_2 = 0$$

$$\frac{B}{A}\vec{w}_1 + \vec{w}_2 = 0$$

Therefore,

$$M\omega_{RA}^2 = \frac{8}{3}(\alpha_1 + 2\beta).$$

The X point

At the X point, $\vec{k} = \frac{2\pi}{a}(1,0,0)$. The matrices A, B, C, D and $\mathcal{E}$ become

$$A = 0, \quad B = 4\begin{pmatrix} 0 & 0 & 0 \\ 0 & 0 & 1 \\ 0 & 1 & 0 \end{pmatrix}, \quad C = -4\begin{pmatrix} 1 & 0 & 0 \\ 0 & 0 & 0 \\ 0 & 0 & 0 \end{pmatrix},$$

$$D = 4\begin{pmatrix} 0 & 0 & 0 \\ 0 & 0 & -1 \\ 0 & +1 & 0 \end{pmatrix}, \qquad \mathcal{E} = 4\begin{pmatrix} 0 & 0 & 0 \\ 0 & 0 & 1 \\ 0 & 1 & 0 \end{pmatrix}.$$

From (A-3.3.31) and (A-3.3.32),

$$\vec{w}_1 = \frac{2B/a}{4A^2 - B^2}\begin{pmatrix} 0 & 0 & 0 \\ 0 & -1 & 0 \\ 0 & 0 & +1 \end{pmatrix}\vec{u}_1 + \frac{4A/a}{4A^2 - B^2}\begin{pmatrix} 0 & 0 & 0 \\ 0 & 0 & -1 \\ 0 & +1 & 0 \end{pmatrix}\vec{u}_2$$

$$\vec{w}_2 = \frac{-4A/a}{4A^2 - B^2}\begin{pmatrix} 0 & 0 & 0 \\ 0 & 0 & -1 \\ 0 & +1 & 0 \end{pmatrix}\vec{u}_1 - \frac{2B/a}{4A^2 - B^2}\begin{pmatrix} 0 & 0 & 0 \\ 0 & -1 & 0 \\ 0 & 0 & +1 \end{pmatrix}\vec{u}_2$$

$$\frac{a}{8}D\vec{w}_2 = \frac{2A}{4A^2 - B^2}\begin{pmatrix} 0 & 0 & 0 \\ 0 & 1 & 0 \\ 0 & 0 & 1 \end{pmatrix}\vec{u}_1 + \frac{B}{4A^2 - B^2}\begin{pmatrix} 0 & 0 & 0 \\ 0 & 0 & 1 \\ 0 & 1 & 0 \end{pmatrix}\vec{u}_2$$

$$\frac{a}{8}D^*\vec{w}_1 = \frac{B}{4A^2 - B^2}\begin{pmatrix} 0 & 0 & 0 \\ 0 & 0 & 1 \\ 0 & 1 & 0 \end{pmatrix}\vec{u}_1 + \frac{2A}{4A^2 - B^2}\begin{pmatrix} 0 & 0 & 0 \\ 0 & 1 & 0 \\ 0 & 0 & 1 \end{pmatrix}\vec{u}_2,$$

and the dynamical matrix is

$$MD^{(X)} = \begin{matrix} P & 0 & 0 & 0 & 0 & 0 \\ 0 & Q & 0 & 0 & 0 & R \\ 0 & 0 & Q & 0 & R & 0 \\ 0 & 0 & 0 & P & 0 & 0 \\ 0 & 0 & R & 0 & Q & 0 \\ 0 & R & 0 & 0 & 0 & Q \end{matrix}$$

The eigenvalues and eigenvectors of this matrix are

$$(LA + LO): \qquad P \qquad (100000), (000100),$$

$$(TO): \qquad Q - R \qquad (010000\bar{1}), (001010\bar{1}0),$$

$$(TA): \qquad Q + R \qquad (010001), (001010).$$

For this model,

$$P = \frac{4}{3}\alpha_1 + 8\alpha_2 + \frac{8}{3}\beta$$

$$Q = \frac{4}{3}\alpha_1 + 4\alpha_2 + \left(\frac{8}{3} - \frac{2A}{4A^2 - B^2}\right)\beta$$

$$R = -\frac{4}{3}\alpha_1 + \left(\frac{4}{3} - \frac{B}{4A^2 - B^2}\right)\beta.$$

Therefore,

$$M\omega_{TA}^2(X) = 4\alpha_2 + \left(4 - \frac{1}{2A - B}\right)\beta$$

$$M\omega_{LA}^2(X) = M\omega_{LO}^2(X) = \frac{4}{3}\alpha_1 + 8\alpha_2 + \frac{8}{3}\beta$$

$$M\omega_{TO}^2(X) = \frac{8}{3}\alpha_1 + 4\alpha_2 + \left(\frac{4}{3} - \frac{1}{2A + B}\right)\beta.$$

The L point

At the L point, $\vec{k} = \frac{2\pi}{a}(1/2, 1/2, 1/2)$. The matrices A, B, C, D and $\mathcal{E}$ become

$$A = -2, \quad B = 2\begin{pmatrix} -1 & 1 & 1 \\ 1 & -1 & 1 \\ 1 & 1 & -1 \end{pmatrix}, \quad C = -2\begin{pmatrix} 0 & 1 & 1 \\ 1 & 0 & 1 \\ 1 & 1 & 0 \end{pmatrix},$$

$$D = 2\begin{pmatrix} 0 & -1 & 1 \\ 1 & 0 & -1 \\ -1 & 1 & 0 \end{pmatrix}, \qquad \mathcal{E} = 2\begin{pmatrix} 2 & 1 & 1 \\ 1 & 2 & 1 \\ 1 & 1 & 2 \end{pmatrix}.$$

To calculate (A-3.3.31) and (A-3.3.32), we note that $D^* = -D$, and also that if $\mathcal{F}$ is any symmetric matrix of the form

$$\mathcal{F} = \begin{pmatrix} x & y & y \\ y & x & y \\ y & y & x \end{pmatrix}, \qquad (A-3.3.33)$$

then

$$\mathcal{F}D = D\mathcal{F} = (x-y)D \qquad (A-3.3.34)$$

and

$$\mathcal{F}^{-1} = \begin{pmatrix} w & z & z \\ z & w & z \\ z & z & w \end{pmatrix} \qquad (A-3.3.35)$$

where

$$w = \frac{-(x+y)}{(y-x)(2y+x)}, \qquad z = \frac{y}{(y-x)(2y+x)}.$$

Now,

$$\mathcal{E}\mathcal{E}^* = \mathcal{E}^*\mathcal{E} = 4\begin{pmatrix} 6 & 5 & 5 \\ 5 & 6 & 5 \\ 5 & 5 & 6 \end{pmatrix}$$

Therefore, $\left(1 - \frac{B^2}{64A^2}\mathcal{E}\,\mathcal{E}^*\right)^{-1}$ has the form (A-3.3.35), with

$$x = 1 - \frac{3B^2}{8A^2}, \qquad y = -\frac{5B^2}{16A^2}$$

or

$$z = \frac{\frac{5B^2}{16A^2}}{(1-\frac{B^2}{16A^2})(1-\frac{B^2}{A^2})}, \qquad w = \frac{1-\frac{11B^2}{16A^2}}{(1-\frac{B^2}{16A^2})(1-\frac{B^2}{A^2})},$$

and

$$w - z = \frac{1}{1-\frac{B^2}{16A^2}}.$$

Now (A-3.3.31) and (A-3.3.32) become

$$\mathbb{W}_1 = \frac{1}{1-\frac{B^2}{16A^2}}\left[\frac{-B}{16A^2a}D\mathbb{u}_1 + \frac{1}{4Aa}D\mathbb{u}_2\right]$$

$$\mathbb{W}_2 = \frac{1}{1-\frac{B^2}{16A^2}}\left[-\frac{1}{4Aa}D\mathbb{u}_1 + \frac{B}{16A^2a}D\mathbb{u}_1\right].$$

therefore,

$$\frac{a}{8}D\mathbb{W}_2 = \frac{1}{16A^2-B^2}\left[-\frac{A}{2}D^2\mathbb{u}_1 + \frac{B}{8}D^2\mathbb{u}_2\right]$$

$$\frac{a}{8}D^*\mathbb{W}_1 = \frac{1}{16A^2-B^2}\left[\frac{B}{8}D^2\mathbb{u}_1 - \frac{A}{2}D^2\mathbb{u}_2\right]$$

where

$$D^2 = 4\begin{pmatrix} -2 & 1 & 1 \\ 1 & -2 & 1 \\ 1 & 1 & -2 \end{pmatrix}.$$

We can now write down the dynamical matrix:

$$MD^{(L)} = \begin{matrix} P & Q & Q & R & S & S \\ Q & P & Q & S & R & S \\ Q & Q & P & S & S & R \\ R & S & S & P & Q & Q \\ S & R & S & Q & P & Q \\ S & S & R & Q & Q & P \end{matrix}.$$

The eigenvalues and eigenvectors are:

$$LA: \quad P+2Q+R+2S \quad (111111),$$

$$LO: \quad P+2Q-R-2S \quad (111\bar{1}\bar{1}\bar{1}),$$

$$TO: \quad P-Q+R-S \quad (1\bar{1}01\bar{1}0),(10\bar{1}10\bar{1}),$$

$$TA: \quad P-Q-R+S \quad (1\bar{1}0\bar{1}10),(10\bar{1}\bar{1}01).$$

For this model,

$$P=\frac{4}{3}\alpha_1+4\alpha_2+\left(\frac{8}{3}-\frac{4A}{16A^2-B^2}\right)\beta$$

$$Q=2\alpha_2+\frac{2A}{16A^2-B^2}\beta$$

$$R=\frac{2}{3}\alpha_1+\left(\frac{4}{3}+\frac{B}{16A^2-B^2}\right)\beta$$

$$S=-\frac{2}{3}\alpha_1+\left(\frac{2}{3}-\frac{B/2}{16A^2-B^2}\right)\beta.$$

Therefore,

$$M\omega_{TA}^2(L)=2\alpha_2+\left(2-\frac{3/2}{4A-B}\right)\beta$$

$$M\omega_{LA}^2(L)=\frac{2}{3}\alpha_1+8\alpha_2+\frac{16}{3}\beta$$

$$M\omega_{LO}^2(L)=2\alpha_1+8\alpha_2$$

$$M\omega_{TO}^2(L)=\frac{8}{3}\alpha_1+2\alpha_2+\left(\frac{10}{3}-\frac{3/2}{4A+B}\right)\beta.$$

Δ points

At a Δ point,

$$\vec{k} = \frac{2\pi}{a}(x, 0, 0). \qquad (A - 3.3.36)$$

The matrices A, B, C, D and $\mathcal{E}$ of (A-3.3.22), (A-3.3.13), (A-3.3.16), (A-3.3.18) and (A-3.3.25) become

$$A = 2(1 + e^{-i\pi x})$$

$$B = 2(1 + e^{-i\pi x})\begin{pmatrix} 1 & 0 & 0 \\ 0 & 1 & 0 \\ 0 & 0 & 1 \end{pmatrix} + 2(1 - e^{-i\pi x})\begin{pmatrix} 0 & 0 & 0 \\ 0 & 0 & 1 \\ 0 & 1 & 0 \end{pmatrix},$$

$$C = 2\begin{pmatrix} 0 & 0 & 0 \\ 0 & 1 & 0 \\ 0 & 0 & 1 \end{pmatrix} + 2\cos(\pi x)\begin{pmatrix} 2 & 0 & 0 \\ 0 & 1 & 0 \\ 0 & 0 & 1 \end{pmatrix},$$

$$D = 2(1 - e^{-i\pi x})\begin{pmatrix} 0 & 0 & 0 \\ 0 & 0 & -1 \\ 0 & 1 & 0 \end{pmatrix},$$

$$\mathcal{E} = -4(1 + e^{-i\pi x})\begin{pmatrix} 1 & 0 & 0 \\ 0 & 1 & 0 \\ 0 & 0 & 1 \end{pmatrix} + 2(1 - e^{-i\pi x})\begin{pmatrix} 0 & 0 & 0 \\ 0 & 0 & 1 \\ 0 & 1 & 0 \end{pmatrix}.$$

The inverted matrices in (A-3.3.31) and (A-3.3.32) are easy to calculate, since both $\mathcal{E}\mathcal{E}^*$ and $\mathcal{E}^*\mathcal{E}$ are diagonal matrices:

$$\mathcal{E}\mathcal{E}^* = \mathcal{E}^*\mathcal{E} = 8\begin{pmatrix} 4 & 0 & 0 \\ 0 & 5 & 0 \\ 0 & 0 & 5 \end{pmatrix} + 8\cos(\pi x)\begin{pmatrix} 4 & 0 & 0 \\ 0 & 3 & 0 \\ 0 & 0 & 3 \end{pmatrix}.$$

Thus,

$$\left(1 - \frac{B^2}{64A^2}\mathcal{E}\mathcal{E}^*\right)^{-1} = \begin{pmatrix} z & 0 & 0 \\ 0 & y & 0 \\ 0 & 0 & y \end{pmatrix} \qquad (A - 3.3.37)$$

$$\left(1 - \frac{B^2}{64A^2}\mathcal{E}^*\mathcal{E}\right)^{-1} = \begin{pmatrix} z & 0 & 0 \\ 0 & y & 0 \\ 0 & 0 & y \end{pmatrix}$$

where

$$z = \frac{1}{1 - \frac{B^2}{A^2}(\frac{1+\cos x}{2})}, \qquad y = \frac{1}{1 - \frac{B^2}{A^2}(\frac{5+3\cos x}{8})}.$$

We can now use this expression to obtain $\tilde{\mathbf{w}}_1$ and $\tilde{\mathbf{w}}_2$, the rotations of the atomic coordinate systems, from (A-3.3.31) and (A-3.3.32), using the fact that both D and D^* commute with (A-3.3.37). We also make use of the identities

$$DD^* = 8(1-\cos\pi x)\begin{pmatrix} 0 & 0 & 0 \\ 0 & 1 & 0 \\ 0 & 0 & 1 \end{pmatrix}, \quad D\mathcal{E}^*D = 8(1-e^{-i\pi x})^2\left[\begin{pmatrix} 0 & 0 & 0 \\ 0 & 2 & 1 \\ 0 & 1 & 2 \end{pmatrix} + e^{i\pi x}\begin{pmatrix} 0 & 0 & 0 \\ 0 & 2 & -1 \\ 0 & -1 & 2 \end{pmatrix}\right]$$

to obtain

$$\frac{a}{8}D\tilde{\mathbf{w}}_2 = \frac{1}{8A^2 - B^2(5+3\cos x)}\left[2A(1-\cos\pi x)\begin{pmatrix} 0 & 0 & 0 \\ 0 & 1 & 0 \\ 0 & 0 & 1 \end{pmatrix}\tilde{\mathbf{u}}_1 + \frac{B}{4}\begin{pmatrix} 0 & 0 & 0 \\ 0 & r & s \\ 0 & s & r \end{pmatrix}\tilde{\mathbf{u}}_2\right]$$

$$\frac{a}{8}D^*\tilde{\mathbf{w}}_1 = \frac{1}{8A^2 - B^2(5+3\cos x)}\left[\frac{B}{4}\begin{pmatrix} 0 & 0 & 0 \\ 0 & r & s \\ 0 & s & r \end{pmatrix}^*\tilde{\mathbf{u}}_1 + 2A(1-\cos\pi x)\begin{pmatrix} 0 & 0 & 0 \\ 0 & 1 & 0 \\ 0 & 0 & 1 \end{pmatrix}\tilde{\mathbf{u}}_2\right]$$

where

$$r = 2(1-e^{-i\pi x})^2(1+e^{i\pi x}), \qquad s = (1-e^{-i\pi x})^2(1-e^{i\pi x}).$$

Since $\tilde{\mathbf{w}}_1$ and $\tilde{\mathbf{w}}_2$ are bounded for all values of x, it follows that the denominator

$$8A^2 - B(5+3\cos x)$$

cannot change sign. Therefore, one can write the stability conditions for the phonon band structure as

$$\text{either} \quad |A| > |B| \qquad \text{or} \quad |4A| < |B|.$$

We shall see in our treatment for Λ points that a similar stability condition in that direction is

$$\text{either} \quad |A| > |B| \qquad \text{or} \quad |16A| < |B|,$$

and in general, the only possible stability condition that will hold in every direction is

$$|A| > |B|. \qquad (A-3.3.38)$$

We can now write down the dynamical matrix,

$$MD^{(\Delta)} = \begin{matrix} P & 0 & 0 & R & 0 & 0 \\ 0 & Q & 0 & 0 & S & T \\ 0 & 0 & Q & 0 & T & S \\ R^* & 0 & 0 & P & 0 & 0 \\ 0 & S^* & T^* & 0 & Q & 0 \\ 0 & T^* & S^* & 0 & 0 & Q \end{matrix}$$

where symmetry considerations require

$$|S+T| = |S-T|. \qquad (A-3.3.41)$$

The eigenvalues and eigenvectors are:

$$LA: \quad P-|R|, \quad (100\varsigma 00), \quad \varsigma = \frac{-R^*}{|R|}$$

$$LO: \quad P+|R|, \quad (100\varsigma 00), \quad \varsigma = \frac{R^*}{|R|}$$

$$TA: \quad Q-|T+S|, \quad (0110\bar{\eta}\bar{\eta}), (01\bar{1}0\theta\bar{\theta})$$

$$TO: \quad Q+|T+S|, \quad (0110\eta\eta), (01\bar{1}0\bar{\theta}\theta)$$

$$\eta = \frac{S^*+T^*}{|S+T|}, \qquad \theta = \frac{T^*-S^*}{|T-S|}.$$

For this model,

$$P = \frac{4}{3}\alpha_1 + 4(1-\cos\pi x)\alpha_2 + \frac{8}{3}\beta$$

$$Q = \frac{4}{3}\alpha_1 + 2(1-\cos\pi x)\alpha_2 + \left(\frac{8}{3} - \frac{2A(1-\cos\pi x)}{8A^2 - B^2(5+3\cos\pi x)}\right)\beta$$

$$R = -\frac{2}{3}(1+e^{-i\pi x})\alpha_1 - \frac{4}{3}(1+e^{-i\pi x})\beta$$

$$S = -\frac{2}{3}(1+e^{-i\pi x})\alpha_1 + \left(\frac{-4(1+e^{-i\pi x})}{3} - \frac{(B/2)(1-e^{-i\pi x})^2(1+e^{i\pi x})}{8A^2 - B^2(5+3\cos\pi x)}\right)\beta$$

$$T = -\frac{2}{3}(1-e^{-i\pi x})\alpha_1 + \left(\frac{2(1-e^{-i\pi x})}{3} - \frac{(B/4)(1-e^{-i\pi x})^2(1-e^{i\pi x})}{8A^2 - B^2(5+3\cos\pi x)}\right)\beta.$$

At first, it is not clear that S and T satisfy (A-3.3.41), but they actually do. In fact

$$e^{i\pi x}(S-T) = S^* + T^*.$$

Sound velocity in the (100) direction

Taking the limit $x \to 0$ in (A-3.3.36) and expanding up to second order the expressions for the acoustic frequencies, one obtains

$$P \approx \frac{4}{3}\alpha_1 + 2(\pi x)^2\alpha_2 + \frac{8}{3}\beta$$

$$Q \approx \frac{4}{3}\alpha_1 + (\pi x)^2\alpha_2 + \left(\frac{8}{3} - \frac{A(\pi x)^2}{8(A^2-B^2)}\right)\beta$$

$$|R| \approx \frac{4}{3}(\alpha_1 + 2\beta)(1 - \frac{(\pi x)^2}{8})$$

$$S+T \approx -\frac{4}{3}\alpha_1 + \left(\frac{-2}{3}(4+3i\pi x) + \frac{B(\pi x)^2}{8(A^2-B^2)} + (\pi x)^2\right)\beta$$

$$|S+T| \approx \frac{4}{3}\alpha_1 + \frac{8}{3}\beta - \left(\frac{B}{8(A^2-B^2)} + \frac{2\alpha_1+\beta}{2\alpha_1+4\beta}\right)(\pi x)^2\beta.$$

Therefore,

$$M\omega_{LA}^2 = P - |R| \approx \left(\frac{\alpha_1}{6} + 2\alpha_2 + \frac{\beta}{3}\right)\left(\frac{ka}{2}\right)^2$$

$$\begin{aligned} M\omega_{TA}^2 = Q - |S+T| &\approx \left[\alpha_2 - \frac{\beta}{8(A+B)} + \frac{2\alpha_1+\beta}{2\alpha_1+4\beta}\beta\right]\left(\frac{ka}{2}\right)^2 \\ &= \left[\alpha_2 - \frac{\beta}{4} + \frac{2\alpha_1+\beta}{2\alpha_1+4\beta}\beta\right]\left(\frac{ka}{2}\right)^2 \\ &= \left[\alpha_2 + \frac{3\beta}{4} - \frac{3\beta^2}{2\alpha_1+4\beta}\right]\left(\frac{ka}{2}\right)^2, \end{aligned}$$

from which we can obtain the sound velocities in the (100) direction:

$$v_L = \lim_{k\to 0}\left(\frac{\omega_{LA}}{k}\right) = \frac{a}{2\sqrt{M}}\sqrt{\frac{\alpha_1}{6} + 2\alpha_2 + \frac{\beta}{3}}$$

$$v_T = \lim_{k\to 0}\left(\frac{\omega_{TA}}{k}\right) = \frac{a}{2\sqrt{M}}\sqrt{\alpha_2 + \frac{3}{4}\beta - \frac{3\beta^2}{2\alpha_1 + 4\beta}}.$$

Recalling that the atomic volume is $a^3/8$, one can also find the static elastic constants, c_{11} and c_{44}, from these dispersion relations[2].

$$c_{11} = \frac{8M}{a}\lim k\to 0\frac{\omega_{LA}^2}{k^2} = \frac{1}{a}\left(\frac{\alpha_1}{3} + 4\alpha_2 + \frac{2\beta}{3}\right) \tag{39}$$

$$c_{44} = \frac{8M}{a}\lim k\to 0\frac{\omega_{TA}^2}{k^2} = \frac{1}{a}\left(2\alpha_2 + \frac{3}{2}\beta - \frac{3\beta^2}{\alpha_1 + 2\beta}\right) \tag{40}$$

These two equations prove (A-3.3.8) and (A-3.3.10).

Λ points

At a Λ point,

$$\vec{k} = \frac{2\pi}{a}(x, x, x). \qquad (A-3.3.42)$$

The matrices A, B, C, D and $\mathcal{E}$ of (A-3.3.22), (A-3.3.13), (A-3.3.16), (A-3.3.18) and (A-3.3.25) become

$$A = 1 + 3e^{-2i\pi x}, \quad B = (1 + 3e^{-2i\pi x})\begin{pmatrix} 1 & 0 & 0 \\ 0 & 1 & 0 \\ 0 & 0 & 1 \end{pmatrix} + (1 - e^{-2i\pi x})\begin{pmatrix} 0 & 1 & 1 \\ 1 & 0 & 1 \\ 1 & 1 & 0 \end{pmatrix},$$

$$C = 2(1 + \cos 2\pi x)\begin{pmatrix} 1 & 0 & 0 \\ 0 & 1 & 0 \\ 0 & 0 & 1 \end{pmatrix} + (-1 + \cos 2\pi x)\begin{pmatrix} 0 & 1 & 1 \\ 1 & 0 & 1 \\ 1 & 1 & 0 \end{pmatrix},$$

$$D = (1-e^{-2i\pi x})\begin{pmatrix} 0 & -1 & 1 \\ 1 & 0 & -1 \\ -1 & 1 & 0 \end{pmatrix}, \qquad \mathcal{E} = -2(1+3e^{-2i\pi x})\begin{pmatrix} 1 & 0 & 0 \\ 0 & 1 & 0 \\ 0 & 0 & 1 \end{pmatrix}+(1-e^{-2i\pi x})\begin{pmatrix} 0 & 1 & 1 \\ 1 & 0 & 1 \\ 1 & 1 & 0 \end{pmatrix}.$$

The inverted matrices in (A-3.3.31) and (A-3.3.32) are easy to calculate, since both $\mathcal{E}\mathcal{E}^*$ and $\mathcal{E}^*\mathcal{E}$ have a simple form

$$\mathcal{E}\mathcal{E}^* = \mathcal{E}^*\mathcal{E} = (44 + 20\cos 2\pi x)\begin{pmatrix} 1 & 0 & 0 \\ 0 & 1 & 0 \\ 0 & 0 & 1 \end{pmatrix} + (10 - 10\cos 2\pi x)\begin{pmatrix} 0 & 1 & 1 \\ 1 & 0 & 1 \\ 1 & 1 & 0 \end{pmatrix}.$$

Thus, using (A-3.3.35),

$$\left(1 - \frac{B^2}{64A^2}\mathcal{E}\mathcal{E}^*\right)^{-1} = w\begin{pmatrix} 1 & 0 & 0 \\ 0 & 1 & 0 \\ 0 & 0 & 1 \end{pmatrix} + z\begin{pmatrix} 0 & 1 & 1 \\ 1 & 0 & 1 \\ 1 & 1 & 0 \end{pmatrix} \qquad (A-3.3.43)$$

$$\left(1 - \frac{B^2}{64A^2}\mathcal{E}^*\mathcal{E}\right)^{-1} = w\begin{pmatrix} 1 & 0 & 0 \\ 0 & 1 & 0 \\ 0 & 0 & 1 \end{pmatrix} + z\begin{pmatrix} 0 & 1 & 1 \\ 1 & 0 & 1 \\ 1 & 1 & 0 \end{pmatrix}$$

where

$$w = \frac{1 - \frac{B^2}{A^2}(\frac{27+5\cos 2\pi x}{32})}{(1 - \frac{B^2}{A^2})(-1 + \frac{B^2}{A^2}\frac{17+15\cos 2\pi x}{32})}$$

$$z = \frac{\frac{B^2}{A^2}(\frac{5-5\cos 2\pi x}{32.})}{(1 - \frac{B^2}{A^2})(-1 + \frac{B^2}{A^2}\frac{17+15\cos 2\pi x}{32})}$$

$$w - z = \frac{1}{-1 + \frac{B^2}{A^2}\frac{17+15\cos 2\pi x}{32}}.$$

Therefore, using (A-3.3.34), one can write

$$\mathbb{w}_1 = (w-z)\Big[\frac{B}{32A^2a}(-3-5e^{-2i\pi x})(-1+e^{+2i\pi x})\begin{pmatrix}0&-1&1\\1&0&-1\\-1&1&0\end{pmatrix}\mathbb{u}_1 + \frac{1}{4Aa}(1-e^{-2i\pi x})\begin{pmatrix}0&-1&1\\1&0&-1\\-1&1&0\end{pmatrix}\mathbb{u}_2\Big]$$

$$\mathbb{w}_2 = (w-z)\Big[\frac{1}{4Aa}(-1+e^{+2i\pi x})\begin{pmatrix}0&-1&1\\1&0&-1\\-1&1&0\end{pmatrix}\mathbb{u}_1 + \frac{B}{32A^2a}(-3-5e^{+2i\pi x})(1-e^{-2i\pi x})\begin{pmatrix}0&-1&1\\1&0&-1\\-1&1&0\end{pmatrix}\mathbb{u}_2\Big]$$

and

$$\frac{a}{8}D\mathbb{w}_2 = (w-z)\Big[\frac{-1}{16A}(1-\cos 2\pi x)\begin{pmatrix}-2&1&1\\1&-2&1\\1&1&-2\end{pmatrix}\mathbb{u}_1 + \frac{B(-3-5e^{+2i\pi x})(1-e^{-2i\pi x})^2}{256A^2}\begin{pmatrix}-2&1&1\\1&-2&1\\1&1&-2\end{pmatrix}\mathbb{u}_2\Big]$$

$$\frac{a}{8}D^*\mathbb{w}_1 = (w-z)\Big[\frac{B(-3-5e^{-2i\pi x})(-1+e^{+2i\pi x})^2}{256A^2}\begin{pmatrix}-2&1&1\\1&-2&1\\1&1&-2\end{pmatrix}\mathbb{u}_1 - \frac{1}{16A}(1-\cos 2\pi x)\begin{pmatrix}-2&1&1\\1&-2&1\\1&1&-2\end{pmatrix}\mathbb{u}_2\Big].$$

We can now write down the dynamical matrix,

$$MD^{(\Lambda)} = \begin{matrix} P & Q & Q & R & S & S \\ Q & P & Q & S & R & S \\ Q & Q & P & S & R & S \\ R^* & S^* & S^* & P & Q & Q \\ S^* & R^* & S^* & Q & P & Q \\ S^* & S^* & R^* & Q & Q & P \end{matrix}$$

whose eigenvalues and eigenvectors are

$$LA, LO: \quad P+2Q \pm |R+2S| \quad (111\varsigma\varsigma\varsigma), \quad \varsigma = \pm\sqrt{\frac{R^*+2S^*}{R+2S}}$$

$$TA, TO: \quad P - Q \pm |R - S| \quad (1\bar{1}0\eta\bar{\eta}0), \quad \eta = \pm\sqrt{\frac{R^* - S^*}{R - S}}$$

where

$$P = \frac{4}{3}\alpha_1 + 2(1 - \cos 2\pi x)\alpha_2 + \left[\frac{8}{3} - \frac{4A(1 - \cos 2\pi x)}{32A^2 - B^2(17 + 15\cos 2\pi x)}\right]\beta$$

$$Q = \quad (1 - \cos 2\pi x)\alpha_2 + \left[\frac{2A(1 - \cos 2\pi x)}{32A^2 - B^2(17 + 15\cos 2\pi x)}\right]\beta$$

$$R = -\left(\frac{1}{3} + e^{-2i\pi x}\right)\alpha_1 + \left[-\frac{2}{3} - 2e^{-2i\pi x} - \frac{(B/4)(3 + 5e^{+2i\pi x})(1 - e^{-2i\pi x})^2}{32A^2 - B^2(17 + 15\cos 2\pi x)}\right]\beta$$

$$S = \left(-\frac{1}{3} + \frac{e^{-2i\pi x}}{3}\right)\alpha_1 + \left[\frac{1 - e^{-2i\pi x}}{3} + \frac{(B/8)(3 + 5e^{+2i\pi x})(1 - e^{-2i\pi x})^2}{32A^2 - B^2(17 + 15\cos 2\pi x)}\right]\beta.$$

Sound velocity in the (111) direction

Taking the limit $x \to 0$ in (A-3.3.42) and expanding up to second order the expressions for acoustic frequencies, one obtains

$$P \approx \frac{4}{3}\alpha_1 + \frac{8}{3}\beta + \left(\alpha_2 - \frac{A\beta}{16(A^2 - B^2)}\right)(2\pi x)^2$$

$$Q \approx \left(\frac{\alpha_2}{2} + \frac{A\beta}{32(A^2 - B^2)}\right)(2\pi x)^2$$

$$|R + 2S| \approx \frac{4}{3}\alpha_1 + \frac{8}{3}\beta - \left(\frac{\alpha_1 + 8\beta}{\alpha_1 + 2\beta} \cdot \frac{\alpha_1}{8}\right)(2\pi x)^2$$

$$|R - S| \approx \frac{4}{3}\alpha_1 + \frac{8}{3}\beta - \left(\frac{3\beta B}{32(A^2 - B^2)} + \frac{4\alpha_1 + 5\beta}{\alpha_1 + 2\beta} \cdot \frac{\beta}{8}\right)(2\pi x)^2.$$

Therefore,

$$M\omega_{LA}^2 = P + 2Q - |R + 2S| \approx \left(2\alpha_2 + \frac{\alpha_1 + 8\beta}{\alpha_1 + 2\beta} \cdot \frac{\alpha_1}{8}\right) \cdot \frac{(ak)^2}{3}$$

$$M\omega_{TA}^2 = P - Q - |R - S| \approx \left(\frac{\alpha_2}{2} - \frac{3\beta}{32(A+B)} + \frac{4\alpha_1 + 5\beta}{\alpha_1 + 2\beta} \cdot \frac{\beta}{8}\right) \cdot \frac{(ak)^2}{3}$$
$$= \left(\frac{\alpha_2}{2} - \frac{3\beta}{16} + \frac{4\alpha_1 + 5\beta}{\alpha_1 + 2\beta} \cdot \frac{\beta}{8}\right) \cdot \frac{(ak)^2}{3}.$$

from which we can obtain the sound velocities in the (111) direction:

$$v_L = \lim_{k \to 0}\left(\frac{\omega_{LA}}{k}\right) = \frac{a}{\sqrt{3M}}\sqrt{\frac{\alpha_1}{8} + 2\alpha_2 + \frac{3}{4}\frac{\alpha_1\beta}{\alpha_1 + 2\beta}}$$

$$v_T = \lim_{k \to 0}\left(\frac{\omega_{TA}}{k}\right) = \frac{a}{\sqrt{3M}}\sqrt{\frac{1}{2}\alpha_2 + \frac{5}{16}\beta - \frac{3\beta^2}{8\alpha_1 + 16\beta}}.$$

One can also find the static elastic constants, $c_{11} + 2c_{12} = 4c_{44}$ and $c_{11} - c_{12} + c_{44}$ from these dispersion relations.

$$c_{11} + 2c_{12} + 4c_{44} = \frac{24M}{a} \lim k \to 0 \frac{\omega_{LA}^2}{k^2} = \frac{1}{a}\left(\alpha_1 + 16\alpha_2 + \frac{6\alpha_1\beta}{\alpha_1 + 2\beta}\right) \qquad (A - 3.3.44)$$

$$c_{11} - c_{12} + c_{44} = \frac{24M}{a} \lim k \to 0 \frac{\omega_{TA}^2}{k^2} = \frac{1}{a}\left(4\alpha_2 + \frac{5}{2}\beta - \frac{3\beta^2}{\alpha_1 + 2\beta}\right) \qquad (A - 3.3.45)$$

These two equations, together with (A-3.3.39) and (A-3.3.40) prove (A-3.3.9).

References to Appendix A-3.3.

1. L. N. Vasil'ev, Yu. A. Logachev, V. Ya. Moizhes, and M. S. Yur'ev, *Soviet Physics - Solid State*, **13**, 363 (1971).
2. C. Kittel, *Introduction to Solid State Physics*, 3rd ed., p.121, Wiley, New York (1966).

Appendix A-3.4. Fitting the parameters of Vasil'ev's model to Si_5H_{12} cluster calculations

The model proposed by Vasil'ev *et al.* is not easily fitted to the cluster. In all the previous models, the elastic energy depended directly on explicit geometrical objects like bond lengths and angles. Therefore, one could make sure that only such geometrical objects that involve only silicon atoms will be changed, and by doing so, one could disregard the silicon – hydrogen interaction. This is no longer the case whenever there are hidden coordinates in the system. All the relevant interactions, that is, both $Si-Si$, $Si-H$ and $H-H$ interactions, should be taken into account. Only then, can the $Si-Si$ interaction coefficients for the phonon band structure calculations be extracted. In this appendix we shall retain the notation of Appendix A-3.3 as much as possible, but the interaction coefficients α_1, α_2, β and A, will now have extra superscript notation to denote whether they belong to a $Si-Si$, $Si-H$ or an $H-H$ interaction. All told, there are nine independent parameters: one central first-nearest-neighbor interaction $\alpha_1^{(\mathrm{Si\cdot Si})}$; four central second nearest neighbor interactions $\alpha_2^{(\mathrm{Si\cdot Si})}$, $\alpha_2^{(\mathrm{Si\cdot H})}$, $\alpha_2^{(\mathrm{H\cdot H})}(1)$ and $\alpha_2^{(\mathrm{H\cdot H})}(2)$ (the last two refer to hydrogens bonded to two different silicon atoms, and bonded to the same silicon atom); two non-central interactions, $\beta^{(\mathrm{Si\cdot Si})}$ and $\beta^{(\mathrm{Si\cdot H})}$; and finally, two torque coefficients $A^{(\mathrm{Si\cdot Si})}$ and $A^{(\mathrm{Si\cdot H})}$. The meanings of these force constants were explained in detail in the previous appendix (A-3.3).

We now investigate the geometry of the Si_5H_{12} cluster and obtain the expressions for the various forces and torques operating on the atoms under a given

deformation. The central Si atom is at the origin and at rest. Its four nearest neighbors are moving slightly around their equilibrium positions. These equilibrium positions are

$$\vec{\mathbf{r}}_1 = \frac{a}{4}(111), \quad \vec{\mathbf{r}}_2 = \frac{a}{4}(1\bar{1}\bar{1}), \quad \vec{\mathbf{r}}_3 = \frac{a}{4}(\bar{1}1\bar{1}), \quad \vec{\mathbf{r}}_4 = \frac{a}{4}(\bar{1}\bar{1}1).$$

The hydrogen atoms, H_{ij} are all second nearest neighbors to the central silicon atom, and as such, have coordinates that are lattice translations.

$$H_{11}, H_{21}, H_{31}: \qquad (a/2)(011), (a/2)(101), (a/2)(110)$$

$$H_{12}, H_{22}, H_{32}: \qquad (a/2)(1\bar{1}0), (a/2)(10\bar{1}), (a/2)(0\bar{1}\bar{1})$$

$$H_{13}, H_{23}, H_{33}: \qquad (a/2)(01\bar{1}), (a/2)(\bar{1}0\bar{1}), (a/2)(\bar{1}10)$$

$$H_{14}, H_{24}, H_{34}: \qquad (a/2)(\bar{1}\bar{1}0), (a/2)(\bar{1}01), (a/2)(0\bar{1}1)$$

It is easy to verify that if $\vec{\mathbf{s}}_{ij}$ is the equilibrium position of H_{ij}, and $\vec{\mathbf{r}}_{ji}$ is the vector from Si_j to H_{ij} at equilibrium, then

$$\vec{\mathbf{s}}_{ij} = \vec{\mathbf{r}}_j - \vec{\mathbf{r}}_k, \qquad \vec{\mathbf{r}}_{ji} = -\vec{\mathbf{r}}_k, \qquad k \equiv i + j \,(\mathrm{mod}\ 4).$$

In each mode treated in this section, each one of the non-central silicons, Si_j, will move by an amount $\vec{\mathbf{u}}_j$, and each one of the twelve hydrogen atoms, H_{ij}, will move by an amount $\vec{\mathbf{v}}_{ij}$. These sixteen vector quantities, namely, $\vec{\mathbf{u}}_1, \ldots, \vec{\mathbf{u}}_4$ and $\vec{\mathbf{v}}_{11}, \ldots, \vec{\mathbf{v}}_{34}$, are all given as functions of the mode parameter t. Since we are working in the harmonic approximation, we may assume that t is very small, and only the linear terms in the expansions of these functions are relevant for our calculations. These linear terms for each one of the 23 modes are given in Table A-3.4.1.

TABLE I. Differential change in position of the four silicon and twelve hydrogen atoms in the cluster Si_5H_{12}. $\vec{\mathbf{u}}_j(t)$ is the differential change in position (i.e., the position for a given t minus the equilibrium position). This table lists $\left(\frac{\partial \vec{\mathbf{u}}_j}{\partial t}\right)_{t=0}$ and $\left(\frac{\partial \vec{\mathbf{v}}_{ij}}{\partial t}\right)_{t=0}$ for the various modes used in this chapter. For brevity, several modes are not listed here because they can be expressed as linear combinations of other modes: (8)=(3)+(7); (9)=(3)−(7); (22)=(1)+(20); and (23)=(3)+(21).

Mode	$\left(\frac{\partial \vec{\mathbf{u}}_1}{\partial t}\right)_{t=0}$	$\left(\frac{\partial \vec{\mathbf{v}}_{11}}{\partial t}\right)_{t=0}$	$\left(\frac{\partial \vec{\mathbf{v}}_{21}}{\partial t}\right)_{t=0}$	$\left(\frac{\partial \vec{\mathbf{v}}_{31}}{\partial t}\right)_{t=0}$
Mode 1	$\frac{1}{\sqrt{3}}(1,1,1)$	$\frac{1}{\sqrt{3}}(1,1,1)$	$\frac{1}{\sqrt{3}}(1,1,1)$	$\frac{1}{\sqrt{3}}(1,1,1)$
Mode 2	$\frac{1}{\sqrt{3}}(1,1,1)$	$\frac{1}{\sqrt{3}}(1,1,1)$	$\frac{1}{\sqrt{3}}(1,1,1)$	$\frac{1}{\sqrt{3}}(1,1,1)$
Mode 3	$\frac{1}{\sqrt{3}}(1,1,1)$	$\frac{1}{\sqrt{3}}(1,1,1)$	$\frac{1}{\sqrt{3}}(1,1,1)$	$\frac{1}{\sqrt{3}}(1,1,1)$
Mode 4	$\frac{r_0}{2\sqrt{3}}(\bar{1},1,0)$	$\frac{r_0}{\sqrt{3}}(\bar{1},0,0)$	$\frac{r_0}{\sqrt{3}}(0,1,0)$	$\frac{r_0}{\sqrt{3}}(\bar{1},1,0)$
Mode 5	$\frac{r_0}{\sqrt{6}}(1,1,\bar{2})$	$\frac{r_0\sqrt{2}}{\sqrt{3}}(1,1,\bar{1})$	$\frac{r_0\sqrt{2}}{\sqrt{3}}(1,1,\bar{1})$	$\frac{r_0\sqrt{2}}{\sqrt{3}}(0,0,\bar{2})$
Mode 6	$\frac{r_0}{\sqrt{6}}(1,1,\bar{2})$	$\frac{r_0\sqrt{2}}{\sqrt{3}}(1,1,\bar{1})$	$\frac{r_0\sqrt{2}}{\sqrt{3}}(1,1,\bar{1})$	$\frac{r_0\sqrt{2}}{\sqrt{3}}(0,0,\bar{2})$
Mode 7	$\frac{r_0}{\sqrt{6}}(1,1,\bar{2})$	$\frac{r_0\sqrt{2}}{\sqrt{3}}(1,1,\bar{1})$	$\frac{r_0\sqrt{2}}{\sqrt{3}}(1,1,\bar{1})$	$\frac{r_0\sqrt{2}}{\sqrt{3}}(0,0,\bar{2})$
Mode 10	$\frac{1}{\sqrt{3}}(2,2,\bar{1})$	$\frac{1}{\sqrt{3}}(3,3,\bar{1})$	$\frac{1}{\sqrt{3}}(3,3,\bar{1})$	$\frac{1}{\sqrt{3}}(1,1,\bar{3})$
Mode 11	$\frac{1}{\sqrt{3}}(0,0,3)$	$\frac{1}{\sqrt{3}}(\bar{1},\bar{1},3)$	$\frac{1}{\sqrt{3}}(\bar{1},\bar{1},3)$	$\frac{1}{\sqrt{3}}(1,1,5)$
Mode 12	$\frac{1}{\sqrt{3}}(2,2,\bar{1})$	$\frac{1}{\sqrt{3}}(3,3,\bar{1})$	$\frac{1}{\sqrt{3}}(3,3,\bar{1})$	$\frac{1}{\sqrt{3}}(1,1,\bar{3})$
Mode 13	$\frac{1}{\sqrt{3}}(0,0,3)$	$\frac{1}{\sqrt{3}}(\bar{1},\bar{1},3)$	$\frac{1}{\sqrt{3}}(\bar{1},\bar{1},3)$	$\frac{1}{\sqrt{3}}(1,1,5)$
Mode 14	$\frac{1}{4\sqrt{3}}(5,5,2)$	$\frac{1}{2\sqrt{3}}(3,3,1)$	$\frac{1}{2\sqrt{3}}(3,3,1)$	$\frac{1}{\sqrt{3}}(1,1,0)$
Mode 15	$\frac{1}{4\sqrt{3}}(3,3,6)$	$\frac{1}{2\sqrt{3}}(1,1,3)$	$\frac{1}{2\sqrt{3}}(1,1,3)$	$\frac{1}{\sqrt{3}}(1,1,2)$
Mode 16	0	$\frac{1}{\sqrt{6}}(\bar{2},\bar{1},\bar{1})$	$\frac{1}{\sqrt{6}}(\bar{1},\bar{2},\bar{1})$	$\frac{1}{\sqrt{6}}(\bar{1},\bar{1},\bar{2})$
Mode 17	$\frac{1}{\sqrt{3}}(0,0,1)$	$\frac{1}{\sqrt{3}}(0,0,1)$	$\frac{1}{\sqrt{3}}(0,0,1)$	$\frac{1}{\sqrt{3}}(0,0,1)$
Mode 18	0	$\frac{1}{\sqrt{6}}(\bar{2},\bar{1},\bar{1})$	$\frac{1}{\sqrt{6}}(\bar{1},\bar{2},\bar{1})$	$\frac{1}{\sqrt{6}}(\bar{1},\bar{1},\bar{2})$
Mode 19	$\frac{1}{\sqrt{3}}(0,0,1)$	$\frac{1}{\sqrt{3}}(0,0,1)$	$\frac{1}{\sqrt{3}}(0,0,1)$	$\frac{1}{\sqrt{3}}(0,0,1)$
Mode 20	$\frac{1}{\sqrt{6}}(1,1,\bar{2})$	$\frac{1}{\sqrt{6}}(0,2,\bar{4})$	$\frac{1}{\sqrt{6}}(2,0,\bar{4})$	$\frac{1}{\sqrt{6}}(2,2,0)$
Mode 21	$\frac{1}{\sqrt{6}}(1,1,\bar{2})$	$\frac{1}{\sqrt{6}}(0,2,\bar{4})$	$\frac{1}{\sqrt{6}}(2,0,\bar{4})$	$\frac{1}{\sqrt{6}}(2,2,0)$

Table A-3.4.1 (Continued)

Mode	$\left(\frac{\partial \vec{\mathbf{u}}_2}{\partial t}\right)_{t=0}$	$\left(\frac{\partial \vec{\mathbf{v}}_{12}}{\partial t}\right)_{t=0}$	$\left(\frac{\partial \vec{\mathbf{v}}_{22}}{\partial t}\right)_{t=0}$	$\left(\frac{\partial \vec{\mathbf{v}}_{32}}{\partial t}\right)_{t=0}$
Mode 1	$\frac{1}{\sqrt{3}}(1,\bar{1},\bar{1})$	$\frac{1}{\sqrt{3}}(1,\bar{1},\bar{1})$	$\frac{1}{\sqrt{3}}(1,\bar{1},\bar{1})$	$\frac{1}{\sqrt{3}}(1,\bar{1},\bar{1})$
Mode 2	0	0	0	0
Mode 3	$\frac{1}{\sqrt{3}}(\bar{1},1,1)$	$\frac{1}{\sqrt{3}}(\bar{1},1,1)$	$\frac{1}{\sqrt{3}}(\bar{1},1,1)$	$\frac{1}{\sqrt{3}}(\bar{1},1,1)$
Mode 4	$\frac{r_0}{2\sqrt{3}}(\bar{1},\bar{1},0)$	$\frac{r_0}{\sqrt{3}}(\bar{1},\bar{1},0)$	$\frac{r_0}{\sqrt{3}}(0,\bar{1},0)$	$\frac{r_0}{\sqrt{3}}(\bar{1},0,0)$
Mode 5	$\frac{r_0}{\sqrt{6}}(1,\bar{1},2)$	$\frac{r_0\sqrt{2}}{\sqrt{3}}(0,0,2)$	$\frac{r_0\sqrt{2}}{\sqrt{3}}(1,\bar{1},1)$	$\frac{r_0\sqrt{2}}{\sqrt{3}}(1,\bar{1},1)$
Mode 6	0	0	0	0
Mode 7	$\frac{r_0}{\sqrt{6}}(\bar{1},1,\bar{2})$	$\frac{r_0\sqrt{2}}{\sqrt{3}}(0,0,\bar{2})$	$\frac{r_0\sqrt{2}}{\sqrt{3}}(\bar{1},1,\bar{1})$	$\frac{r_0\sqrt{2}}{\sqrt{3}}(\bar{1},1,\bar{1})$
Mode 10	$\frac{1}{\sqrt{3}}(\bar{2},2,\bar{1})$	$\frac{1}{\sqrt{3}}(\bar{1},1,\bar{3})$	$\frac{1}{\sqrt{3}}(\bar{3},3,\bar{1})$	$\frac{1}{\sqrt{3}}(\bar{3},3,\bar{1})$
Mode 11	$\frac{1}{\sqrt{3}}(0,0,3)$	$\frac{1}{\sqrt{3}}(\bar{1},1,5)$	$\frac{1}{\sqrt{3}}(1,\bar{1},3)$	$\frac{1}{\sqrt{3}}(1,\bar{1},3)$
Mode 12	$\frac{1}{\sqrt{3}}(2,\bar{2},1)$	$\frac{1}{\sqrt{3}}(1,\bar{1},3)$	$\frac{1}{\sqrt{3}}(3,\bar{3},1)$	$\frac{1}{\sqrt{3}}(3,\bar{3},1)$
Mode 13	$\frac{1}{\sqrt{3}}(0,0,\bar{3})$	$\frac{1}{\sqrt{3}}(1,\bar{1},\bar{5})$	$\frac{1}{\sqrt{3}}(\bar{1},1,\bar{3})$	$\frac{1}{\sqrt{3}}(\bar{1},1,\bar{3})$
Mode 14	$\frac{1}{4\sqrt{3}}(\bar{5},5,2)$	$\frac{1}{\sqrt{3}}(\bar{1},1,0)$	$\frac{1}{2\sqrt{3}}(\bar{3},3,1)$	$\frac{1}{2\sqrt{3}}(\bar{3},3,1)$
Mode 15	$\frac{1}{4\sqrt{3}}(\bar{3},3,6)$	$\frac{1}{\sqrt{3}}(\bar{1},1,2)$	$\frac{1}{2\sqrt{3}}(\bar{1},1,3)$	$\frac{1}{2\sqrt{3}}(\bar{1},1,3)$
Mode 16	0	$\frac{1}{\sqrt{6}}(\bar{1},1,2)$	$\frac{1}{\sqrt{6}}(\bar{1},2,1)$	$\frac{1}{\sqrt{6}}(\bar{2},1,1)$
Mode 17	$\frac{1}{\sqrt{3}}(0,0,\bar{1})$	$\frac{1}{\sqrt{3}}(0,0,\bar{1})$	$\frac{1}{\sqrt{3}}(0,0,\bar{1})$	$\frac{1}{\sqrt{3}}(0,0,\bar{1})$
Mode 18	0	$\frac{1}{\sqrt{6}}(1,\bar{1},\bar{2})$	$\frac{1}{\sqrt{6}}(1,\bar{2},\bar{1})$	$\frac{1}{\sqrt{6}}(2,\bar{1},\bar{1})$
Mode 19	$\frac{1}{\sqrt{3}}(0,0,1)$	$\frac{1}{\sqrt{3}}(0,0,1)$	$\frac{1}{\sqrt{3}}(0,0,1)$	$\frac{1}{\sqrt{3}}(0,0,1)$
Mode 20	$\frac{1}{\sqrt{6}}(1,\bar{1},2)$	$\frac{1}{\sqrt{6}}(2,\bar{2},0)$	$\frac{1}{\sqrt{6}}(2,0,4)$	$\frac{1}{\sqrt{6}}(0,\bar{2},4)$
Mode 21	$\frac{1}{\sqrt{6}}(\bar{1},1,\bar{2})$	$\frac{1}{\sqrt{6}}(\bar{2},2,0)$	$\frac{1}{\sqrt{6}}(\bar{2},0,\bar{4})$	$\frac{1}{\sqrt{6}}(0,2,\bar{4})$

Table A-3.4.1 (Continued)

Mode	$\left(\frac{\partial \vec{\mathbf{u}}_3}{\partial t}\right)_{t=0}$	$\left(\frac{\partial \vec{\mathbf{v}}_{13}}{\partial t}\right)_{t=0}$	$\left(\frac{\partial \vec{\mathbf{v}}_{23}}{\partial t}\right)_{t=0}$	$\left(\frac{\partial \vec{\mathbf{v}}_{33}}{\partial t}\right)_{t=0}$
Mode 1	$\frac{1}{\sqrt{3}}(\bar{1}, 1, \bar{1})$	$\frac{1}{\sqrt{3}}(\bar{1}, 1, \bar{1})$	$\frac{1}{\sqrt{3}}(\bar{1}, 1, \bar{1})$	$\frac{1}{\sqrt{3}}(\bar{1}, 1, \bar{1})$
Mode 2	0	0	0	0
Mode 3	$\frac{1}{\sqrt{3}}(1, \bar{1}, 1)$	$\frac{1}{\sqrt{3}}(1, \bar{1}, 1)$	$\frac{1}{\sqrt{3}}(1, \bar{1}, 1)$	$\frac{1}{\sqrt{3}}(1, \bar{1}, 1)$
Mode 4	$\frac{r_0}{2\sqrt{3}}(1, 1, 0)$	$\frac{r_0}{\sqrt{3}}(1, 0, 0)$	$\frac{r_0}{\sqrt{3}}(0, 1, 0)$	$\frac{r_0}{\sqrt{3}}(1, 1, 0)$
Mode 5	$\frac{r_0}{\sqrt{6}}(\bar{1}, 1, 2)$	$\frac{r_0\sqrt{2}}{\sqrt{3}}(\bar{1}, 1, 1)$	$\frac{r_0\sqrt{2}}{\sqrt{3}}(\bar{1}, 1, 1)$	$\frac{r_0\sqrt{2}}{\sqrt{3}}(0, 0, 2)$
Mode 6	0	0	0	0
Mode 7	$\frac{r_0}{\sqrt{6}}(1, \bar{1}, \bar{2})$	$\frac{r_0\sqrt{2}}{\sqrt{3}}(1, \bar{1}, \bar{1})$	$\frac{r_0\sqrt{2}}{\sqrt{3}}(1, \bar{1}, \bar{1})$	$\frac{r_0\sqrt{2}}{\sqrt{3}}(0, 0, \bar{2})$
Mode 10	$\frac{1}{\sqrt{3}}(2, \bar{2}, \bar{1})$	$\frac{1}{\sqrt{3}}(3, \bar{3}, \bar{1})$	$\frac{1}{\sqrt{3}}(3, \bar{3}, \bar{1})$	$\frac{1}{\sqrt{3}}(1, \bar{1}, \bar{3})$
Mode 11	$\frac{1}{\sqrt{3}}(0, 0, 3)$	$\frac{1}{\sqrt{3}}(\bar{1}, 1, 3)$	$\frac{1}{\sqrt{3}}(\bar{1}, 1, 3)$	$\frac{1}{\sqrt{3}}(1, \bar{1}, 5)$
Mode 12	$\frac{1}{\sqrt{3}}(\bar{2}, 2, 1)$	$\frac{1}{\sqrt{3}}(\bar{3}, 3, 1)$	$\frac{1}{\sqrt{3}}(\bar{3}, 3, 1)$	$\frac{1}{\sqrt{3}}(\bar{1}, 1, 3)$
Mode 13	$\frac{1}{\sqrt{3}}(0, 0, \bar{3})$	$\frac{1}{\sqrt{3}}(1, \bar{1}, \bar{3})$	$\frac{1}{\sqrt{3}}(1, \bar{1}, \bar{3})$	$\frac{1}{\sqrt{3}}(\bar{1}, 1, \bar{5})$
Mode 14	$\frac{1}{4\sqrt{3}}(5, \bar{5}, 2)$	$\frac{1}{2\sqrt{3}}(3, \bar{3}, 1)$	$\frac{1}{2\sqrt{3}}(3, \bar{3}, 1)$	$\frac{1}{\sqrt{3}}(1, \bar{1}, 0)$
Mode 15	$\frac{1}{4\sqrt{3}}(3, \bar{3}, 6)$	$\frac{1}{2\sqrt{3}}(1, \bar{1}, 3)$	$\frac{1}{2\sqrt{3}}(1, \bar{1}, 3)$	$\frac{1}{\sqrt{3}}(1, \bar{1}, 2)$
Mode 16	0	$\frac{1}{\sqrt{6}}(2, \bar{1}, 1)$	$\frac{1}{\sqrt{6}}(1, \bar{2}, 1)$	$\frac{1}{\sqrt{6}}(1, \bar{1}, 2)$
Mode 17	$\frac{1}{\sqrt{3}}(0, 0, \bar{1})$	$\frac{1}{\sqrt{3}}(0, 0, \bar{1})$	$\frac{1}{\sqrt{3}}(0, 0, \bar{1})$	$\frac{1}{\sqrt{3}}(0, 0, \bar{1})$
Mode 18	0	$\frac{1}{\sqrt{6}}(\bar{2}, 1, \bar{1})$	$\frac{1}{\sqrt{6}}(\bar{1}, 2, \bar{1})$	$\frac{1}{\sqrt{6}}(\bar{1}, 1, \bar{2})$
Mode 19	$\frac{1}{\sqrt{3}}(0, 0, 1)$	$\frac{1}{\sqrt{3}}(0, 0, 1)$	$\frac{1}{\sqrt{3}}(0, 0, 1)$	$\frac{1}{\sqrt{3}}(0, 0, 1)$
Mode 20	$\frac{1}{\sqrt{6}}(\bar{1}, 1, 2)$	$\frac{1}{\sqrt{6}}(0, 2, 4)$	$\frac{1}{\sqrt{6}}(\bar{2}, 0, 4)$	$\frac{1}{\sqrt{6}}(\bar{2}, 2, 0)$
Mode 21	$\frac{1}{\sqrt{6}}(1, \bar{1}, \bar{2})$	$\frac{1}{\sqrt{6}}(0, \bar{2}, \bar{4})$	$\frac{1}{\sqrt{6}}(2, 0, \bar{4})$	$\frac{1}{\sqrt{6}}(2, \bar{2}, 0)$

Table A-3.4.1 (Continued)

Mode	$\left(\frac{\partial \vec{\mathbf{u}}_4}{\partial t}\right)_{t=0}$	$\left(\frac{\partial \vec{\mathbf{v}}_{14}}{\partial t}\right)_{t=0}$	$\left(\frac{\partial \vec{\mathbf{v}}_{24}}{\partial t}\right)_{t=0}$	$\left(\frac{\partial \vec{\mathbf{v}}_{34}}{\partial t}\right)_{t=0}$
Mode 1	$\frac{1}{\sqrt{3}}(\bar{1},\bar{1},1)$	$\frac{1}{\sqrt{3}}(\bar{1},\bar{1},1)$	$\frac{1}{\sqrt{3}}(\bar{1},\bar{1},1)$	$\frac{1}{\sqrt{3}}(\bar{1},\bar{1},1)$
Mode 2	$\frac{1}{\sqrt{3}}(\bar{1},\bar{1},1)$	$\frac{1}{\sqrt{3}}(\bar{1},\bar{1},1)$	$\frac{1}{\sqrt{3}}(\bar{1},\bar{1},1)$	$\frac{1}{\sqrt{3}}(\bar{1},\bar{1},1)$
Mode 3	$\frac{1}{\sqrt{3}}(\bar{1},\bar{1},1)$	$\frac{1}{\sqrt{3}}(\bar{1},\bar{1},1)$	$\frac{1}{\sqrt{3}}(\bar{1},\bar{1},1)$	$\frac{1}{\sqrt{3}}(\bar{1},\bar{1},1)$
Mode 4	$\frac{r_0}{2\sqrt{3}}(1,\bar{1},0)$	$\frac{r_0}{\sqrt{3}}(1,\bar{1},0)$	$\frac{r_0}{\sqrt{3}}(0,\bar{1},0)$	$\frac{r_0}{\sqrt{3}}(1,0,0)$
Mode 5	$\frac{r_0}{\sqrt{6}}(\bar{1},\bar{1},\bar{2})$	$\frac{r_0\sqrt{2}}{\sqrt{3}}(0,0,\bar{2})$	$\frac{r_0\sqrt{2}}{\sqrt{3}}(\bar{1},\bar{1},\bar{1})$	$\frac{r_0\sqrt{2}}{\sqrt{3}}(\bar{1},\bar{1},\bar{1})$
Mode 6	$\frac{r_0}{\sqrt{6}}(\bar{1},\bar{1},\bar{2})$	$\frac{r_0\sqrt{2}}{\sqrt{3}}(0,0,\bar{2})$	$\frac{r_0\sqrt{2}}{\sqrt{3}}(\bar{1},\bar{1},\bar{1})$	$\frac{r_0\sqrt{2}}{\sqrt{3}}(\bar{1},\bar{1},\bar{1})$
Mode 7	$\frac{r_0}{\sqrt{6}}(\bar{1},\bar{1},\bar{2})$	$\frac{r_0\sqrt{2}}{\sqrt{3}}(0,0,\bar{2})$	$\frac{r_0\sqrt{2}}{\sqrt{3}}(\bar{1},\bar{1},\bar{1})$	$\frac{r_0\sqrt{2}}{\sqrt{3}}(\bar{1},\bar{1},\bar{1})$
Mode 10	$\frac{1}{\sqrt{3}}(\bar{2},\bar{2},\bar{1})$	$\frac{1}{\sqrt{3}}(\bar{1},\bar{1},\bar{3})$	$\frac{1}{\sqrt{3}}(\bar{3},\bar{3},\bar{1})$	$\frac{1}{\sqrt{3}}(\bar{3},\bar{3},\bar{1})$
Mode 11	$\frac{1}{\sqrt{3}}(0,0,3)$	$\frac{1}{\sqrt{3}}(\bar{1},\bar{1},5)$	$\frac{1}{\sqrt{3}}(1,1,3)$	$\frac{1}{\sqrt{3}}(1,1,3)$
Mode 12	$\frac{1}{\sqrt{3}}(\bar{2},\bar{2},\bar{1})$	$\frac{1}{\sqrt{3}}(\bar{1},\bar{1},\bar{3})$	$\frac{1}{\sqrt{3}}(\bar{3},\bar{3},\bar{1})$	$\frac{1}{\sqrt{3}}(\bar{3},\bar{3},\bar{1})$
Mode 13	$\frac{1}{\sqrt{3}}(0,0,3)$	$\frac{1}{\sqrt{3}}(\bar{1},\bar{1},5)$	$\frac{1}{\sqrt{3}}(1,1,3)$	$\frac{1}{\sqrt{3}}(1,1,3)$
Mode 14	$\frac{1}{4\sqrt{3}}(\bar{5},\bar{5},2)$	$\frac{1}{\sqrt{3}}(\bar{1},\bar{1},0)$	$\frac{1}{2\sqrt{3}}(\bar{3},\bar{3},1)$	$\frac{1}{2\sqrt{3}}(\bar{3},\bar{3},1)$
Mode 15	$\frac{1}{4\sqrt{3}}(\bar{3},\bar{3},6)$	$\frac{1}{\sqrt{3}}(\bar{1},\bar{1},2)$	$\frac{1}{2\sqrt{3}}(\bar{1},\bar{1},3)$	$\frac{1}{2\sqrt{3}}(\bar{1},\bar{1},3)$
Mode 16	0	$\frac{1}{\sqrt{6}}(1,1,\bar{2})$	$\frac{1}{\sqrt{6}}(1,2,\bar{1})$	$\frac{1}{\sqrt{6}}(2,1,\bar{1})$
Mode 17	$\frac{1}{\sqrt{3}}(0,0,1)$	$\frac{1}{\sqrt{3}}(0,0,1)$	$\frac{1}{\sqrt{3}}(0,0,1)$	$\frac{1}{\sqrt{3}}(0,0,1)$
Mode 18	0	$\frac{1}{\sqrt{6}}(1,1,\bar{2})$	$\frac{1}{\sqrt{6}}(1,2,\bar{1})$	$\frac{1}{\sqrt{6}}(2,1,\bar{1})$
Mode 19	$\frac{1}{\sqrt{3}}(0,0,1)$	$\frac{1}{\sqrt{3}}(0,0,1)$	$\frac{1}{\sqrt{3}}(0,0,1)$	$\frac{1}{\sqrt{3}}(0,0,1)$
Mode 20	$\frac{1}{\sqrt{6}}(\bar{1},\bar{1},\bar{2})$	$\frac{1}{\sqrt{6}}(\bar{2},\bar{2},0)$	$\frac{1}{\sqrt{6}}(\bar{2},0,\bar{4})$	$\frac{1}{\sqrt{6}}(0,\bar{2},\bar{4})$
Mode 21	$\frac{1}{\sqrt{6}}(\bar{1},\bar{1},\bar{2})$	$\frac{1}{\sqrt{6}}(\bar{2},\bar{2},0)$	$\frac{1}{\sqrt{6}}(\bar{2},0,\bar{4})$	$\frac{1}{\sqrt{6}}(0,\bar{2},\bar{4})$

It is now left to find the five hidden variables $\vec{w}_0, \ldots, \vec{w}_4$ which are the internal rotations of the coordinate systems associated with the five silicon atoms. First we have to find the torque on the local coordinate system at any one of the five silicon atoms. This was done before for the central silicon, since it is surrounded only by other silicon atoms. By (A-3.3-7),

$$\vec{w}_0 = \sum_{j=1}^{4} \left[\frac{1}{4A^{(\mathrm{Si\cdot Si})}a} D_j \vec{u}_j + \frac{B}{8A^{(\mathrm{Si\cdot Si})}} \mathcal{E}_j \vec{w}_j \right]. \qquad (A-3.4.1)$$

For any one of the other silicon atoms, there are different expressions for the torque applied by the central silicon atom and by the three hydrogen atoms:

$$\vec{\tau}^{(0j)} = \beta^{(\mathrm{Si\cdot Si})} \left[\frac{\vec{r}_j \times \vec{u}_j}{2} - A^{(\mathrm{Si\cdot Si})} \vec{r}_j \times (\vec{w}_j \times \vec{r}_j) - B \vec{r}_j \times (\vec{w}_0 \times \vec{r}_j) \right] \qquad (A-3.4.2)$$

$$\begin{aligned} \vec{\tau}^{(ij)} &= \beta^{(\mathrm{Si\cdot H})} \left[\frac{g\vec{r}_{ji} \times (\vec{v}_{ij} - \vec{u}_j)}{2} - A^{(\mathrm{Si\cdot H})} \vec{r}_{ji} \times (\vec{w}_j \times \vec{r}_{ji}) \right] \\ &= \beta^{(\mathrm{Si\cdot H})} \left[\frac{g\vec{r}_k \times (\vec{u}_j - \vec{v}_{ij})}{2} - A^{(\mathrm{Si\cdot H})} \vec{r}_k \times (\vec{w}_j \times \vec{r}_k) \right] \end{aligned} \qquad (A-3.4.3)$$

Therefore, summing (A-3.4.3) over the four nearest neighbors of the j-th silicon atom with $k \equiv i + j (\mathrm{mod}\ 4)$, we obtain

$$\begin{aligned} &(\beta^{(\mathrm{Si\cdot Si})} - g\beta^{(\mathrm{Si\cdot H})}) \frac{\vec{r}_j \times \vec{u}_j}{2} - g\beta^{(\mathrm{Si\cdot H})} \sum_{i=1}^{3} \frac{\vec{r}_k \times \vec{v}_{ij}}{2} \\ &\quad + (\beta^{(\mathrm{Si\cdot Si})} A^{(\mathrm{Si\cdot Si})} - \beta^{(\mathrm{Si\cdot H})} A^{(\mathrm{Si\cdot H})}) \vec{r}_j \times (\vec{r}_j \times \vec{w}_j) \\ &\quad + \beta^{(\mathrm{Si\cdot H})} A^{(\mathrm{Si\cdot H})} \sum_{1}^{4} \vec{r}_k \times (\vec{r}_k \times \vec{w}_j) + \beta^{(\mathrm{Si\cdot Si})} B \vec{r}_j \times (\vec{r}_j \times \vec{w}_0) = 0, \end{aligned}$$

or equivalently, using matrices to express cross product, and dividing by a,

$$\begin{aligned} &\frac{(\beta^{(\mathrm{Si\cdot Si})} A^{(\mathrm{Si\cdot Si})} - \beta^{(\mathrm{Si\cdot H})} A^{(\mathrm{Si\cdot H})})}{16} \mathcal{E}_j \vec{w}_j - \frac{\beta^{(\mathrm{Si\cdot H})} A^{(\mathrm{Si\cdot H})}}{2} \vec{w}_j + \frac{\beta^{(\mathrm{Si\cdot Si})} B}{16} \mathcal{E}_j \vec{w}_0 \\ &\quad = \frac{g\beta^{(\mathrm{Si\cdot H})}}{8a} \sum_{i=1}^{3} D_k \vec{v}_{ij} + \frac{g\beta^{(\mathrm{Si\cdot H})} - \beta^{(\mathrm{Si\cdot Si})}}{8a} D_j \vec{u}_j. \end{aligned} \qquad (A-3.4.4)$$

Here

$$\mathcal{D}_1 = \begin{pmatrix} 0 & -1 & +1 \\ +1 & 0 & -1 \\ -1 & +1 & 0 \end{pmatrix}, \quad \mathcal{D}_2 = \begin{pmatrix} 0 & +1 & -1 \\ -1 & 0 & -1 \\ +1 & +1 & 0 \end{pmatrix}, \quad \mathcal{D}_3 = \begin{pmatrix} 0 & +1 & +1 \\ -1 & 0 & +1 \\ -1 & -1 & 0 \end{pmatrix}, \quad \mathcal{D}_4 = \begin{pmatrix} 0 & -1 & -1 \\ +1 & 0 & +1 \\ +1 & -1 & 0 \end{pmatrix},$$

and

$$\mathcal{E}_1 = \begin{pmatrix} -2 & +1 & +1 \\ +1 & -2 & +1 \\ +1 & +1 & -2 \end{pmatrix}, \quad \mathcal{E}_2 = \begin{pmatrix} -2 & -1 & -1 \\ -1 & -2 & +1 \\ -1 & +1 & -2 \end{pmatrix}, \quad \mathcal{E}_3 = \begin{pmatrix} -2 & -1 & +1 \\ -1 & -2 & -1 \\ +1 & -1 & -2 \end{pmatrix}, \quad \mathcal{E}_4 = \begin{pmatrix} -2 & +1 & -1 \\ +1 & -2 & -1 \\ -1 & -1 & -2 \end{pmatrix},$$

and for a general vector $\vec{\mathbf{u}}$,

$$\vec{\mathbf{r}}_j \times \vec{\mathbf{u}} = \frac{a}{4}\mathcal{D}_j\vec{\mathbf{u}}, \qquad \vec{\mathbf{r}}_j \times (\vec{\mathbf{u}} \times \vec{\mathbf{r}}_j) = -\frac{a^2}{16}\mathcal{E}_j\vec{\mathbf{u}}, \qquad \mathcal{E}_j = \mathcal{D}_j^2.$$

One should notice that the four adjustable parameters $A^{(\mathrm{Si\cdot Si})}$, $A^{(\mathrm{Si\cdot H})}$, B and g are not independent, and that the equations $(A-3.4.2)$, $(A-3.4.3)$ and $(A-3.4.4)$ are not written in a rotationally invariant form. To have them in that form, we rotate the equilibrium cluster by an angle $\vec{\mathbf{w}}$ about the origin, and impose the condition that the resulting torque will vanish. Then,

$$\vec{\mathbf{u}}_j = \vec{\mathbf{w}} \times \vec{\mathbf{r}}_j, \qquad \vec{\mathbf{v}}_{ij} = \vec{\mathbf{w}} \times (\vec{\mathbf{r}}_j - \vec{\mathbf{r}}_k) \qquad (A-3.4.5)$$

and from $(A-3.4.2)$, $(A-3.4.3)$ and $(A-3.4.5)$ one obtains

$$A^{(\mathrm{Si\cdot Si})} + B = \frac{1}{2}, \qquad A^{(\mathrm{Si\cdot H})} = \frac{g}{2}. \qquad (A-3.4.6)$$

Equations $(A-3.4.2)$ and $(A-3.4.3)$ are rotationally invariant once the conditions $(A-3.4.6)$ are imposed.

One can further solve (A-3.4.1) and (A-3.4.4), to obtain $\vec{\mathbf{w}}_j$ in terms of $\vec{\mathbf{u}}_j$ and $\vec{\mathbf{v}}_{ij}$. However, to do this, we have to introduce some notation. We define the matrices $\mathcal{F}_j = \mathcal{F}_j(x, y)$ to be

$$\mathcal{F}_1 = \begin{pmatrix} x & y & y \\ y & x & y \\ y & y & x \end{pmatrix} \quad \mathcal{F}_2 = \begin{pmatrix} x & -y & -y \\ -y & x & y \\ -y & y & x \end{pmatrix} \quad \mathcal{F}_3 = \begin{pmatrix} x & -y & y \\ -y & x & -y \\ y & -y & x \end{pmatrix} \quad \mathcal{F}_4 = \begin{pmatrix} x & y & -y \\ y & x & -y \\ -y & -y & x \end{pmatrix}$$

These matrices play an important role in the following calculations. They have some useful properties. First, for any given $j = 1, \ldots, 4$ the matrices $\mathcal{F}_j(x, y)$ with real x and y form a commutative group with the following multiplication rule:

$$\mathcal{F}_j(x_1, y_1)\mathcal{F}_j(x_2, y_2) = \mathcal{F}_j(x_3, y_3)$$

with

$$x_3 = x_1 x_2 + 2y_1 y_2, \qquad y_3 = x_1 y_2 + y_1 x_2 + y_1 y_2.$$

Therefore,

$$\mathcal{F}_j^{-1}(x, y) = \mathcal{F}_j\left(\frac{x + y}{(x - y)(x + 2y)}, \frac{-y}{(x - y)(x + 2y)}\right).$$

Another property of the matrices $\mathcal{F}_j(x, y)$ is

$$\mathcal{F}_j(x, y)\mathcal{D}_j = (x - y)\mathcal{D}_j, \qquad \mathcal{F}_j(x, y)\mathcal{E}_j = (x - y)\mathcal{E}_j.$$

Now we can write (A-3.4.4) as

$$\begin{aligned} &\mathcal{F}_j\left(\frac{-\gamma_1 - 3\gamma_2}{8}, \frac{\gamma_1 - \gamma_2}{16}\right)\vec{\mathfrak{w}}_j + \frac{\beta^{(\mathrm{Si\cdot Si})}B}{16}\mathcal{E}_j\vec{\mathfrak{w}}_0 \\ &\quad = \frac{g\beta^{(\mathrm{Si\cdot H})}}{8a}\sum_{i=1}^{3}\mathcal{D}_k\vec{\mathfrak{v}}_{ij} + \frac{g\beta^{(\mathrm{Si\cdot H})} - \beta^{(\mathrm{Si\cdot Si})}}{8a}\mathcal{D}_j\vec{\mathfrak{u}}_j \end{aligned} \qquad (A - 3.4.7)$$

where

$$\gamma_1 = \beta^{(\mathrm{Si\cdot Si})}A^{(\mathrm{Si\cdot Si})}, \qquad \gamma_2 = \beta^{(\mathrm{Si\cdot H})}A^{(\mathrm{Si\cdot H})}. \qquad (A - 3.4.8)$$

Now we multiply (A-3.4.7) by

$$\mathcal{F}_j^{-1}\left(\frac{-\gamma_1 - 3\gamma_2}{8}, \frac{\gamma_1 - \gamma_2}{16}\right) = \frac{-2}{\gamma_2(3\gamma_1 + 5\gamma_2)}\mathcal{F}_j(\gamma_1 + 7\gamma_2, \gamma_1 - \gamma_2)$$

to obtain

$$\vec{\mathbf{w}}_j = \frac{\beta^{(\mathrm{Si\cdot Si})}B}{3\gamma_1+5\gamma_2}\mathcal{E}_j\vec{\mathbf{w}}_0 - \frac{g\beta^{(\mathrm{Si\cdot H})}}{4a\gamma_2(3\gamma_1+5\gamma_2)}\sum_{i=1}^{3}\mathcal{F}_j(\gamma_1+7\gamma_2,\gamma_1-\gamma_2)\mathcal{D}_k\vec{\mathbf{v}}_{ij} - \frac{2g\beta^{(\mathrm{Si\cdot H})}-2\beta^{(\mathrm{Si\cdot Si})}}{a(3\gamma_1+5\gamma_2)}\mathcal{D}_j\vec{\mathbf{u}}_j$$

or

$$\mathcal{E}_j\vec{\mathbf{w}}_j = -\frac{3\beta^{(\mathrm{Si\cdot Si})}B}{3\gamma_1+5\gamma_2}\mathcal{E}_j\vec{\mathbf{w}}_0 - \frac{2g\beta^{(\mathrm{Si\cdot H})}}{a(3\gamma_1+5\gamma_2)}\sum_{i=1}^{3}\mathcal{E}_j\mathcal{D}_k\vec{\mathbf{v}}_{ij} + 6\frac{g\beta^{(\mathrm{Si\cdot H})}-\beta^{(\mathrm{Si\cdot Si})}}{a(3\gamma_1+5\gamma_2)}\mathcal{D}_j\vec{\mathbf{u}}_j.$$

Now we sum it from j=1 to j=4:

$$\sum_{j=1}^{4}\mathcal{E}_j\vec{\mathbf{w}}_j = \frac{24\beta^{(\mathrm{Si\cdot Si})}B}{3\gamma_1+5\gamma_2}\vec{\mathbf{w}}_0 - \frac{2g\beta^{(\mathrm{Si\cdot H})}}{a(3\gamma_1+5\gamma_2)}\sum_{j=1}^{4}\sum_{i=1}^{3}\mathcal{E}_j\mathcal{D}_k\vec{\mathbf{v}}_{ij} + 6\frac{g\beta^{(\mathrm{Si\cdot H})}-\beta^{(\mathrm{Si\cdot Si})}}{a(3\gamma_1+5\gamma_2)}\sum_{j=1}^{4}\mathcal{D}_j\vec{\mathbf{u}}_j.$$

This can be inserted back into (A-3.4.1) to obtain $\vec{\mathbf{w}}_0$:

$$\vec{\mathbf{w}}_0 = \lambda_1\sum_{j=1}^{4}\mathcal{D}_j\vec{\mathbf{u}}_j + \lambda_2\sum_{j=1}^{4}\sum_{i=1}^{3}\mathcal{E}_j\mathcal{D}_{\mathrm{i+j\ (mod\ 4)}}\vec{\mathbf{v}}_{ij}$$

where

$$\lambda_1 = \frac{1}{4a}\left(\frac{\beta^{(\mathrm{Si\cdot Si})}(3A^{(\mathrm{Si\cdot Si})}-3B)+\beta^{(\mathrm{Si\cdot H})}(5A^{(\mathrm{Si\cdot H})}+3gB)}{\beta^{(\mathrm{Si\cdot Si})}(3(A^{(\mathrm{Si\cdot Si})})^2-3B^2)+\beta^{(\mathrm{Si\cdot H})}\cdot 5A^{(\mathrm{Si\cdot Si})}A^{(\mathrm{Si\cdot H})}}\right)$$

$$\lambda_2 = -\frac{1}{4a}\left(\frac{g\beta^{(\mathrm{Si\cdot H})}B}{\beta^{(\mathrm{Si\cdot Si})}(3(A^{(\mathrm{Si\cdot Si})})^2-3B^2)+\beta^{(\mathrm{Si\cdot H})}\cdot 5A^{(\mathrm{Si\cdot Si})}A^{(\mathrm{Si\cdot H})}}\right).$$

Now we can write all the non-central restoring forces acting on the atoms of the cluster. We use the expressions for the forces acting on the four non-central silicon atoms (labeled by j) and the twelve hydrogen atoms (labeled by ij), ($1\leq i\leq 3$),

$(1 \leq j \leq 4)$; k always means i+j (mod 4).

$$\vec{\mathbf{F}}_{nc}^{(j)} = \beta^{(\mathrm{Si\cdot Si})}\left[-\vec{\mathbf{u}}_j + \left(\frac{\vec{\mathbf{u}}_j \cdot \vec{\mathbf{r}}_j}{|\vec{\mathbf{r}}_j|}\right)\frac{\vec{\mathbf{r}}_j}{|\vec{\mathbf{r}}_j|} - \frac{\vec{\mathbf{r}}_j \times (\vec{\mathbf{w}}_0 + \vec{\mathbf{w}}_j)}{2}\right] + \beta^{(\mathrm{Si\cdot H})}\sum_{i=1}^{3}\left[\vec{\mathbf{v}}_{ij} - \vec{\mathbf{u}}_j - \left(\frac{(\vec{\mathbf{v}}_{ij} - \vec{\mathbf{u}}_j)\cdot \vec{\mathbf{r}}_k}{|\vec{\mathbf{r}}_k|}\right)\frac{\vec{\mathbf{r}}_k}{|\vec{\mathbf{r}}_k|} - \frac{\vec{\mathbf{r}}_k \times \vec{\mathbf{w}}_j}{2}\right]$$

But

$$\sum_{k=1}^{4}\left(\frac{\vec{\mathbf{u}}\cdot\vec{\mathbf{r}}_k}{|\vec{\mathbf{r}}_k|}\right)\frac{\vec{\mathbf{r}}_k}{|\vec{\mathbf{r}}_k|} = \frac{4}{3}\vec{\mathbf{u}}, \qquad \sum_{k=1}^{4}\left(\frac{\vec{\mathbf{r}}_k\cdot\vec{\mathbf{u}}}{2}\right) = 0,$$

or

$$\sum_{i=1}^{3}\left(\frac{\vec{\mathbf{u}}\cdot\vec{\mathbf{r}}_k}{|\vec{\mathbf{r}}_k|}\right)\frac{\vec{\mathbf{r}}_k}{|\vec{\mathbf{r}}_k|} = \frac{4}{3}\vec{\mathbf{u}} - \left(\frac{\vec{\mathbf{u}}\cdot\vec{\mathbf{r}}_j}{|\vec{\mathbf{r}}_j|}\right)\frac{\vec{\mathbf{r}}_j}{|\vec{\mathbf{r}}_j|}, \qquad \sum_{i=1}^{3}\left(\frac{\vec{\mathbf{r}}_k\times\vec{\mathbf{u}}}{2}\right) = -\left(\frac{\vec{\mathbf{r}}_j\times\vec{\mathbf{u}}}{2}\right).$$

Therefore,

$$\begin{aligned}\vec{\mathbf{F}}_{nc}^{(j)} &= \beta^{(\mathrm{Si\cdot Si})}\left[-\vec{\mathbf{u}}_j + \left(\frac{\vec{\mathbf{u}}_j\cdot\vec{\mathbf{r}}_j}{|\vec{\mathbf{r}}_j|}\right)\frac{\vec{\mathbf{r}}_j}{|\vec{\mathbf{r}}_j|} - \frac{\vec{\mathbf{r}}_j\times(\vec{\mathbf{w}}_0+\vec{\mathbf{w}}_j)}{2}\right] \\ &\quad + \beta^{(\mathrm{Si\cdot H})}\left[-\frac{5}{3}\vec{\mathbf{u}}_j - \left(\frac{\vec{\mathbf{u}}_j\cdot\vec{\mathbf{r}}_j}{|\vec{\mathbf{r}}_j|}\right)\frac{\vec{\mathbf{r}}_j}{|\vec{\mathbf{r}}_j|} + \frac{\vec{\mathbf{r}}_j\times\vec{\mathbf{w}}_j}{2}\right] \\ &\quad + \beta^{(\mathrm{Si\cdot H})}\sum_{i=1}^{3}\left[\vec{\mathbf{v}}_{ij} - \left(\frac{\vec{\mathbf{v}}_{ij}\cdot\vec{\mathbf{r}}_k}{|\vec{\mathbf{r}}_k|}\right)\frac{\vec{\mathbf{r}}_k}{|\vec{\mathbf{r}}_k|}\right] \\ &= \beta^{(\mathrm{Si\cdot Si})}\left[-\vec{\mathbf{u}}_j + \frac{1}{3}B_j\vec{\mathbf{u}}_j - \frac{a}{8}D_j\vec{\mathbf{w}}_0 - \frac{a}{8}D_j\vec{\mathbf{w}}_j\right] \\ &\quad + \beta^{(\mathrm{Si\cdot H})}\left(-\frac{5}{3}\vec{\mathbf{u}}_j - \frac{1}{3}B_j\vec{\mathbf{u}}_j + \frac{a}{8}D_j\vec{\mathbf{w}}_j\right) \\ &\quad + \beta^{(\mathrm{Si\cdot H})}\sum_{i=1}^{3}\left(\vec{\mathbf{v}}_{ij} - \frac{1}{3}B_k\vec{\mathbf{v}}_{ij}\right)\end{aligned}$$

Here,

$$B_1 = \begin{pmatrix} +1 & +1 & +1 \\ +1 & +1 & +1 \\ +1 & +1 & +1 \end{pmatrix}, \quad B_2 = \begin{pmatrix} +1 & -1 & -1 \\ -1 & +1 & +1 \\ -1 & +1 & +1 \end{pmatrix}, \quad B_3 = \begin{pmatrix} +1 & -1 & +1 \\ -1 & +1 & -1 \\ +1 & -1 & +1 \end{pmatrix}, \quad B_4 = \begin{pmatrix} +1 & +1 & -1 \\ +1 & +1 & -1 \\ -1 & -1 & +1 \end{pmatrix},$$

and

$$\left(\frac{\vec{\mathbf{u}}\cdot\vec{\mathbf{r}}_j}{|\vec{\mathbf{r}}_j|}\right)\frac{\vec{\mathbf{r}}_j}{|\vec{\mathbf{r}}_j|} = \frac{1}{3}B_j\vec{\mathbf{u}}.$$

However,

$$D_j\vec{\mathbf{w}}_j = \frac{-3\beta^{(\mathrm{Si\cdot Si})}B}{3\gamma_1+5\gamma_2}D_j\vec{\mathbf{w}}_0 - \frac{2g\beta^{(\mathrm{Si\cdot H})}}{a(3\gamma_1+5\gamma_2)}\sum_{i=1}^{3}D_jD_k\vec{\mathbf{v}}_{ij} - \frac{2g\beta^{(\mathrm{Si\cdot H})}-2\beta^{(\mathrm{Si\cdot Si})}}{a(3\gamma_1+5\gamma_2)}\mathcal{E}_j\vec{\mathbf{u}}_j,$$

and for all the modes described in this chapter,

$$\sum_{j=1}^{4}D_j\vec{\mathbf{u}}_j = 0, \qquad \sum_{j=1}^{4}\sum_{i=1}^{3}D_jD_k\vec{\mathbf{v}}_{ij} = 0.$$

Therefore, we can write the non-central force acting on the j-th silicon atom:

$$\vec{\mathbf{F}}_{nc}^{(j)} = \beta^{(\mathrm{Si\cdot Si})}\left(\frac{1}{3}B_j-1\right)\vec{\mathbf{u}}_j + \beta^{(\mathrm{Si\cdot H})}\left[-\left(\frac{1}{3}B_j+\frac{5}{3}\right)\vec{\mathbf{u}}_j + \sum_{i=1}^{3}\left(1-\frac{1}{3}B_k\right)\vec{\mathbf{v}}_{ij}\right] + \mu_1\sum_{i=1}^{3}D_jD_k\vec{\mathbf{v}}_{ij} + \mu_2\mathcal{E}_j\vec{\mathbf{u}}_j$$

where

$$\mu_1 = \frac{g\beta^{(\mathrm{Si\cdot H})}(\beta^{(\mathrm{Si\cdot Si})}-\beta^{(\mathrm{Si\cdot H})})}{4(3\gamma_1+5\gamma_2)}, \qquad (A-3.4.9)$$

$$\mu_2 = \frac{(g\beta^{(\mathrm{Si\cdot H})}-\beta^{(\mathrm{Si\cdot Si})})(\beta^{(\mathrm{Si\cdot Si})}-\beta^{(\mathrm{Si\cdot H})})}{4(3\gamma_1+5\gamma_2)}, \qquad (A-3.4.10)$$

and γ_1, γ_2 are given by $(A-3.4.8)$. Similarly, we can write the non-central force acting on H_{ij}, this time due to only one neighbor, Si_j.

$$\vec{\mathbf{F}}_{nc}^{(ij)} = \beta^{(\mathrm{Si\cdot H})}\left[(\vec{\mathbf{u}}_j-\vec{\mathbf{v}}_{ij}) - \left(\frac{(\vec{\mathbf{u}}_j-\vec{\mathbf{v}}_{ij})\cdot\vec{\mathbf{r}}_k}{|\vec{\mathbf{r}}_k|}\right)\frac{\vec{\mathbf{r}}_k}{|\vec{\mathbf{r}}_k|} - \frac{\vec{\mathbf{w}}_j\times\vec{\mathbf{r}}_k}{2}\right]$$
$$= \beta^{(\mathrm{Si\cdot H})}\left[\left(1-\frac{1}{3}B_k\right)\vec{\mathbf{u}}_j - \left(1-\frac{1}{3}B_k\right)\vec{\mathbf{v}}_{ij} + \frac{a}{8}D_k\vec{\mathbf{w}}_j\right]$$

or

$$\vec{\mathbf{F}}_{nc}^{(ij)} = \beta^{(\mathrm{Si\cdot H})}\left[\left(1-\frac{1}{3}B_k\right)(\vec{\mathbf{u}}_j-\vec{\mathbf{v}}_{ij})\right] + \mu_3\sum_{l=1}^{3}D_jD_{\mathrm{j+1\ (mod\ 4)}}\vec{\mathbf{v}}_{lj} + \mu_4\mathcal{E}_j\vec{\mathbf{u}}_j,$$

where

$$\mu_3 = \frac{-g(\beta^{(\mathrm{Si\cdot H})})^2}{4(3\gamma_1 + 5\gamma_2)}, \qquad (A - 3.4.11)$$

$$\mu_4 = \frac{-\beta^{(\mathrm{Si\cdot H})}(g\beta^{(\mathrm{Si\cdot H})} - \beta^{(\mathrm{Si\cdot Si})})}{4(3\gamma_1 + 5\gamma_2)}. \qquad (A - 3.4.12)$$

The remaining central forces are obtained from simple geometric considerations. Their contributions to the spring constants of the various modes are listed in Table A-3.4.2, expressed as linear combinations in the parameters $\alpha_1^{(\mathrm{Si\cdot Si})}$, $\alpha_2^{(\mathrm{Si\cdot Si})}$, $\alpha_2^{(\mathrm{Si\cdot H})}$, $\alpha_2^{(\mathrm{H\cdot H})}(1)$ and $\alpha_2^{(\mathrm{H\cdot H})}(2)$. The expressions for the contributions of the non-central forces are much more complicated. Instead of expressing them as non-linear combinations in the parameters $\beta^{(\mathrm{Si\cdot Si})}$, $\beta^{(\mathrm{Si\cdot H})}$, $A^{(\mathrm{Si\cdot Si})}$ and $A^{(\mathrm{Si\cdot H})}$, we express them as linear combinations in the variables $\beta^{(\mathrm{Si\cdot Si})}$, $\beta^{(\mathrm{Si\cdot H})}$, μ_1, μ_2, μ_3 and μ_4. The expressions for $\mu_1, \ldots, \mu_4$ are given in $(A - 3.4.9 - 12)$.

TABLE A-3.4.2. Components of the central force contributions to the spring constants of the various modes.

Mode	$\alpha_1^{(Si\cdot Si)}$	$\alpha_2^{(Si\cdot Si)}$	$\alpha_2^{(Si\cdot H)}$	$\alpha_2^{(H\cdot H)}(1)$	$\alpha_2^{(H\cdot H)}(2)$
Mode 1	4	16	8	32	0
Mode 2	2	16/3	4	32/3	0
Mode 3	4	16/3	8	32/3	0
Mode 4	0	$\frac{2}{3}r_0^2$	0	$\frac{16}{3}r_0^2$	0
Mode 5	0	$4r_0^2$	0	$32r_0^2$	0
Mode 6	0	$\frac{5}{3}r_0^2$	0	$16r_0^2$	0
Mode 7	0	$\frac{8}{3}r_0^2$	0	$32r_0^2$	0
Mode 8	4	37.81	8	258.65	0
Mode 9	4	2.346	8	116.7	0
Mode 10	4	$\frac{64}{3}$	8	$\frac{352}{3}$	0
Mode 11	4	0	8	32	0
Mode 12	4	24	8	96	0
Mode 13	4	24	8	96	0
Mode 14	4	$\frac{25}{3}$	8	$\frac{76}{3}$	0
Mode 15	4	3	8	4	0
Mode 16	0	0	4	36	4
Mode 17	$\frac{4}{9}$	$\frac{8}{3}$	$\frac{4}{3}$	$\frac{16}{3}$	0
Mode 18	0	0	4	12	4
Mode 19	$\frac{4}{9}$	0	$\frac{4}{3}$	0	0
Mode 20	0	4	8	8	8
Mode 21	0	$\frac{8}{3}$	8	$\frac{88}{3}$	8
Mode 22	4	20	16	40	8
Mode 23	4	20	16	40	8

TABLE A-3.4.3. Components of the non-central force contributions to the spring constants of the various modes.

Mode	$\beta^{(Si\cdot Si)}$	$\beta^{(Si\cdot H)}$	μ_1	μ_2	μ_3	μ_4
Mode 1	0	0	0	0	0	0
Mode 2	0	0	0	0	0	0
Mode 3	0	0	0	0	0	0
Mode 4	$\frac{2}{3}r_0^2$	$2r_0^2$	$\frac{-16}{3}r_0^2$	$2r_0^2$	$\frac{-64}{3}r_0^2$	$8r_0^2$
Mode 5	$4r_0^2$	$\frac{20}{3}r_0^2$	$-32r_0^2$	$12r_0^2$	$-128r_0^2$	$48r_0^2$
Mode 6	$2r_0^2$	$\frac{10}{3}r_0^2$	$-16r_0^2$	$6r_0^2$	$-64r_0^2$	$24r_0^2$
Mode 7	$4r_0^2$	$\frac{20}{3}r_0^2$	$-32r_0^2$	$12r_0^2$	$-128r_0^2$	$48r_0^2$
Mode 8	$4r_0^2$	$\frac{20}{3}r_0^2$	$-32r_0^2$	$12r_0^2$	$-128r_0^2$	$48r_0^2$
Mode 9	$4r_0^2$	$\frac{20}{3}r_0^2$	$-32r_0^2$	$12r_0^2$	$-128r_0^2$	$48r_0^2$
Mode 10	8	$\frac{40}{3}$	-64	24	-256	96
Mode 11	8	$\frac{40}{3}$	-64	24	-256	96
Mode 12	8	$\frac{40}{3}$	-64	24	-256	96
Mode 13	8	$\frac{40}{3}$	-64	24	-256	96
Mode 14	$\frac{1}{2}$	$\frac{5}{6}$	-4	$\frac{3}{2}$	-16	6
Mode 15	$\frac{1}{2}$	$\frac{5}{6}$	-4	$\frac{3}{2}$	-16	6
Mode 16	0	12	0	0	0	0
Mode 17	$\frac{8}{9}$	0	$\frac{-8}{3}$	$\frac{8}{3}$	-8	8
Mode 18	0	12	0	0	0	0
Mode 19	$\frac{8}{9}$	0	$\frac{-8}{3}$	$\frac{8}{3}$	-8	8
Mode 20	4	12	0	12	0	48
Mode 21	4	12	0	12	0	48
Mode 22	4	12	0	12	0	48
Mode 23	4	12	0	12	0	48

Fitting the parameters of this model to the cluster calculations is somewhat more complicated than it was for the other models, since the expressions relating the spring constants to the parameters are nonlinear. Moreover, some of the parameters of the model have to be in a certain range to obey stability conditions. In particular, we must have

$$\frac{1}{4} \leq A^{(\mathrm{Si\cdot Si})} \leq \frac{1}{2}, \qquad 0 \leq A^{(\mathrm{Si\cdot H})}. \tag{$A-3.4.13$}$$

The best fit under these conditions is obtained when

$$\beta^{(\mathrm{Si\cdot H})} = 0. \tag{$A-3.4.14$}$$

Substituting $(A-3.4.14)$ in $(A-3.4.9-12)$, we obtain

$$\mu_1 = 0, \quad \mu_2 = \frac{-\beta^{(\mathrm{Si\cdot Si})}}{12A^{(\mathrm{Si\cdot Si})}}, \quad \mu_3 = 0, \quad \mu_4 = 0.$$

Now the expressions defining the parameters of the model become a set of linear equations in the six parameters $\alpha_1^{(\mathrm{Si\cdot Si})}$, $\alpha_2^{(\mathrm{Si\cdot Si})}$, $\alpha_2^{(\mathrm{Si\cdot H})}$, $\alpha_2^{(\mathrm{H\cdot H})}(1)$, $\alpha_2^{(\mathrm{H\cdot H})}(2)$, and $\beta^{(\mathrm{Si\cdot Si})}(1 - A^{(\mathrm{Si\cdot Si})}/12)$. A regular least-squares fitting scheme can now be applied to extract the best values of these parameters. Unfortunately, there is no way to find the values of $\beta^{(\mathrm{Si\cdot Si})}$ and $A^{(\mathrm{Si\cdot Si})}$ separately using these 23 modes. The values of these parameters that best fit our cluster calculations are given in Table A–3.4.4.

TABLE A–3.4.4. Parameters of the Vasil'ev model fitted to the 23 ab-initio cluster calculations. All the parameters are given in units of $eV \cdot \mathring{A}^{-2}$.

	HF	GVB	R-CI	GVB-CI
$\alpha_1^{(Si\cdot Si)}$	11.35	9.99	12.19	12.33
$\alpha_2^{(Si\cdot Si)}$	0.68	0.41	0.44	0.35
$\alpha_2^{(Si\cdot H)}$	-0.57	0.08	-0.95	-0.95
$\alpha_2^{(H\cdot H)}(1)$	-0.03	-0.03	-0.03	-0.03
$\alpha_2^{(H\cdot H)}(2)$	1.99	1.36	2.39	2.37
$\beta^{(Si\cdot Si)}\left(1-\frac{1}{12A^{(Si\cdot Si)}}\right)$	0.38	0.44	0.38	0.38
$\alpha_1^{(Si\cdot Si)}+2\alpha_2^{(Si\cdot H)}$	10.20	10.15	10.29	10.42

One can see in Table A-3.4.4 that the system of 23 equations defining the overdetermined system is unstable. For example, the very small difference in the spring constants calculated using GVB and R-CI methods induce major changes in $\alpha_1^{(Si\cdot Si)}$ and $\alpha_2^{(Si\cdot H)}$. One can see in Table A-3.4.2 that in eleven modes, $\alpha_2^{(Si\cdot H)}$ appears in the combination $\alpha_1^{(Si\cdot Si)}+2\alpha_2^{(Si\cdot H)}$. This combination is much more stable than either one of its components separately, as can be seen in the last row of Table A-3.4.4. Moreover, $\alpha_1^{(Si\cdot Si)}$ is over an order of magnitude larger than any of the other parameters. Therefore, any small change in the spring constants of the modes involving $\alpha_1^{(Si\cdot Si)}$ is coupled very strongly to $\alpha_2^{(Si\cdot H)}$. To overcome this instability, one should first find the approximate values of the smaller parameters. These parameters are $\alpha_2^{(Si\cdot Si)}$, $\alpha_2^{(Si\cdot H)}$, $\alpha_2^{(H\cdot H)}(1)$, $\alpha_2^{(H\cdot H)}(2)$, and $\beta^{(Si\cdot Si)}(1-1/12A^{(Si\cdot Si)})$. They should be obtained only from these modes that do not involve $\alpha_1^{(Si\cdot Si)}$, and later these values should be reinserted as extra conditions to the overdetermined

system, to find $\alpha_1^{(Si\cdot Si)}$. There are altogether eight modes that do not involve $\alpha_1^{(Si\cdot Si)}$, namely, modes $4-7, 16, 18, 20$ and 21. In all of them $\alpha_2^{(Si\cdot H)}$ and $\alpha_2^{(H\cdot H)}(2)$ appear in the combination $\alpha_2^{(Si\cdot H)} + \alpha_2^{(H\cdot H)}(2)$. Therefore, one cannot separate these two variables, and we shall assume, ad-hoc, that they are equal. Using a least square fit method, the values of these parameters were found, and later these values were used to find $\alpha_1^{(Si\cdot Si)}$. These new set of parameters is given in Table A–3.4.5.

TABLE A–3.4.5. Parameters of the Vasil'ev model fitted to the cluster calculations in a stable way. First the smaller parameters were obtained, then, in a second iteration, $\alpha_1^{(Si\cdot Si)}$ was determined. All the parameters are given in units of $eV\cdot\mathring{A}^{-2}$.

	HF	GVB	R-CI	GVB-CI
$\alpha_1^{(Si\cdot Si)}$	8.65	8.63	8.57	8.76
$\alpha_2^{(Si\cdot Si)}$	0.593	0.449	0.533	0.430
$\alpha_2^{(Si\cdot H)}$	0.705	0.699	0.705	0.702
$\alpha_2^{(H\cdot H)}(1)$	-0.022	-0.019	-0.014	-0.014
$\alpha_2^{(H\cdot H)}(2)$	0.705	0.699	0.705	0.702
$\beta^{(Si\cdot Si)}\left(1-\frac{1}{12A^{(Si\cdot Si)}}\right)$	0.430	0.503	0.365	0.411